

Title	Thin film technology for optoelectronics and their thermal management
Authors	Quan, Zhiheng
Publication date	2017
Original Citation	Quan, Z. 2017. Thin film technology for optoelectronics and their thermal management. PhD Thesis, University College Cork.
Type of publication	Doctoral thesis
Rights	© 2017, Zhiheng Quan. - <a href="http://creativecommons.org/licenses/by-nc-nd/3.0/">http://creativecommons.org/licenses/by-nc-nd/3.0/</a>
Download date	2024-04-26 02:44:01
Item downloaded from	<a href="https://hdl.handle.net/10468/4053">https://hdl.handle.net/10468/4053</a>

# **Thin film technology for optoelectronics and their thermal management**

Zhiheng Quan

A thesis submitted in fulfilment of the requirements for the degree of  
Doctor of Philosophy



**NATIONAL UNIVERSITY OF IRELAND, CORK**

School of Engineering

Department of Electrical and Electronic Engineering

May 2017

Supervisors: Prof. Peter J. Parbrook

Mr. Brian Corbett

Head of School of Engineering: Prof. William P. Marnane



## **Declaration**

This thesis is the candidate's own work and has not been submitted for another degree, either at the University College Cork or elsewhere.

Zhiheng Quan

## Abstract

Thin-film semiconductor optoelectronics are important for applications from communication, solid-state lighting, and wearable electronics to biomedical sensors. It is now possible to separate the micrometer-thick device layers from their native substrate and transfer them onto new platforms to optimise system performance and integration. The understanding of thermal management for such devices is very important to control the junction temperature effectively.

In this thesis, the laser-lift-off technique was theoretically and experimentally studied for GaN and AlGaIn layers. The temperature distribution at the III-nitride/sapphire interface induced by the absorption of 248-nm KrF excimer laser pulse energy was simulated to verify the experimental results. A 1.5- $\mu\text{m}$ -thick Si-doped n-type  $\text{Al}_{0.6}\text{Ga}_{0.4}\text{N}$  membrane was separated from a (0001) c-plane sapphire substrate and then bonded with eutectic  $\text{Au}_{0.8}\text{Sn}_{0.2}$  alloys to a (100) Si substrate. The electrical behavior of Ti/Al/Ti/Au contacts on the N-polar n- $\text{Al}_{0.6}\text{Ga}_{0.4}\text{N}$  membrane was characterized. Furthermore, free-standing semipolar (11 $\bar{2}$ 2) InGaIn/GaN light-emitting diodes (LEDs) emitting at 445 nm were first realized by separation from patterned (10 $\bar{1}$ 2) r-plane sapphire substrate using LLO. The LEDs showed a turn-on voltage of 3.6 V and output power of 0.87 mW at 20 mA. Electroluminescence measurements showed stronger emission intensity along the  $[11\bar{2}3]_{\text{InGaIn/GaN}}$  direction than along the  $[1\bar{1}00]_{\text{InGaIn/GaN}}$  direction. The polarization anisotropy was estimated to be 0.14. The small-signal bandwidth at -3 dB of the LEDs is in excess of 150 MHz at 20 mA and a back-to-back data transmission rate at 300 Mbps is demonstrated. This indicates that the LEDs can be used in visible light free-space communications.

For thermal management of thin-film optoelectronics, an AlGaAs/GaAs based laser diode was investigated. The 2-dimensional temperature distribution and particularly the junction temperature of a transfer-bonded AlGaAs/GaAs based laser diode were simulated; where the power dissipation, the thermal resistance of different cavity lengths and configurations (e.g. thickness of p-metal,  $\text{SiO}_2$  passivation layer and substrate) and different interposers were investigated. This can be utilized to optimize the design of device and carrier substrate for efficient thermal management of thin film optoelectronics.

## Acknowledgements

First and foremost I would like to express my sincerest thanks to my PhD supervisors, Mr. Brian Corbett and Prof. Peter J. Parbrook for giving me the opportunity to pursue a PhD in their group at Tyndall National Institute. I am very grateful for their guidance, advice, support and encouragement during my PhD study, and their efforts of helping me to understand the intricacies of research which prepared me for my future endeavors.

Many thanks go to my group members who were always ready to help whenever I met difficulties in fabrication and characterization, especially Mr. Pleun Maaskant, Dr. Mahbub Akhter, Dr. Donagh O'Mahony, Dr. Vitaly Zubialevich, Dr. Van Duc Dinh, and Dr. Brendan Roycroft. I would like to thank Dr. Vitaly Zubialevich and Dr. Van Duc Dinh for III-nitride materials epitaxial growth and characterization, and Dr. Michele Conroy for taking SEM images. Furthermore, Mr. Pleun Maaskant, Dr. Mahbub Akhter, Dr. Brendan Roycroft, Dr. Silvino Presa and Pietro Pamili provided technical advice on device process, training and advice on measurements which has been greatly appreciated. Especially, I would like to thank Dr. Van Duc Dinh for proof reading and giving comments on my thesis.

I would like to acknowledge my friends in Ireland for their company, Zixiang Cong, Xiao Cheng, Xingcan Wang Yukui Yu, Yangxing Ou, Yan Zhao, and Nan Ye in Cork. I am also indebted to Mr. Marcus Mooney and Dr. Mark Gubbins for hosting me in Seagate Technology's Research and Development department in Derry, Northern Ireland, where I have spent my third year of my PhD training. I would like to especially thank Dr. Xuefeng Hu, Dr. Xintong Xu, Dr. Zhiran Wang, Dr. Tuyuan Cheng, and Dr. Lu Zhang in Derry for their assistances during my visit in Seagate.

Finally, I would like to thank my parents, Ms. Shuqin Zhang and Mr. Youcai Quan, for their selfless loving concerns, firm trust in me, and support without any complaint over all the time. I also would like to thank my girlfriend Ms. Rui Wang for her kindness, patience, encouragement and being always willing to share my thoughts. I accredit any success to their inspiration and encouragement, which has always motivated me to work hard and achieve the best that I am capable of.

## List of Publications

### Journal publications

D. V. Dinh, **Z. H. Quan**, B. Roycroft, P. J. Parbrook and B. Corbett, “GHz bandwidth semipolar (11-22) InGaN/GaN light-emitting diodes,” *Optics Letters*, vol. 41, no. 24, pp. 5620-5763, Dec. 2016.

**Z. H. Quan**, D. V. Dinh, S. Presa, B. Roycroft, A. Foley, M. Akhter, D. O’Mahony, P. P. Maaskant, M. Caliebe, F. Scholz, P. J. Parbrook and B. Corbett, “High bandwidth freestanding semipolar (11-22) InGaN/GaN light emitting diodes”, *IEEE Photonics Journal*, vol. 8, no. 5, pp. 1-8, Oct. 2016.

**Z. H. Quan**, J. Justice, M. Mooney, M. Gubbins, P. J. Parbrook and B. Corbett, “Thermal modeling of transfer-bonded thin film GaAs laser diode”, *IET Optoelectronics*, vol. 10, no. 2, pp. 51-56, Apr. 2016.

M. Akhter, P. Pampili, V. Z. Zubialeovich, C. Eason, **Z. H. Quan**, P. P. Maaskant, P. J. Parbrook and B. Corbett, “Over 20 MHz modulation bandwidth on 250 nm emission of AlGaIn micro-LEDs”, *Electronics Letters*, vol. 51, no. 4, pp. 354-355, 2015.

### Conference publications

B. Corbett, **Z. H. Quan**, D. V. Dinh, G. Kozlowski, D. O'Mahony, M. Akhter, S. Schulz, P. J. Parbrook, P. Maaskant, M. Caliebe, M. Hocker, K. Thonke, F. Scholz, M. Pristovsek, Y. Han, C. J. Humphreys, F. Brunner, M. Weyers, T. M. Meyer and L. Lymperakis, “Development of semipolar (11-22) LEDs on GaN templates”, *Proc. SPIE 9768, Light-Emitting Diodes: Materials, Devices, and Applications for Solid State Lighting XX*, 97681G, Mar. 2016.

## Table of contents

Declaration .....	i
Abstract .....	ii
Acknowledgements .....	iii
List of Publications .....	iv
Table of contents .....	v
List of Figures .....	viii
List of Tables.....	xv
List of Acronyms .....	xvi
List of used parameters .....	xvii
 <b>Chapter 1 Introduction.....</b>	 <b>1</b>
1.1 Overview of thin film optoelectronics emitters.....	1
1.2 The state of art of laser lift-off on III-nitride materials .....	7
1.3 Summary .....	11
1.4 Structure of this thesis .....	13
1.5 References .....	14
 <b>Chapter 2 Development of laser lift-off for nitride materials .....</b>	 <b>21</b>
2.1 Overview of laser lift-off.....	21
2.1.1 GaN epitaxial thin film lift-off.....	21
2.1.2 Laser lift-off principle.....	23
2.1.3 The laser beam interaction on GaN .....	24
2.1.4 Thermal analysis .....	25
2.2 Laser lift-off method and experiment.....	34
2.2.1 Laser lift-off apparatus.....	34
2.2.2 Excimer laser beam spot energy density.....	36
2.2.3 Wafer attachment and experiments.....	41
2.2.3-1 Review of wafer attachment for laser lift-off .....	41
2.2.3-2 Experimental results .....	44
2.3 Characterization methods for laser lift-off .....	45
2.3.1 Nomarski microscopy .....	46
2.3.2 Scanning Electron Microscope (SEM) .....	47
2.3.3 X-ray diffraction (XRD) .....	48
2.4 Conclusions .....	49
2.5 References .....	50
 <b>Chapter 3 Fabrication of free-standing semipolar (11<math>\bar{2}</math>2) InGaN LEDs.....</b>	 <b>55</b>
3.1 Introduction .....	55
3.2 Fabrication of free-standing semipolar (11 $\bar{2}$ 2) GaN membrane .....	57
3.2.1 Semipolar GaN thin film transfer and laser lift-off process .....	58
3.2.2 Chemical-mechanical planarization.....	60

3.2.2-1 Overview of chemical mechanical planarization.....	60
3.2.2-2 Chemical mechanical planarization on FS-GaN membrane.....	62
3.3 Fabrication of free-standing (11 $\bar{2}2$ ) InGa <sub>N</sub> /Ga <sub>N</sub> MQW LEDs.....	64
3.3.1 Structure of LED epitaxial layers .....	65
3.3.2 Fabrication process .....	66
3.4 Electro-optical characterization of free-standing semipolar LEDs .....	72
3.4.1 Current-voltage characteristics of p-contacts .....	72
3.4.2 Electrical characteristics .....	73
3.4.3 Fluorescence microscopy.....	76
3.4.4 Electroluminescence measurements .....	77
3.4.5 Optical polarization measurement .....	78
3.4.6 Electro-optical bandwidth measurement .....	81
3.4.6-1 Small signal bandwidth.....	81
3.4.6-2 Data transmission measurement .....	85
3.5 Conclusions .....	87
3.6 References .....	87
<b>Chapter 4 Fabrication of vertical conduction AlGa<sub>N</sub> membrane.....</b>	<b>93</b>
4.1 Introduction .....	93
4.2 Fabrication of AlGa <sub>N</sub> membrane by laser lift-off.....	95
4.2.1 Sacrificial layer.....	96
4.2.2 Laser lift-off process for Al <sub>x</sub> Ga <sub>1-x</sub> N epitaxial thin film .....	97
4.2.3 Thermal analysis .....	101
4.3 Wafer bonding for AlGa <sub>N</sub> and experiment.....	108
4.3.1 Eutectic reaction of Au <sub>0.8</sub> Sn <sub>0.2</sub> foil to Au layer.....	108
4.3.2 Wafer bonding system and laser lift-off experiment .....	109
4.4 Experimental characterizations .....	114
4.4.1 Surface morphology of AlGa <sub>N</sub> membranes after LLO .....	114
4.4.2 X-ray diffraction scan intensity of layer structure after LLO .....	115
4.4.3 I-V characteristics of metal contact on N-face n-AlGa <sub>N</sub> .....	116
4.5 Conclusions .....	118
4.6 References .....	119
<b>Chapter 5 Thermal modeling of transfer-bonder GaAs laser diode .....</b>	<b>123</b>
5.1 Introduction .....	123
5.2 The structure of the laser diode .....	126
5.3 Thermal models of the laser diode .....	127
5.3.1 Analytical modeling of laser diode.....	129
5.3.2 Numerical modeling of laser diode.....	133
5.3.2-1 Introduction of numerical approach.....	133
5.3.2-2 FEM thermal model of the laser diode .....	135
5.4 Thermal analysis of laser diode on different types of submount.....	139
5.5 Conclusions .....	141



5.6 References .....	141
<b>Chapter 6 Conclusions and future work</b> .....	143
6.1 Conclusions .....	143
6.2 Future work .....	145

## List of Figures

Figure 1.1 Cross section of the thin Fabry-Perot AlInGaAs laser (etch facet) with an AlAs sacrificial layer that can be selectively removed by HCl.	2
Figure 1.2 Energy bandgap of III-V zinc blende and III-nitride wurtzite semiconductor compounds employing Al, In and Ga, versus lattice constant and their corresponding photoluminescence emission wavelength at room temperature. Solid lines indicate direct-band gap compounds, dotted line indicate indirect-band gap compounds and dashed lines are estimated due to relative uncertainty in bowing parameters.	3
Figure 1.3 III-nitride materials with different surface orientations. The $\alpha$ angles were calculated for the direction of inclined plane with respect to c-plane (0001) ( $\alpha = 0^\circ$ ).	11
Figure 2.1 (a) Schematic view of band-gap structure of sapphire/GaN. (b) Schematic view of LLO process. High energy intensity laser pulse enters the sample through sapphire substrate that thermally decomposes a thin GaN layer at the GaN/sapphire interface.	24
Figure 2.2 Schematic of 1-D laser induced heat conduction model, the reference point $z = 0$ sets at the GaN/sapphire interface.	26
Figure 2.3 Simulated maximum temperature at the GaN/sapphire interface for a KrF laser pulse irradiation of different pulse durations at different laser pulse energy densities.	31
Figure 2.4 Simulated temperature distribution of GaN film irradiated at the GaN/sapphire interface for a KrF laser pulse of different pulse duration at energy density of $400 \text{ mJ/cm}^2$ .	31
Figure 2.5 Simulated temperature in the GaN film at different depth ( $z$ ) from the GaN/sapphire interface for a 6 ns KrF laser pulse, at an energy density of $400 \text{ mJ/cm}^2$ .	32
Figure 2.6 Simulated temperature at the GaN/sapphire interface vs. depth for a range of time for a pulse energy density of $400 \text{ mJ/cm}^2$ (for 6 ns pulse).	33
Figure 2.7 Simulated temperature distribution of GaN film irradiated at the GaN/sapphire interface for a laser pulse energy density of $400 \text{ mJ/cm}^2$ .	33
Figure 2.8 The LLO apparatus with KrF excimer laser system (a) photograph of the set-up (b) Schematic of the light delivery of the excimer laser system.	35
Figure 2.9 Schematic of optical distance adjustment to vary the beam image area.	37
Figure 2.10 Photograph of beam spots (size scale) of laser pulse at different demagnification factors (DM) of LLO apparatus on photoresist.	38
Figure 2.11 Optical microscope image of a beam spot irradiated at $400 \text{ mJ/cm}^2$ on photoresist (PR).	39

Figure 2.12 Experimental results of beam spot area and corresponding laser pulse energy density at different DM factors on photoresist (PR).-----	39
Figure 2.13 The thermal decomposed thickness of GaN calculated for a single incident laser pulse energy densities from 400 to 800 mJ/cm <sup>2</sup> for $\tau_i = 25$ ns. -----	40
Figure 2.14 Schematic of adhesive bonding-----	42
Figure 2.15 Schematic diagram of soldering metal bonding method: (a) Sn <sub>0.6</sub> Pb <sub>0.6</sub> with electroplated Cu layer and (b) Au <sub>0.8</sub> Sn <sub>0.2</sub> with thin Au layer.-----	44
Figure 2.16 Transferred GaN LED epitaxial layer (~ 4- $\mu$ m-thick) on a carrier substrate structures in different bonding methods and processed by the use of LLO with a single laser pulse irradiation at the energy density 500 mJ/cm <sup>2</sup> : (a) GaN/epoxy adhesive/glass slide; (b) GaN/Ti/Au/Au/Ti/Si substrate (Au-Au direct bonding) (c) GaN/Ti/Au/Cu/Sn <sub>0.6</sub> Pb <sub>0.4</sub> /Cu/Au/Ti/Si substrate)-----	45
Figure 2.17 Photograph of beam spots at GaN/sapphire interface on GaN wafer after excimer laser pulse irradiation at $E_i$ over threshold energy density.-----	46
Figure 2.18 Cross-sectional SEM micrograph of (a) a GaN LED epitaxial layer grown on sapphire bonded to a glass slide with epoxy, (b) the GaN LED epitaxial layer after LLO bonded to the glass slide with epoxy. A single laser pulse energy density irradiated through the sapphire to separate the GaN at 500 mJ/cm <sup>2</sup> .-----	48
Figure 2.19 Schematic diagram of XRD setup. -----	48
Figure 2.20 XRD $\omega$ -2 $\theta$ scans of c-plane GaN LED sample before and after lift-off from sapphire substrate. A pulse of energy density 500 mJ/cm <sup>2</sup> was used for LLO.-----	49
Figure 3.1 Cross section of HVPE GaN/sapphire sample (in the $m = (1\bar{1}00)$ -plane of a direction of $o[11\bar{2}2]$ , the directions $x[11\bar{2}0]$ , $c'[1\bar{1}23]$ and $c[0001]$ projected onto the sample surface, all given directions relate to the crystal structure of GaN. (a) Schematic of the layered structure of the HVPE template (inset: GaN crystal structure), (b) SEM image.-----	57
Figure 3.2 Wafer bonding of semipolar (11 $\bar{2}2$ ) GaN template wafer sample using wax adhesive.-----	58
Figure 3.3 Schematic of laser lift-off on semipolar GaN on patterned sapphire substrate (b) Photography of the top view of a ~ 50 $\mu$ m thick free-standing semipolar GaN membrane (size 1.5 $\times$ 1 cm <sup>2</sup> ).-----	59
Figure 3.4 Nomarski microscopy image of a sample after LLO (a) back surface and (b) top surface.-----	60
Figure 3.5 Schematic diagram of CMP. -----	61
Figure 3.6 G & P POLI-500 CMP system. -----	61
Figure 3.7 CMP parameters.-----	62
Figure 3.8 Free-standing semipolar GaN membrane (size 1.5 $\times$ 1 cm <sup>2</sup> ) bonded on Si substrate (a) before CMP and (b) after CMP-----	63

Figure 3.9 The film debonding process for semipolar HVPE GaN thin film after CMP.	63
Figure 3.10 Optical microscope images of back surface morphology of free-standing (11 $\bar{2}2$ ) GaN: (a) before CMP, (b) after CMP.	64
Figure 3.11 The schematic diagram of epitaxial structure.	65
Figure 3.12 Schematic diagram of the LED structure fabrication procedure.	66
Figure 3.13 Schematic of 3D view of standard substrate emission LEDs on sapphire substrate. Example of (a) Type A and (b) Type B.	67
Figure 3.14 Nomarski microscopy image of the fabricated semipolar (11 $\bar{2}2$ ) substrate emission LEDs on sapphire substrate.	68
Figure 3.15 Schematic diagram of the fabrication process for obtaining free-standing (11 $\bar{2}2$ ) LEDs by the use of LLO and CMP techniques. (a) Fabrication of LEDs on patterned sapphire substrate ( $300 \times 300 \mu\text{m}^2$ mesa LED chip on PSS), (b) Wafer flip-bonded with thermal adhesive on glass carrier substrate, (c) Laser lift-off of LED wafer and removal of the PSS, (d) De-bond sample and dissolve the adhesive layer, (e) Free-standing LEDs with grooves (LLO-LED), (f) Flip-bond and CMP, (g) De-bond and dissolve adhesive layer, (h) Free-standing LEDs without grooves (CMP-LED).	69
Figure 3.16 Photograph images of the LED wafer in $1 \times 1 \text{ cm}^2$ area bonded with wax adhesive layer (crystal-bond 509) on a glass slide after LLO (a) the back surface before cleaning and (b) the back surface after cleaning in HCl: DI (1:1) solution.	70
Figure 3.17 Nomarski microscopy images of the back surface of the sample wafer (a) before/ (b) after surface cleaning in HCl: DI (1:1) for 2 min.	70
Figure 3.18 Nomarski microscopy image of the back surface of the (11 $\bar{2}2$ ) LLO-LEDs wafer after CMP.	71
Figure 3.19 Photograph images of the light emission from top side of a free-standing semipolar LED device (with stripes) on the wafer (a) under room light ambient and (b) under dark ambient at injection current 5 mA.	71
Figure 3.20 Current-voltage I-V characteristics of a $50 \mu\text{m}$ diameter disk contact with a gap of $280 \mu\text{m}$ on c-TLM pattern (inset) of Pd (40nm) as-deposited and Ni (1 nm)/Ag (100 nm)/Ni (2 nm) before and after anneal at $500^\circ\text{C}$ .	73
Figure 3.21 L-I and V-I characteristics of the LEDs before LLO/after LLO measured with NA = 0.5 and after CMP (measured with NA = 1).	74
Figure 3.22 log-I-V of free-standing semipolar GaN LED after CMP.	75
Figure 3.23 FM images ( $560 \times 560 \mu\text{m}^2$ ) of the backside of the LEDs (a) after LLO (inset: the photography in top view of the fabricated LEDs, where area 1 is p-metal and area 2 is n-metal) and (b) after CMP. (Exposure time of 100 ms).	77

Figure 3.24 (a) EL spectra of the free-standing semipolar LED as a function of current up to 10 mA ( $11 \text{ A/cm}^2$ ); (b) Normalized EL spectra of the freestanding semipolar LEDs at 1 and 10 mA.	78
Figure 3.25 Schematic diagram of the experimental set-up to measure the optical polarization revolved EL spectra of the LEDs.	79
Figure 3.26 EL intensity with polarization angle for the freestanding semipolar ( $11\bar{2}2$ ) InGa <sub>N</sub> /Ga <sub>N</sub> LED (LLO-LED and CMP-LED). The inset shows (a) anisotropic light emission profile after LLO and (b) after CMP more uniform spot like emission.	80
Figure 3.27 EL intensity at polarizer angle of $0^\circ$ and $90^\circ$ for the freestanding semipolar ( $11\bar{2}2$ ) InGa <sub>N</sub> /Ga <sub>N</sub> LED (LLO-LED).	81
Figure 3.28 A schematic diagram of bandwidth measurement experimental set-up.	82
Figure 3.29 Normalized frequency response of LEDs at different injection current: (a) $300 \times 300 \mu\text{m}^2$ FS-LED and (b) $300 \times 300 \mu\text{m}^2$ c-plane LED.	82
Figure 3.30 -3dB small signal signal bandwidth of the ( $\circ$ ) $300 \times 300 \mu\text{m}^2$ freestanding ( $11\bar{2}2$ ) LED and ( $\square$ ) $300 \times 300 \mu\text{m}^2$ c-plane Ga <sub>N</sub> LED as compared with the high speed Ga <sub>N</sub> based LEDs reported in literature. ( $\Delta$ ) Reference [56] $300 \times 300 \mu\text{m}^2$ ( $11\bar{2}2$ ) blue LED, ( $\nabla$ ) Reference [56] $300 \times 300 \mu\text{m}^2$ ( $11\bar{2}2$ ) green LED, ( $\diamond$ ) 72- $\mu\text{m}$ -diameter c-plane Ga <sub>N</sub> LED, ( $\star$ ) 44- $\mu\text{m}$ -diameter c-plane Ga <sub>N</sub> LED, ( $\diamond$ ) 75- $\mu\text{m}$ -diameter c-plane Ga <sub>N</sub> LED.	84
Figure 3.31 A schematic diagram of data transmission measurement under large signal modulation experimental set-up.	85
Figure 3.32 Eye diagrams of the free-standing semipolar ( $11\bar{2}2$ ) InGa <sub>N</sub> /Ga <sub>N</sub> LED at 300 Mbps and 200 Mbps at $I_{\text{inject}} = 20 \text{ mA}$ .	86
Figure 4.1 Schematic diagrams of an AlGa <sub>N</sub> -based DUV LED structure with sacrificial layer on a sapphire substrate for fabrication of vertical conduction thin-film LEDs: (a) DUV LED ( $\lambda=322 \text{ nm}$ ) using a thin-GaN buffer (thickness $< 150 \text{ nm}$ ) as both a seeding and LLO sacrificial layer, (b) DUV LED ( $\lambda=325 \text{ nm}$ , $280 \text{ nm}$ ) using a Ga <sub>N</sub> buffer as a sacrificial layer with an AlN interlayer, and (c) DUV LED ( $\lambda=280 \text{ nm}$ ) using an AlN/Al <sub>0.8</sub> Ga <sub>0.2</sub> N superlattice on AlN buffer.	94
Figure 4.2 Schematic diagrams of n-type AlGa <sub>N</sub> structure grown on AlN buffer layer on double polished (0001) sapphire substrate for laser-lift-off: (a) n-Al <sub>0.6</sub> Ga <sub>0.4</sub> N layer with Ga <sub>N</sub> interlayer, (b) n-Al <sub>0.75</sub> Ga <sub>0.25</sub> N layer with n-Al <sub>0.5</sub> Ga <sub>0.5</sub> N interlayer and (c) n-Al <sub>0.6</sub> Ga <sub>0.4</sub> N layer.	97
Figure 4.3 Schematic view of (a) band diagram of photoabsorption AlGa <sub>N</sub> layer on AlN/sapphire, (b) the view of LLO process on an n-Al <sub>x</sub> Ga <sub>1-x</sub> N ( $x \leq 60\%$ ). High intensity laser pulses enter the sample visa the sapphire substrate and AlN buffer layer thermally decompose a thin AlGa <sub>N</sub> layer at the AlGa <sub>N</sub> /AlN interface.	98

Figure 4.4 Measured optical absorption spectra at RT of n-Al <sub>0.6</sub> Ga <sub>0.4</sub> N layer and n-Al <sub>0.66</sub> Ga <sub>0.34</sub> N layer grown on AlN/sapphire. The insertion (a) the sample structure of n-Al <sub>0.6</sub> Ga <sub>0.4</sub> N layer, (b) the sample structure of n-Al <sub>0.66</sub> Ga <sub>0.34</sub> N layer.-----	99
Figure 4.5 Measured transmission spectra of n-Al <sub>0.6</sub> Ga <sub>0.4</sub> N layer and n-Al <sub>0.66</sub> Ga <sub>0.34</sub> N layer samples both grown on AlN/sapphire.-----	100
Figure 4.6 Measured transmittance of n-Al <sub>0.75</sub> Ga <sub>0.25</sub> N/n-Al <sub>0.5</sub> Ga <sub>0.5</sub> layer grown on AlN/sapphire.-----	101
Figure 4.7 Al <sub>x</sub> Ga <sub>1-x</sub> N thermal conductivity as a function of Al mole fraction x at room temperature.-----	102
Figure 4.8 Temperature dependent thermal conductivities of Al <sub>x</sub> Ga <sub>1-x</sub> N layer shown as (a) experimental measured thermal conductivities of HVPE GaN, Al <sub>0.09</sub> Ga <sub>0.9</sub> N, Al <sub>0.23</sub> Ga <sub>0.77</sub> N, Al <sub>0.33</sub> Ga <sub>0.67</sub> N, and Al <sub>0.4</sub> Ga <sub>0.6</sub> N layers in the temperature range from 80 to 400 K, (b) simulated thermal conductivity as a function of temperature for alloy Al <sub>x</sub> Ga <sub>1-x</sub> N with x=1.0, 0.9, 0.5, and 0.-----	103
Figure 4.9 Simulated maximum temperature induced in Al <sub>0.6</sub> Ga <sub>0.4</sub> N/AlN/sapphire for a 6 ns KrF laser pulse at different energy density. Inset: schematic of 1-D laser induced heat conduction model with reference point z=0 at Al <sub>0.6</sub> Ga <sub>0.4</sub> N/AlN interface.-----	105
Figure 4.10 Simulated temperature in the Al <sub>0.6</sub> Ga <sub>0.4</sub> N film at different time (t) from Al <sub>0.6</sub> Ga <sub>0.4</sub> N/AlN interface for a 6 ns KrF laser pulse, at energy density of 600 mJ/cm <sup>2</sup> .-----	106
Figure 4.11 Simulated temperature at the Al <sub>0.6</sub> Ga <sub>0.4</sub> N/AlN interface v.s. depth (z) for a 6 ns KrF laser pulse at energy density of 600 mJ/cm <sup>2</sup> .-----	106
Figure 4.12 The temperature distribution of Al <sub>0.6</sub> Ga <sub>0.4</sub> N film irradiated at the Al <sub>0.6</sub> Ga <sub>0.4</sub> N/AlN interface for a 6 ns laser pulse at energy density 600 mJ/cm <sup>2</sup> .-----	106
Figure 4.13 The phase diagram of Au-Sn alloy.-----	108
Figure 4.14 Wafer-bonding system.-----	110
Figure 4.15 (a) Schematic of bonding process for AlGaIn wafer onto Si substrate and (b) Au <sub>0.8</sub> Sn <sub>0.2</sub> soldering foil sheet.-----	109
Figure 4.16 Au <sub>0.8</sub> Sn <sub>0.2</sub> soldering foil pieces for test sample.-----	111
Figure 4.17 The temperature profile during the Au-Sn reflow. The yellow line is the setting temperature; the green line is the tracked temperature profile from the bottom heater and the top heater.-----	111
Figure 4.18 (a) Schematic of an n-Al <sub>0.6</sub> Ga <sub>0.4</sub> N wafer sample after bonding and (b) Photograph of an n-Al <sub>0.6</sub> Ga <sub>0.4</sub> N wafer sample after bonding.-----	112
Figure 4.19 (a) Schematic of c-TLM patterns deposited on N-polar n-Al <sub>0.6</sub> Ga <sub>0.4</sub> N wafer sample bonded on Au coated Si substrate, (b) Photograph of c-TLM patterns deposited on N-polar n-Al <sub>0.6</sub> Ga <sub>0.4</sub> N layer.-----	113

Figure 4.20 Optical microscope image of c-TLM patterns deposited on the N-polar  $n\text{-Al}_{0.6}\text{Ga}_{0.4}\text{N}$  wafer sample bonded on Au coated Si substrate.-----113

Figure 4.21 (a) Transferred GaN interlayer/ $n\text{-Al}_{0.5}\text{Ga}_{0.5}\text{N}$  thin film by LLO on a Si substrate with a single laser pulse energy density of  $500 \text{ mJ/cm}^2$ , (b) transferred  $n\text{-Al}_{0.5}\text{Ga}_{0.5}\text{N}/n\text{-Al}_{0.75}\text{Ga}_{0.25}\text{N}$  film by LLO on a Si substrate at  $600 \text{ mJ/cm}^2$  and (c) transferred  $n\text{-Al}_{0.6}\text{Ga}_{0.4}\text{N}$  film by LLO on a Si substrate at  $600 \text{ mJ/cm}^2$ . --114

Figure 4.22 XRD  $2\theta$  scan of (red plot) an as-grown  $n\text{-Al}_{0.6}\text{Ga}_{0.4}\text{N}$  sample, (green plot) an as-grown sample after LLO, and (blue plot) the sample after LLO with NaOH clean.-----115

Figure 4.23 XRD  $\omega$ - $2\theta$  scans (blue plot) of an as-grown  $n\text{-Al}_{0.6}\text{Ga}_{0.4}\text{N}$  sample of, (green plot) an as-deposited Ti/Al/Ti/Au on the as-grown sample and (red plot) the sample after LLO.-----116

Figure 4.24 I-V characteristics of Ti/Al/Ti/Au contact to metal-polar  $n\text{-Al}_{0.6}\text{Ga}_{0.4}\text{N}$  template.-----117

Figure 4.25 Schematic of I-V characterization on the metal contacts of N-polar  $n\text{-AlGaN}$ .-----117

Figure 4.26 I-V characteristics of the as-deposited Ti/Al/Ti/Au metal contacts to N-polar  $n\text{-Al}_{0.6}\text{Ga}_{0.4}\text{N}$ .-----118

Figure 5.1 Optical microscope image (top view) of (a) an array of lasers tethered to the GaAs growth substrate after the removal of sacrificial layer(AlAs), and some laser devices have been picked up by the use of transfer-printing elastomer stamp[6]; (b) a transfer-bonded ridge laser on part processed AlTiC substrate of a magnetic recording read-write head transducer for data storage hard drive.-----124

Figure 5.2 Schematic of the GaAs based MQW LD cross-section and the location of the heat source.-----126

Figure 5.3 Schematic of a simplified laser thermal model consisting of heat flow (solid line with arrow) from a uniform heat source in the active region and the heat flow spreads from the active region both upward and downward. The device length, width and source width of the laser are labelled as  $L$ ,  $W$  and  $w$ . Other terms are as described in the text. (a) Schematic of the simplified laser structure used for the analytical model and (b) Device with symmetry at heat core position.----- 130

Figure 5.4 Thermal resistance network of the simplified analytical laser model.---132

Figure 5.5 Simulated temperature profile and thermal contour plots of a laser with  $40 \text{ mW}$  heat load ( $L=200 \mu\text{m}$ ) for (a) Laser device with  $100 \mu\text{m}$  thick GaAs substrate; inset: thermal contour plot at the ridge region, and (b) Transfer-bonded laser (inset: thermal contour plot at the ridge region)-----136

Figure 5.6 Comparison of the thermal resistances of a laser as a function of cavity length for the configuration with  $100\text{-}\mu\text{m}$ -thick GaAs substrate and with substrate fully removed and different thickness of p-metal (Au layer) and  $\text{SiO}_2$  dielectric layer on a perfect heat sink at constant  $40 \text{ mW}$  heat load by FEM model. The thermal

resistance  $R_{down}$  calculated by analytical method for downward heat flow is also presented.-----137

Figure 5.7 Thermal resistance of a laser for different residual GaAs substrate thicknesses and the laser cavity length on a perfect heat sink (corresponding to the bonding on metal) by FEM model.-----138

Figure 5.8 Simulated temperature distribution of a transfer-bonded thin-film laser on 10  $\mu\text{m}$  thick submount ((a) alumina, (b) GaAs, and (c) Si at 40 mW heat load at room temperature  $T_0 = 20^\circ\text{C}$  by FEM model. A perfect heat sink is assumed on the bottom face.-----139

Figure 5.9 Simulated temperature at the junction of a transfer-bonded thin-film laser with 40 mW heat load at room temperature ( $T_0 = 20^\circ\text{C}$ ) as a function of submount thickness composed of alumina, GaAs and Si respectively.-----140



## List of Tables

Table 2.1 Materials properties of III-nitrides (e.g. wurtzite(w-) GaN, InN and AlN) and dissimilar material substrates, such as sapphire, hexagonal structure 6H-SiC, diamond structure Si and zinc blend structure GaAs .-----	23
Table 2.2 Thermal and optical physical parameters at room temperature.-----	30
Table 4.1 Material properties used for thermal analysis of laser-lift-off on $\text{Al}_{0.6}\text{Ga}_{0.4}\text{N}$ grown on AlN/sapphire.-----	104
Table 5.1 Thermal property of the materials.-----	129
Table 5.2 The list of laser device geometry simulated-----	137

## List of Acronyms

Acronym	Definition
CMP	Chemical Mechanical Polishing
C-TLM	Circular Transmission Line Method
DM	Demagnification
EL	Electroluminescence
FEA	Finite Element Analysis
FM	Fluorescence microscopy
FS	Free-standing
HCl	Hydrochloric acid
HVPE	Hydride Vapor Phase Epitaxy
ICP	Inductively Coupled Plasma
KrF	Krypton Fluoride
LD	Laser Diode
LED	Light Emitting Diode
LEE	Light Extraction Efficiency
LLO	Laser Lift-Off
MOVPE	Metal-Organic Vapor Phase Epitaxy
MQW	Multiple-Quantum-Well
Mbps	Megabits per second
PDE	Partial Differential Equation
PL	Photoluminescence
PSS	Patterned Sapphire Substrates
QCSE	Quantum-Confined Stark Effect
RTA	Rapid Thermal Annealing
RT	Room Temperature
SEM	Scanning Electron Microscopy
SMA	SubMiniature-version-A
TEM	Transmission Electron Microscopy
TIA	Transimpedance amplifier
Nd:YAG	Neodymium-doped yttrium aluminium garnet
UV	Ultraviolet
XRD	X-Ray Diffraction

## List of parameters used

$\lambda$	-	Wavelength
$\tau_i$	-	Laser pulse duration
$D$	-	Thermal diffusivity
$\xi$	-	Thermal diffusion length
$\rho$	-	Mass density
$C_p$	-	Thermal conductivity
$R$	-	Reflectivity
$\alpha$	-	Absorption coefficient
$\alpha_{GaN}$	-	Absorption coefficient of GaN
$I_0$	-	The incident energy of a laser pulse
$A_0$	-	The beam shaper aperture opening area
$A$	-	The exposed area of laser beam irradiation
$f$	-	Focus length of objective projection lens
$d$	-	Decomposed thickness per pulse of GaN (i.e.thermal decomposed thickness)
$E_i$	-	Incident energy density of a laser pulse
$E_{th}$	-	Threshold energy density of laser for material thermal decomposition
$\tau_R$	-	Carrier radiative recombination time
$f_{-3dB}$	-	Frequency response at – 3dB point
$Q$	-	Overall heat generated in laser diode
$P_{in}$	-	Total input power
$P_o$	-	Optical output power
$T_j$	-	Junction temperature of laser diode
$T_0$	-	Room temperature
$R_{th}$	-	Thermal resistance

# **Chapter 1**

## **Introduction**

In the recent years, in order to reduce the occupied chip area and the total power consumption in current computer processors, there is a large demand for photonic interconnects both for intrachip and interchip communications. Such interconnects can therefore help to meet the ever increasing consumer demand for new higher bandwidth online and mobile services. Secondly, heat assisted magnetic recording (HAMR) with integrated light emitter and optical delivery path has been proposed as a new technology for the purpose of higher densities for data storage on hard-disc drives [1, 2]. Furthermore, for the next generation technology of optical sensors, flexible displays, wearable semiconductor based microsystems, and biomedical or biointegrated optoelectronic devices [3-6], the fabrication of thin film semiconductor direct band-gap optoelectronics devices is vital as integrating of the direct band-gap materials onto the suitable platforms for providing the light signals will enable these applications. The thermal properties of such devices are rarely revealed and would be very important to the considerations in their thermal management.

This chapter will start with the background of thin film semiconductor optoelectronic emitter fabrication (i.e. laser diodes (LD), light emitting diodes (LED)) and epitaxial lift-off methods. Additionally, device transfer-print method technology, III-nitride materials and highlights of epitaxial lift-off research on these materials, concentrating particularly on the laser lift-off (LLO) method for GaN based LEDs will be introduced. Next, a review of thermal modeling of transfer bonded thin film GaAs based LDs is introduced. Finally, the structure of the remaining chapters in the thesis is described.

### **1.1 Overview of thin film optoelectronics emitters**

Thin film devices are attractive for photonics researchers due to the facility of integration on a heterogeneous substrate and high thermal conductivity substrate which can be more suitable for temperature control of high power devices.

For the hybrid integration of a thin film optoelectronic device, the epitaxial material of the device is separated from the original growth substrate and then transfer printing can be used by releasing the device from the source wafer and printing to another target wafer which has a different physical property compared to the source wafer [1]. Transfer printing is performed using a microfabricated stamp consisting of polymeric elastomer and glass layers. The stamp, mounted on a precision motion platform, is designed to pick up the device from the original substrate through a shear stress enhanced transfer process, which creates Van der Waals bonds between the device and the stamp. Afterwards, the device is attached on a new substrate as the printing step [1, 2]. The thinner material layer stacks potentially exert less strain after removing the sacrificial layer underneath. This provides a flat contact surface when the device is printed. Especially, after that the epitaxial thin film is stripped off and transferred onto the low thermal impedance substrate (such as silicon, Cu), the heat from the active region of the high-power thin film optoelectronics emitter can be distributed more efficiently [7].

Releasing the active layers could be the first building block to achieve the thin film device. As it is demonstrated in Fig. 1.1, an AlInGaAs quantum-well (active gain region) Fabry-Perot laser (etch facet) is fabricated in the edge emitting scheme on GaAs substrate. A 1- $\mu\text{m}$ -thick AlAs layer in between the active layers and the GaAs substrate works as a sacrificial layer. After the AlAs layer is etched by hydrochloric acid (HCl), the thin film laser device can be picked up from the source wafer substrate [1, 2, 8].

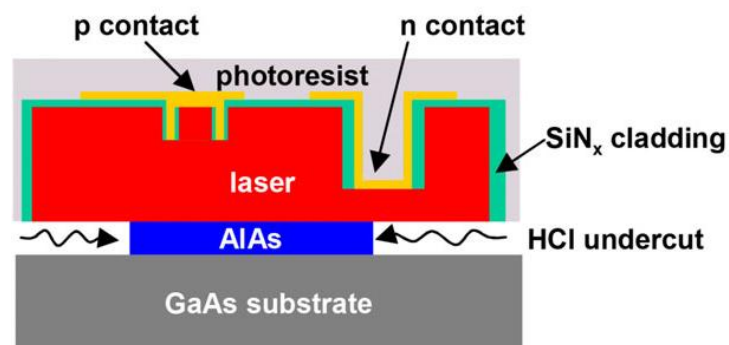


*Figure 1.1 Cross section of a thin Fabry-Perot AlInGaAs laser (etch facet) with an AlAs sacrificial layer that can be selectively removed by HCl [8].*

Therefore, the epitaxial thin film lift-off of the heterojunction from its grown substrate is recognized as the vital and challenging technology to implement the fabrication of optoelectronics devices. The materials and processing schemes are important for the envisioned and promising applications, such as Si photonics system deployment, hard drive storage and biomedical sensors etc.

Over the past 20 years, tremendous progress on high efficiency III-nitride-based optoelectronic devices working in the visible to ultraviolet spectral range has been achieved, since the good controlling of the basic material issues related to heterojunction epitaxial growth for GaN and its relevant alloys [9]. The high performance visible LEDs and LDs are starting to flood the commercial market in lighting, optical communications, medical sensors, backlighting, optical data storage devices, etc. The direct band-gap GaN ( $E_g = 3.4$  eV) compound can be alloyed with Indium (In) or Aluminum (Al) providing a range of optical emission from visible to deep ultraviolet (UV) spectral range (as shown in Fig. 1.2). Thus, the binary compound (GaN, AlN, and InN), ternary compound (AlGaIn, InGaIn and InAlIn) and quaternary (InAlGaIn) systems have promising applications for optoelectronics devices, especially blue/UV LEDs and LDs.

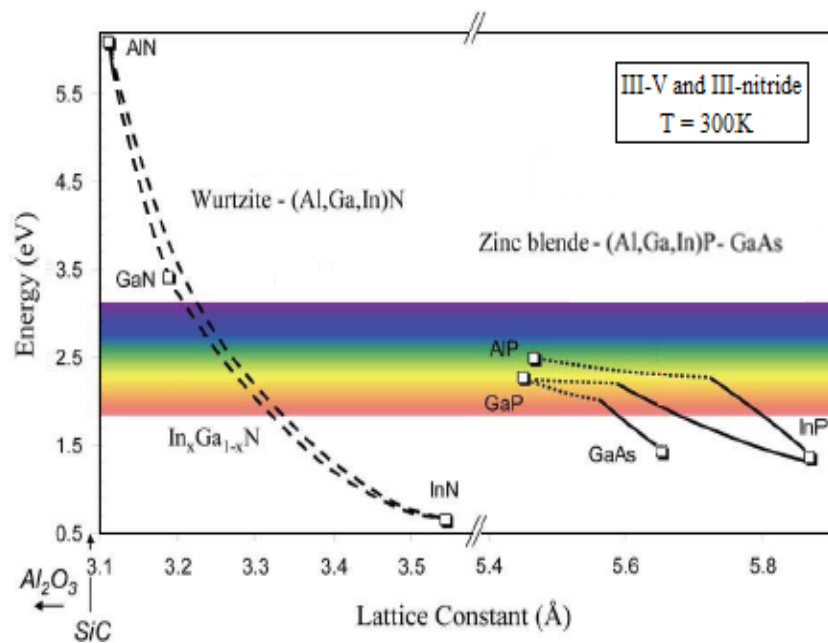


*Figure 1.2 Energy bandgap of III-V zinc blende and III-nitride wurtzite semiconductor compounds employing Al, In and Ga, versus lattice constant and their corresponding photoluminescence emission wavelength at room temperature. Solid lines indicate direct-band gap compounds, dotted lines indicate indirect-band gap compounds and dashed lines are estimated due to relative uncertainty in bowing parameters [10].*

Due to the high growth temperature for high-quality GaN crystal structure, the direct deposition onto common semiconductor substrates, such as Si and GaAs is difficult. Moreover, freestanding polar and semipolar GaN and AlN substrates are expensive and still difficult to fabricate on a large scale, so they are not suitable for mass-production. Thus, it is necessary to grow heterostructure epitaxy low-cost substrates, such as sapphire, which is the most commonly used growth substrate for III-nitrides. However, sapphire also imposes constraints on the III-nitride film quality due to the lattice mismatch, low thermal conductivity and thermal expansion coefficient mismatch. After development over several decades, high quality GaN LED epitaxy has already been achieved on c-plane (0001) sapphire substrates and remains the dominant commercial market. In recent years, the GaN LEDs are able to grow and be fabricated on Si substrates by introducing AlN nucleation layers and AlGaIn buffers [11-17]. One important practical goal is to realize such device epitaxial releasing and transfer to specific dissimilar material based deployment substrates or on large, flexible and affordable substrates, on which direct growth of nitride semiconductors with sufficient quality is problematic. Several techniques have been investigated to enable such transfer.

All of the issues mentioned above make it highly desirable to develop a process which enables a fast, reliable, and high-yield detachment of III-nitride layers from sapphire and Si dissimilar substrates. In practice, such a process will involve a sacrificial layer (as seen in Fig. 1.1 for a GaAs LD) somewhere between the substrate and the III-nitride layers, which is removed by a specific chemical or thermal treatment. Several techniques have been investigated to enable the transfer of III-nitride devices from one substrate to another. One possibility would be to deposit a sacrificial layer which makes use of selective chemical etching, e.g. AlN versus GaN in potassium hydroxide (KOH) [18]. As to the GaN based LEDs grown on Si substrate, the procedure for releasing these device from the underlaying substrate exploits the anisotropic etching to remove planes of (110) Si compared to (111) Si with wet chemical etching baths of hot KOH or tetramethylammonium hydroxide [19]. Moreover, a selective etch of Si to III-nitride layer can be realized by the use of isotropic wet etch HNA solution ( $\text{HF}:\text{HNO}_3:\text{CH}_3\text{COOH}:\text{H}_2\text{O}$ ) [20]. However, in this case the detachment of large area III-nitride pseudo-substrates would be slowed down by chemical diffusion and would impose additional boundary

conditions for the deposition of buffer layers. Alternatively, a self-detached epitaxial structure can be developed to produce separation of GaN film from sapphire substrate by thermo-mechanical expansion that is induced during cooling from the growth temperature. It is due to the accumulation of thermal stress and the lattice mismatch between GaN and sapphire [21]. In this case, a rather complex pretreatment of the wafer including lithography is needed, which limits the relevance of such a processing step for future mass production schemes. Moreover, in 2012, Kobayashi *et al.* reported that the use of a single-crystal hexagonal-boron nitride (h-BN) layer with a flat surface enables the growth of InGaN based multiple-quantum-well (MQW) LED structures and the release of the structure from the host c-plane (0001) sapphire substrate and its transfer to an indium sheet on a substrate by mechanical lift-off [22]. However, damage, the limited size of the released GaN and limited throughput in mechanical releases have remained serious issues. Meanwhile, it is difficult and time-consuming to grow a single-crystal h-BN layer on c-plane (0001) sapphire with a smooth surface [22-24]. Another approach is the complete removal of the substrate by etching or polishing. This, however, is quite time-consuming, especially in the case of sapphire or SiC substrates. Alternatively, a process which is much more flexible and significantly faster than the above mentioned methods, is the laser-induced delamination of III-nitrides from a transparent sapphire substrate, the so called “laser lift off (LLO)” process. In this process, the separation of III-nitride layer from the substrate is achieved by irradiation of the substrate/film interface through the substrate with high energy laser pulses at a wavelength which is transmitted in the substrate, but is strongly absorbed in the III-nitride layer. In the case of GaN on sapphire, the most suitable laser systems in this context are the third harmonic of a Nd:YAG laser [25, 26] or KrF excimer lasers [27]. The absorption of such high intensity laser pulses causes a rapid thermal decomposition of the irradiated GaN interfacial layer into metallic Ga and gaseous N<sub>2</sub>.

The intrinsic advantages of such an LLO process compared the other possibilities mentioned above have been reported [28]:

- High performance III-nitride based LEDs have been developed on sapphire substrates. Sapphire is a well developed, reasonably cheap and large size substrate material. It would be even possible to recycle the separated sapphire



substrates after LLO for further deposition runs.

- The LLO process does not require any specific sacrificial layers in the growth sequence, as AlN or GaN buffer layers are removed together with the substrate in the same process.
- The LLO method is quite fast. Using standard Nd:YAG or excimer laser systems with pulse repetition rate of 1000 Hz, a 2" in diameter wafer in principle could be lifted-off in a few seconds.
- Since LLO does not require any direct mechanical or chemical contact with the wafer, the lift-off process could also occur directly after deposition of the III-nitride film in the deposition reactor before cooling to room temperature. However, it would require a suitable optical window and an external laser scanning arrangement, but at the same time it would avoid the build-up of critical thermal strain, which occurs in thick GaN films on heterosubstrates during the cooling from the deposition temperature of 1000 °C to room temperature because of the large mismatch between the thermal lattice expansion coefficients of the two materials.
- Because sapphire substrates and GaN lack an effective wet-chemical etch, the other aforementioned techniques are hard to be realized as an efficient lift-off process for those devices.

The LLO process is confined at the interface of the buffer/substrate and protects the main active region from any potential damage caused by laser light absorption. The separation of GaN from sapphire/GaN structures is accomplished here using a single short-duration laser pulse. The incident pulse directly passes through the transparent sapphire and when absorbed in GaN at the interface induces a highly localized, rapid thermal decomposition of GaN, yielding metallic Ga and N<sub>2</sub> gas. Heating the interface above the melting point of Ga (30 °C) allows the separation of GaN from sapphire.

In the following sections, the state of art of LLO on III-nitride epitaxial thin film in the published literature will be summarized.

## 1.2 The state of art of laser lift-off on III-nitride materials

LLO of III-nitride thin films was firstly demonstrated on GaN grown on c-plane (0001) sapphire substrate and the research has been very attractive since 1996 [29]. It appears to be an excellent candidate for solid-state platforms, especially, a viable technology to increase the brightness of III-nitride based light emitters (e.g. LEDs). There were two important development stages based on the research over these three decades. At the first stage (before 1999), most of the research was focused on the feasibility of the LLO of the entire area of GaN thin film and the introduction of damage on the LLO created GaN surface, such surface crystal damages, micro-crackings. At the second stage, following the previous work, researchers found that the laser irradiation and lift-off process parameters, such as laser pulse energy density, pulse duration, scanning speeds and energy variation of single pulse, can affect the interface surface of GaN thin film/sapphire. The research progress of the LLO III-nitrides and the related issues of this technologies are presented below.

In 1996, M. K. Kelly *et al.* used a YAG laser operating at 355 nm with 5 ns pulses to etch the surface of GaN epitaxial thin film to produce interface gratings [29]. They found the high energy laser irradiated on GaN, causing rapid nitrogen (N<sub>2</sub>) effusion and gallium (Ga) droplets. At a laser pulse energy density of 400 mJ/cm<sup>2</sup>, they observed the etch rates of 50 to 70 nm per pulse [29]. In 1997, they first implemented the separation of nitride films from transparent c-plane sapphire substrate by LLO by the use of the 3<sup>rd</sup> harmonic of a Q-switched Nd:YAG laser at 355 nm with 6 ns pulse width [30]. In 1998, W. S. Wong *et al.* bonded a GaN thin film with ethyl cyanoacrylate-based adhesive onto Si support substrate, then lifted-off the transparent sapphire substrate by the directed irradiation of a single laser pulse of energy density 600 mJ/cm<sup>2</sup>, 38 ns pulse width from KrF excimer laser ( $\lambda_{\text{peak}} = 248$  nm) at the sapphire/GaN interface [31]. They found no damage or changes in the GaN thin film crystal quality by x-ray diffraction (XRD) and scanning electron microscopy (SEM). Then, they realized the LLO on sapphire/GaN (3  $\mu\text{m}$ )/epoxy/Si bonding structure by KrF laser pulse of energy density 600 mJ/cm<sup>2</sup> in 38 ns width. They found no degradation in surface morphology, crystalline and the optical properties of the GaN thin film before and after LLO [32]. In 1999, they demonstrated the potential for using LLO to create 20  $\times$  500  $\mu\text{m}^2$  free-standing c-plane GaN-based thin-film LEDs by applying LLO process on sapphire/InGaN

MQW LED/adhesive/Si structure with a single laser pulse of  $600 \text{ mJ/cm}^2$ , rastering a  $0.03 \text{ cm}^2$  beam spot from KrF laser with 38 ns pulse width [33]. Their LED mesa devices experienced microcracking due to thermal shock or excessive heating during laser pulse irradiation and they found no discernable change in electrical and electroluminescence characteristics after separating the InGaN LEDs from sapphire compared to an adjoining device fabricated on the same substrate. In 2000, E. A. Stach *et al.* utilized transmission electron microscopy (TEM) techniques to characterize the modifications that occur at the resulting GaN surfaces [34]. The structural alteration and chemical intermixing (interdiffusion between components) following LLO by KrF excimer laser (pulse width 30 ns) in pulse energy density of  $600 \text{ mJ/cm}^2$  are confined approximately to the first 50 nm of the epilayer thickness. In 2002, T. Bret *et al.* carried out LLO of GaN on both polished and unpolished back surface of sapphire substrate and presented that the laser intensity at the GaN/sapphire interface strongly depends on the roughness of the sapphire backside [35].

In 2007, W. H. Chen *et al.* analyzed the GaN surface after LLO by high resolution TEM and found damage within approximately 40 nm of the created surface of GaN epilayer [36]. A sequential series of half loops lattice deforming configuration (sequential series dislocation) end to end spreads over the LLO interface within approximately 170 nm above the created surface compared to the films before the LLO process and the depth of top of the half loop cluster varies from several tens of nanometers to about 200 nm with the fluctuation of the laser radiation energy. Their theory is that laser-induced shock wave was caused by  $\text{N}_2$  high vapour pressure and thermal stress generated by the laser-induced diffusion, which induced crystal damage on the created surface by LLO.

In 2009, J. H. Cheng *et al.* studied the LLO effects on structural damage of created surface of GaN epitaxial thin film by employing frequency-tripled Nd:YAG laser (355 nm peak wavelength, 5 ns pulse width) and the KrF excimer laser (35 ns pulse width) respectively [37]. By the TEM observation, they found the surface damaged depth below the LLO surface of 35 ns pulse width, KrF laser is 5 times greater than 5 ns pulse width of the Nd: YAG laser. They believed that the laser-induced shock wave appears only when the pulse width is longer than 10 ns, thus the laser pulse of width 5 ns should cause minor damage on the LLO created surface of GaN.

In 2009, X. L. Tong *et al.* investigated the influence of laser scanning speed on the structural and optical properties of thin GaN films before and after LLO by KrF excimer laser with a single pulse energy density of  $600 \text{ mJ/cm}^2$  in 20 ns pulse width [38]. They found the crystal structure and optical properties of GaN separated from sapphire at the laser scanning speed of 1.0 mm/s was comparatively better. In 2011, T. Ueda *et al.* found that the created LLO surface morphology of GaN got worse after LLO, if the GaN epitaxial layer thickness was thinner, and partial exfoliation was observed on GaN film during LLO when the thickness was less than  $4 \mu\text{m}$  [39]. They deemed the thinner of the GaN film thickness has a lower mechanical strength, which can not balance the biaxial stress relief and high  $\text{N}_2$  vapor pressure after LLO. Meanwhile, they speculate a weaker  $\text{N}_2$  vapor pressure for thinner decomposed GaN film.

Until recently, research has mainly focused on the LLO of GaN thin films and has made good progress. However, there are still many unknowns and the need for more research extends to III-nitride materials for UV emitters such as AlN and AlGaIn. Firstly, there was no clear report on the systematic research of the effect of pulse width on LLO, and the LLO mechanism is not clear. Secondly, there is no investigation reported on the impact of III-nitride thin film thickness, types of materials in different thermal conductivity used as bonding materials and support substrate on LLO. The intrinsic stress can be different for GaN grown on sapphire substrates with different thickness. Before LLO, a bonding process must be required to attach the III-nitride thin film onto a support substrate by various bonding materials of different thermal conductivity. Thirdly, the microcracking of III-nitride thin films in LLO should be avoided by optimizing LLO process parameters and developing novel process methods.

### **The laser lift-off on AlGaIn based deep UV LEDs**

At present, there are many reports on improving the light extraction efficiency (LEE) in III-nitride based LED by LLO method [40], many of which are GaN/sapphire LLO; however, the LLO for AlGaIn is rarely reported and can be employed for fabrication of AlGaIn-based deep ultraviolet (DUV) LEDs [41]. The realization of LEDs having wavelengths shorter than 350 nm requires the use of AlGaIn-related

materials [42]. The AlN p-i-n LED, which emits the shortest emission wavelength of 210 nm, using an AlGaIn material system has been reported [43-45]. Within the DUV regions obtained by AlGaIn materials, wavelengths of 325 and 254 nm are particularly important as replacements for the He-Cd laser and the mercury lamp, respectively. In general, AlGaIn materials are grown on c-plane (0001) sapphire substrates by metal organic vapor phase epitaxy (MOVPE).

In 2006, K. Kawasaki *et al.* fabricated vertical AlGaIn DUV LED emitting at 322 nm by LLO GaN buffer layer grown between AlGaIn based DUV LED epitaxial layers and sapphire substrate [46]. In the same year, L. Zhou *et al.* reported  $700 \times 700 \mu\text{m}^2$  vertical thin film DUV LEDs emitting at 280 nm and 325 nm were fabricated by LLO. A low-temperature metamorphic AlN strain-relief interlayer which enabled the insertion of a GaN lift-off layer and allowed reliable substrate removal via excimer laser excitation [47]. In 2009, M. Takeuchi *et al.* demonstrated LLO on AlN/AlGaIn short-period superlattice sacrificial layers to separate AlN/sapphire growth templates by a Q-switched Nd:YVO laser ( $\lambda = 266 \text{ nm}$ ) for vertical type AlGaIn-based deep ultraviolet LEDs [48]. A 200-period AlN/ $\text{Al}_{0.22}\text{Ga}_{0.78}\text{N}$  short-period superlattice (SPSL) functioned as the photoabsorbing and mechanically weakened layer was used to replace conventional GaN photoabsorbing layers as the sacrificial layers. In the same year, V. Adivarahan *et al.* demonstrated the fabrication using LLO process to achieve vertically conducting thin film high power DUV LEDs with peak emission at 280 nm [49]. In 2011, S. Hwang *et al.* reported first substrate-free flip-chip AlGaIn LEDs emitting at 276 nm grown over a 10- $\mu\text{m}$ -thick pulsed lateral epitaxial overgrown (PLOG) AlN/(0001) sapphire template [50]. In 2012, H. Aoshima *et al.* reported LLO of AlN to separate sapphire by the use of ArF pulsed excimer laser ( $\lambda = 193 \text{ nm}$ , pulse width of 15 ns) with a pulse energy density of  $1000 \text{ mJ/cm}^2$ , for the fabrication of thin-film flip-chip UV LEDs with a peak wavelength of 343 nm [51]. In 2013, F. Asif *et al.* demonstrated a substrate-lift-off lateral conduction flip-chip DUV LEDs ( $1500 \times 1800 \mu\text{m}^2$ ) in  $3 \times 3$  small periphery pixel-LED arrays (single chip device size  $180 \times 180 \mu\text{m}^2$ ) emitting at a peak wavelength of 285 nm that were implemented by LLO. The LED epitaxial layers were subsequently grown on the AlGaIn/AlN short period superlattice structure on a low-defect 2- $\mu\text{m}$ -thick AlN/(0001) sapphire template [52, 53].

### 1.3 Summary

Up to now, the LLO process of GaN thin film membranes is mature for c-plane (0001) GaN/sapphire structure and has been realized on GaN based blue LED epitaxy for transferring to various substrate or deployment platforms, such as Si, Cu and flexible polymer, etc [54-56]. The c-plane of III-nitride is also called “polar” plane, in contrast to the polar c-plane, other crystal planes are called semipolar and non-polar planes (as shown in Fig. 1.3). To our best knowledge, there is no report of LLO of GaN epitaxial thin film on other crystal planes, such as semipolar and non-polar so far.

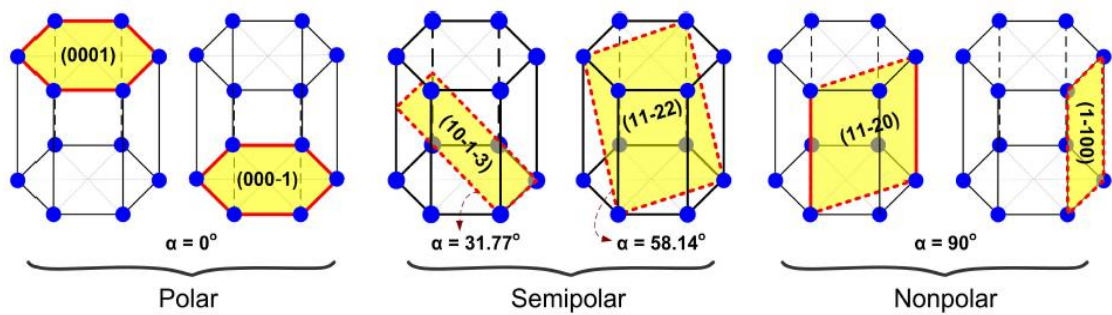


Figure 1.3 III-nitride materials with different surface orientations. The  $\alpha$  angles were calculated for the direction of inclined plane with respect to c-plane (0001) ( $\alpha = 0^\circ$ ) [57].

Comparing to wurtzite InGaN MQW based LEDs grown on c-plane oriented surface, the LED growth on semipolar and non-polar planes of crystal reduces the quantum-confined Stark effect (QCSE) induced by built-in piezoelectric fields at the InGaN/GaN interface of QW [58, 59]. The reduction in the QCSE increases the overlap of electron and hole wave-functions, and therefore increases the radiative recombination rate [60-67]. Hence, it provides carriers in the QW with shorter radiative recombination life-time, promoting bandwidth and transmission speed of the devices. Therefore, it is suitable as emitters for visible light communication applications. The semipolar  $(11\bar{2}2)$  oriented surface is of special interest because high-efficiency has been reported [68-71] with the best results having been reported for devices grown on bulk  $(11\bar{2}2)$  GaN substrates [67]. Such substrates are very expensive and small in size which is not suitable for mass-production; thus, it is preferable to grow LEDs on a low-cost sapphire substrate. However,  $(11\bar{2}2)$  GaN films grown on  $(10\bar{1}0)$  m-plane patterned sapphire substrates (PSS) normally contain a high density of extended defects such as basal-plane stacking faults, prismatic

stacking faults and partial dislocations [72]. The light scattering at GaN stripes/groove patterned sapphire interface and light absorption at defects layer reduce light output through substrate emission of the devices. Therefore, to reduce light output loss, more work should be focused on the growth approach to reduce template defects and find a new scheme to release the device epitaxial layer by LLO.

At this moment, the LLO of AlN, AlGaIn thin films is rarely reported. Most of the AlGaIn based DUV LEDs fabricated by the use of LLO utilized sacrificial layers which are GaN buffer, AlN buffer and AlN/AlGaIn superlattice layer. New sacrificial layer structure schemes based on Si-doped n-type AlGaIn only for AlGaIn based DUV LEDs would be proposed to maintain the high-quality epitaxy growth and fabrication process should be considered for vertical structure ultra-thin AlGaIn DUV LEDs. Compared to AlN buffer, the high Al mole fraction  $\text{Al}_x\text{Ga}_{1-x}\text{N}$  ( $x \geq 0.5$ ) thin films grown on GaN buffer have low crystalline quality (higher dislocation density) epitaxy growth, however, is more relaxed (with less strain). Also, AlGaIn layer grown on sapphire with GaN buffer can easily crack with the increase of Al mole fraction and the layer thickness. There is only a relatively small lattice constant difference between AlN and AlGaIn of high Al mole fraction, high-quality epitaxial growth of AlGaIn layers on AlN buffer is easier to achieve by MOVPE method. While, it requires a different LLO process with the photon energy of a short pulse laser irradiation higher than AlN band-gap energy (i.e. 6.0 eV) [10]. It only can be satisfied by the use of 193 nm ArF excimer laser [51]. Instead, AlN/AlGaIn superlattice layer was used as both laser heating absorption and strain management layer in AlGaIn-based DUV LEDs for LLO process; however, the growth of the superlattice layer in the LED epitaxial structure increases the complexity of the epitaxial growth. Meanwhile, all these three sacrificial structures have to employ inductively coupled plasma (ICP) dry etch to remove the remaining layer of the sacrificial layer to access the n-AlGaIn for vertical structure LEDs, which increases the fabrication cost.

In addition, the thermal performance of such optoelectronics emitter transfer-bonded on substrates of different material is critical and especially in these new environments. The performance of a semiconductor laser or a LED is strongly dependent on the junction temperature which is set by the ambient temperature together with Joule heating in the device or from surrounding components, which

leads to temperature gradients [73, 74] as the heat is transferred to a heat sink. High junction temperature leads to the degradation of the electro-optical properties through loss in device efficiency or other premature failure mechanisms of the device. Furthermore, mechanical strain induced by thermal gradients is generally detrimental. Thus, to provide the best power and emission spectral performance and assure the semiconductor laser lifetime, the diode junction temperature must be controlled [75, 76] by minimising the excess heat generation and managing its removal from the active region. Thermal modeling of the transfer-bonded GaAs laser diodes would be informative for the device thermal management.

This thesis presents device fabrication and characterization for solving the above-mentioned challenges to obtain the III-nitride thin film optoelectronics emitter and it also presents an evaluation of the thermal performance.

## **1.4 Structure of this thesis**

This thesis is divided into 6 chapters.

Chapter 1 includes a brief introduction of the fabrication of thin film semiconductor optoelectronics devices, the transfer-printing method and the III-nitride based light emitters. A review of the published work on epitaxial lift-off on III-nitride materials to fabricate thin film GaN based visible LEDs and AlGaN based UV LEDs is given. The state of the art work on LLO on GaN in the literature is highlighted. Moreover, the literature review of thermal modeling of thin film semiconductor optoelectronics device, especially the thin film transfer bonded GaAs laser diode are presented.

Chapter 2 introduces the background theory of LLO process on c-plane GaN/sapphire. The relevant process technique required for non-damaged lift-off of the GaN membranes grown on c-plane sapphire is outlined and the characterization methods are presented.

Chapter 3 presents a new fabrication process sequence to obtain a free-standing semipolar ( $11\bar{2}2$ ) InGaN/GaN MQW LEDs (FS-LEDs) emitting at 445 nm by the use of LLO and a chemical mechanical polishing (CMP) process. The electrical and optical characterization of the FS-LEDs before and after fully polish of GaN stripes on the back surface of the LEDs by CMP are investigated for the first time.



Chapter 4 describes a new sacrificial layer structure scheme for LLO on c-plane AlGaIn. It is used to implement vertical conduction AlGaIn membrane as a critical process for realizing AlGaIn based vertical DUV LEDs. The  $\text{Au}_{0.8}\text{Sn}_{0.2}$  eutectic metal bonding method is applied to attach the AlGaIn wafer on Au coated Si substrate as mechanical support for LLO and electrode of metal contact. The electrical contact behaviour of the metal contact on N-polar Si-doped n-type AlGaIn created by LLO is investigated.

Chapter 5 demonstrates a thermal model of the transfer-bonded thin film GaAs based ridge laser diode. It focuses on the simulation of a two-dimensional temperature distribution on the transfer-bonded ridge laser diode on a dissimilar material substrate by using finite element analysis (FEA) software COMSOL Multiphysics. A simplified 2-D thermal analytical model for thermal resistance calculation is presented as a comparison.

Chapter 6 summarizes the findings in this thesis and outlines a few suggestions for further work.

## 1.5 References

- [1] J. Justice, C. Bower, M. Meitl, M. B. Mooney, M. A. Gubbins and B. Corbett, "Wafer-scale integration of group III-V lasers on silicon using transfer printing of epitaxial layers," *Nature Photonics*, vol. 6, no. 9, pp. 610-614, Feb. 2012.
- [2] B. Corbett, C. Bower, A. Fecioru, M. Mooney, M. Gubbins and J. Justice, "Strategies for integration of lasers on silicon," *Semicond. Sci. Technol.*, vol. 28, no. 9, pp. 1-6, Aug. 2013.
- [3] J. A. Rogers and Y. Huang, "A curvy, stretchy future for electronics", *Proc. Nat. Acad. Sci. United States Amer.*, vol. 106, no. 27, pp. 10875-10876, Jul. 2009.
- [4] R. H. Kim, "Waterproof AlInGaP optoelectronics on stretchable substrates with applications in biomedicine and robotics", *Nature Mater.*, vol. 9, pp. 929-937, Oct. 2010.
- [5] M. Koo, S. Y. Park and K. Lee, "Biointegrated flexible inorganic light emitting diodes", *Nanobiosensors Disease Diag.*, vol. 1, pp. 5-15, Jan. 2012.
- [6] S. Lee, "Water-resistant flexible GaN LED on a liquid crystal polymersubstrate for implantable biomedical application", *Nano Energy*, vol. 1, no. 1, pp. 145-151, Jan. 2012.

- [7] W. S. Wong, M. Kneissl, P. Mei, D. W. Treat, M. Teepe, N. M. Johnson, "Continuous wave InGaN multiple-quantum-well laser diodes on copper substrates," *Appl. Phys. Lett.*, vol. 78, no. 9, pp. 1198-1200, 2001.
- [8] S. Xing, et al. "Transfer printing of fully formed thin-film microscale GaAs lasers on silicon with a thermally conductive interface material." *Laser & Photonics Reviews*, 9.4 (2015): L17-L22.
- [9] S. Nakamura and G. Fasol, 2000 "The Blue Laser Diode-GaN Based Light Emitters and Lasers" (Berlin: Springer).
- [10] M. R. Krames, O. B. Shchekin, R. M. Mach, G. O. Mueller, L. Zhou, G. Harbers and M. G. Craford, "Status and future of high-power light-emitting diodes for solid-state lighting," *IEEE J. Display Tech.*, vol. 3, no. 2, pp. 160-175, Jun. 2007.
- [11] A. Krost and A. Dadgar, "Heteroepitaxy of GaN on Si(111)," *Semiconducting and Insulating Materials*, 2002. *SIMC-XII-2002. 12th International Conference on*, pp. 41-47, 2002.
- [12] J. W. Wang, A. Lunev, G. Simin, A. Chitnis, M. Shatalov, M. Asif Khan, J. E. Van Nostrand and R. Gaska, "Selective area deposited blue GaN-InGaN multiple-quantum well light emitting diodes over silicon substrates," *Appl. Phys. Lett.*, vol. 76, no. 3, pp. 273-275, Jan. 2000.
- [13] M. Umeno, T. Egawa, H. Ishikawa, "GaN-based optoelectronic devices on sapphire and Si substrates," *Mater. Science in Semiconductor Proc.*, vol. 4, no. 6, pp. 459-466, Jan. 2001.
- [14] A. Reiher, J. Blasing, A. Dadgar, A. Diez, A. Krost, "Efficient stress relief in GaN heteroepitaxy on Si (111) using low-temperature AlN interlayers," *J. Cryst. Growth.*, vol. 248, no. 5, pp. 563-567, Feb. 2003.
- [15] A. Dadgar, C. Hums, A. Diez, J. Blasing, A. Krost, "Growth of blue GaN LED structures on 150-mm Si (111)," *J. Cryst. Growth.*, vol. 297, no. 2, pp. 279-282, Nov. 2006.
- [16] D. Zhu and C. J. Humphreys, "Low-cost high-efficiency GaN LED on large-area Si substrate." *CS MANTECH Conf.*, May 13th-16th, 2013, New Orleans, Louisiana, USA.
- [17] S. J. Lee, J. C. Song, H. J. Park, J. B. Park, S. R. Jeon, C. R. Lee, D. W. Jeon, and J. H. Baek, "High Brightness, Large Scale GaN Based Light-Emitting Diode grown on 8-inch Si substrate," *ECE J. of Solid State Science and Technology.*, vol. 4, no. 8, pp. 92-95, Jun. 2015.
- [18] C. F. Lin, J. J. Dai, M. S. Lin, K. T. W. Chen, W. C. Huang, C. M. Lin, R. H. Jiang, and Y. C. Huang, "An AlN sacrificial buffer layer inserted into the GaN/patterned sapphire substrate for a chemical lift-off process," *Appl. Phys. Express.*, vol. 3, no. 1001, pp. 1-3, Feb. 2010.
- [19] H. S. Kim, E. Brueckner, J. Song, Y. Li, S. Kim, C. Lu, J. Sulkin, K. Choquette, Y. Huang, R. G. Nuzzo, and J. A. Rogers, "Unusual strategies for using indium

gallium nitride grown on silicon (111) for solid-state lighting,” *Proceedings of the National Academy of Sciences of the United States of America*, vol. 108, no. 25, pp. 10072-10077, June. 2011.

[20] N. P. Pham, M. Rosmeulen, Z. Li, D. Sabuncuoglu and H. Osman, “Substrate transfer for GaN-based LEDs on 200 mm Si,” *Electronics Packaging Technology Conference (EPTC 2013), 2013 IEEE 15th*, Singapore, 2013, pp. 324-328.

[21] K. Tomita, T. Kachi, S. Nagai, A. Kojima, S. Yamasaki, and M. Koike, “Self-separation of Freestanding GaN from sapphire substrate by hydride vapor phase epitaxy,” *Phys. Stat. Sol. (a)*., vol. 194, no. 2, pp. 563-567, Dec. 2002.

[22] Y. Kobayashi, T. Akasaka, “Hexagonal BN epitaxial growth on (0001) sapphire substrate by MOVPE,” *J. Cryst. Growth*., vol. 310, no. 23, pp. 5044–5047, Nov. 2008.

[23] Y. Kobayashi, C. L. Tsai and T. Akasaka, “Optical band gap of h-BN epitaxial film grown on c-plane sapphire substrate,” *Phys. Stat. Sol. (c)*., vol. 7, no. 7-8, pp. 1906–1908, May. 2010.

[24] Y. Kobayashi, K. Kumakura, T. Akasaka, T. Makimoto, “Layered boron nitride as a release layer for mechanical transfer of GaN-based devices,” *Nature* 484, pp. 223-227, Apr. 2012

[25] M. K. Kelly, R. P. Vaudo, V. M. Phanse, L. Görgens, O. Ambacher, and M. Stutzmann, “Large free-standing GaN substrates by hydride vapor phase epitaxy and laser-induced liftoff,” *Jpn. J. Appl. Phys.* vol. 38, no. 3A, pp. L217-L219, Feb. 1999.

[26] M. Kelly, O. Ambacher, M. Stutzmann, M. Brandt, R. Dimitrov, and R. Handschuh, “Method of separating two layers of material from one another and electronic components produced using this process,” U.S. Patent 6,559,075, B1, 2003.

[27] W. S. Wong, A. B. Wengrow, Y. Cho, A. Salleo, N. J. Quitoriano, N. M. Cheung and T. Sands, “Integration of GaN thin films with dissimilar substrate materials by Pd-In metal bonding and laser lift-off,” *J. Electron. Mater.*, vol. 28, no. 12, pp. 1409-1413, Dec. 1999.

[28] C. R. Miskys, M. K. Kelly, O. Ambacher, and M. Stutzmann, “Freestanding GaN-substrates and devices,” *Phys. Stat. Sol. (c)*., vol. 0, no. 6, pp. 1627-1650, Jul. 2003.

[29] M. K. Kelly, O. Ambacher, B. Dahlheimer, M. Stutzmann, “Optical patterning of GaN films,” *Appl. Phys. Lett.*, vol. 69, no. 12, pp. 1749-1751, Sep. 1996.

[30] M. K. Kelly, O. Ambacher, R. Dimitrov, “Optical process for lift off of group III-nitride films,” *Phys. Stat. Sol. (a)*., vol. 159, no. 1, pp. R3-R4, Nov. 1997.

[31] W. S. Wong, J. Krüger, Y. Cho, et al. “Selective UV-laser processing for lift-off of GaN thin films from sapphire substrates”. *Proceedings of the Symposium on LED for Optoelectronic Applications and the 28<sup>th</sup> State-of-the-Art Programs on Compound Semiconductors*, vol. 98, no. 2, pp. 377, 1998.

- [32] W. S. Wong, T. Sands, N. W. Cheung, "Damage-free separation of GaN thin films from sapphire substrates", *Appl. Phys. Lett.*, vol. 72, no. 5, pp. 599-601, Oct. 1998.
- [33] W. S. Wong, T. Sands, N. W. Cheung, M. Kneissl, D. P. Bour, P. Mei, L. T. Romano, and N. M. Johnson, "Fabrication of thin-film InGaN light-emitting diode membranes by laser lift-off," *Appl. Phys. Lett.*, vol. 75, no. 10, pp. 1360-1362, Jul. 1999.
- [34] E. A. Stach, M. Kelsch, E. C. Nelson, *et al.*, "Structural and chemical characterization of free-standing GaN films separated from sapphire substrates by laser lift-off," *Appl. Phys. Lett.*, vol. 77, no. 12, pp. 1819-1821, Jul. 2000.
- [35] T. Bret, V. Wagner, D. Martin, *et al.* "A Mechanistic Study of GaN Laser Lift Off," *Phys. stat. sol. (a)*, vol. 194, no. 2, pp. 559-562, Oct. 2002.
- [36] W. H. Chen, X. D. Kang, X. D. Hu, *et al.* "Study of the structural damage in the (0001) GaN epilayer processed by laser lift-off techniques," *Appl. Phys. Lett.*, vol. 91, no. 12, pp. 121114(1-3), Sep. 2007.
- [37] J. H. Cheng, Y. C. S. Wu, W. C. Peng, *et al.*, "Effects of laser sources on damage mechanisms and reverse-bias leakages of laser lift-off GaN-based LEDs", *J. Electrochem. Soc.*, vol. 156, no. 8, pp. H640-H643, Jun. 2009.
- [38] X. L. Tong, L. Li, D. S. Zhang, *et al.*, "The influences of laser scanning speed on the structural and optical properties of thin GaN films separated from sapphire substrates by excimer laser lift-off," *J. Phys. D: Appl. Phys.*, vol. 42, no. 4, pp. 045414(1-4), Jan. 2009.
- [39] T. Ueda, M. Ishida, M. Yuri. "Separation of thin GaN from sapphire by laser lift-off technique," *Jpn. J. Appl. Phys.*, vol. 50, no. 4, pp. 041001(1-6), Apr. 2011.
- [40] T. Fujii, Y. Gao, R. Sharma, E. L. Hu, S. P. DenBaars, and S. Nakamura, "Increase in the extraction efficiency of GaN-based light-emitting diodes via surface roughening," *Appl. Phys. Lett.*, vol. 84, no. 6, pp. 855-857, Dec. 2004.
- [41] M. Kneissl and J. Rass, "III-Nitride Ultraviolet Emitters: Technology and Applications," (Springer International publishing, Switzerland, 2016, 1st edn).
- [42] H. Hirayama, T. Yatabe, N. Noguchi, and N. Kamata, "Development of 230–270 nm AlGaIn-based deep-UV LEDs," *Electronics and Communications in Japan*, vol. 93, pp. 24-33, Feb. 2010.
- [43] A. Khan, "Ultraviolet light-emitting diodes based on group three nitrides," *Nature Photonics*, vol. 2, pp. 77-84, Feb. 2008.
- [44] M. Kneissl, T. Kolbe, C. Chua, V. Kueller, N. Lobo, J. Stellmach, A. Knauer, H. Rodriguez, S. Einfeldt, Z. Yang, N. M. Johnson, and M. Weyers, "Advances in group III-nitride-based deep UV light-emitting diode technology," *Semicond. Sci. Technol.*, vol. 26, pp. 14036-14041, 2011.
- [45] Y. Taniyasu, M. Kasu, and T. Makimoto, "An aluminium nitride light-emitting diode with a wavelength of 210 nanometres," *Nature*, vol. 441, pp. 325-328, 2006.

- [46] K. Kawasaki, C. Koike, Y. Aoyagi and M. Takeuchi, "Vertical AlGa<sub>N</sub> deep ultraviolet light emitting diode emitting at 322 nm fabricated by the laser lift-off technique," *Appl. Phys. Lett.*, vol. 89, no. 26, pp. 261114, Dec. 2006.
- [47] L. Zhou, et al "Vertical injection thin-film AlGa<sub>N</sub>/AlGa<sub>N</sub> multiple-quantum-well deep ultraviolet light-emitting diodes," *Appl. Phys Lett.*, vol. 89, pp. 241113(1-3), Dec. 2006.
- [48] M. Takeuchi, T. Maegawa, H. Shimizu, S. Ooishi, T. Ohtsuka and Y. Aoyagi, "AlN/AlGa<sub>N</sub> short-period superlattice sacrificial layers in laser lift-off for vertical-type AlGa<sub>N</sub>-based deep ultraviolet light emitting diodes," *Appl. Phys. Lett.*, vol. 94, pp. 061117(1-3), Feb. 2009.
- [49] V. Adivarahan, A. Heidari, B. Zhang, Q. Fareed, M. Islam, S. Hwang, K. Balakrishnan, and A. Khan, "Vertical Injection Thin Film Deep Ultraviolet Light Emitting Diodes with AlGa<sub>N</sub> Multiple-Quantum Wells Active Region," *Appl. Phys. Express.*, vol. 2, pp. 092102 (1-3), Sep. 2009.
- [50] S. Hwang, D. Morgan, A. Kesler, M. Lachab, B. Zhang, A. Heidari, H. Nazir, I. Ahmad, J. Dion, Q. Fareed, V. Adivarahan, M. Islam, and A. Khan, "276nm Substrate-Free Flip-Chip AlGa<sub>N</sub> Light-Emitting Diodes," *Appl. Phys. Express.*, Vol. 4, No. 3, pp. 032102, Feb. 2011.
- [51] H. Aoshima, K. Takeda, K. Takehara, S. Ito, M. Mori, M. Iwawa, T. Takeuchi, S. Kamiyama, I. Akasaki, and H. Amano, "Laser lift-off of AlN/sapphire for UV light-emitting diodes," *Phys. Stat. Sol. (c)*, Vol. 9, No. 3-4, pp. 753-756, Feb. 2012.
- [52] F. Asif, C. Chen, A. Coleman, M. Lachab, I. Ahmad, B. Zhang, Q. Fareed, V. Adivarahan, A. Khan, "Substrate Lifted-off AlGa<sub>N</sub>/AlGa<sub>N</sub> Lateral Conduction thin film Light-Emitting-Diodes Operating at 285 nm", *J. J. Appl. Phys.* vol. 52, no. 8S, May. 2013.
- [53] M. Lachab, F. Asif, B. Zhang, I. Ahmad, A. Heidari, Q. Fareed, V. Adivarahan, A. Khan, "Enhancement of light extraction efficiency in sub-300 nm nitride thin-film flip-chip light-emitting diodes", *Solid-State Electronics*, vol. 89, pp. 156-160, Sep. 2013.
- [54] S. C. Hsu, and C. Y. Liu, "Fabrication of Thin-GaN LED Structures by Au-Si Wafer Bonding," *Electrochemical and Solid-State Letters*, vol. 9, no. 5, pp. G171-G173, Jan. 2006.
- [55] L. Wang, E. Guo, Z. Liu, X. Yi, and G. Wang, "High-Performance Nitride Vertical Light-Emitting Diodes Based on Cu Electroplating Technical Route," *IEEE Transactions on Electron Devices.*, vol. 63, no. 3, pp. 892-902, Mar. 2016.
- [56] T. Kim, Y. H. Jung, J. Song, D. Kim, Y. Li, H. Kim, I. Song, J. J. Wierer, H. A. Pao, Y. Huang, and J. A. Rogers, "High-Efficiency, Microscale GaN Light-Emitting Diodes and Their Thermal Properties on Unusual Substrates," *Small*, vol. 8, No. 11, pp. 1643-1649, Jun. 2012.
- [57] D. V. Dinh, "MOVPE growth of InN and InGa<sub>N</sub> with different surface orientations," PhD Thesis, Technical University of Berlin (2012).

- [58] D. F. Feezell, J. S. Speck, S. P. DenBaars, and S. Nakamura, "Semipolar (20-2-1) InGaN/GaN Light-Emitting Diodes for High-Efficiency Solid-State Lighting," *J. Display Technol.*, vol. 9, no. 4, pp.190-198, Apr. 2013.
- [59] C. Wetzel, M. Zhu, J. Senawiratne, T. Detchprohm, P. D. Persans, L. Liu, E. A. Preble, D. Hanser, "Light-emitting diode development on polar and non-polar substrates," *J. Cryst. Growth*, vol. 310, no. 17, pp. 3987-3991, Aug. 2008.
- [60] T. Wang, D. Nakagawa, J. Wang, T. Sugahara and S. Sakai, "Photoluminescence investigation of InGaN/GaN single quantum well and multiple quantum wells," *Appl. Phys. Lett.*, vol. 73, no. 24, pp. 3571, Oct. 1998.
- [61] P. Waltereit, O. Brandt, A. Trampert, H. T. Grahn, J. Menniger, M. Ramsteiner, M. Reiche, and K. H. Ploog, "Nitride semiconductors free of electrostatic fields for efficient white light emitting diodes," *Nature*, vol. 406, no. 6798, pp. 865-868, Aug. 2000.
- [62] M. C. Schmidt, K. C. Kim, H. Sato, N. Fellows, H. Masui, S. Nakamura, S. P. DenBaars, and J.S. Speck, " Demonstration of Nonpolar m-plane InGaN/GaN Laser Diodes," *Jpn. J. Appl. Phys.*, vol. 46, no. 2, pp. 8-11, Feb. 2007.
- [63] Y. Zhao, J. Sonoda, I. Koslow, C.C.Pan, H. Ohta, J. S. Ha, S. P. DenBaars, and S. Nakamura, "Optimization of Device Structures for Bright Blue Semipolar (1011) Light Emitting Diodes via Metalorganic Chemical Vapor Deposition", *Jpn. J. Appl. Phys.*, vol. 49, no. 7R, pp. 070206, July. 2010.
- [64] N. F. Gardner, J. C. Kim, J. J. Wierer, Y. C. Shen, and M. R. Krames, "Polarization anisotropy in the electroluminescence of m-plane InGaN-GaN multiple-quantum-well light emitting diodes," *Appl. Phys. Lett.*, vol. 86, no. 11, pp. 111101, Jan. 2005.
- [65] F. Scholz, "Semipolar GaN grown on foreign substrates: a review," *Semicond. Sci.Technol.*, vol. 27, no. 2, 024002 Jan. 2012.
- [66] T. Wunderer, M. Feneberg, F. Lipski, J. Wang, R. A. R. Leute, S. Schwaiger, K. Thonke, A. Chuvilin, U. Kaiser, and F. Scholz, "Three-dimensional GaN for semipolar light emitters", *Phys. Stat. Soli. (b).*, vol. 248, no. 3, pp. 549-560, Mar. 2011.
- [67] H. Sato, H. Hirasawa, H. Asamizu, N. Fellows A. Tyagi, M. Saito, K. Fujito, J.S.Speck, S. P. DenBaars, and S. Nakamura, "High power and high efficiency semipolar InGaN Light Emitting Diodes," *J. Light Visual Environ.*, vol. 32, no. 2, pp. 107-110, Feb. 2008.
- [68] H. Sato, R. B. Chung, H. Hirasawa, N. Fellows, H. Masui, F. Wu, M. Saito, K. Fujito, J. S. Speck, S. P. DenBaars, and S. Nakamura, "Optical properties of yellow light-emitting diodes grown on semipolar (11-22) bulk GaN substrates," *Appl. Phys. Lett.*, vol. 92, no. 22, 221110, Jun. 2008.
- [69] S. H. Park, D. Mishra, Y. E. Pak, K. Kang, C. Y. Park, S. H. Yoo, Y. H. Cho, M. B. Shim, and S. Kim, "Polarization characteristics of semipolar (11-22) InGaN/GaN quantum well structures grown on relaxed InGaN buffer layers and comparison with experiment," *Opt. Express.*, vol. 22, no. 12, pp. 14850-14858, Jun. 2014.

- [70] N. Okada, K. Uchida, S. Miyoshi and K. Tadatomo, "Green light-emitting diodes fabricated on semipolar (11-22) GaN on r-plane patterned sapphire substrate," *Phys. Stat. Soli. (a)*., vol. 209, no 3, pp. 469–472, Mar. 2012.
- [71] D. V. Dinh, M. Akhter, S. Presa, G. Kozlowski, D. O'Mahony, P. P. Maaskant, F. Brunner, M. Caliebe, M. Weyers, F. Scholz, B. Corbett, and P. J. Parbrook, "Semipolar (11-22) InGaN light emitting diodes grown on chemically–mechanically polished GaN templates," *Phys. Stat. Soli. (a)*., vol. 212, no. 10, pp. 2196–2200, Jun. 2015.
- [72] T. Wernicke, C. Netzel, M. Weyers, and M. Kneissl, "Semipolar GaN grown on m-plane sapphire using MOVPE", *Phys. Stat. Soli. (c)*., vol. 5, no. 6, pp. 1815-1817, Apr. 2008.
- [73] H. Yi, J. Diaz, I. Eliashevich, *et al*: "Temperature dependence of threshold current density  $J_{th}$  and differential efficiency  $\eta_d$  of high-power In GaAsP/GaAs ( $\lambda=0.8$   $\mu$ m) lasers," *Appl. Phys. Lett.*, vol. 66, no. 3, pp. 253-255, Feb. 1995.
- [74] H. K. Choi, G. W. Turner,: Mid-infrared semiconductor lasers based on antimonide compounds,' in Manasreh, M.O. (Ed.): "Optoelectronic properties of Semiconductors and Superlattices", (Press, 1997), vol, 3, p 369.
- [75] V. P. Gribkovskii, "Injection lasers", *Prog. Quant. Electron.*, vol. 19, no. 1, pp. 41–88, 1995.
- [76] L. A. Coldren, and S. W. Corzine, "Diode Lasers and Photonic Integrated Circuits" (John Wiley, 1995, 1st edn).

## Chapter 2

### Development of laser lift-off for nitride materials

In this chapter, the concept and physical principle of laser lift-off (LLO) of GaN layers grown on sapphire substrates is initially described. Afterwards, the 1-dimensional (1D) thermal analysis at GaN/sapphire interface caused by the heat induced from laser irradiation is demonstrated by simulations in the COMSOL Multiphysics software. The experimental process includes a brief introduction to the LLO apparatus based on a Krypton Fluoride (KrF) excimer laser (peak wavelength  $\lambda_{peak} = 248$  nm) system; the control of laser beam spot energy density and wafer attachment on a carrier substrate in dissimilar material are also discussed. Finally, the experimental and characterization techniques used to verify the LLO processes are introduced.

#### 2.1 Overview of laser lift-off

In this section, the motivation and concept of LLO to selectively etch c-plane GaN thin films for the separation of sapphire are emphasized. For development of LLO process on nitride materials, the fundamentals of LLO at the interface of GaN/sapphire is firstly described. Due to the difference in band-gap absorption of GaN and sapphire in the UV spectrum, the short pulsed UV laser is selectively absorbed in the GaN resulting in its thermal decomposition. This occurs if the energy density of the laser pulse generates enough heat in a sufficiently short time. The thermal diffusion analyses of the laser beam interaction with GaN will be presented.

##### 2.1.1 GaN epitaxial thin film lift-off

GaN heteroepitaxial layers are grown on dissimilar material substrates because of the cost in the preparation of large area high crystalline quality bulk GaN. At present, the most commonly used substrate is c-plane sapphire ( $\text{Al}_2\text{O}_3$ ) substrate due to the low cost, high growth temperature of GaN, large scale wafer (e.g. 6" in diameter) and relatively well-established development of growth methods [1-4]. However, the lattice mismatch (14%) and the different thermal expansion coefficients between GaN and sapphire result in high threading dislocation density of  $10^9$ - $10^{10}\text{cm}^{-2}$  in



GaN/sapphire [5-7]. In particular, the radiative carrier recombination and carrier transport can be detrimentally affected by threading dislocations [8, 9]. Moreover, as GaN and sapphire have relatively high refractive indexes ( $n_{\text{GaN}} = 2.5$ ,  $n_{\text{sapphire}} = 1.77$ ) compared to air ( $n_{\text{air}} = 1$ ), the low light extract efficiency (LEE) for GaN-based LEDs is due to a narrow escape cone [10]. Additionally, the low thermal conductivity of sapphire ( $k = 35 \text{ W/mK}$ ) [29, 37] adversely affects heat dissipation of the device. Hence, the sapphire substrate removal can be necessary to improve the optical and thermal performance of GaN-based devices.

Due to the low cost and electronic integration potential, the Si substrate is an attractive choice for the growth of GaN-based devices, but the even larger lattice mismatch (18%) and higher difference in the thermal expansion coefficients between silicon and GaN make silicon quite difficult for high quality crystal growth compared to the use of sapphire substrate [11]. Active research is still being carried out on Si substrates to engineer the mismatch and improve GaN/Si heteroepitaxial crystal quality [12]. Alternatively, GaN material grown on sapphire can be transferred to any dissimilar material substrates, such as Si, GaAs and Ge, by epitaxial thin film lift-off process and associated wafer bonding process as a more applicable approach to integrate GaN devices. Also, this method is promising to provide bulk GaN substrates [13]. The sapphire substrate may be eliminated by various techniques, including electro-chemical etching of the sacrificial layer [14], chemical-mechanical removal of the substrate [15], and pulsed ultraviolet (UV) LLO processing [16-19]. Due to the lack of an effective wet-chemical etchant for GaN or materials compatible with GaN and the relative hardness of sapphire [20], LLO technique is the more efficient and viable process among other mentioned techniques.

The basic material properties of wurtzite (w) III-nitride materials and selected substrates are shown in Table 2.1.

Material	Lattice parameter (Å)	Lattice mismatch with GaN (%)	Bandgap (eV)	Density (kg/m <sup>3</sup> )	Thermal conductivity (W/mK)	Heat Capacity (J/kgK)	Thermal Expansion Coefficient (10 <sup>-6</sup> /K)
w-GaN	$a = 3.189$ $c = 5.185$	0	3.42	6150	130	490	$a = 5.59$ $c = 3.17$
w-AlN	$a = 3.112$ $c = 4.982$	2.5	6.0	3266	350	600	$a = 4.2$ $c = 5.3$
w-InN	$a = 3.548$ $c = 5.760$	-10.1	1.89	6810	45-176	320	$a = 3.8$ $c = 2.9$
Sapphire	$a = 4.758$ $c = 12.99$	-14.0	9.9	3980	41.9	875	$a = 7.5$ $c = 8.5$
6H-SiC	$a = 3.08$ $c = 15.12$	3.5	2.996	3210	490	690	$a = 4.3$ $c = 4.7$
Si	$a = 5.430$	-17.0	1.12	2329	150	700	$a = 2.6$
GaAs	$a = 5.653$	-20.2	1.519	5320	55	330	$a = 5.73$

*Table 2.1 Materials properties of III-nitrides (e.g. wurtzite (w-)GaN, InN and AlN) and dissimilar material substrates, such as sapphire, hexagonal structure 6H-SiC, diamond structure Si and zinc blend structure GaAs [21, 22].*

### 2.1.2 Laser lift-off principle

A high power UV pulsed laser is irradiated to the interfacial GaN/sapphire from the back surface of the sapphire substrate. A carrier substrate (e.g. Si, Cu, glass slide) with a bonding material to hold the GaN/sapphire wafer is required as a mechanical support. At the KrF laser light wavelength of 248 nm (photon energy  $E_{\text{photon}} = 5.0$  eV), the sapphire substrate ( $E_g = 9.9$  eV) is transparent, and the light is strongly absorbed by GaN. Only if laser pulse energy density is high enough, localized decomposition of GaN is induced by the intensive light absorption of photon energies (e.g. 5 eV for KrF excimer laser photon energy) over the GaN band-gap of 3.42 eV, as shown in Fig. 2.1 (a). The absorption results in a selective spatially localized heating effect at the GaN/sapphire interface to a temperature that

is sufficient to cause the thermal decomposition of GaN into its constituent components, metallic Ga droplets and N<sub>2</sub> gas as shown in Fig. 2.1 (b) and a separation gap is formed at the interface of GaN/sapphire, where the chemical reaction is expressed as  $2\text{GaN (solid)} \rightarrow 2\text{Ga (liquid)} + \text{N}_2 \text{ (gas)}$ . As the Ga turns to solid droplets at room temperature at the interface, a slight warming of the material above the Ga melting point (i.e. 29°C) [23] is required for lifting up sapphire; thereafter, it releases the GaN layer material.

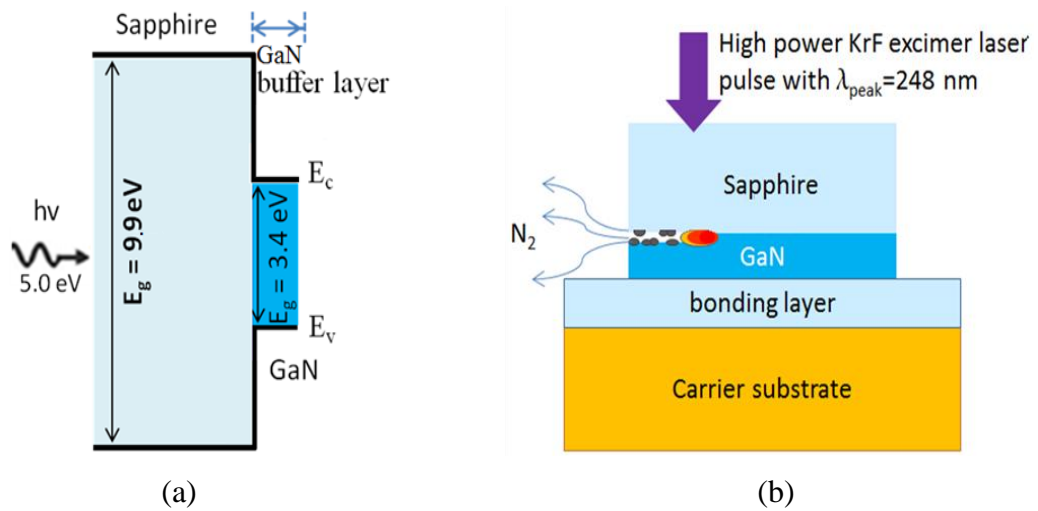


Figure 2.1 (a) Schematic view of band-gap structure of sapphire/GaN. (b) Schematic view of LLO process. High energy intensity laser pulse enters the sample through sapphire substrate that thermally decomposes a thin GaN layer at the GaN/sapphire interface.

GaN undergoes photo-induced decomposition at the interface. A high energy density laser pulse can produce an interfacial temperature over 850°C (900°C to 1000°C) that causes the thermal decomposition of GaN [24]. The laser light creates a localized explosive shock wave due to the debonding of the interface by the N<sub>2</sub> gas generated. Metallic Ga is responsible for visible dark areas that appear after the laser irradiation, that will be seen later in Fig. 2.17.

### 2.1.3 The laser beam interaction on GaN

If the excimer laser light irradiates GaN with sufficient energy density, several interactions occur, including photon energy absorption in GaN, rapid thermalization at the GaN surface and heat transport (e.g. thermal diffusion, expansion), surface vaporization, and bond-breaking induced material ablation. Generally, they can be

divided into two main mechanisms, including thermal-chemical reaction and photo-thermal reaction [25] as shown in Fig. 2.1 (b). These interaction mechanisms are affected by laser wavelength ( $\lambda$ ), laser irradiation energy density ( $E_i$ ) and laser pulse duration ( $\tau_i$ ). As to the photo-chemical reaction, the photon energy of the irradiated laser light is higher than the bond energy (e.g. 1.92 eV between Ga and N in GaN) [26], the chemical bonds between Ga and N are broken under the heating induced by the photons generated in the laser pulse duration, resulting in the material ablation. During the photo-thermal reaction, the photon energy is absorbed on the surface of material, inducing a significant increase in the free electron density and kinetic energy at a very short time scale. The thermal energy of the phonons therefore is converted from the kinetic energy of free electrons. It is able to thermalize the film surface resulting in vaporization of material to attain surface modification (i.e. thermal decomposition) [27]. Moreover, rapid and high energy plasma may be produced during laser irradiation on the surface of material at a constant laser pulse energy density ( $E_i$ ), depending on laser pulse duration ( $\tau_i$ ) [28]:

- If  $\tau_i$  is longer than one microsecond ( $\mu\text{s}$ ), the power density of a laser pulse can be lower than  $10^5 \text{ W/cm}^2$ . Vaporization dominates the elimination of material at surface.
- If  $\tau_i$  is on the nanoseconds (ns) scale, the power density of a laser pulse can reach  $10^7 \text{ W/cm}^2$ . Thus, laser induced surface plasma can be produced by the rapid rise of temperature in material [29].

Therefore, during the interaction of laser irradiation and III-nitride materials (e.g. GaN, AlGaN), both photo-chemical reaction and photo-thermal reaction are generated to induce the laser ablation (i.e. thermal decomposition) at III-nitride material surface.

#### 2.1.4 Thermal analysis

Due to intensive thermal decomposition occurring during the interaction of the laser light on GaN, micro-cracking and damage might occur to affect the film crystal quality [30-32]. An optimization of process parameters is required. Initially,  $E_i$  is required to be higher than the threshold energy density ( $E_{th}$ ) for ensuring that the decomposition temperature will be generated at the GaN/sapphire interface. The

laser energy can not be too high; otherwise micro-cracking might occur [33, 34]. The laser pulse scanning speed is important [35], as it requires enough time for the dissipation of laser-induced heat before irradiation with the next incident laser pulse. The bonding method of the wafer on a carrier substrate is vital to manage the intrinsic strain relief of the GaN thin film. Additionally,  $\tau_i$  is also an important factor. During the laser light pulse, the carriers (i.e. electrons) absorb the laser photon energy and reach on equilibrium condition in  $10^{-13}$  s (0.1 ps). Afterwards, hot electrons pass the energy absorbed from laser photons to the lattice by phonons. As the lattice relaxation time  $\sim 10^{-11}$  s (10 ps) is much shorter than  $\tau_i$  ( $\sim$  ns), hot electrons have sufficient time to pass the energy to the lattice and then finally both the electrons and lattice reach thermal equilibrium. The thermal diffusion time constant ( $10^{-5} \sim 10^{-7}$  s) is in  $\sim \mu$ s scale, which is much longer than  $\tau_i$ , so the heat transport at the interface is mainly thermal conduction. In this point of view, the laser interaction with GaN is a thermal interaction and can be considered as a conventional Fourier thermal conduction in a solid [36].

A 1-D schematic diagram of an incident laser pulse irradiating the GaN/sapphire interface through a sapphire substrate is shown in Fig. 2.2. In the heat conduction model, an induced heat source at the interface is produced by the laser beam spot.

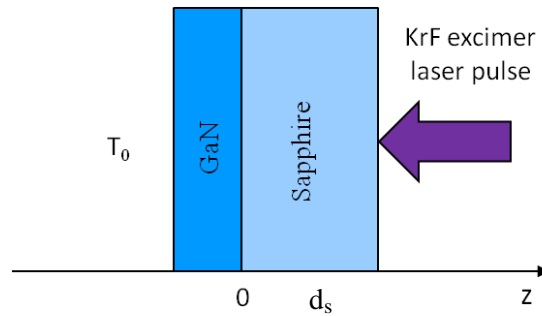


*Figure 2.2 Schematic of 1-D laser induced heat conduction model, the reference point  $z = 0$  sets at the GaN/sapphire interface.*

The laser beam is incident through the back surface of the sapphire. GaN is assumed as a homogeneous absorbing medium, considering the reflection on GaN at the interface and absorption by sapphire, the power of the incident laser light  $P(t)$  at time  $t$  is absorbed by the GaN at the interface of GaN/sapphire ( $z = 0$ ) and can be expressed as below.

$$\begin{aligned}
P(t) &= [P_i(t) - P_i(t)R_s]e^{-\alpha_s d_s}(1 - R_{GaN})e^{-\alpha_{GaN} z} \\
&= P_i(t)(1 - R_s)e^{-\alpha_s d_s}(1 - R_{GaN}),
\end{aligned} \tag{2.1}$$

Where is  $P_i(t)$  (in  $W/m^2$ ) is laser system output power density,  $R_s$  is the reflectivity at the back surface of the sapphire,  $R_{GaN}$  is the reflectivity on GaN at the interface of GaN/sapphire,  $\alpha_s$ ,  $\alpha_{GaN}$  is the absorption coefficient of sapphire, GaN and  $d_s$  is the thickness of the sapphire.

For laser irradiation with a rectangular pulse, the incident light power can be expressed as:

$$P_i(t) = \begin{cases} \frac{E_i}{\tau}, & 0 \leq t \leq \tau_i \\ 0, & t > \tau_i \end{cases}, \tag{2.2}$$

where is  $E_i$  (in  $mJ/cm^2$ ) is the laser system output energy density in a pulse width (i.e. pulse duration  $\tau_i$ ). And  $E_i = I_0/A$ ,  $I_0$  is laser system output energy and  $A$  is beam spot area. Substitute equation (2.1) into equation (2.2),

$$P(t) = \begin{cases} \frac{E_i}{\tau}(1 - R_s)(1 - R_{GaN})e^{-\alpha_s d_s}, & 0 \leq t \leq \tau_i \\ 0, & t > \tau_i \end{cases}. \tag{2.3}$$

During LLO process, the laser pulse irradiation causes the photo-induced thermal decomposition of GaN. In order to simplify and approximate the physics in implementation of the model to attain the temperature distribution at the interface of GaN/sapphire for solving the partial differentiation equation (PDE) of the heat condition in COMSOL Multiphysics, some assumptions are made below.

- The incident pulse laser light can be approximated as a surface heat source with power  $P_i$ , because of the most of the laser light is absorbed at the GaN/sapphire interface. The absorption length of GaN at 248 nm wavelength (5.0 eV) laser

light is  $\sim 20$  nm, which is 200 times less than the thickness of the GaN device ( $\geq 4$   $\mu\text{m}$ ).

- The heat radiation and convection can be ignored. Only heat conduction from the GaN/sapphire interface spreading in both of materials is considered. The time duration of the laser pulse interacting with GaN material is very short (i.e. ns scale), thereby the negligible heat exchange of GaN and sapphire in the ambient environment can be assumed.
- The heat diffusion length ( $\xi = 2\sqrt{D\tau_i}$ ) is approximately 1.06  $\mu\text{m}$  in GaN, where the thermal diffusivity  $D = 4.69 \times 10^{-5}$   $\mu\text{m}^2/\text{s}$  and  $\tau_i$  of 6 ns. It is much less than the thickness of the GaN device ( $\geq 4$   $\mu\text{m}$ ). Thus the temperature increase is confined to 1- $\mu\text{m}$ -depth inside the material from the GaN/sapphire interface. So, the thickness of GaN can be considered as semi-infinite.
- The optical and thermo-mechanical properties of GaN are assumed to be temperature independent constants. Additionally, there are no phase change, enhanced reflectivity, thermal conductivity change due to the Ga formation, and plasma generation [37].

Consequently, relying on the assumptions above, temperature increase in the photo-induced thermal decomposition of GaN could be a bit lower than the expected result in the model. However, the model is able to provide more detailed understanding of the LLO process, which requires a quantitative analysis of the temporal and spatial temperature field distribution at the III-nitride/sapphire interface during and after the laser pulse irradiation.

The heat condition equation in solid material can be presented as Fourier's law [36]:

$$\rho C_p \frac{dT(z, t)}{dt} - k \frac{d^2 T(z, t)}{dz^2} = \sum Q_n(z, t) . \quad (2.4)$$

where  $\rho$  and  $C_p$  are the material density and heat capacity at a constant pressure, respectively.  $T(z, t)$  is the temperature distribution at time  $t$ .  $\sum Q_n(z, t)$  is the sum of the heat power generation in unit volume ( $\text{W}/\text{m}^3$ ),  $k$  is the thermal conductivity of the material.

According to assumptions of the model, a diffusion heat source at the interface can be used to approximate the photo-induced heating where the lateral heat flow is negligible, thus 1-D heat conduction in z-direction dominates. The heat power generated:

$$\Sigma Q_n(z, t) = P(z, t) . \quad (2.5)$$

Therefore, eqn. (2.4) can be rewritten as,

$$\begin{aligned} \rho c_p \frac{d T(z, t)}{dt} &= k \frac{d^2 T(z, t)}{dz^2} + \frac{E_i}{\tau_i} (1 - R_s) e^{-\alpha_s z_s} (1 - R_{GaN}) e^{-\alpha_{GaN} z_{GaN}} , \text{ for } 0 \leq t \leq \tau_i \\ \rho c_p \frac{d T(z, t)}{dt} &= k \frac{d^2 T(z, t)}{dz^2} , \text{ for } t \geq \tau_i \end{aligned} \quad (2.6)$$

As seen in Fig. 2.2, the 1-D spatial temperature field distribution  $T_{GaN}(z, t)$  in GaN thin film ( $z \leq 0$ ) and  $T_s(z, t)$  for sapphire ( $z \geq 0$ ) can be solved by using eqn. (2.6), when the initial conditions and boundary conditions are applied.

Initial condition at  $t = 0$ :

$$T_{GaN}(z, 0) = T_s(z, 0) = T_0 . \quad (2.7)$$

As for the boundary conditions,  $T_{GaN}(0, t) = T_s(0, t)$  for  $z = 0, t \geq 0$  at all the time  $t$ , and  $T_{GaN}(+\infty, 0) = T_s(-\infty, 0) = T_0$  for  $z = \pm \infty, t = 0$  for eqn. (2.4):

$$0 = k_s \frac{d^2 T_s(0, t)}{dz^2} + k_{GaN} \frac{d^2 T_{GaN}(0, t)}{dz^2} + \frac{E_i}{\tau_i} (1 - R_s) (1 - R_{GaN}), \quad \text{at } z = 0 \quad (2.8)$$

$$T_{GaN}(+\infty, 0) = T_s(-\infty, 0) = T_0 , \quad \text{at } z = \pm \infty \quad (2.9)$$

where  $k_s, k_{GaN}$  is the thermal conductivity of sapphire and GaN.

For temperature continuity at the interface ( $z = 0$ ),



$$T_{\text{GaN}}(0, t) = T_s(0, t), \quad \text{for } t \geq 0. \quad (2.10)$$

A 1-D numerical model was implemented using COMSOL. The heat conduction eqn. (2.6) was solved by using the boundary conditions (eqns. (2.7) to (2.10)). The temperature-independent values of the physical parameters, such as absorption coefficients of GaN, and the thermal properties (heat capacitance and conductivity) of GaN and sapphire [38-42] applied in the thermal analysis are listed in Table 2.2.

Material	Diffusion Length $\xi = 2\sqrt{D\tau}$	Thermal diffusivity $D = \frac{k}{\rho C_p}$	Density $\rho$ (g/cm <sup>3</sup> )	Heat capacity $C_p$ (J/kg°C)	Thermal conductivity $k$ (W/mK)	Reflectivity $R$	Absorp Coeff. at 248 nm $\alpha$ (cm <sup>-1</sup> )
GaN	~1.06 $\mu\text{m}$	$4.69 \times 10^{-5}$	6.15	490	130	0.2	$4.4 \times 10^5$
Sapphire	~0.54 $\mu\text{m}$	$1.16 \times 10^{-5}$	3.980	875	35	0.3	0

*Table 2.2 Thermal and optical physical parameters at room temperature [38-42].*

The interface was subjected to a 6 ns flat-top pulse profile to model the KrF laser pulse with absorption of the irradiation occurring at the sapphire/GaN interface. In COMSOL, it calculated the temperature distribution every 0.1 ns from 0 ns up to an ending time of 50 ns. The simulations assumed a sample (4- $\mu\text{m}$ -thick GaN film on 430- $\mu\text{m}$ -thick sapphire) was used in the simulation. The laser pulse in flat-top profile started at 0 ns to 6 ns. At different laser pulse energy density, the maximum temperature induced at GaN/sapphire interface ( $T_{\text{GaN/sapphire}}$ ) was simulated for the laser pulse duration  $\tau_i = 6$  ns. It is compared with other  $T_{\text{GaN/sapphire}}$  simulations for KrF laser single pulse with  $\tau_i = 10$  ns, 25 ns, and 38 ns, as shown in Fig. 2.3.

As seen in Fig. 2.3,  $T_{\text{GaN/sapphire}}$  is linearly increased with laser pulse energy density  $E_i$  at a constant  $\tau_i$ . At the same  $E_i$ , shorter  $\tau_i$  give higher temperatures, due to higher power densities of laser pulse.

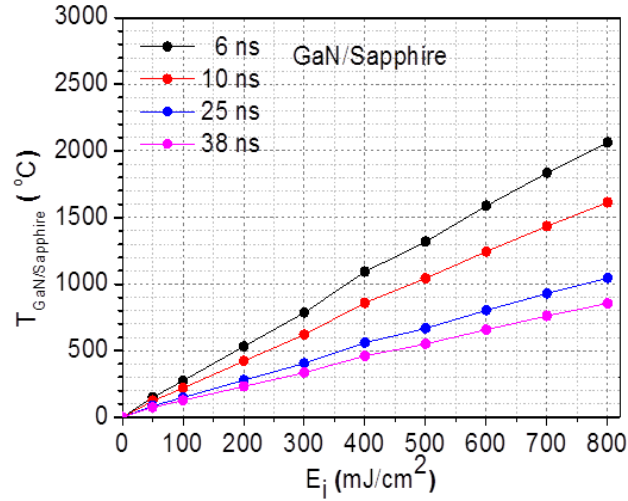


Figure 2.3 Simulated maximum temperature at the GaN/sapphire interface for a KrF laser pulse irradiation of different pulse durations at different laser pulse energy densities.

For a single KrF laser pulse with 6 ns pulse duration, an approximately 400 mJ/cm<sup>2</sup> is required to induce the surface decomposition temperature of GaN (i.e. 900°C to 1000°C). To achieve such thermal decomposition of GaN, higher pulse energy density is required for longer  $\tau_i$ , 500 mJ/cm<sup>2</sup>, 800 mJ/cm<sup>2</sup> and 900 mJ/cm<sup>2</sup> are requested for a pulse of  $\tau_i = 10$  ns, 25 ns, and 38 ns, respectively. The corresponding temperature distribution at these pulse durations was illustrated in Fig. 2.4.

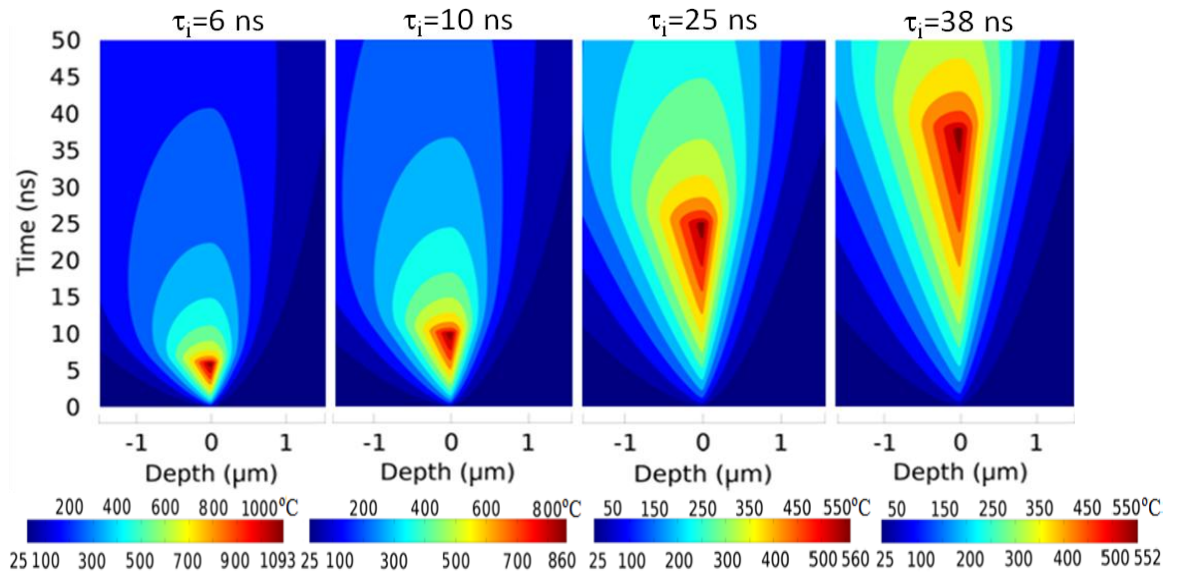


Figure 2.4 Simulated temperature distribution of GaN film irradiated at the GaN/sapphire interface for a KrF laser pulse of different pulse duration at energy density of 400 mJ/cm<sup>2</sup>. The calculation was done using temperature-independent GaN and sapphire properties.

At  $E_i = 400 \text{ mJ/cm}^2$ , the temperature spatial distribution at the GaN/sapphire interface varying with time, for a single pulse for different  $\tau_i$  is presented in Fig. 2.4. The heat spot (red color region) is induced at the interface and heat diffuses into both GaN and sapphire. For shorter  $\tau_i$ , heat induced has shorter thermal diffusion length ( $\xi$ ) which causes less spatial spreading of the heat than a pulse of longer  $\tau_i$ . This helps to keep the high temperature confined at the interface. Compared  $T_{\text{GaN/sapphire}}$  and  $\xi$  induced by a laser pulse of  $\tau_i = 6 \text{ ns}$  to  $\tau_i = 38 \text{ ns}$  at  $E_i = 400 \text{ mJ/cm}^2$ , the  $T_{\text{GaN/sapphire}}$  of 6 ns pulse ( $1093^\circ\text{C}$ ) is almost an order of magnitude higher than 38 ns ( $552^\circ\text{C}$ ), however,  $\xi$  is  $1.06 \mu\text{m}$  and  $2.67 \mu\text{m}$  respectively.

The temperature in the GaN film at different depths from the interface is simulated for a 6 ns pulse and shown in Fig. 2.5, where  $z = 0$  is at the interface and the depth at  $1 \mu\text{m}$ ,  $2 \mu\text{m}$ ,  $3 \mu\text{m}$  and  $4 \mu\text{m}$  in the GaN thin film was applied. It shows the GaN film is heating up from 0 to 6 ns that reaches at maximum temperature at the interface. Afterwards, a cooling starts from 6 ns to 50 ns for a decay of interface temperature to  $250^\circ\text{C}$ . However, there is only a very small temperature rise at  $3\text{-}\mu\text{m}$ -depth ( $\sim 100^\circ\text{C}$ ) during the pulse duration.

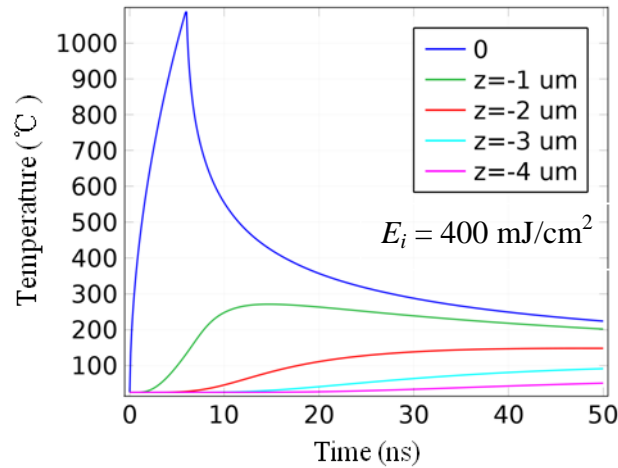


Figure 2.5 Simulated temperature in the GaN film at different depths ( $z$ ) from the GaN/sapphire interface for a 6 ns KrF laser pulse, at an energy density of  $400 \text{ mJ/cm}^2$ .

Therefore, the temperature in GaN film starts to rise after a pulse irradiation, due to the heat conduction from the GaN material at the GaN/sapphire interface. The pulse induced heat is dominant at the interface, and temperature rise becomes less obvious as one progresses into the GaN film, away from the interface. It also can be

confirmed that the temperature rise is confined to a region less than 2- $\mu\text{m}$  thick in the GaN and less than 1- $\mu\text{m}$  in the sapphire, during a pulse heating time of 6 ns, as shown in Fig. 2.6.

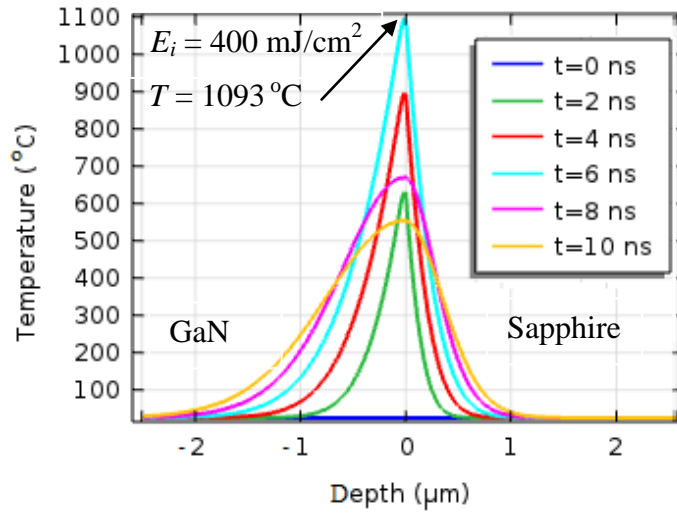


Figure 2.6 Simulated temperature at the GaN/sapphire interface vs. depth for a range of time for a pulse energy density of  $400 \text{ mJ/cm}^2$  (for 6 ns pulse).

A simulated temperature profile at the GaN/sapphire interface as a function of time and depth for a 6 ns single laser pulse with an energy density of  $400 \text{ mJ/cm}^2$  is shown in Fig. 2.7.

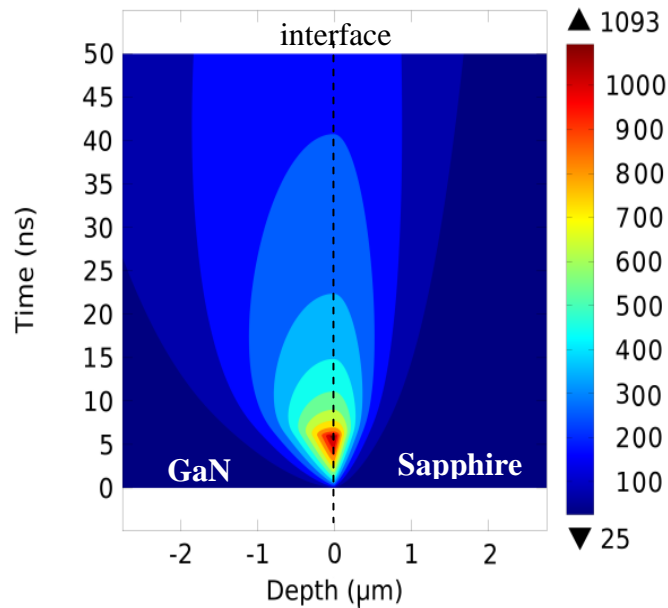


Figure 2.7 Simulated temperature distribution of GaN film irradiated at the GaN/sapphire interface for a laser pulse energy density of  $400 \text{ mJ/cm}^2$ . The calculation was done using temperature-independent GaN properties and the maximum temperature at the interface is  $1093^{\circ}\text{C}$ .

This model created was used to predict  $E_i$  that is required to induce thermal decomposition of GaN at the interface of GaN/sapphire. This model would help to determine  $E_i$  of KrF laser pulse to perform the LLO process. The simulation showed that the interface temperature raises over 1000°C, when a 6 ns, 400 mJ/cm<sup>2</sup> KrF laser pulse is applied. As seen in Fig. 2.7, the localized heat generated at the GaN/sapphire interface induces a temperature rise as laser irradiation on the GaN surface at the interface. A large temperature gradient across the thickness of the GaN film occurs in a highly localized heated region which is within 100 nm below the interface at 400 mJ/cm<sup>2</sup>. Due to the relatively higher thermal conductivity of GaN compared to sapphire, a weaker temperature gradient is distributed in sapphire. The temperature at the 1-μm-depth in GaN below the interface is 200°C at 6 ns. Meanwhile, the temperature rise of sapphire substrate is not neglectable during the laser irradiation.

The experimental findings were used to confirm  $E_i$  predicted in the model. A GaN LED epitaxy of ~ 4 μm-thick on sapphire substrate was irradiated by the use of KrF laser with 6 ns pulse width at different  $E_i$ . The surface morphology of GaN surface at the GaN/sapphire interface was examined by optical microscope. For  $E_i = 400$  mJ/cm<sup>2</sup>, rough surface features with metallic silver colors occurred, and the features were more noticeable at 500 mJ/cm<sup>2</sup>. Therefore, it showed that  $E_i$  should be over 400 mJ/cm<sup>2</sup> to decompose GaN – this is consistent with the prediction.

## **2.2 Laser lift-off method and experiment**

As seen in section 2.1,  $E_i$  required for the KrF excimer laser can be approximately predicted by the thermal diffusion model. Thus, a LLO system was required to delivery such energy density per laser pulse irradiation to GaN film. By adjusting the area of image plane projected at the sample,  $E_i$  can be obtained. Wafer attachment process before LLO to integrate the sample to a carrier substrate is also described and that will be seen later in the section 2.2.3.

### **2.2.1 Laser lift-off apparatus**

The experimental apparatus for the laser was based on a system originally used for micromachining on polymer. The LLO was carried out in an ambient air

environment using the KrF excimer laser, with a pulse duration of 6 ns. The maximum output pulse energy of the laser chamber is approximately 10 mJ with  $\pm 10\%$  variation. In order to maintain the relative stability of energy density for each single laser pulse in a pulse scan, the laser has to be kept in energy stabilizing mode. A fused quartz beam splitter reflects a fraction of the energy to a pyroelectric sensor which measures the pulse energy. This signal drives a feedback loop by automatic adjustment of the high voltage discharge in the range of 12 kV to 14 kV to stabilize the laser output to the pre-set energy level required.

$E_i$  of the incident laser light was varied between  $400 \text{ mJ/cm}^2$  and  $800 \text{ mJ/cm}^2$  by defocusing the laser beam with a fused silica (quartz) plano-convex projection lens, with effective focal length of 87 mm.

The LLO apparatus consists of three subsystems, as shown in Fig. 2.8 (a):

- ATLEX 300-SI KrF pulsed excimer laser chamber with a gas refill system
- OPTEC Light Deck process programme stage
- Computer with system controller

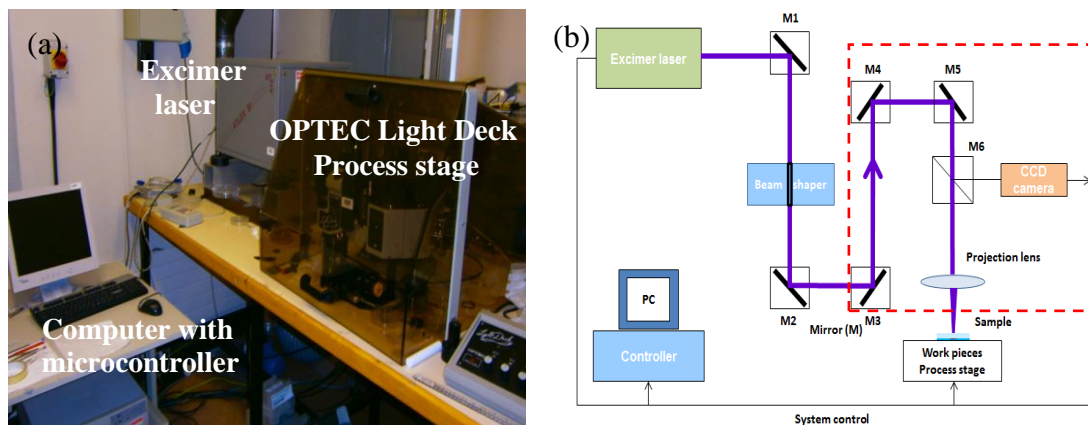


Figure 2.8 The LLO apparatus with KrF excimer laser system (a) photograph of the set-up (b) Schematic of the light delivery of the excimer laser system.

Fig. 2.8 (b) shows a schematic of the excimer laser process equipment. The OPTEC Light Deck process programme stage constitutes of 3 sections: laser beam delivery system with UV light reflection mirrors and the silica convex projection lens, automatic control moving process stage and video imaging.

### 2.2.2 Excimer laser beam spot energy density

For a set-up to perform areal laser processing, a homogenized beam profile would be expected. The KrF excimer laser system provides a flat-top quasi-rectangular Gaussian beam profile (e.g. typical cross section of  $8 \times 20 \text{ mm}^2$ ) on the target with homogeneity better than  $\pm 5\%$  [43]. In order to manipulate the system to be suitable for the LLO process, the two parameters are important.

- Homogeneity of spatial laser beam profile.
- Laser beam energy density.

Due to the intrinsic non-uniformity in output beam profile that is typically found in a gas laser, this beam must be reshaped to provide an LLO process window for the GaN decomposition. A local homogenized high intensity uniform region is made by cropping the centre area within the irradiation area.

The laser beam profile was adjusted by the use of a simple knife-edge technique. A beam shaper is an aperture where a razor blade edge is placed across the laser beam. The shape of the beam spot is a rectangle with a uniform flat top, by opening the aperture either in the vertical or horizontal direction. The energy of an incident laser beam spot directly irradiating on the back surface of the sample is a function of the aperture opening area. The energy density of an incident laser pulse beam spot can be expressed as  $E_i = I_0/A$ , where  $I_0$  (in mJ) is the incident laser energy on the sample (or the system output energy), and  $A$  is the exposed area of irradiation, namely the beam spot area.

The beam spot area can be manipulated by changing the demagnification (DM) factor of the light path control system, which basically adjusts the ratio objective distance and image distance to shrink the area of the beam spot in image plane projected on the sample. The beam shaper aperture opening area ( $A_0$ ) was kept constant as  $\sim 6 \times 5 \text{ mm}^2$ . Thus, the adjustment of exposed area of irradiation  $A$  can be provided by varying the ratio of objective distance and image distance (Fig. 2.9), where BM2 is the distance between beam shaper (B) to reflective mirror 2 (M2), M6l is the distance between reflective mirror 6 (M6) to the objective lens (l) and  $L_m$  is the distance from the lens to the sample. The rest of the labels are the distances between the correlated mirrors. However, only M3M4, M5M6, M6l and  $L_m$  are

variable and can be automatically controlled in the system. The rest of the distances in Fig. 2.9 are constant.

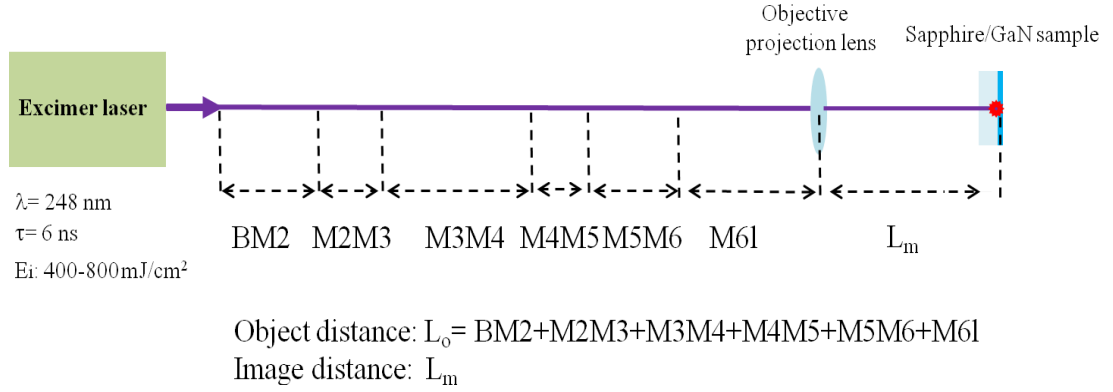


Figure 2.9 Schematic of optical distance adjustment to vary the beam image area.

The DM factor can be expressed as:

$$DM = \frac{L_o}{L_m}, \quad (2.11)$$

$L_o$  is objective distance that from beam aperture to objective lens, and  $L_m$  is image distance that from objective lens to target sample.

Thus, the beam spot area in the image plane ( $A$ ) (i.e. exposed area of laser pulse) irradiation can be obtained:

$$A = \frac{A_0}{DM}. \quad (2.12)$$

Recall the thin lens equation in geometric optics, the relationship between the beam aperture, imaging lens and projective image on the target material can be described as:

$$\frac{1}{L_o} + \frac{1}{L_m} = \frac{1}{f}, \quad (2.13)$$

where  $f$  is the focal length of the objective lens

To relate the objective and image distance to the demagnification by substituting eqn. (2.11) into eqn. (2.13),

$$L_o = (DM + 1) f, \quad (2.14)$$



Thus, the image distance can be obtained:

$$L_m = \frac{DM+1}{DM} f . \quad (2.15)$$

Then, after DM factor was put in the system control software, the  $L_o$  and  $L_m$  values/factors can be calculated as the eqns. (2.14) and (2.15) in the optical light path control system and automatically adjusted by the position translation of the mirrors M4, M5 and the position of the lens.

At the start of the experiment, the system output energy at the target sample position should be measured by the portable calorimeter, and then the system calibrated to give the incident energy of the laser pulse ( $I_0$ ) of 5.5 mJ. The opening positions of the aperture and the distance between the beam shaper and the mirror 2 (M2) are always the same. The beam spot area can be changed by automatically adjusting the distance between M3 to M4, M5 and M6 to objective lens, corresponds to a variation of both  $L_o$  and  $L_m$  in geometric optics. Hence, a variation in beam spot area in image plane is produced. A mark of laser beam spot can be obtained by simply irradiating incident beam directly on photoresist (PR) covered on Si substrate as shown in Fig. 2.10, which indicates the size of beam spot and beam profile uniformity.

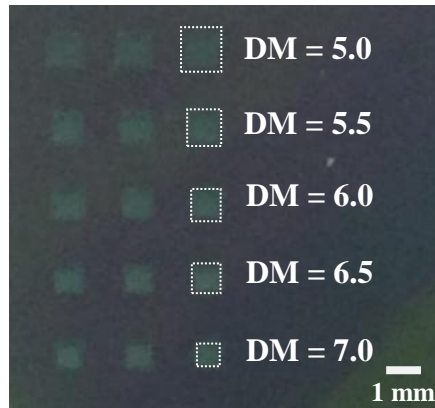


*Figure 2.10 Photograph of beam spots (size scale) of laser pulse at different demagnification factors (DM) of LLO apparatus on photoresist.*

In Fig. 2.10, the photography shows rectangular shape laser beam spots on PR at different DM factors. At the same DM factor, the laser beam spot was irradiated in 3 times which aligned in one row. The beam spot area is clear and its shape and size decreases with increasing DM factor.

As seen in Fig. 2.11, a clear rectangular shape beam spot area of  $1.2 \times 1.09 \text{ mm}^2$  in size on PR at the incident laser energy density  $400 \text{ mJ/cm}^2$  (i.e. DM = 5.0) is presented. It shows sharp edges at each side of this rectangular shape area that indicates a good beam profile of the laser irradiation. There are some very fine silk-type lines surrounding the edges that are the residues of PR after laser irradiation.

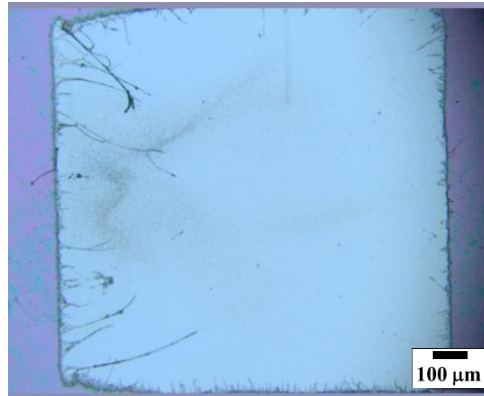


*Figure 2.11 Optical microscope image of a beam spot irradiated at  $400 \text{ mJ/cm}^2$  on photoresist (PR).*

The beam spot area (A) was measured at different DM factors and the corresponding energy density is then able to be calculated, shown in Fig. 2.12.

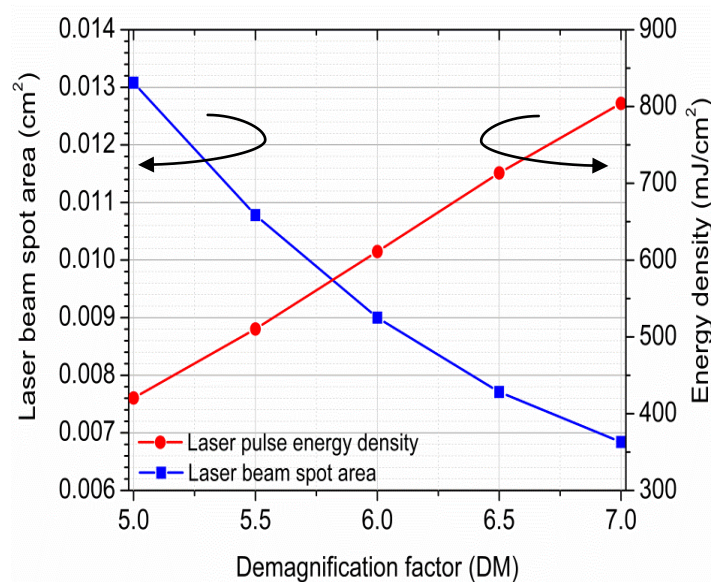


*Figure 2.12 Experimental results of beam spot area and corresponding laser pulse energy density at different DM factors on photoresist (PR).*

The higher DM factors result in smaller A, which leads to higher beam spot energy density. In the process, the incident laser pulse energy density can be selected just by simply choosing the DM factor required. The beam spot area almost linearly decreases with the increase of DM factor. The  $E_i$  value linearly increases with increasing DM factor. Thus, at DM factors of 5.0, 5.5, 6.0, 6.5 and 7.0, the corresponding energy densities are around 400 mJ/cm<sup>2</sup>, 500 mJ/cm<sup>2</sup>, 600 mJ/cm<sup>2</sup>, 700 mJ/cm<sup>2</sup> and 800 mJ/cm<sup>2</sup>, respectively.

The attenuation of the KrF excimer laser through about 430-μm-thick transparent sapphire substrate is approximately zero ( $\alpha_s = 0$ ) and the reflection at the GaN/sapphire interface is about 20% [39]. According to C. F. Chu *et al.* [40], the relationship of the laser induced GaN decomposition thickness (d) and the incident laser energy density ( $E_i$ ) for a single laser pulse can be estimated by the Beer-Lambert law [45]:

$$d = \left( \frac{1}{\alpha_{\text{GaN}}} \right) \ln \left( \frac{E_i}{E_{th}} \right) \quad (2.16)$$

As seen in Table 2.2, the absorption coefficient at  $\lambda = 248$  nm in GaN ( $\alpha_{\text{GaN}}$ ) is  $4.4 \times 10^5$  cm<sup>-1</sup>, and the threshold energy density for GaN decomposition ( $E_{th}$ ) is 300 mJ/cm<sup>2</sup> [41-44].

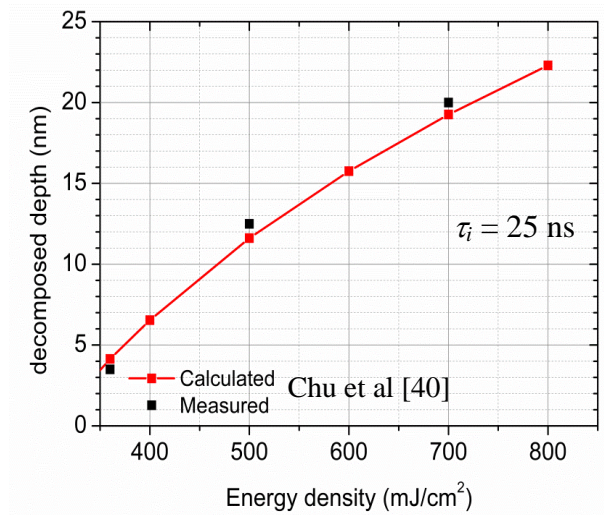


Figure 2.13 The thermal decomposed thickness of GaN calculated for a single incident laser pulse with energy densities from 400 to 800 mJ/cm<sup>2</sup> for  $\tau_i = 25$  ns.

Thus, the calculated and measured GaN decomposition thicknesses [40] and the measured data for a single incident laser beam of  $E_i$  from 400 to 800 mJ/cm<sup>2</sup> for

$\tau_i = 25$  ns, are plotted in Fig. 2.13. The thickness is estimated to be around 13 nm at  $E_i = 500$  mJ/cm<sup>2</sup> [11, 34, 40] and it is close to the calculated decomposition thickness of GaN that is about 12 nm at 500 mJ/cm<sup>2</sup>.

### 2.2.3 Wafer attachment and experiments

To completely remove a transferred nitride material from its original growth substrate, a thin film has to be bonded on a carrier substrate. The wafer bonding process is critical for mechanically keeping the material on the substrate. This flexible method for epitaxial integration has many advantages; any type of lattice mismatched or crystal direction mismatched materials can be simply integrated. The material characteristics are not affected because the bonding process only occurs at the surface of the bonded materials. A major issue in wafer bonding is the choice of the optimal bonding layer. The bonding material has to adhere to both the epitaxial film and the carrier substrate. The temperature necessary to achieve bonding should be relatively low to avoid thermal stress and without leaving behind any phase with a melting point below the bonding temperature. Moreover, it should have low electrical resistance to allow easy contact formation with the bonded device and high thermal conductivity. According to the bonding intermediate, wafer bonding technology can mainly be divided into adhesive bonding, metal bonding, and the method of electroplating a thick metal substrate.

#### 2.2.3-1 Review of wafer attachment for laser lift-off

For the adhesive bonding method, a polymer material is the bonding intermediate, such as thermoplastic, ethylcyanoacrylate (H<sub>6</sub>H<sub>7</sub>NO<sub>2</sub>) based adhesive epoxy resin and photoresist etc, as shown in Fig. 2.14. W. S. Wong *et al.* [46] reported a  $5 \times 5$  mm<sup>2</sup> free-standing c-plane GaN membrane realized, when an Si (001) wafer was bonded to the surface of the GaN thin film using a low-melting temperature wax from a sapphire/GaN/wax/Si structure. The LLO process, followed by a 40°C anneal, was used to remove the sapphire. Free-standing GaN membranes were then fabricated by dissolving the wax bond in acetone, allowing the membranes to float off the supporting Si substrate. W. C. Peng *et al.* [47] fabricated vertical conducting GaN LED with a metal reflector deposited and bonded the GaN LED epitaxial layer

on Si substrate by epoxy adhesive bonding and LLO. The device demonstrated an obvious improvement in its electrical characteristics and light extraction. R. H. Hong *et al.* [48] reported a GaN/Ag-reflector/Si substrate vertical conduction LED by the use of adhesive bonding and LLO.

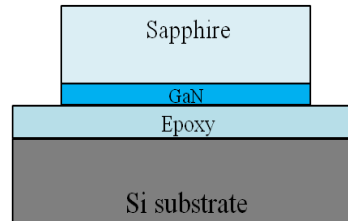


Figure 2.14 Schematic of adhesive bonding

For the metal bonding method, good electrical and thermal conduction metals were deposited on the wafer surface as a bonding intermediate. By taking advantage of metal diffusion or eutectic melting, the wafer with metal can be bonded on the metal evaporated on the carrier substrate. W. S. Wong *et al.* used a Pd-In metal bonding to connect GaN to Si [37, 49], whereas J. Jasinski *et al.* have succeeded in producing a GaN on GaAs substrate by direct wafer fusion [50].

T. Fujii *et al.* fabricated high optical output GaN-LED on Si substrates by using Au/Sn metal bonding and LLO process [51]. Moreover, S. K. Kim *et al.* fabricated an N-face vertical GaN/Ag-reflector/Cu substrate LED by bonding the Cu substrate and GaN LED epitaxial layer with deposited ITO and Ag and LLO process [52]. C. F. Chu *et al.* reported a vertical LED on Cu substrate fabricated by bonding the In deposited on Cu and GaN LED with Ni/Pd/Au as p-type contact metal at 200°C [40]. Even though the metal bonding method provides good thermal dissipation and electrical conduction which can further improve electrical and optical characteristics of devices, the bonding process is complicated. There are a few drawbacks that cause the bonding process to be difficult in operation:

- The cleaning, roughness and uniformity on the sample bonding surface are extremely critical.
- The curvature of the sapphire wafer makes it difficult to bond as it can induce an additive compressive stress during wafer bonding, which

results in a non-uniformity of the bonding layer, weak bond adhesion and then further cause the instability of laser lift-off.

- Thermal compression is generally required for metal bonding process, which could lead to the damage in the active region of the device [53].

In the electroplating method, a uniform metal layer is deposited by electroplating on the wafer surface as the carrier substrate. Because of the good thermal and electrical conductivity and simple operation of electroplating metal layer, it is widely applied in photonics device fabrication. S. J. Wang *et al.* [54] fabricated vertical GaN LED on Ni electroplated Ni substrate. Y. K. Song *et al.* [55] made vertical GaN RCLED on electroplated Cu substrate (~ 100- $\mu\text{m}$ -thick) for even better thermal dissipation than electroplated Ni substrate. However, the thickness of the metal layer electroplated needs to be carefully controlled, as it affects the curvature of the nitride epitaxial wafer both before and after LLO and even causes damages on the transfer GaN LED epitaxial [56, 57]. Both the metal bonding and electroplated metal substrate methods all have their disadvantages.

In this work, therefore, a soldering bonding method was proposed and used for GaN, AlGaIn grown on c-plane sapphire. Two types of approaches in this method are described in this chapter as shown in Fig. 2.15. Ti (20 nm)/Au (200 nm) metal stack is required to be evaporated on both p-contact metal of GaN LED wafer and Si substrate.

Approach I: a 30- $\mu\text{m}$ -thick Cu layer was electroplated on both the Au layer surface of GaN LED wafer and Si substrate. In order to integrate the GaN LED wafer on the Si substrate, a piece of  $\text{Sn}_{0.6}\text{Pb}_{0.4}$  soldering alloy was placed at the centre of Cu/Au/Ti/Si substrate. The wafer/p-contact metal/Ti/Au/Cu was thermal compressed on the Cu/Au/Ti/Si substrate at 200 °C for 2 to 5 minutes under a uniaxial force applied on the back surface of the wafer. Then, cooling down in ambient, a III-nitride material/p-contact metal/Ti/Au/Cu/ $\text{Sn}_{0.6}\text{Pb}_{0.4}$ /Cu/Au/Ti/Si was formed, which is ready for the laser irradiation process.

Approach II: a suitable size of thin  $\text{Au}_{80}\text{Sn}_{20}$  foil sheet was placed on the surface at Au/Ti/Si substrate and then the LED-wafer/p-contact metal/Ti/Au/Cu was thermal compressed with Au/Ti/Si substrate at 300 °C for 10 minutes under uniaxial force applied on the back surface of the wafer. Then, cooling it down in ambient

environment, the III-nitride LED material/p-contact metal/Ti/Au/AuSn/Au/Ti/Si substrate was formed, which would be ready for the laser irradiation process. This approach is used later on for AlGaN based DUV LEDs described in Chapter 4.

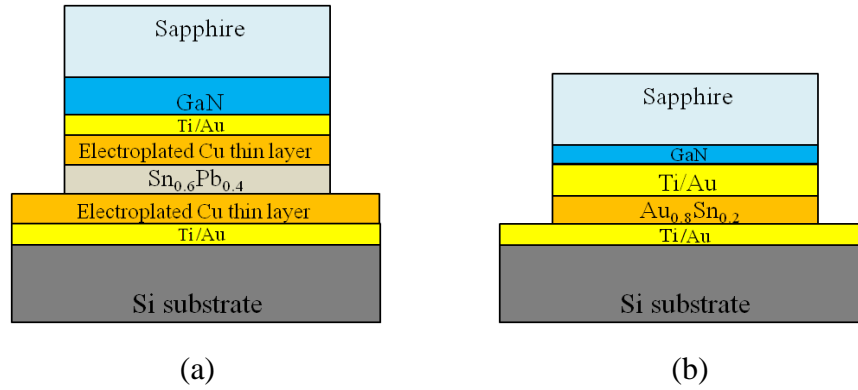


Figure 2.15 Schematic diagram of soldering metal bonding method: (a)  $\text{Sn}_{0.6}\text{Pb}_{0.6}$  with electroplated Cu layer and (b)  $\text{Au}_{0.8}\text{Sn}_{0.2}$  with thin Au layer.

The advantages of soldering metal bonding method are:

- Good thermal and electrical conductivity
- Not strictly need the sample surface to be very clean, low roughness and low uniformity.
- Both are low-temperature bonding, not affecting the p-contact metal and active region.
- Forms a thick bonding stack, the influence of wafer curvature is not so significant.

### 2.2.3-2 Experimental results

The LLO experimental results for a  $15 \times 20 \text{ mm}^2$  GaN LED wafer sample bonded on carrier substrate with the different bonding methods are shown in Fig. 2.16. All samples were processed at  $500 \text{ mJ/cm}^2$  laser pulse energy density. In Fig. 2.16, the transferred GaN LED on glass with epoxy is shown as Fig. 2.16 (a); (b) with Au coating layer direct bonded on Au layer that coated on Si substrate by thermal compressing; and (c) the transferred GaN LED on Si with  $\text{Sn}_{0.6}\text{Pb}_{0.4}$  soldering bonding method. Fig. 2.16 (a) shows that there are no any damages on the transferred GaN thin film (at left of the figure) and the sapphire substrate separated is beside. Fig. 2.16 (c) showed a clear surface on the transferred GaN LED wafer with



mesa patterned p-metal contact (i.e. the presented patterns when seen through the GaN LED layer in the figure). However, Fig. 2.16 (b) shows that localized delimitations of the transferred GaN film were observed after the removal of sapphire. It may be due to the weak adhesion of Au to Au thermal diffusion bond, which could be caused by the unclean surface on the Au layers and non-optimized recipe in the thermal compression. Therefore, the adhesive bonding and the metal soldering bonding method are easier and stable for the wafer attachment.

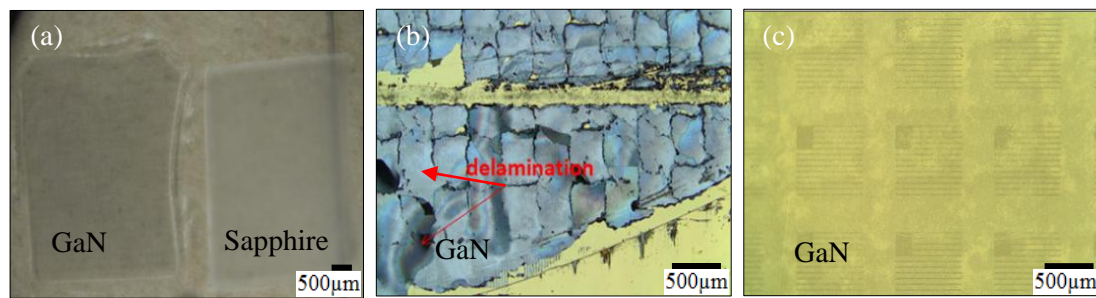


*Figure 2.16 Transferred GaN LED epitaxial layer ( $\sim 4\text{-}\mu\text{m}$ -thick) on carrier substrate structures with different bonding methods and processed by the use of LLO with a single laser pulse irradiation at an energy density  $500\text{ mJ/cm}^2$ : (a) GaN/epoxy adhesive/glass slide; (b) GaN/Ti/Au/Au/Ti/Si substrate (Au-Au direct bonding) and (c) GaN/Ti/Au/Cu/Sn<sub>0.6</sub>Pb<sub>0.4</sub>/Cu/Au/Ti/Si substrate.*

To conclude, the adhesive and soldering wafer bonding method can be good candidates for fabrication of transferred nitride material membranes on wafer-scale by LLO. For the LLO on III-nitride material wafer samples, a step-and-repeat laser pulse scanning method was used for successful lift-off.

### 2.3 Characterization methods for laser lift-off

This section outlines experimental techniques for evaluation of substrate lift-off nitride membranes (e.g. c-plane GaN) that were implemented by LLO. The characterization techniques in this study include the Nomaski image of laser beam spot at nitride material/sapphire interface at an incident laser pulse energy density, cross-section imaging by scanning electron microscope (SEM) and material quality characterization by X-ray diffraction (XRD). In this section, the evaluation of laser lift-off on GaN LED wafer grown on c-plane sapphire was taken as an example.



### 2.3.1 Nomarski microscopy

An optical microscope is used to capture the laser beam spot produced at the nitride material/sapphire interface. A successful laser induced-thermal decomposition of the nitride material at the interface requires sufficient incident laser pulse energy density of each single laser pulse. It produces a dark color rectangular pattern (i.e. beam spot) at the interface as Ga metallic droplets present, which leaves a separation gap between the nitride material and the sapphire and changes the transparency and reflection at the interface after LLO. Therefore, the minimum energy density required could be indicated to induce a uniform dark beam spot at the interface. Thus, for successful LLO on a nitride material wafer sample, the single laser pulse used in the step-and-repeat laser pulse scanning on the sample, should possess an incident energy density higher than the threshold value. The beam spot area can be estimated by the use of Nomarski optical microscope image presented.

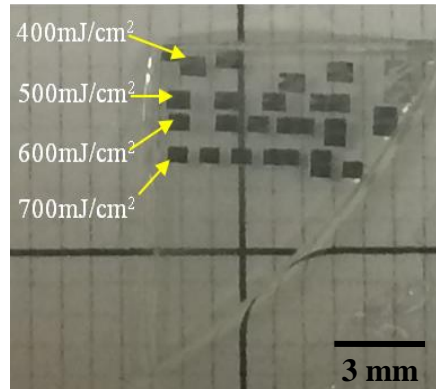


*Figure 2.17 Photograph of beam spots at GaN/sapphire interface on GaN wafer after excimer laser pulse irradiation at  $E_i$  over threshold energy density.*

In Fig. 2.17, a  $1 \times 1 \text{ cm}^2$  GaN/sapphire wafer sample was flip bonded on a glass slide with epoxy. The top surface is the back surface of double polished sapphire substrate. There are four rows of laser beam spots, which an incident laser pulse energy corresponds to a single row of beam spots, as labeled in the figure. The beam spots are smaller, when a higher incident laser pulse energy density required. It was found that the minimum energy density is  $400 \text{ mJ/cm}^2$  to produce a mark, which was induced by the GaN thermal decomposition.

### 2.3.2 Scanning Electron Microscope (SEM)

The scanning electron microscope (SEM) is an important imaging technique and tool that is widely applied in the examination of the surface of a variety of materials. This technique can provide high magnification images with a good depth of field and high resolution. Moreover, it can present dynamic experimental imaging of the sample in heated up, cooling and starching conditions. The basic principle is a beam of electrons is generated by a suitable source, typically a tungsten filament of a field emission gun [58]. The electron beam is accelerated through a high voltage (e.g. 20 kV) and passes through a system of apertures and electromagnetic lenses to focus and then produce a thin beam of electrons. The beam scans the surface of the sample by means of scan coils, and then the secondary electrons and back scattering electrons are emitted from the specimen. All the electrons produced by the interaction between the beam and sample are collected by a suitably-positioned detector, and then converted to electrical signals passing to a display tube. Finally, the magnified image of the sample surface can be displayed on the screen. The plan-view and cross-sectional configurations of the sample can be examined with this technique. Plan-view SEM is used to study the surface morphology of the materials as well as the microstructure or nanostructure in the plane of the devices. On the other hand, the cross-section SEM can be used to measure the depth distribution of features within the sample to be studied.

In this study, SEM in cross-section configuration measurement was carried out to examine the nitride material (e.g. GaN) after LLO. The measurements were taken using a Philips scanning electron microscope operating at 5 kV. Fig. 2.18 (a) shows a cross-sectional SEM image of a GaN LED wafer sample that was flip-bonded to a glass slide with Araldite epoxy before laser pulse irradiation. The sapphire substrate capped the GaN epitaxial layer on the epoxy resin. In contrast, Fig. 2.18 (b) shows the 57° tilted cross-sectional view of the GaN LED wafer sample after LLO and sapphire substrate removal. The thickness of the GaN LED epitaxial layer is around 4-μm-thick and it remains on the epoxy. No micro-cracking, buckling or damage on the GaN layer were observed, which indicates the LLO and the transfer of the GaN epitaxial layer was successful.

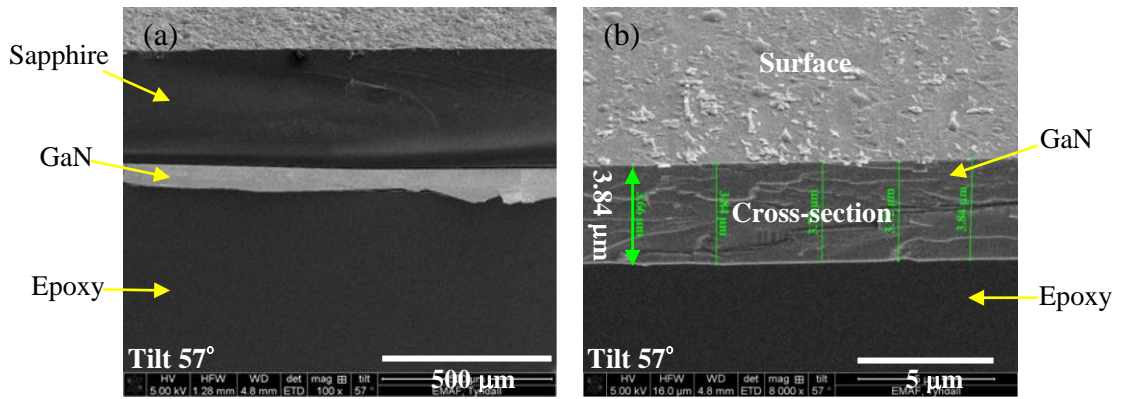


Figure 2.18 Cross-sectional SEM micrograph of (a) a GaN LED epitaxial layer grown on sapphire bonded to a glass slide with epoxy, (b) the GaN LED epitaxial layer after LLO bonded to the glass slide with epoxy. A single laser pulse energy density irradiated through the sapphire to separate the GaN at 500 mJ/cm.<sup>2</sup>

### 2.3.3 X-ray diffraction (XRD)

X-ray diffraction (XRD) is a useful tool as a non-destructive technique to study the crystal quality of materials, compositional information of alloys and thickness of epitaxial films. This technique relies on the diffraction of incident x-ray radiation from the periodic lattice planes of a crystal. X-rays are generated by bombarding a metal (typically Cu) with electrons in an evacuated tube and monochromatic x-rays are selected. These x-rays are scattered by the electron cloud surrounding each atom in the crystal. The diffraction of plane wave radiation can be described by Bragg's equation [59]:

$$n\lambda = 2d \sin\theta$$

where  $n$  is the order of diffraction,  $\lambda$  is the wavelength of the incident radiation,  $d$  is the distance between lattice planes and  $\theta$  is the Bragg angle

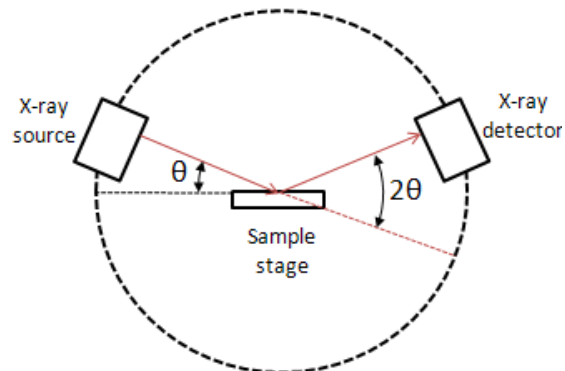
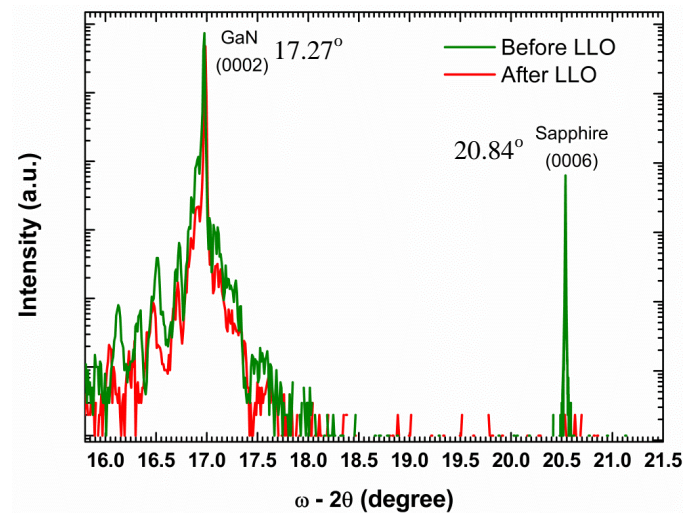


Figure 2.19 Schematic diagram of XRD setup.

In this work, the XRD measurements were carried out using a high-resolution x-ray diffractometer. The x-ray wavelength is close to the crystal lattice spacing. In order to obtain the compositional information of the sample before and after LLO,  $\omega$ - $2\theta$  measurements were carried out whereby the sample was scanned through the Bragg angle whilst simultaneously scanning the detector through twice the angle of the sample as shown in Fig. 2.19. A sample of GaN MQW LED grown on sapphire substrate was flip-bonded with epoxy adhesive on the glass slide, the LLO was applied on the sample.



*Figure 2.20 XRD  $\omega$ - $2\theta$  scans of c-plane GaN LED sample before and after lift-off from sapphire substrate. A pulse of energy density  $500 \text{ mJ/cm}^2$  was used for LLO.*

In Fig. 2.20, the  $\omega$ - $2\theta$  scan curves of the sample as-grown (i.e. before LLO) and after LLO are presented. Compared to the diffraction peaks on the curve of the as-grown sample and after LLO, it showed no sapphire peak of the sample after LLO, which indicated a successful fully removal and only GaN epitaxial layer remains. The successful lift-off of sapphire can be verified by the compared XRD scans before/after LLO.

## 2.4 Conclusions

The principle and physical mechanism of LLO on III-nitride thin film are described in the chapter, with the demonstration of GaN thin film on sapphire substrate. A thermal model is developed on the finite element modeling in COMSOL Multiphysics 5.0 to simulate the thermal conduction of laser irradiation in GaN and

evaluate the temperature distribution at the interface of GaN/sapphire. It shows that with a 6 ns laser pulse energy density over  $400 \text{ mJ/cm}^2$ , the temperature is over  $1000^\circ\text{C}$  that is required to induce thermal decomposition of GaN. To verify the results, the LLO process with a single pulse energy density at  $500 \text{ mJ/cm}^2$  was used for a successful LLO by step and repeat laser scanning on a  $15 \times 20 \text{ mm}^2$  GaN LED wafer sample bonded on a glass slide (1-mm-thick) with epoxy, and bonded on Si substrate (500- $\mu\text{m}$ -thick) with metal bonding. This chapter summarized the process procedures and parameters for successful lift-off of sapphire substrate and transfer of GaN thin film to carrier substrate, which can be applied to process other III-nitride materials, such as semipolar GaN grown on patterned r-plane (10 $\bar{1}2$ ) sapphire substrate and AlGaIn material grown on non-patterned c-plane (0001) sapphire substrate.

## 2.5 References

- [1] A. Sakai, H. Sunakawa, A. Usui, "Defect structure in selectively grown GaN films with low threading dislocation density," *Appl. Phys. Lett.*, vol. 71, no. 16, pp. 2259-2261, Aug. 1997.
- [2] T. Egawa, H. Ohmura, H. Ishikawa, T. Jimbo, "Demonstration of an InGaIn-based light-emitting diode on an AlN/sapphire template by metalorganic chemical vapor deposition," *Appl. Phys. Lett.*, vol. 81, no. 2, pp.292-294, Jul. 2002.
- [3] X. Q. Shen, H. Matsuhata, H. Okumura, "Reduction of the threading dislocation density in GaN films grown on vicinal sapphire (0001) substrates," *Appl. Phys. Lett.*, vol 86, no. 2, pp. 021912(1-3), Jan. 2005.
- [4] Y. J. Lin, "Activation mechanism of annealed Mg-doped GaN in air," *Appl. Phys. Lett.*, vol. 84, no. 15, pp. 2760-2762, Apr. 2004.
- [5] L. Sugiura *et al.*, "Dislocation motion in GaN light-emitting devices and its effect on device life time", *J. Appl. Phys.*, vol. 81, no. 4, pp. 1633-1638, Feb. 1997.
- [6] T. Wang, Y. Fang, X. Guo, G. Shen and Z. Cui, "Experimental and numerical investigation on GaN/Al<sub>2</sub>O<sub>3</sub> laser lift-off technique", *Thin Solid Films*, vol. 515, no. 7-8, pp. 3854-3857, Feb. 2007.
- [7] T. Ueda, M. Ishida and M. Yuri, et al, "Laser lift-off of very thin AlGaIn film from sapphire using selective decomposition of GaN interlayer", *Appl. Surf. Sci.*, vol. 216, pp. 512–518, Jun. 2003.
- [8] S. J. Rosner, E. C. Carr, M. J. Ludowise, G. Girolami and H. Erikson, "Correlation of cathodoluminescence inhomogeneity with microstructural defects in

epitaxial GaN grown by metalorganic chemical-vapor deposition,” *J. Appl. Phys. Lett.*, vol. 70, no. 4, pp. 420-422, Jan. 1997.

[9] S. Nakamura, M. Senoh, S. Nagahama, N. Iwasa, T. Yamada, T. Matsushita, Y. Sugimoto and H. Kiyoku, “High-Power, Long-Lifetime InGaN Multi-Quantum-Well-Structure Laser Diodes,” *Jpn. J. Appl. Phys.*, vol. 36, no. 28B, pp. 1059-1061, Aug. 1997.

[10] C. Huh, K. S. Lee, E. J. Kang, and S. J. Park, “Improved light-output and electrical performance of InGaN-based light-emitting diode by microroughening of the p-GaN surface,” *J. Appl. Phys.*, vol. 93, no. 11, pp. 9383-9395, Jun. 2003.

[11] E. A. Stach, M. E. Kelsch, C. Nelson, W. S. Wong, T. Sands and N. W. Cheung, “Structural and chemical characterization of free-standing GaN films separated from sapphire substrates by laser lift-off”, *Appl. Phys. Lett.*, vol. 77, no. 12, pp. 1819–1821, Sep. 2000.

[12] K. K. Leung, C. P. Chan, W. K. Fong, M. Pilkuhn, H. Schweizer and C. Surya, “High-resolution x-ray diffraction study of laser lift-off AlGaIn/GaN HEMTs grown by MOCVD method,” *J. Cryst. Growth.*, vol. 298, pp. 840–842, May. 2007.

[13] T. Detchprohm, H. Amano, K. Hiramatsu, and I. Akasaki, “The growth of thick GaN film on sapphire substrate by using ZnO buffer layer,” *J. Cryst. Growth.*, vol. 128, no. 1-4, pp. 384-390, Mar. 1993.

[14] S. J. Pearton, W. T. Lim, F. Ren and D. P. Norton, “Wet Chemical Etching of Wide Bandgap Semiconductors-GaN, ZnO and SiC,” *ECS Transactions*, vol. 6 no. 2, pp. 501-512, Jan. 2007.

[15] D. Zhuang, J. H. Edgar, “Wet etching of GaN, AlN, and SiC: a review”, *Materials Science and Engineering: R: Reports*, vol. 48, no. 1, pp. 1–46, Jan. 2005

[16] J. Haisma, G. A. C. M. Spierings, U. K. B. Biermann, and J. A. Pals, “Silicon-on-Insulator wafer bonding-wafer thinning technological evaluations,” *Jpn. J. Appl. Phys.*, vol. 28, no. 8, pp. 1426-1443, Aug. 1989.

[17] W. S. Wong, T. Sands, and N. W. Cheung, “Damage-free separation of GaN thin films from sapphire substrates,” *Appl. Phys. Lett.*, vol. 72, no. 5, pp. 599-601, Feb. 1998.

[18] W. S. Wong, J. Krüger, Y. Cho, B. P. Linder, E. R. Weber, N. W. Cheung, and T. Sands, Proceedings of the Symposium on LED for Optoelectronic Applications and the 28th State of the Art Programs on Compound Semiconductors 98-2, 377, 1998.

[19] M. K. Kelly, O. Ambacher, R. Dimitrov, R. Handschuh, and M. Stutzmann, “Optical process for lift-off of Group III-nitride films,” *Phys. Stat. Sol. (a)*, vol. 159, pp. R3-R4, Feb. 1997.

[20] M. K. Kelly, O. Ambacher, R. Dimitrov, H. Angerer, R. Handschuh, and M. Stutzmann, *Mat. Res. Soc. Symp. Proc.*, vol. 482, no. 973, Feb. 1998.

[21] <http://www.ioffe.ru/SVA/NSM/Semicond/>

- [22] F. Medjdoub and K. Iniewski, "Gallium Nitride (GaN): Physics, Devices, and Technology," (CRC Press, Taylor & Francis Group, LLC, New York, 2016).
- [23] <https://en.wikipedia.org/wiki/Gallium>
- [24] R. Groh, G. Gerey, L. Bartha and J. I. Pankove, "On the thermal decomposition of GaN in vacuum," *Phys. Stat. Soli. (a)*, vol. 26, no. 1, pp. 353-357, Nov. 1974.
- [25] E. Sancaktar, H. Lu, "The effects of excimer laser irradiation at 248 nm on the surface mass loss and thermal properties of PS, ABS, PA6, and PC polymers," *Journal of Applied Polymer Science*, vol. 99, no. 3, pp. 1024-1037, Feb. 2006.
- [26] V. Jindal "N-terminated (0001) surface, Development of III-nitride Nanostructures by Metal-organic Chemical Vapour Deposition", University at Albany, State University of New York, PhD dissertation (2008).
- [27] R. Srinivasan, W. J. Leigh, Ablative photodecomposition: action of far-ultraviolet (193 nm) laser radiation on poly(ethylene terephthalate) films," *J. Am. Chem. Soc.*, vol. 104, no. 24, pp. 6784-6785, Dec. 1982.
- [28] M. Von Allmen and A. Blastter, "Laser-Beam Interactions with Materials, Physical Principles and Applications, 2nd ed." (Springer, Berlin, 1995).
- [29] K. Niemax, W. Sdorra, "Optical emission spectrometry and laser-induced fluorescence of laser produced sample plumes," *Applied Optics*, vol. 29, no. 33, pp. 5001-5006, Nov. 1990.
- [30] R. Miskys, K. Kelly, O. Ambacher, M. Stutzmann, "Freestanding GaN substrates and devices," *Phys. Stat. Soli. (c)*, vol. 0, No. 6, pp. 1627-1650, Sep. 2003.
- [31] W. S. Wong, Y. Cho, E. R. Weber, *et al.*, "Structural and optical quality of GaN/metal/Si hetero-structure fabricated by excimer laser lift-off," *J. App. Phys. Lett.*, vol. 75, no. 13, pp. 1887-1889, Sep. 1999.
- [32] H. P. Ho, K. C. Lo, G. G. Siu, C. Surya, K. F. Li and K. W. Cheah, "Raman and photoluminescence spectroscopy of free-standing GaN separated from sapphire substrate by 532 nm Nd: YAG laser lift-off," *J. Mater. Chem. Phys.*, vol. 81, no.1, pp. 99-103, Jul. 2003.
- [33] T. Ueda, M. Ishida and M. Yuri, "Separation of thin GaN from sapphire by laser lift-off technique," *Jpn. J. Appl. Phys.*, vol. 50, no. 4, pp. 041001(1-6), Apr. 2011.
- [34] J. H. Cheng, Y. C. S. Wu, and W. C. Peng, "Effects of laser sources on damage mechanisms and reverse-bias leakages of Laser lift-off GaN-based LEDs," *J. Electrochem. Soc.*, vol. 156, no. 8, pp. H640-H643, Jun. 2009.
- [35] X. L. Tong, L. Li, D. S. Zhang and H. Long, "The influences of laser scanning speed on the structural and optical properties of thin GaN films separated from sapphire substrate by excimer laser lift-off," *J. Phys. D: Appl. Phys.*, vol. 42, no. 4, pp. 045414(1-4), Jan. 2009.
- [36] L. M. Jiji, "Heat conduction, 3rd edn" (Springer Verlag Berlin Heidelberg, 2009)

- [37] W. S. Wong, "Integration of GaN Thin Films with Dissimilar Substrate Materials by Wafer Bonding and Laser Lift-off," University of California, Berkeley, PhD dissertation (1999).
- [38] O. Knacke, O. Kubaschewski, and K. Hesselmann, "Thermochemical Properties of Inorganic Substances," (Springer Verlag, Berlin, 1991).
- [39] H. Chen, R. D. Vispute, V. Talyansky, R. Enck, S. B. Ogale, T. Dahmas, S. Chooon, R. P. Sharma, T. Venkatesan, A. A. Iliadis, L. G. Salamanca-Riba, and K. A. Jones, *Mater. Res. Soc. Symp. Proc.*, pp. 482-1015, 1998.
- [40] C. F. Chu, F. I. Lai, J. T. Chu, C. C. Yu, C. F. Lin, H. C. Kuo and S. C. Wang, "Study of GaN light-emitting diodes fabricated by laser lift-off technique," *J. Appl. Phys.*, vol. 95, no. 8, pp. 3916-3922, Apr. 2004.
- [41] K. Osamura, K. Nakajima, Y. Murakami, "Fundamental absorption edge in GaN, InN and their alloys," *Solid State Commun.*, vol. 11, no. 5, pp. 617-621, Sep. 1972.
- [42] G. Y. Mak, E. Y. Lam, H. W. Choi, "Liquid-immersion laser micromachining of GaN grown on sapphire," *J. Appl. Phys. A*, vol. 102, no. 2, pp. 441-447, Feb. 2011.
- [43] E. K. Sichel and J. I. Pankove, "Thermal conductivity of GaN, 25-360 K," *J. Phys. Chem. Solids*, vol. 38, no. 3, pp. 330, Jul. 1977.
- [44] J. F. Muth, J. H. Lee, I. K. Shmagin, R. M. Kolbas, H. C. Casey, B. P. Keller, U. K. Mishra, and S. P. DenBaars, "Absorption coefficient, energy gap, exciton binding energy, and recombination lifetime of GaN obtained from transmission measurements," *Appl. Phys. Lett.*, vol. 71, no. 18, pp. 2572-2574, Nov. 1997.
- [45] L. Migliore, "Laser Materials Processing" (Markcel Dekker, New York, 1996).
- [46] E. T. Yu, "III-V Nitride Semiconductors: Applications and Devices" (CRC Press, Taylor & Francis, New York, 2003).
- [47] W. C. Peng, Y. C. S. Wu, "Performance of InGaN-GaN LEDs fabricated using glue bonding on 50 mm Si substrate," *IEEE. Photon. Tech. Lett.*, vol. 18, no. 4, pp. 613-615, Feb. 2006.
- [48] R. H. Hong, W. K. Wang, S. Y. Huang and D. S. Wu, "Effect of resonant cavity in wafer-bonded green InGaN green LED with dielectric and silver mirrors," *IEEE. Photon. Tech. Lett.*, vol. 18, no. 3, pp. 457-459, Feb. 2006.
- [49] W. S. Wong, T. Sands, N. W. Cheung, M. Kneissl, D. P. Bour, P. Mei, L. T. Romano, and N. M. Johnson, "In<sub>x</sub>Ga<sub>1-x</sub>N light emitting diodes on Si substrates fabricated by Pd-In metal bonding and laser lift-off," *Appl. Phys. Lett.*, vol. 77, no. 18, pp. 2822-2824, Oct. 2000.
- [50] J. Jasinski, Z. Liliental-Weber, S. Estrada, and E. Hu, "Microstructure of GaAs/GaN interfaces produced by direct wafer fusion," *Appl. Phys. Lett.*, vol. 81, no. 17, pp. 3152-3154, Oct. 2002.
- [51] T. Fujii, Y. Gao, R. Shama, E. L. Hu, S. P. DenBaars and S. Nakamura, "Increase in the extraction efficiency of GaN-based light emitting diodes via surface roughening," *Appl. Phys. Lett.*, vol. 84, no. 6, pp. 855-857, Feb. 2004.



- [52] S. K. Kim, J. W. Lee, H. S. Ee, Y. T. Moon, S. H. Kwon, H. K. and H. G. Park, "High efficiency vertical GaN slab light-emitting diodes using self-coherent direction emitters," *Opti. Express*, vol. 18, no. 11, pp. 11025-11032, May. 2010
- [53] J. W. Jang, S. Hayes, J. K. Lin and D. R. Frear, "Interfacial reaction of eutectic AuSi solder with Si (100) and Si (111) surfaces," *J. Appl. Phys.*, vol. 95, no. 11, pp. 6077-6081, Jun. 2004.
- [54] S. J. Wang, K. M. Uang, S. L. Chen, Y. C. Yang, S. C. Chang and T. M. Chen, "Use of patterned laser liftoff process and electroplating nickle layer for the fabrication of vertical-structured GaN-based light-emitting diodes," *Appl. Phys. Lett.*, vol. 87, no. 011111, Jul. 2005.
- [55] Y. K. Song, M. Diagne, H. Zhou, and A. V. Nurmikko, C. Carter-Coman, R. S. Kern, F. A. Kish and M. R. Krames, "A vertical injection blue light emitting diode in substrate separated InGaN heterostructures," *Appl. Phys. Lett.*, vol. 74, no. 24, pp. 3720-3722, Jun. 1999.
- [56] S. Kim, J. H. Jang, J. S. Lee, D. J. Duquette, "Stress behavior of electrodeposited copper films as mechanical supporters for light emitting diodes," *Electrochimica Acta.*, vol. 52, no. 16, pp. 5258-5265, Feb. 2007.
- [57] S. Kim, "Effect of residual stress of thin and thick layer on laser lifted-off light emitting diodes," *J. Electro. Soc.*, vol. 158, no. 9, pp. H904-H907, Jul. 2011.
- [58] [http://serc.carleton.edu/research\\_education/gechemsheets/techniques/SEM.html](http://serc.carleton.edu/research_education/gechemsheets/techniques/SEM.html)
- [59] B. D. Cullity and S. R. Stock, "Elements of X-Ray Diffraction 3<sup>rd</sup> edn." (Englewood Cliffs, NJ: Prentice-Hall, 2001).

## Chapter 3

### Fabrication of free-standing semipolar (11 $\bar{2}2$ ) InGaN LEDs

In this chapter, the fabrication process development of free-standing semipolar (11 $\bar{2}2$ ) InGaN/GaN multiple-quantum-well (MQW) light-emitting diodes (LEDs) membrane by the use of laser lift-off (LLO) is presented. Different methods such as light output power, current-voltage (I-V) characteristics, fluorescence microscopy imaging, electroluminescence (EL), optical polarization resolved EL and electro-optical modulation bandwidth measurements were used to characterize the electrical and optical properties of the LEDs.

#### 3.1 Introduction

Wurtzite indium gallium nitride (InGaN) based LEDs have demonstrated exceptional efficiency and output powers in the visible spectral range (420 nm - 700 nm) [1-3]. Commercially available InGaN-based LEDs have been grown on the *c*-plane (0001) oriented surface, which has strong built-in piezoelectric fields. The piezoelectric polarization fields at the InGaN/GaN interface tilt the energy band of the QW based active region. This induces a quantum-confined Stark effect (QCSE), lowering the electron-hole wave-function overlap and device efficiency [4], as well as inducing wavelength shift with current. A reduction in the QCSE will increase the overlap and, therefore, increase the radiative recombination rate. Hence, it is desirable to produce InGaN/GaN QW LEDs with a suppression of the internal fields [4-11] for high bandwidth devices [12-15].

The fields can be reduced by growing LEDs on semipolar and nonpolar oriented surfaces of the crystal [16, 17]. The semipolar (11 $\bar{2}2$ ) surface is of special interest because high-efficiency green and yellow packaged LEDs have been previously reported [18-21] with best results for devices grown on bulk (11 $\bar{2}2$ ) GaN substrates [18]. Such substrates are very expensive and small in size and thus not suitable for mass-production. Thus, it is preferable to grow LEDs on a low-cost sapphire substrate. However, (11 $\bar{2}2$ ) GaN films grown on non-patterned (10 $\bar{1}0$ ) *m*-plane sapphire substrates normally contain a high density of extended defects such as

basal-plane stacking faults, prismatic stacking faults and partial dislocations [22]. In order to reduce such defects, several approaches have been proposed in recent years [23-25]. Here, LEDs were grown on a 50- $\mu\text{m}$ -thick GaN template which was grown on a patterned (10 $\bar{1}2$ ) *r*-plane sapphire substrate (PSS) using a growth process which has been scaled to 100 mm diameter wafers [26].

Despite the good crystallinity of (11 $\bar{2}2$ ) GaN on PSS, the rough surface morphology with a high density of micro-sized arrow-head features resulted in a luminescence non-uniformity of QWs and LEDs [21, 27]. To overcome this problem, chemical-mechanical polishing (CMP) can be used to planarize directly the template surface [21, 28]. D. V. Dinh *et al.* first reported LEDs grown on (11 $\bar{2}2$ ) GaN-CMP templates (up to 100-mm-diameter) [21]. In order to achieve free-standing (11 $\bar{2}2$ ) GaN LEDs (so-called FS-LEDs) grown on sapphire substrate, an epitaxial lift-off of GaN is required to remove the epitaxial section from the substrate. LLO provides a fast and convenient way to selectively decompose GaN to separate GaN epitaxy section from substrate to achieve a FS-LEDs. To the author's best knowledge, there is no report on the fabrication and electro-optical characterizations of FS-LEDs prepared by the LLO process.

This chapter describes the fabrication of free-standing semipolar (11 $\bar{2}2$ ) LLO-GaN membrane (so called FS-GaN) and the fabrication of InGaN/GaN FS-LEDs with the characterization of the material, electrical and optical properties before and after lift-off and after CMP. An LLO technique was developed for FS MQW LEDs operating at  $\sim 445$  nm and electro-optical characterization of the devices was carried out, which included light output power, current-voltage, electroluminescence spectra and optical polarization at driven current. Meanwhile, the bandwidth measurements of the LEDs were demonstrated to show that they can be suitable for visible light communication (VLC) applications. It was found that the thermally annealed p-contact metal Ni/Ag/Ni performed as a quasi-ohmic metal contact and a good reflector improving the light output through the substrate. The output power of the LED ( $300 \times 300 \mu\text{m}^2$ ) was enhanced after LLO and CMP. A stable light emission with an anisotropic emission pattern was observed. The polarization ratio was calculated for the LED after LLO and after CMP. The small signal bandwidth at the

- 3 dB frequency response of the LEDs (which was not optimized for VLC) can reach 166 MHz at 20 mA.

### 3.2 Fabrication of free-standing semipolar (11 $\bar{2}$ 2) GaN membrane

As the initial specification described in the LLO outlined in Chapter 2, an LLO process for a layer-transfer of a thin film should not adversely affect the properties of the transferred GaN film. To create an FS-GaN membrane can provide a simple way to test this criterion for LLO. The characterization of the FS-GaN membrane can provide details of the material, electrical and optical properties without the effect of the original growth substrate as well as direct comparison to the thin film before laser processing.

Moreover, for the removal of the original growth substrate by LLO, a thin film transfer process is required. It can eliminate the influence of the original growth substrate in the characterization. The material properties of FS-GaN membrane can be examined to determine the effect of substrate removal by laser processing and GaN v-grooves removal by CMP. In this section, the fabrication of the membrane with characterization of the material structure after LLO and CMP are described.

To fabricate FS-GaN membrane based on LLO, GaN templates were grown on PSS by two techniques: metal-organic vapor phase epitaxy (MOVPE) followed by hydride vapor phase epitaxy (HVPE) [46-48]. The cross-section of the HVPE GaN/sapphire sample and its SEM image are shown in Fig. 3.1.

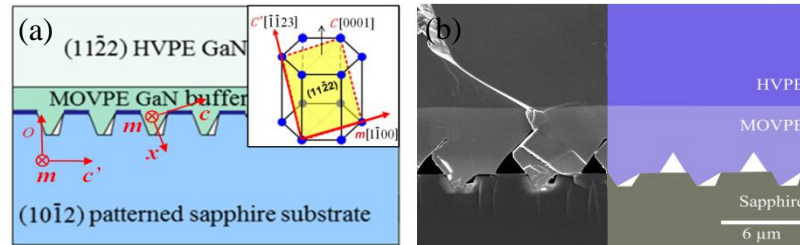


*Figure 3.1 Cross section of HVPE GaN/sapphire sample (in the  $m = (1\bar{1}00)$ -plane of a direction of  $o[11\bar{2}2]$ , the directions  $x[11\bar{2}0]$ ,  $c'[\bar{1}\bar{1}23]$  and  $c[0001]$  projected onto the sample surface, all given directions relate to the crystal structure of GaN. (a) Schematic of the layered structure of the HVPE template (inset: GaN crystal structure), (b) SEM image [30].*

The MOVPE-grown GaN buffer layer has a thickness of  $\sim 6 \mu\text{m}$  and the thickness of HVPE-grown GaN layer is  $\sim 50 \mu\text{m}$ . The HVPE process provides a faster growth rate in comparison to MOVPE, enabling a quicker production of high crystal quality FS-GaN substrate for the subsequent development of devices [29].

### 3.2.1 Semipolar GaN thin film transfer and laser lift-off process

The bonding process used to create FS-GaN membranes was similar to the process previously described in Chapter 2 for c-plane GaN LED wafer. A 2-inch  $(11\bar{2}2)$  HVPE-grown GaN template wafer was diced into different pieces of  $1.5 \times 1 \text{ cm}^2$  and then the pieces were flipped bonded on a carrier substrate (glass slide) using a low-melting temperature thermo-adhesive (crystal-bond 509 clear wax [49]) to form a sapphire/GaN/SiO<sub>2</sub> structure. The wax pieces were placed at the centre of the glass slide, which was going to be prebaked initially by the hot plate at 120 °C for 5 min. The wafer sample was baked on the hot plate at same temperature at the same time. After the wax fully melted in  $\sim 2$  min, the sample was flip-bonded the surface of the GaN template on the melting wax layer as shown in Fig. 3.2. In order to keep the thermal induced stress in the wax bonding layer as small as possible, the bonded wafer sample was left on the hot plate to cool down to the room temperature for  $\sim 30$  min. Afterwards, the wax layer was completely cured, the total thickness of the bonded sample was measured using a micrometer, and the thickness of the wax layer was estimated ( $\sim 70 \mu\text{m}$ ) by subtracting the total thickness and the wafer sample thickness.

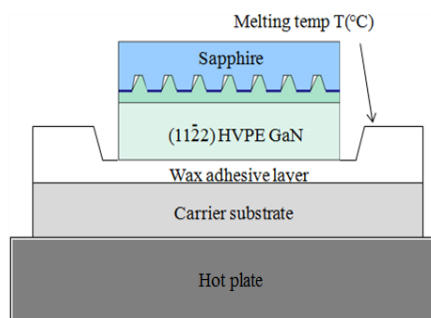


*Figure 3.2 Wafer bonding of semipolar  $(11\bar{2}2)$  GaN template wafer sample using wax adhesive.*

Sapphire substrate removal was achieved by laser-induced delamination of GaN strips enhanced by the air-filled grooves [46-48] at the substrate-GaN film interface. A single-shot laser pulse with an irradiation density of  $500 \text{ mJ/cm}^2$  was scanned across the back surface of PSS of the wafer piece using the KrF excimer laser system (ATLEX-300-SI) to remove GaN film from the substrate without damage was observed due to the LLO process. By using this two-step process of LLO and wafer-debonding, the GaN film up to  $1.5 \times 1 \text{ cm}^2$  in area was successfully transferred by irradiating a  $0.01 \text{ cm}^2$  beam spot across the entire sample as shown in Fig. 3.3(a).

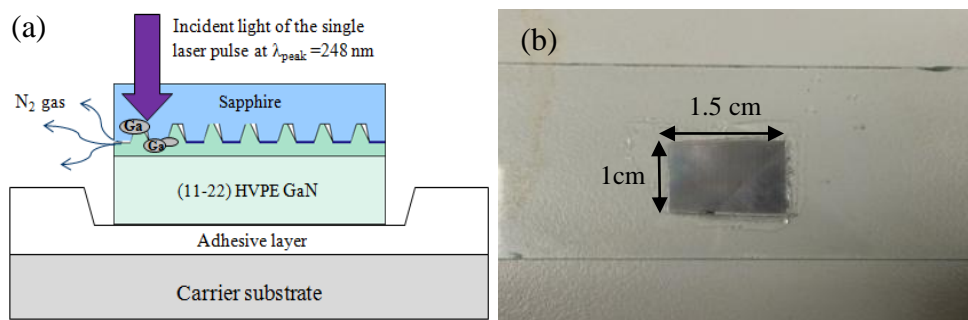


*Figure 3.3 Schematic of laser lift-off on semipolar GaN on patterned sapphire substrate (b) Photography of the top view of a  $\sim 50 \mu\text{m}$  thick free-standing semipolar GaN membrane (size  $1.5 \times 1 \text{ cm}^2$ ).*

The Ga droplets on the back surface of the GaN/sapphire interface were cleaned by HCl: DI (1:1) solution for 2 min, then rinsing in DI in 1 min and dried up with  $\text{N}_2$  gas. After LLO and transfer of the GaN membrane onto the supporting glass slide, the GaN/wax/ $\text{SiO}_2$  was then immersed in acetone to dissolve the wax adhesive bond and release the  $50\text{-}\mu\text{m}$ -thick GaN film creating a FS-GaN membrane. By using the process developed above, the GaN film was successfully lifted-off as shown in Fig. 3.3 (b). Moreover, as shown in Fig. 3.4 there are no cracks and no damage on both the back and top surfaces of GaN layer after LLO; therefore, the process gives no mechanical damage during the laser irradiation. The metal contact patterns for circular transmission line method (c-TLM) were deposited on the top surface of the sample before LLO. After LLO, no detrimental effect on the patterns was observed as shown in Fig. 3.4 (b).

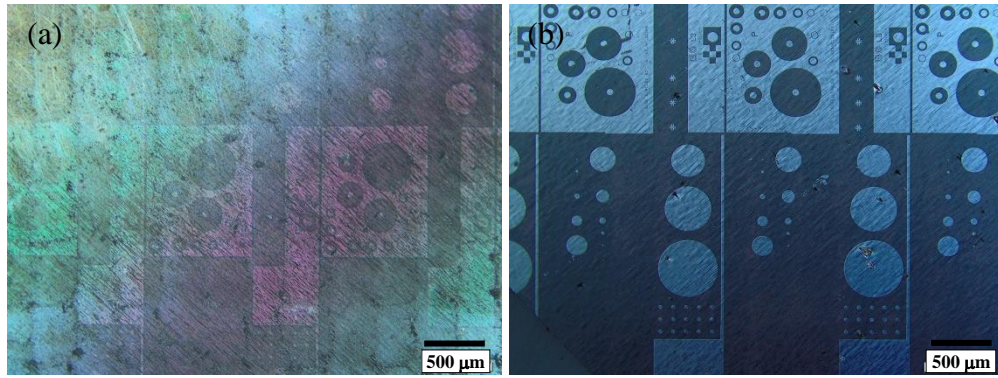


*Figure 3.4 Nomarski microscopy image of a sample after LLO (a) back surface and (b) top surface*

### 3.2.2 Chemical-mechanical planarization

On the back surface of the FS-GaN membrane, there are periodic GaN strips ( $\sim 3\text{-}\mu\text{m}$ -wide) with crystal defects [9]. Thus, it is necessary to polish these GaN strips (v-grooves) to achieve the good crystal quality of the membrane. In order to polish off the strips on the back surface of the membrane, it is then required to be transferred onto a supporting frame. A (001) Si wafer ( $2 \times 2\text{ cm}^2$  size,  $500\text{-}\mu\text{m}$ -thick) was bonded to the top surface of the  $50\text{-}\mu\text{m}$ -thick membrane using a black wax (Mounting wax 100) to form a GaN/wax/Si structure. The CMP is a good candidate for polishing these GaN features (v-grooves) on GaN with high standard surface flatness [21, 28].

#### 3.2.2-1 Overview of chemical mechanical planarization

CMP is a process whereby a chemical reaction increases the mechanical removal rate of a material. CMP is mostly used for material removal by polishing the “hills” on wafer and “flattening” thin film. The chemical reaction between the slurry and wafer is tailored to enhance material removal and bring about quicker planarization of the thin film [31]. The combination of chemical and mechanical reactions was applied to remove material leaving a planarized and damage-free surface. Ideally, material removal is achieved by chemically altering the surface to a mechanically weaker form; this material is then abraded from the surface leaving the bulk undisturbed. Planarization occurs due to the acceleration of both mechanical grinding and chemical transformation at the high points (as seen in Fig. 3.5). Mostly, CMP has

been used to polish sapphire and SiC substrate [32, 33]. J. L. Weyher *et al.* [34] and P. R. Tavernier *et al.* [35] reported GaN CMP studies on N-face (000 $\bar{1}$ ) and achieved smooth surface morphology over small areas on the N-face, the Ga-face (0001) showed no alteration but damage induced to the surface. S. Hayashi *et al.* demonstrated a CMP process on (0001) GaN substrate with a fine polishing to achieve scratch-free surface without crystalline damage [36] and the reports of no crystalline damage CMP process on GaN were reported by others [37-45]. Recently, D. V. Dinh *et al.* has successfully demonstrated CMP for (11 $\bar{2}2$ ) LED wafers up to 100-mm diameter to achieve a smooth surface [21].

At Tyndall National Institute, CMP process on the GaN strips on the back surface of the FS-GaN after LLO, was carried out by the use of G & P technology POLI-500 (Fig. 3.6).

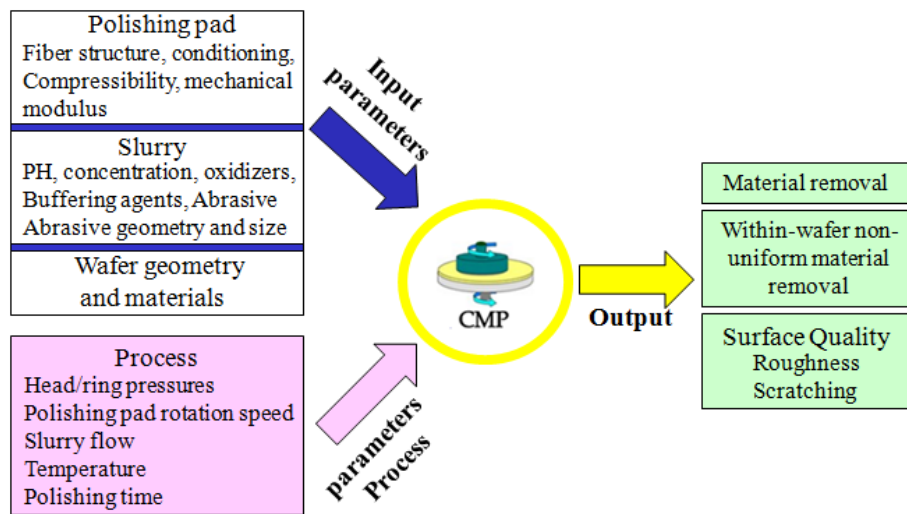


Figure 3.5 Schematic diagram of CMP Figure 3.6 G&P POLI-500 CMP system [51]

The outcome of CMP process is specified by the material removal rate, within wafer non-uniformity and surface quality (roughness, scratching) of a wafer sample. As shown in Fig. 3.7, the process quality is determined by these input parameters and process parameters. The input parameters include details of polishing pad, slurry, wafer geometry and materials. The polishing pad consists of fiber structures on the polishing surface associated with mechanical modulus and compressibility contributed to mechanical polishing. The condition of the pad also influences the



process. The slurry contains small abrasive particles and etching chemical solution in certain pH and concentration value. The geometry and size of abrasive and corrosive colloidal slurry contribute to chemical etching and fine mechanical polishing, as the rotation of polishing pad and retainer ring. The wafer sample materials and geometry can affect the material removal rate and polished surface uniformity. The process parameters were set in the CMP system to control the process, which includes head/ring pressures ( $\text{g/cm}^2$ ), polishing pad rotation speed (rpm), head rotation speed (rpm), slurry flow (rpm), temperature ( $^{\circ}\text{C}$ ) as well as the overall polishing time (s).



*Figure 3.7 CMP parameters*

### 3.2.2-2 Chemical mechanical planarization on FS-GaN membrane

After the GaN film debonding from the glass slide based on the work described in section 3.2.1, the FS-GaN membrane was flip-bonded on a (001) Si substrate ( $2 \times 2 \text{ cm}^2$ ) by black wax (Mounting wax 100). Then, the stripes on back surface of the wafer were polished by CMP. CMP process parameters were: wafer pressure =  $80 \text{ g/cm}^2$ , retainer ring pressure =  $160 \text{ g/cm}^2$ , carrier/platen speed = 60/60 rpm, slurry = 55 rpm, polish time = 45 min. Finally, the FS-GaN membrane wafer was achieved by dissolving the thermo-adhesive bonding layer between the Si carrier substrate and the wafer in trichloroethylene (TCE) solvent. As shown in Fig. 3.8, there is no damage or fractures on the 50- $\mu\text{m}$ -thick HVPE-grown

GaN thin film when the thin film is transfer bonded on Si substrate and after CMP at optimized process parameters. The thin film debonding process after CMP is shown in Fig. 3.9, and a FS-GaN film after CMP was successfully created.

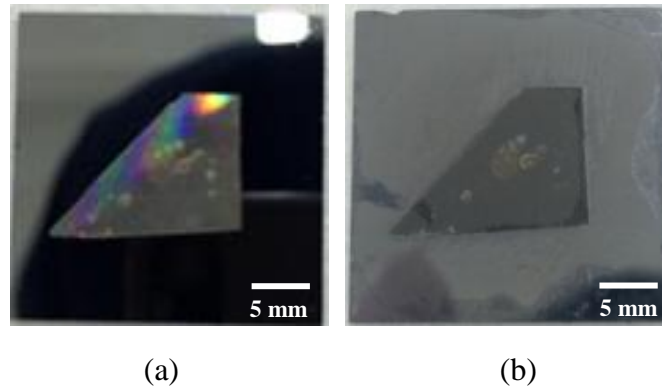


*Figure 3.8 Free-standing semipolar GaN membrane ( $1.5 \times 1 \text{ cm}^2$ ) bonded on Si substrate (a) before CMP and (b) after CMP.*

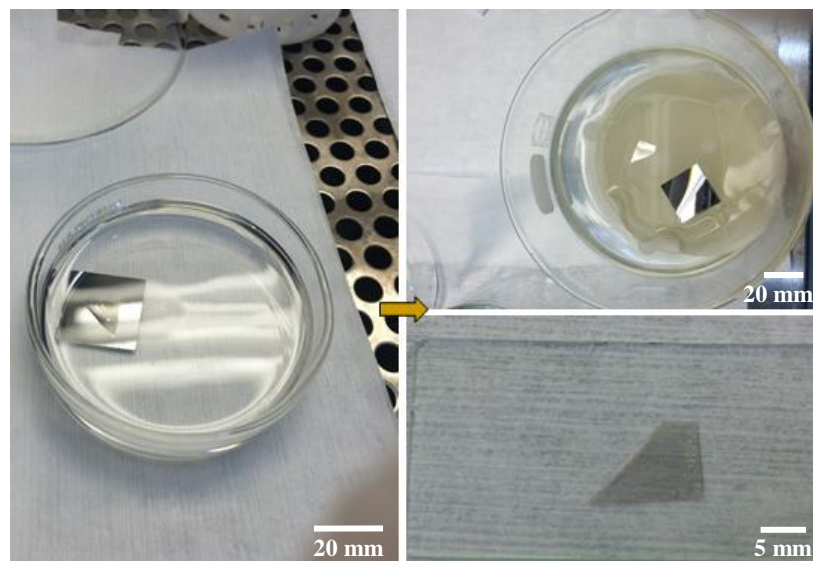


*Figure 3.9 The film debonding process for semipolar HVPE GaN thin film after CMP. (Left: Immersion in TCE; Top right: separation between the GaN thin film and Si substrate after wax was dissolved; Bottom right: the chemical mechanical polished free-standing GaN thin film sitting on a glass slide after thin film debonding)*

Nomarski images of the back surface of the LLO- and CMP-GaN membranes are shown in Figs. 3.10 (a) and (b), respectively. The GaN stripes features on the back surface of the LLO-GaN membrane which is the GaN v-grooves (3- $\mu\text{m}$ -wide and 2- $\mu\text{m}$  in height) can be seen in inset image of Fig. 3.10 (a). After CMP, the GaN stripes

were successfully removed and the morphology of the FS-GaN membrane after CMP is smooth as shown in Fig. 3.10 (b).

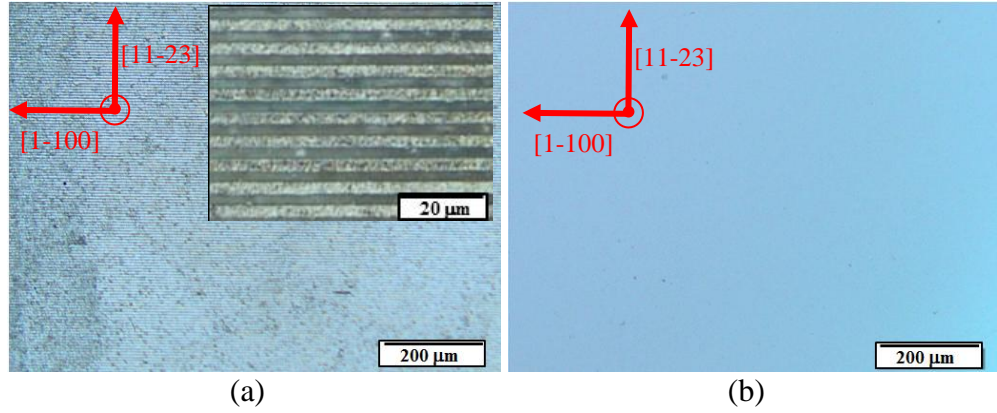


Figure 3.10 Optical microscope images of back surface morphology of free-standing (11 $\bar{2}2$ ) GaN: (a) before CMP, (b) after CMP.

The CMP process was successfully demonstrated that the GaN stripes on the back surface of the FS-GaN films after LLO were fully removed. The successful method by both LLO and CMP to implement FS-GaN membranes was developed. These methods can be used to produce and develop FS-LEDs.

### 3.3 Fabrication of free-standing (11 $\bar{2}2$ ) InGaN/GaN MQW LEDs

A (11 $\bar{2}2$ ) InGaN/GaN MQW LED was grown by MOVPE on HVPE-grown (11 $\bar{2}2$ ) GaN/sapphire template at Tyndall National Institute [21]. In order to make the process easier, the entire fabrication procedures of device mesa structure were carried out on sapphire substrate initially. Eventually, LED chips on wafer were fabricated through the conventional photolithography and dry etching techniques. p-contact and n-contact metals were deposited on p-GaN and n-GaN layers, respectively. As the same method developed for fabrication of FS-GaN membrane by LLO, the pre-processed InGaN/GaN MQW LED on GaN/sapphire templates was lifted-off and transferred from sapphire onto glass slide. The FS-LEDs wafer was obtained by the wafer debonding process with back surface cleaning and then transfer-bonded on a Si substrate for CMP to remove the GaN stripes on the wafer back surface. In this section, the growth structure of LED epitaxial layers, the main

procedures for the fabrication on LED mesa and the process for FS-LEDs are described below.

### 3.3.1 Structure of LED epitaxial layers

The LED structure was grown on the (11 $\bar{2}$ 2) oriented surface of a GaN template on a PSS and is shown schematically in Fig. 3.11. The template was prepared in two stages [20-22]. Firstly, a 6  $\mu\text{m}$ -thick GaN layer was grown by MOVPE on a PSS which was patterned with 1- $\mu\text{m}$ -deep grooves on a 6  $\mu\text{m}$  pitch oriented along the [11 $\bar{2}$ 0]  $a$ -direction of sapphire ([10 $\bar{1}$ 0]  $m$ -direction of GaN). A SiN interlayer was used to reduce the defect density and a very low basal-plane stacking fault density was obtained. Subsequently, a  $\sim 50\text{-}\mu\text{m}$ -thick GaN layer was grown by HVPE. The wafer was diced into  $2 \times 2 \text{ cm}^2$  pieces and CMP was used to smoothen the HVPE-grown template surface. The LED structure was grown on this template and consisted of 1.5  $\mu\text{m}$ -thick Si-doped n-type GaN ([Si]  $\approx 1 \times 10^{19} \text{ cm}^{-3}$ ), 120-nm-thick n-In<sub>0.01</sub>Ga<sub>0.99</sub>N, five periods of InGa<sub>N</sub>/Ga<sub>N</sub> (2.5 nm/6.5 nm) QW active region, 120 nm-thick Mg-doped p-type GaN, and 15 nm heavily doped p-type GaN contact layer. The p-GaN was initially annealed at  $\sim 800^\circ\text{C}$  to activate the p-dopant (Mg). Details of the LED growth conditions and CMP process are reported elsewhere [21].

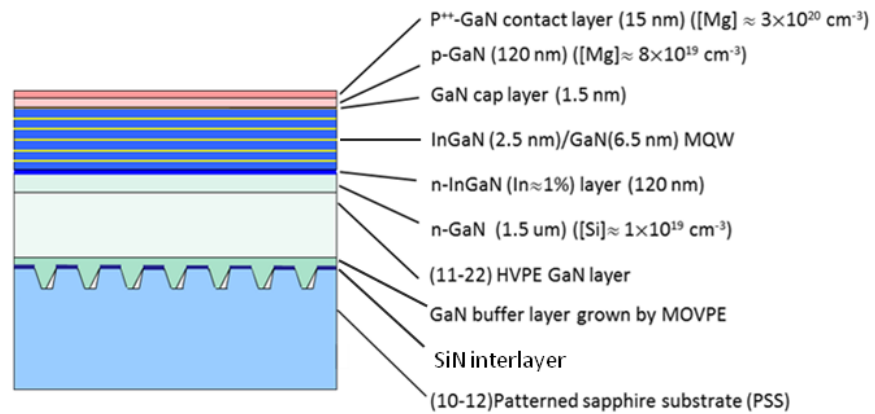


*Figure 3.11 The schematic diagram of epitaxial structure.*

### 3.3.2 Fabrication process

In order to obtain the highest LED performance, the entire fabrication procedures of (11 $\bar{2}2$ ) LEDs were carried out on sapphire substrate initially. The entire fabrication procedures of the LEDs are shown in Fig. 3.12.

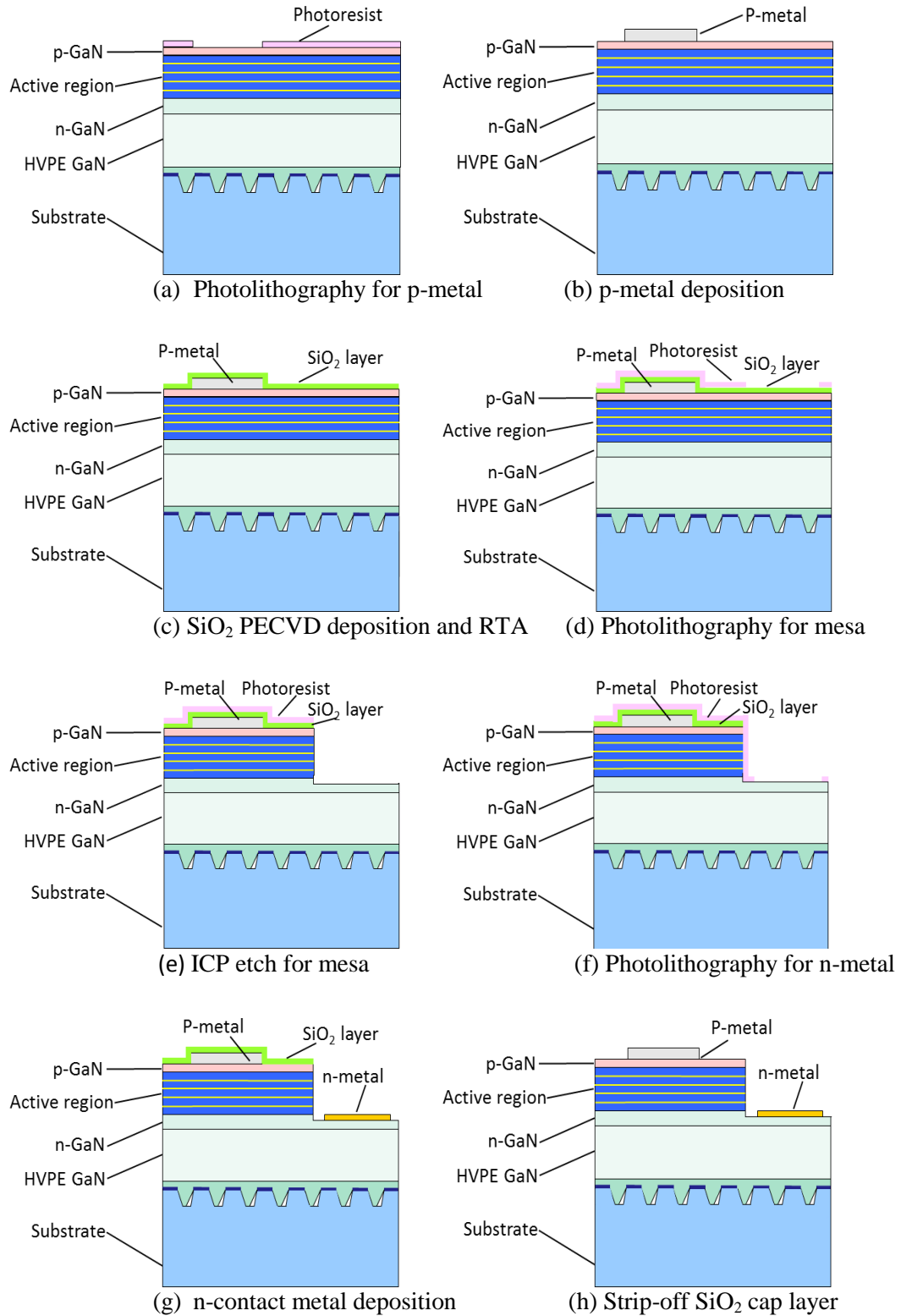
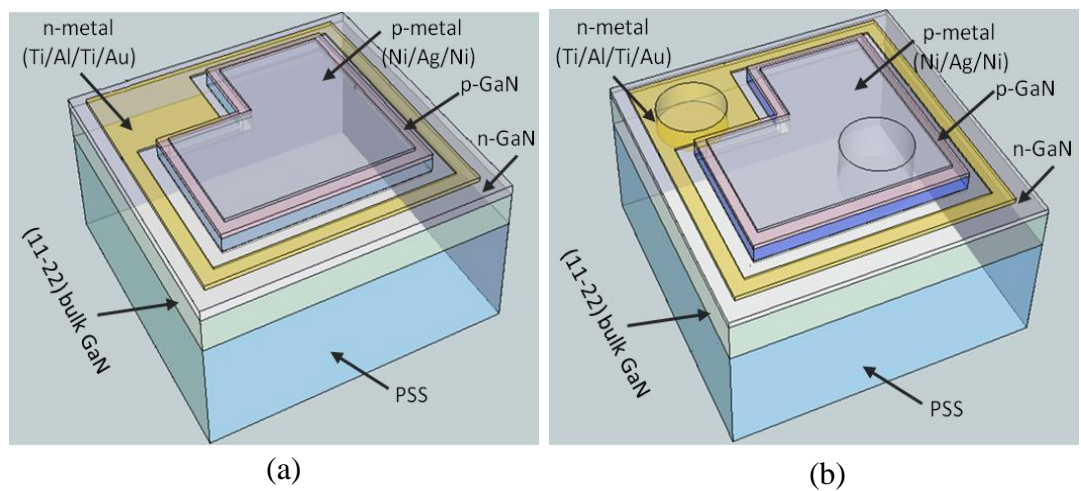


Figure 3.12 Schematic diagram of the LED structure fabrication procedure.

The  $300 \times 300 \mu\text{m}^2$  LED chips on a  $1 \times 1 \text{ cm}^2$  wafer were fabricated through the conventional photolithography, dry/wet etching techniques and electron-beam deposition. The photolithography for the p-contact used a standard mask developed for c-plane  $300 \times 300 \mu\text{m}^2$  LED chips. The p-contacts consisting of Ni (1 nm)/Ag (100 nm)/Ni (2 nm) were deposited on p-GaN by electron-beam evaporation. Afterwards, a thin SiO<sub>2</sub> layer ( $\sim 100\text{-nm}$  thick) was deposited on the p-contact by plasma enhanced chemical vapor deposition to suppress the agglomeration and expansion of Ag during thermal annealing. The p-contacts were then annealed by rapid thermal annealing (RTA) at  $500^\circ\text{C}$  for 60s in O<sub>2</sub> ambient. The sample with chip mesa area was etched in a depth of  $1 \mu\text{m}$  down to n-GaN by using inductively coupled plasma reactive ion etching to expose the n-GaN layer. After the photolithography, Ti (20 nm)/Al (80 nm)/Ti (5 nm)/Au (200 nm) was evaporated on the n-GaN layer to serve as n-contacts by e-beam evaporation. Then, the remaining oxide layer covering the p-contacts was fully stripped off by a diluted buffered oxide etch (BOE), by dipping the sample in the diluted BOE solution (BOE : DI = 1:5) for 6 s.

In Fig. 3.13, a 3-D schematic view of two types of fabricated LEDs on PSS are presented. The device mesa size is  $300 \times 300 \mu\text{m}^2$  and contact areas are the same for both types, except the one in Fig. 3.13 (b) has a circular bond pad area on both p-and n-contact metals. The fabricated substrate-emitting LEDs on sapphire of these two types are shown in Fig. 3.14.



*Figure 3.13. Schematic of 3D view of standard substrate emission LEDs on sapphire substrate. Example of (a) Type A and (b) Type B.*



As seen in Fig. 3.14, Nomarski image of the fabricated LEDs on sapphire substrate is shown in a top-down view. The n-contact metal (Ti/Al/Ti/Au) is exhibited as the dark-gold frame surrounding each LED mesa, and the patterns in light-silver color at centre of each mesa is the annealed Ni/Ag/Ni p-contact metal.

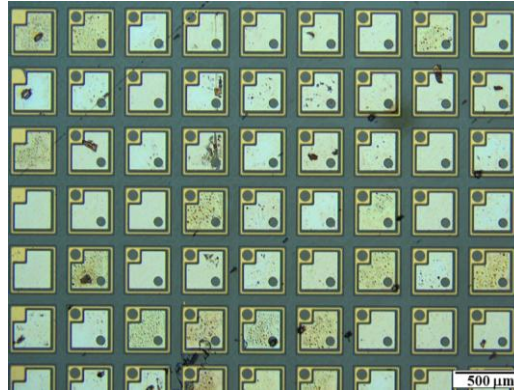


*Figure 3.14 Nomarski microscopy image of the fabricated semipolar (11 $\bar{2}$ 2) substrate emission LEDs on sapphire substrate.*

Moreover, there are some black spots on the wafer surface and some of them on the p-contacts metal. It looks like the wafer surface was not cleaned well and a few of the metal residues after n-metal lift-off and dust still remain. As to the spots on the p-contact metal, they could be the Ag cluster after p-contact annealing.

The process procedure for FS-LEDs is illustrated in Fig. 3.15, which followed the same procedures as the development of FS-GaN membrane by LLO in section 3.2. After the full mesa LEDs has been fabricated on PSS, 5 main steps were required including (1) Flip-bond the LEDs wafer onto a glass carrier substrate, (2) LLO and remove PSS, (3) Debond the LEDs wafer, (4) Flip-bond the FS-LEDs membrane onto an Si substrate and CMP, and (5) Debond the FS-LEDs membrane after CMP.

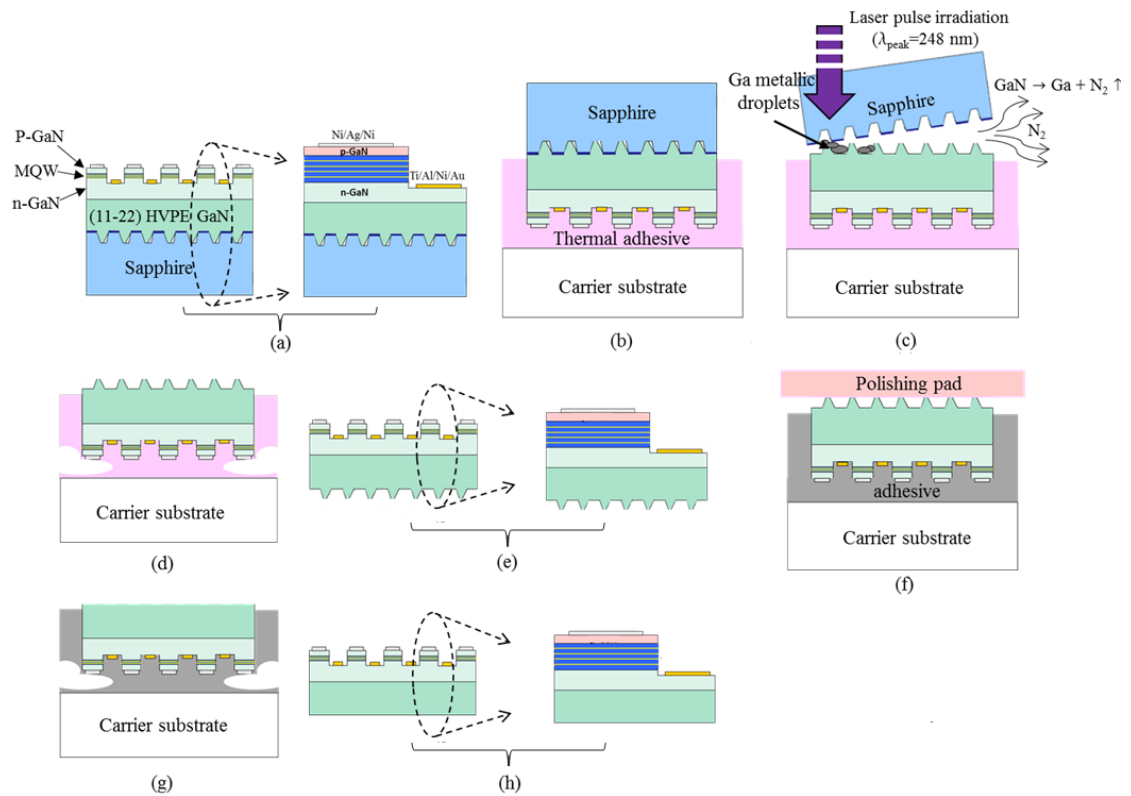


Figure 3.15 Schematic diagram of the fabrication process for obtaining free-standing (11 $\bar{2}2$ ) LEDs by the use of LLO and CMP techniques. (a) Fabrication of LEDs on patterned sapphire substrate ( $300 \times 300 \mu\text{m}^2$  mesa LED chip on PSS), (b) Wafer flip-bonded with thermal adhesive on glass carrier substrate, (c) Laser lift-off of LED wafer and removal of the PSS, (d) De-bond sample and dissolve the adhesive layer, (e) Free-standing LEDs with grooves (LLO-LED), (f) Flip-bond and CMP, (g) De-bond and dissolve adhesive layer, (h) Free-standing LEDs without grooves (CMP-LED).

In the experiment, a wafer sample of fully fabricated mesa LEDs on PSS was diced to a size of  $1 \times 1 \text{ cm}^2$ . After the LLO process, the back surface of the (11 $\bar{2}2$ ) LEDs membrane was cleaned in HCl solution and dried up with  $\text{N}_2$  gas, as seen in the photographs of the back surface of the FS-LED membrane before/after cleaning in Fig. 3.16. Eventually, a  $1 \times 1 \text{ cm}^2$  FS-LEDs membrane with the GaN stripes (v-grooves feature) on the back surface fully polished was achieved.

In Figs. 3.16 (a) and (b), the photograph of the (11 $\bar{2}2$ ) LED wafer after LLO (LLO-LED). The PSS removed was placed beside the LLO-LED wafer. The LLO-LED membrane was still fully attached on the wax-adhesive bonded on a glass slide. During LLO, a cracking occurs across the bottom corner of the PSS, resulting in the break at the bottom corner of the PSS. It might be due to the severe thermal



expansion at the defective region on the patterned surface of PSS. Moreover, it was found that the back surface of the LLO-LED was black as seen in Fig. 3.16 (a). That is due to the Ga metal residuals covered on back surface of the membrane. The back surface was fully cleaned in HCl solution and the membrane appeared to be transparent, as seen in Fig. 3.16 (b).

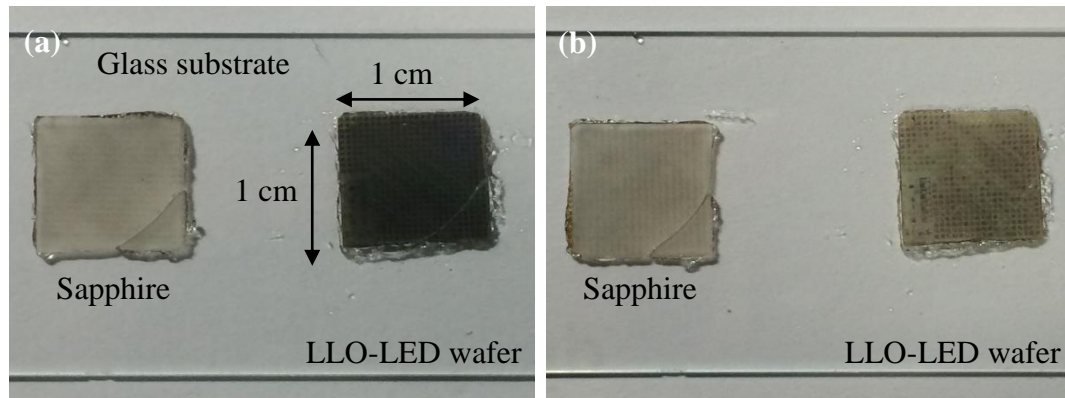


*Figure 3.16. Photograph images of the LED wafer in  $1 \times 1 \text{ cm}^2$  area bonded with wax adhesive layer (crystal-bond 509) on a glass slide after LLO (a) the back surface before cleaning and (b) the back surface after cleaning in HCl:DI (1:1) solution.*

Nomarski images taken on the back surface of the LLO-LEDs wafer are shown in Figs. 3.17 (a) and (b).

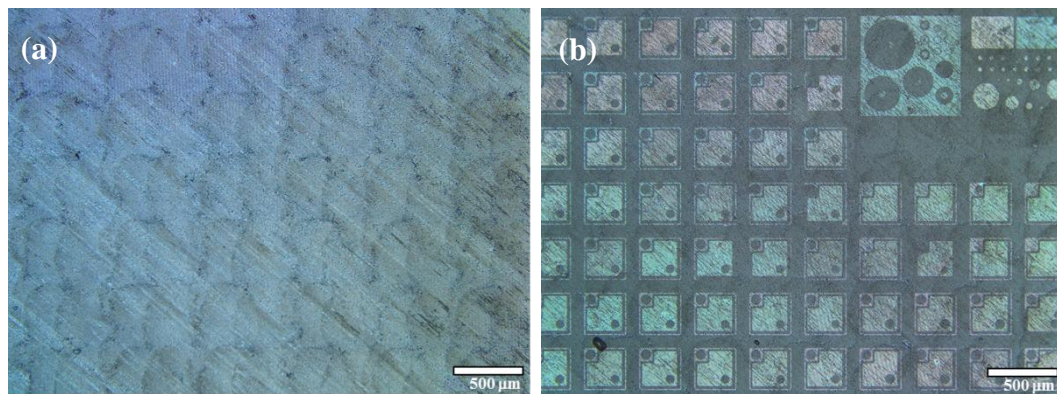


*Figure 3.17 Nomarski microscopy images of the back surface of the sample wafer (a) before and (b) after surface cleaning in HCl:DI (1:1) for 2 min.*

The rough morphology on the back surface of the LLO-LEDs wafer is shown in Fig. 3.17. The device mesa can be clearly seen through the back surface of GaN layer after dipping the sample in diluted HCL solution (Fig. 3.17 (b)), compared to

the sample before surface cleaning (Fig. 3.17 (a)). The smooth morphology of the LLO-LEDs after CMP wafer (CMP-LLO-LEDs) is shown in Fig. 3.18 that shows the GaN stripes were successfully removed during CMP.

The optical microscopy image in Fig. 3.18 shows that the back surface of the CMP-LLO-LEDs membrane is very clean, indicating that the GaN stripes (v-groove features) were fully polished.

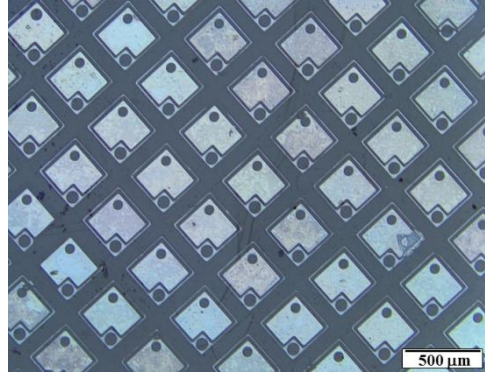


Figure 3.18 Nomarski microscopy image of the back surface of the  $(11\bar{2}2)$  LLO-LEDs wafer after CMP.

After the fabrication process, FS-LEDs (i.e. LLO-LEDs and CMP-LLO-LEDs) on the wafer were probed with an injection current ( $I_{\text{inject}}$ ) for an initial check. In Fig. 3.19, light emission was exhibited on an LLO-GaN LED on the wafer at  $I_{\text{inject}} = 5$  mA, which shows no damage was induced on the LEDs during the process. Under a dark ambient shown in Fig. 3.19 (b), it was found that the light emission demonstrates an anisotropic emission in an elongated direction along the GaN stripe in  $m$   $[1\bar{1}00]$  direction and orthogonal to  $c'$   $[11\bar{2}3]$  direction .

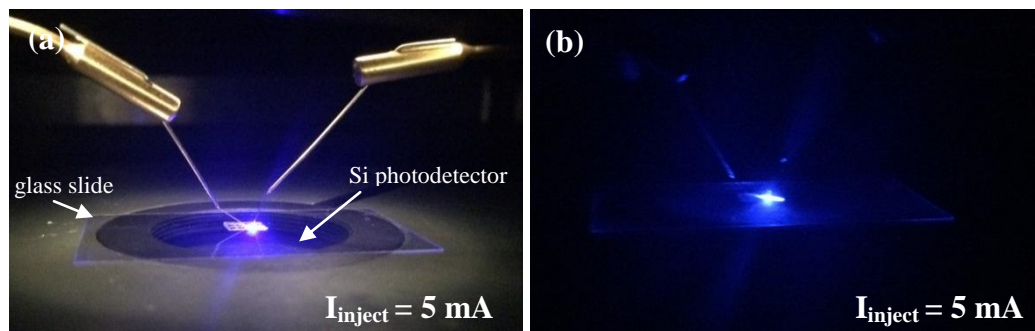


Figure 3.19 Photograph images of the light emission from top side of a free-standing semipolar LED device (with stripes) on the wafer (a) under room light ambient and (b) under dark ambient at injection current 5 mA.

### 3.4 Electro-optical characterization of free-standing semipolar LEDs

The electrical and optical properties of the FS-LEDs were characterized after LLO (LLO-LEDs) and after the CMP process (CMP-LLO-LEDs). The thin-film transfer allowed the LEDs membrane to be flipped over and rigidly supported for probing on the original front-side metal contact pads.

Initially, the current-voltage (I-V) characteristics were collected of two different types of 50- $\mu\text{m}$ -diameter (i) annealed reflective Ni/Ag/Ni p-contacts and (ii) non-reflective 40-nm-thick Pd p-contacts on circular transmission line method (c-TLM) patterns. Light output power ( $P_{\text{opt}}$ ) was collected from the backside of the devices with a numerical aperture (NA) of 0.5 and 1.0 into a calibrated Si photodetector. The contacts were evaporated by electron-beam on the  $(11\bar{2}2)$  p-GaN layer. The LLO-LEDs and CMP-LLO-LEDs were analyzed by fluorescence microscope (FM) respectively. Electroluminescence (EL) measurements of the LEDs with varying injection current were recorded by an optical spectrometer with a silica optical fiber coupled from the backside of the LEDs. As a strong anisotropic optical emission was observed on the device with injection current along a certain elongation direction in the plane of the LEDs, the polarization ratio of the LLO-LED and CMP-LLO-LED were calculated based on the measured data. Moreover, the electrical-to-optical bandwidth of the LLO-LEDs was measured.

#### 3.4.1 Current-voltage characteristics of p-contacts

I-V measurements are important to characterize the electrical properties of a LED. The current from the reverse I-V characteristic can be used as a parameter to determine the quality of the materials.

In the LED configuration, a particular issue with GaN planes is the difficulty in obtaining high p-type doping with Mg. A  $\times 4$  higher Mg flux is required to obtain the same incorporation in the  $(11\bar{2}2)$  surface-oriented crystal as compared with c-plane [18, 51]. The acceptors show higher compensation due to unintentional oxygen impurity and, as a result, it is difficult to obtain a high free hole concentration resulting in non-ohmic p-contacts. 50- $\mu\text{m}$ -diameter Ni/Ag/Ni (1 nm/100 nm/2 nm) and Pd (40 nm) as p-type contacts were compared using the c-TLM measurement.

The Ni/Ag/Ni formed a quasi-ohmic behavior after rapid thermal annealing (RTA) at 500°C under oxygen for 60 s. The Ag interlayer also provides high reflectivity enhancing the light emission through the substrate. Pd is a common ohmic p-contact metal on c-plane p-GaN, therefore the Pd p-contacts were deposited on (11 $\bar{2}2$ ) p-GaN for the comparison. However, the as-deposited Pd contacts showed non-ohmic properties as shown in Fig. 3.20. Due to the high reflection and better electrical properties, annealed Ni/Ag/Ni was applied as p-metal contact, instead of as-deposited Pd.

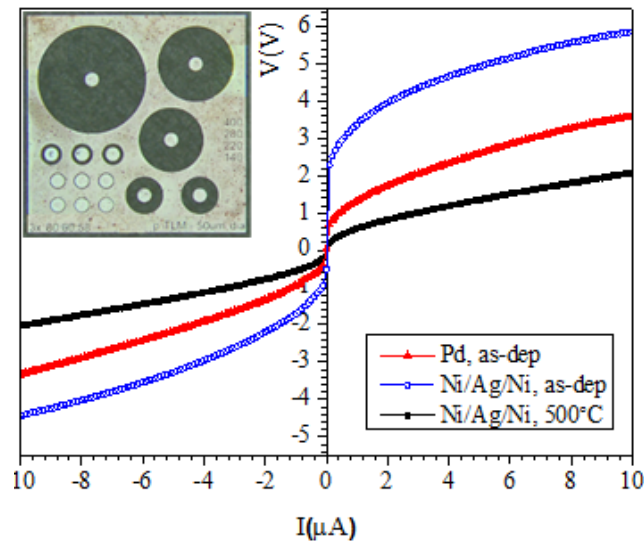


*Figure 3.20 Current-voltage I-V characteristics of a 50- $\mu\text{m}$ -diameter disk contact with a gap of 280  $\mu\text{m}$  on c-TLM pattern (inset) of Pd (40nm) as-deposited and Ni (1 nm)/Ag (100 nm)/Ni (2 nm) before & after anneal at 500 °C.*

### 3.4.2 Electrical characteristics

The L-I-V characteristics provide the relationship of optical light output power with forward injection current and corresponding voltage across the junction. Threading dislocations and BSFs have been found to act as leakage paths for the carriers in semipolar GaN LEDs. In addition, series resistance of an LED can also be obtained from the forward I-V characteristics. The series resistance may be caused by the bulk resistance (due to a high resistivity layer such as the p-GaN layer or n-GaN), contact resistance, as well as the resistance caused by the abrupt heterostructure in the LED. If the series resistance is high, the operating voltage of the LEDs will be increased. The series resistance can be extracted from differential plot at high bias regime (above turn-on voltage) in the I-V characteristic.

The L-I-V measurements were carried out using a Keithley source meter model 2400 [52], Keithley multimeter mode 2000 [53] and a Newport 818-UV photodetector [54]. The photodetector was placed at 1 cm beneath the LEDs sitting on a glass slide ( $\sim 0.5$ -mm thick) for  $NA = 0.5$ . The injection current of the LEDs was provided by the source meter. A labview program was used to control the equipment to perform a current sweep within a specific required range and record the corresponding voltage with photocurrent captured from the detector. For the optical output power measurement, the Newport 818-UV photodetector with a circular active area of  $100 \text{ mm}^2$  was placed directly below the LEDs before LLO (non-LLO LEDs) and after LLO (LLO-LEDs). The responsivity of the photodetector at 445 nm is  $0.2176 \text{ AW}^{-1}$  with a numerical aperture ( $NA = 0.5$ ). In order to collect all the light emission in the vertical direction from the back side of the LEDs, a Si photodiode with a  $NA = 1.0$  was used instead of  $NA = 0.5$ . To compare with the optical power collected with a  $NA = 1.0$ , the CMP-LLO-LED was placed directly on the Thorlabs FDS1010 Si photodiode [55]. The detector has a size of  $10 \times 10 \text{ mm}^2$  and is able to detect the spectrum wavelength range of 350-1100 nm, with a responsivity of  $0.1131 \text{ AW}^{-1}$  at 445 nm. It should be noted that the power was measured only in the substrate direction for both  $NA = 0.5$  and  $1.0$  (i.e. without an integrating sphere). The light has been only partially collected as there was a plenty of uncollected light in the forward and side directions. Thus, a multiple of this power can be collected by structuring and packaging the LED chips.

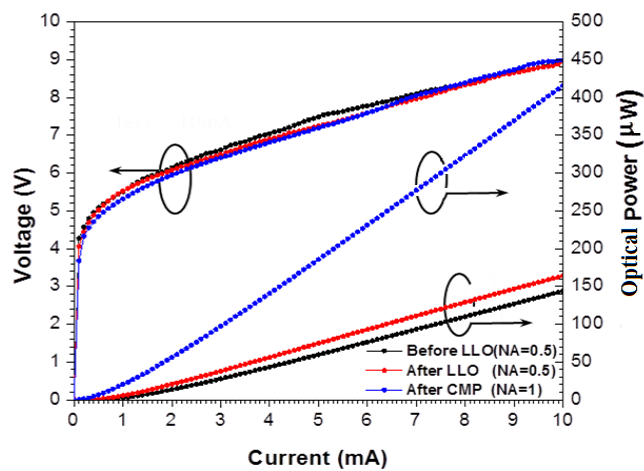
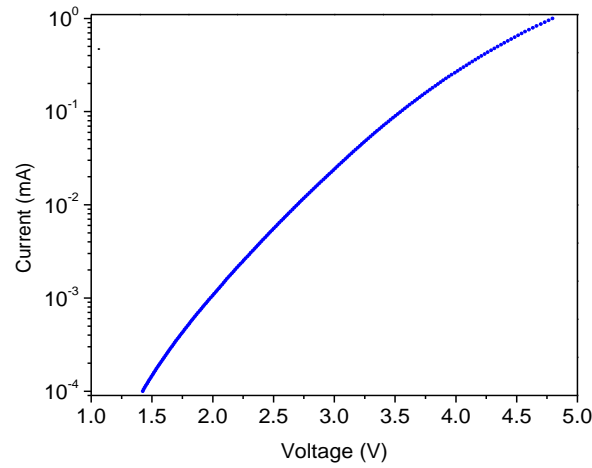


Figure 3.21 L-I and V-I characteristics of the LEDs before LLO/after LLO measured with  $NA = 0.5$  and after CMP (measured with  $NA = 1$ ).



*Figure 3.22 log-I-V of free-standing semipolar GaN LED after CMP.*

The light output power (L-I) and I-V of the LEDs before LLO (non-LLO-LEDs), the LEDs after LLO (LLO-LEDs) and the LEDs after LLO and CMP (CMP-LLO-LED) are shown in Fig. 3.21. The I-V characteristics for the CMP-LLO-LED and LLO-LEDs are similar with a threshold voltage of  $\sim 3.6$  V. The series resistance is found to be  $368 \Omega$  and this may be due to the non-ohmic behaviour of the metal contacts. The light output power of the LLO-LED is enhanced by 14% at 10 mA compared with the non-LLO-LED, which is due to the light scattering caused by the GaN striped features on the back surface. The light output power of the CMP-LLO-LED is lower than the LLO-LED with GaN stripes when measured with  $NA = 0.5$ . However, to compare with results previously reported from other groups, the output power of the CMP-LLO-LED was also measured with  $NA$  of 1. The measured output power of the CMP-LLO-LEDs with  $NA = 1$ , i.e. directly on the photodetector is  $870 \mu\text{W}$  at 20 mA ( $J=22 \text{ A/cm}^2$ ), which is comparable to values previously reported for other blue semipolar ( $11\bar{2}2$ ) InGaN LEDs grown on sapphire substrates [56-58]. For example, an output power of  $\sim 1.8 \text{ mW}$  has been obtained for a packaged ( $11\bar{2}2$ ) LED grown on GaN bulk substrate with a chip size of  $320 \times 320 \mu\text{m}^2$  ( $J=20 \text{ A/cm}^2$ ,  $I=20 \text{ mA}$ ) emitting at 420 nm [56],  $\sim 0.38 \text{ mW}$  has been obtained for a 280- $\mu\text{m}$ -diameter unpackaged ( $11\bar{2}2$ ) LED grown on a GaN/sapphire template ( $J=33 \text{ A/cm}^2$ ,  $I=20 \text{ mA}$ ) emitting at 422 nm [57], and  $\sim 1.0 \text{ mW}$  has been obtained for a unpackaged ( $11\bar{2}2$ ) LED grown on GaN/sapphire template grown on patterned sapphire substrate emitting at 440 nm with the chip size of  $1100 \times 600 \mu\text{m}^2$  ( $J=3 \text{ A/cm}^2$ ,  $I=20 \text{ mA}$ ) [58].



For the LEDs studied here, one can expect that the output power will significantly increase with fully packaged devices through controlled surface roughening and epoxy encapsulation. Fig. 3.22 shows the log I-V characteristics of the FS-LEDs for currents from 100 nA to 1 mA indicating that the LEDs have no shunt paths but a small non-radiative leakage current, which delays the light emission until voltages larger than 3 V.

### 3.4.3 Fluorescence microscopy

Fluorescence microscopy (FM) provides a simple LED and wafer characterization method, which does not require any electrical contacts to inject electrical carriers to the wafer [59]. Conventionally, photoluminescence (PL) is used to qualify the optical properties of QWs grown as part of a heterojunction LED structure where the relative brightness of the wafer when compared with a reference sample or with a low temperature measurement can indicate the quality. Low light emission is generally ascribed to the non-radiative recombination in the QW region and/or due to limited carrier transport into the QW region if the light excitation is absorbed in a GaN layer. The transport issues are nominally avoided by pumping, only the QWs to get an equal electron and hole generation in each well. The LLO-LEDs and CMP-LLO-LEDs were analyzed by FM. In FM measurements, the LEDs were excited optically by a 405 nm line of a mercury vapour lamp as excitation source, which was focused on the samples through the detection objectives, and the resulting PL emission was detected by a microscope. The PL emission was captured by a color camera, thus producing a real-color representation of the QW emission and allows us to investigate the spatial distribution of the luminescence.

The luminescence uniformity of the LLO-LED and CMP-LLO-LED was investigated through the back surface. Fig. 3.23 (a) and (b) show the FM images of the LEDs (peak emission wavelength  $\approx 445$  nm). The uniform luminescence of the LEDs can be observed from both images on the active region.

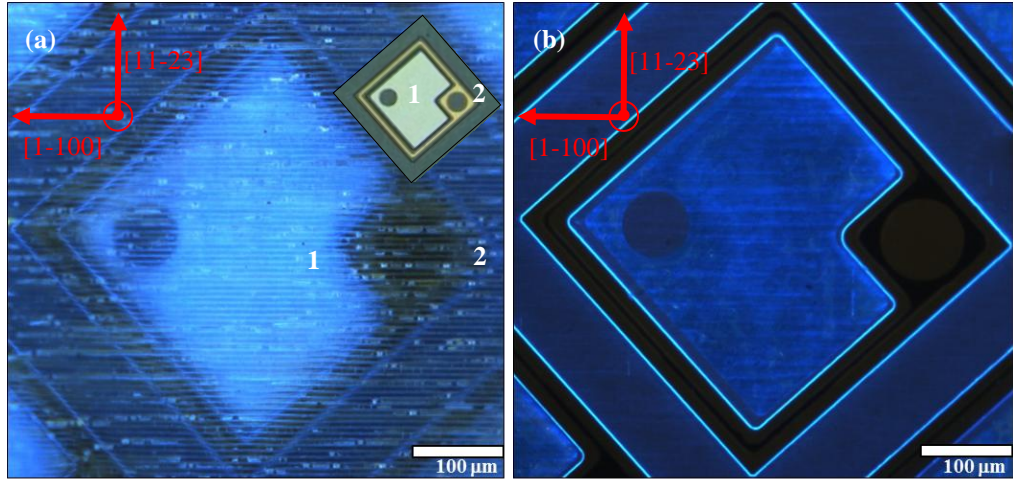


Figure 3.23 FM images ( $560 \times 560 \mu\text{m}^2$ ) of the backside of the LEDs (a) after LLO (inset: the photography in top view of the fabricated LEDs, where area 1 is p-metal and area 2 is n-metal) and (b) after CMP. (Exposure time of 100 ms).

It is seen that the p-contact region is brighter than the region without the p-metal due to the reflection of the Ag interlayer. Moreover, the brightness intensity in Fig. 3.23 (a) is higher than Fig. 3.23 (b), which is due to the light scattering caused by the GaN stripes (v-grooves). Figs. 2.23 (a) and (b) show bright emission from the mesa edges which may indicate stronger light emission in the plane of the QWs but is also due to light scattering at the mesa edges.

### 3.4.4 Electroluminescence measurements

The electroluminescence (EL) measurements of the LEDs are attained by injecting carriers electrically under forward bias. Under forward bias, holes and electrons are both injected into the active region from the p-contact and n-contact layer, respectively. The radiative recombination processes between hole and electron pairs are occurring in the active region to provide photons. The photons escape from the LED material to constitute EL. In this study, EL of the LEDs was measured using Ocean optics 2000 spectrometer [60] (optical resolution is 0.2 nm) coupled to a silica optical fiber with  $\text{NA} = 0.5$ . The EL spectra were recorded using Spectrasuite software [61] provided by the spectrometer manufacturer.

Fig. 3.24 (a) shows the normalized EL spectra at currents up to 10 mA ( $J = 11 \text{ A/cm}^2$ ) of the LLO-LED. With increasing drive current, the EL peak emission at  $\sim 445 \text{ nm}$  is stable.



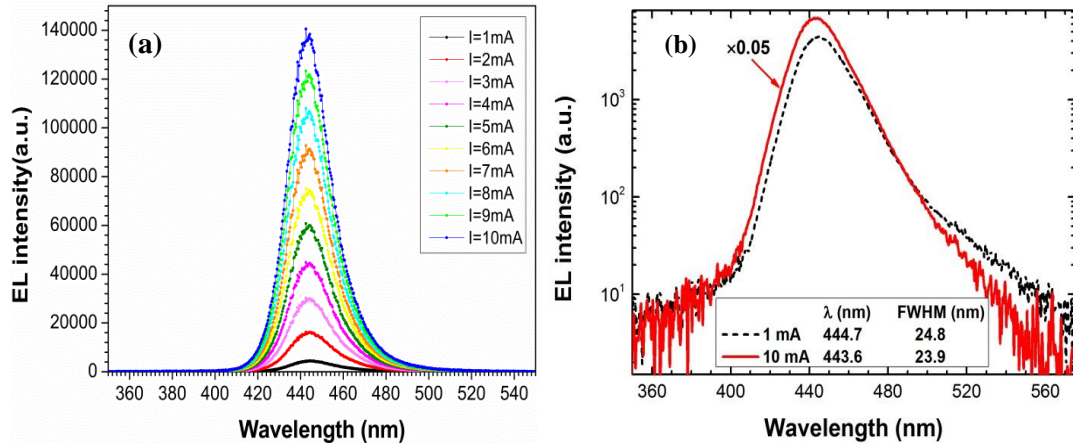


Figure 3.24 (a) EL spectra of the free-standing semipolar LED as a function of current up to 10 mA ( $11 \text{ A/cm}^2$ ); (b) Normalized EL spectra of the freestanding semipolar LEDs at 1 and 10 mA.

As the injection currents increases, the EL emission intensity increases as seen in Fig. 3.24 (a) due to more carrier density pumping into the active region. In Fig. 3.24 (b), the normalized EL spectra of the LED at 1 mA and 10 mA were compared. The LED starts to show EL emission at  $\lambda_{\text{peak}}$  of 444.7 nm with FWHM of 24.8 nm. As injection current increases in the range from 1 to 10 mA,  $\lambda_{\text{peak}}$  is slightly blue shifted to 443.6 nm and the FWHM is reduced to 23.9 nm. The peak-wavelength shift  $\Delta\lambda_{\text{peak}}$  is 1.1 nm and emission line-width changes  $\Delta\text{FWHM}$  is 0.9 nm. Such small variation indicates stable EL spectra of the LEDs, which indicates reduced QCSE and lower band-filling effects in the QW based active region of the LEDs.

### 3.4.5 Optical polarization measurement

An optical polarization measurement was performed in the EL from the LEDs both before and after LLO. It shows a stronger emission intensity along the  $[11\text{-}23]$   $c'$ -plane growth direction, forming an elongated light emission pattern dominated by  $E \perp c'$  polarized. This preferential emission property has a direct consequence on the emitter performance, resulting in a complete difference to the  $c$ -plane InGaN QW blue LEDs, which are predominantly  $E \perp c$  polarized.

Fig. 3.25 shows the schematic diagram of the experimental set-up to measure the EL intensity of LEDs v.s. polarization angle. The sample stage has a copper x-y-z translator stage holding LEDs and it can be rotated around the y-axis. Light emitted along the z-axis passing through a pin-hole at centre of the copper stage and a circular polarizer is coupled to a lens (NA = 0.5) capped with silica optical fibre and ultimately detected by a spectrometer (Ocean Optics USB2000). The polarizer can be rotated about the z-axis to resolve  $E \parallel x$  (electric field along x-axis) and  $E \parallel y$  (electric field along y-axis), where the  $m$ -direction of the LED (i.e. the crystal direction of the v-grooves) is along the elongated direction of the y-axis and  $c'$ -direction of the LED is along the elongated direction of x-axis. The dependences of the EL intensity on the polarization angle for the LLO-LEDs and CMP-LLO-LEDs were measured and presented as Fig. 3.26 and Fig. 3.27.

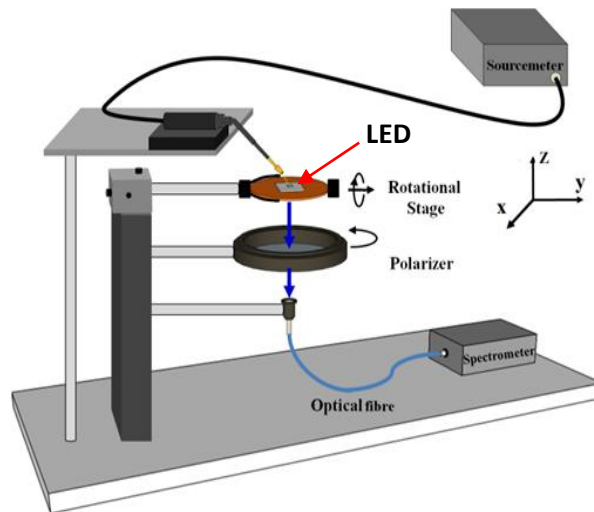


*Figure 3.25 Schematic diagram of the experimental set-up to measure the optical polarization revolved EL spectra of the LEDs.*

The optical polarization anisotropy was observed in the EL intensity from the non-LLO-LEDs and LLO-LEDs with stronger emission intensity along the  $[11\bar{2}3]$  inclined  $c'$ -direction, as shown in Fig. 3.26 (a). An elongated light emission pattern is formed due to the scattering from the grooves. The intensity as a function of polarization angle for LLO-LEDs and CMP-LLO-LEDs, both at 2 mA driven current, was measured. When the polarizer is placed along the elongated direction of the GaN grooves i.e. the  $[11\bar{0}0]$   $m$ -axis (i.e.  $0^\circ$  and  $180^\circ$ ), the EL emission intensity is

maximized. The minimum intensity occurs for the polarizer set along the  $[11\bar{2}3]$   $c'$ -axis (i.e.  $90^\circ$  and  $270^\circ$ ).

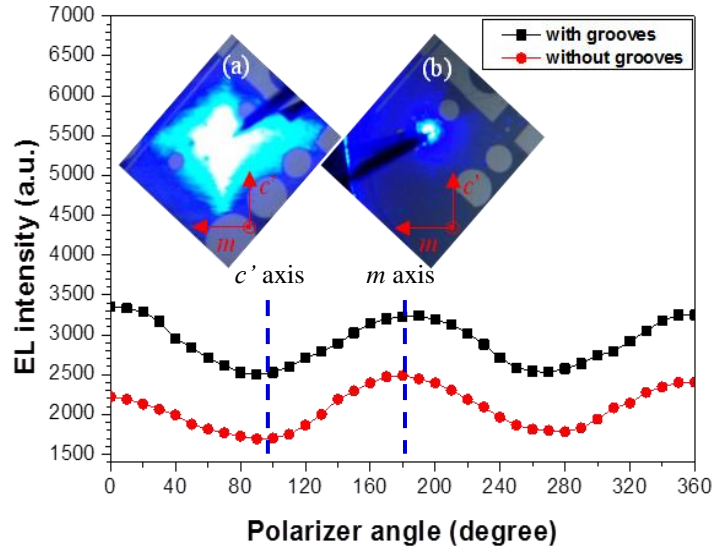


Figure 3.26 EL intensity with polarization angle for the freestanding semipolar ( $11\bar{2}2$ ) InGaN/GaN LED (LLO-LED and CMP-LED). The inset shows (a) anisotropic light emission profile after LLO and (b) after CMP more uniform spot like emission.

The polarization ratio is independent of the GaN grooves, as both the LLO-LED and CMP-LED show a polarization ratio  $\rho_{\text{polar}} = (I_{\text{max}} - I_{\text{min}})/(I_{\text{max}} + I_{\text{min}})$  of 0.14. With the grooves present the light emission shows a larger light broadening along  $m$ - and  $c'$ -directions. After CMP, a uniform spot-like emission is obtained indicating the role of the grooves on the emission pattern. The polarized light provided by FS-LEDs is another advantage above the reduction in QCSE.

As shown in Fig. 3.27, the EL-spectra peak wavelength of the FS-semipolar LED is the same (i.e.  $\lambda_{\text{peak}} \sim 445$  nm) for polarizer angles of  $0^\circ$  and  $90^\circ$ , which is independent of the polarizer angle.

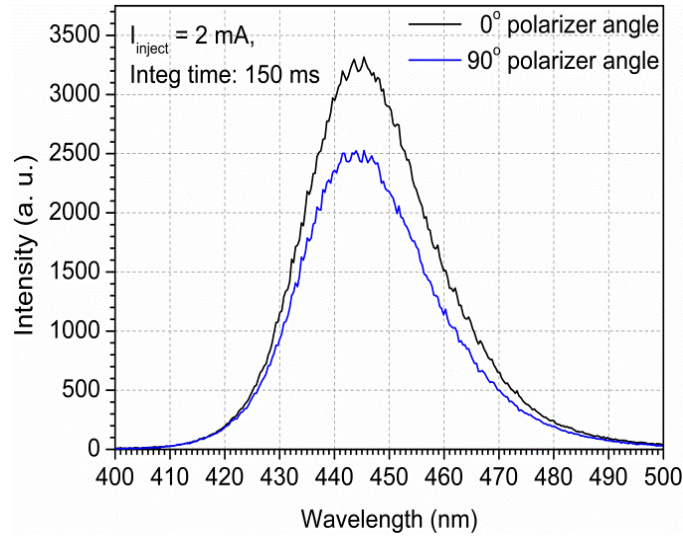


Figure 3.27 EL intensity at polarizer angle of  $0^\circ$  and  $90^\circ$  for the freestanding semipolar (11 $\bar{2}2$ ) InGaN/GaN LED (LLO-LED).

### 3.4.6 Electro-optical bandwidth measurement

Due to the reduced piezoelectric fields in QW on semipolar plane, an increased overlap of the electron and hole wave-functions results in a faster radiative lifetime. The demonstrated LEDs can, therefore, be expected to have a high modulation bandwidth and high data transmission rate, even though the epitaxial structure and the device mesa geometry were not optimized for the bandwidth.

#### 3.4.6-1 Small signal bandwidth

The small-signal frequency response of both the FS-LEDs and a reference commercial c-plane InGaN/GaN QW LED emitting at 466 nm grown on double polished sapphire substrate with the same mesa size (light output power at 20 mA is 2.45 mW) was measured. It was measured on-wafer from the backside of the LEDs as a function of current using a microwave probe (DC to 3.5 GHz) without a heat sink. A sinusoidal signal with low-RF power from a vector network analyzer (Agilent 8753ES) was applied on top of a DC bias using a bias tee (Mini-Circuits 15542 ZFBT-6GW-FT 9628). Keithley 2400 source meters were used as the DC power supplier for the LEDs and photoreceiver. The light output from the LEDs was collected with 2-cm-diameter lens with a corresponding numerical aperture (NA) of  $\sim 0.5$ . SubMiniature-version-A (SMA) coaxial cables (DC to 18 GHz) with  $50\ \Omega$

impedance were used as transmission lines for RF signals. A high bandwidth silicon p-i-n photodiode ( $f_{3dB}$  ranging from 10 kHz to 1.4 GHz) with integrated transimpedance amplifier (TIA) photoreceiver (HAS-X-S-1G4-SI) [62] was used and the frequency response curve was recorded by the vector network analyzer at different bias currents. A schematic of small signal bandwidth measurement set-up is shown in Fig. 3.28.

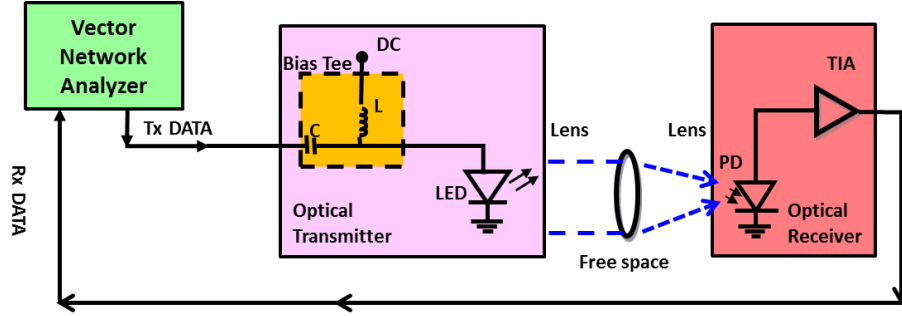


Figure 3.28 A schematic diagram of bandwidth measurement experimental set-up

The measured frequency responses of the FS-LED and referenced c-plane GaN LED for varied injection current ( $I$ ) were shown in Figs. 3.29 (a) and (b) respectively.

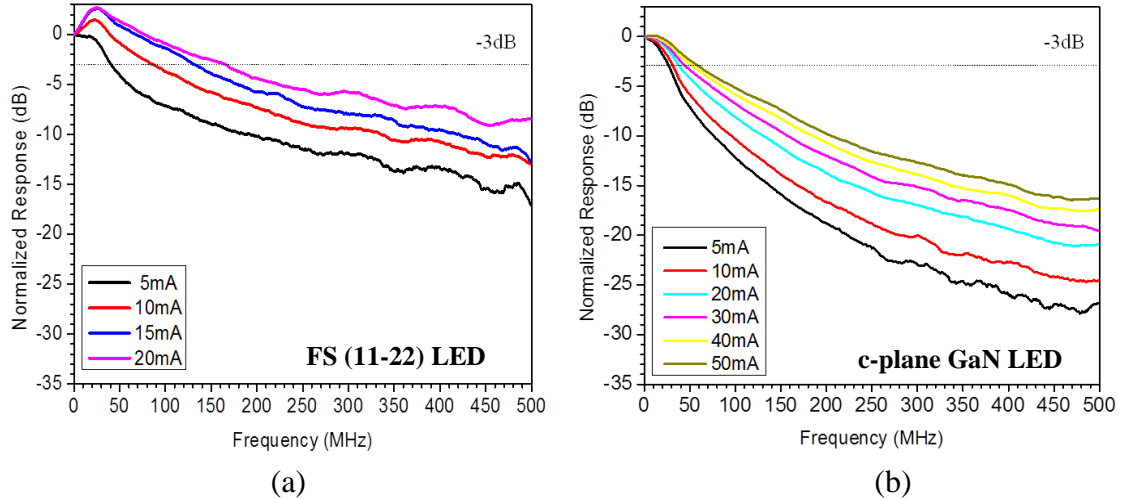


Figure 3.29 Normalized frequency response of LEDs at different injection current: (a)  $300 \times 300 \mu\text{m}^2$  FS-LED and (b)  $300 \times 300 \mu\text{m}^2$  c-plane LED.

At each injection current applied on the LEDs, a low power RF signal added on the injection current was swept in frequency from DC to 500 MHz and the transient optical power (in dB) detected by the photoreceiver was recorded. The maximum

injection current that can be applied on FS-LEDs was 20 mA, otherwise, it would be burnt-out because of excessive heating as the LED membrane is only  $\sim 50\text{-}\mu\text{m}$ -thick, while the reference c-plane GaN LED on sapphire can be driven to 50 mA. At a constant injection current, the frequency response curve of both FS-LED and reference c-plane LED rolls off with increasing frequency. It indicates less efficient radiative recombination rate produced in the active region of the LEDs due to the increase of the carrier radiative recombination life time ( $\tau_r$ ) at the RF signal of higher frequency, resulting in less optical power being detected by the photoreceiver. The -3 dB frequency of an LED can be determined by measuring the frequency at which the photoreceiver signal decreases to a half of the low-frequency value. Fig. 3.29 (a) shows that the -3 dB point on the frequency response curve of the FS-LED significantly increases with the injection current density ( $J$ ) compared with c-plane LED in Fig. 3.29 (b), which presents the -3 dB bandwidth of 166 MHz for the FS-LED and 38 MHz for c-plane LED at  $J = 22\text{ A/cm}^2$  ( $I = 20\text{ mA}$ ). A slightly increase on bandwidth of the c-plane LED shown in Fig. 3.29 (b) can be seen for higher currents. It can be explained by the higher forward current injection pumping more carriers into the active region of the LED, which provides a higher possibility for the carriers to meet each for radiative recombination than is the case for low injection current. However, there is a lower electron-hole wave-function overlap in the QW of c-plane LED due to the stronger QCSE; thus, the increment of bandwidth with  $J$  is less obvious than for the  $(11\bar{2}2)$  LED. Therefore, it was found that the  $(11\bar{2}2)$  LED gave higher bandwidth than the conventional c-plane GaN LED for the same mesa size, which is due to the reduction of  $\tau_r$  produced by the higher overlap of electron/hole wavefunction in the  $(11\bar{2}2)$  QW based active region.

The measured -3 dB bandwidths as a function of injection current are shown in Fig. 3.30 and compared with the reported bandwidth of high-speed LEDs on c-plane (0001) and semipolar  $(11\bar{2}2)$  planes [63-66]. The bandwidth of c-plane LEDs in smaller dimensions is compared with semipolar  $(11\bar{2}2)$  LED in larger dimension to show a dependence on the driving current. The  $300 \times 300\text{ }\mu\text{m}^2$   $(11\bar{2}2)$  LEDs emitting at 500 nm and 450 nm grown on PSS show the bandwidth at 72 MHz and 100 MHz, respectively [63].



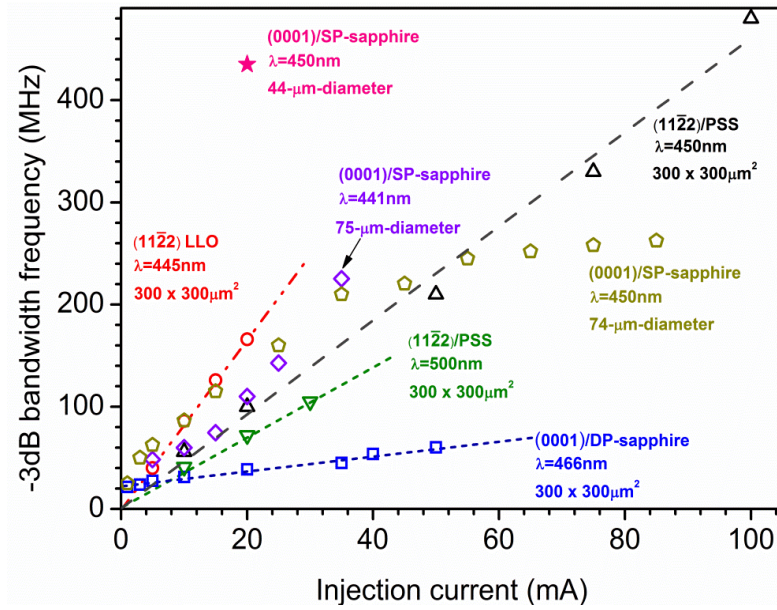


Figure 3.30 -3dB small signal signal bandwidth of the ( $\circ$ )  $300 \times 300 \mu\text{m}^2$  freestanding  $(11\bar{2}2)$  LED and ( $\square$ )  $300 \times 300 \mu\text{m}^2$  c-plane GaN LED as compared with the high speed GaN based LEDs reported in literature. ( $\Delta$ ) Reference [63]  $300 \times 300 \mu\text{m}^2$   $(11\bar{2}2)$  blue LED, ( $\nabla$ ) Reference [63]  $300 \times 300 \mu\text{m}^2$   $(11\bar{2}2)$  green LED, ( $\diamond$ ) Reference [64] 72- $\mu\text{m}$ -diameter c-plane GaN LED, ( $\star$ ) Reference [65] 44- $\mu\text{m}$ -diameter c-plane GaN LED, ( $\diamond$ ) Reference [66] 75- $\mu\text{m}$ -diameter c-plane GaN LED.

The 75- $\mu\text{m}$ -diameter c-plane LEDs emitting at 441 nm and 72- $\mu\text{m}$ -diameter emitting at 450 nm grown on single polished sapphire substrate show the -3 dB bandwidth of 110 MHz ( $J = 450 \text{ A/cm}^2$ ,  $I = 20 \text{ mA}$ ) and 150 MHz ( $J = 490 \text{ A/cm}^2$ ,  $I = 20 \text{ mA}$ ), respectively [64, 65]. The smaller dimensional LED of 44- $\mu\text{m}$ -diameter c-plane LED grown on single polished sapphire substrate ( $J = 1.3 \text{ kA/cm}^2$ ,  $I = 20 \text{ mA}$ ) emitting at 450 nm shows a higher bandwidth of 435 MHz [66]. As shown in Fig. 3.30, the -3 dB bandwidth of all the LEDs is found to increase with increasing injection current. However, the -3 dB bandwidth of the 75- $\mu\text{m}$ -diameter c-plane GaN LED starts to saturate at injection current  $I > 40 \text{ mA}$ . This is likely due to the RC limitations and/or intolerance to higher injection current density which this LED can support [67]. For the  $300 \times 300 \mu\text{m}^2$   $(11\bar{2}2)$  GaN LEDs and the  $300 \times 300 \mu\text{m}^2$  c-plane GaN LED, the c-plane LED has to be driven at about 5 orders of magnitude higher injection current to achieve a similar -3 dB bandwidth value obtained for the  $(11\bar{2}2)$  LEDs. This can be attributed to a shorter effective carrier radiative lifetime ( $\tau_R$ ) in the  $(11\bar{2}2)$  LEDs, resulting in a higher -3 dB bandwidth ( $f_{-3dB}$ ). The  $\tau_R - f_{-3dB}$  relationship can be described as  $\tau_R = \sqrt{3} \cdot (2\pi f_{-3dB})^{-1}$  [68]. According to the data

points shown in Fig. 3.30, at  $I = 20$  mA, a calculated  $\tau_R$  for the  $300 \times 300 \mu\text{m}^2$  c-plane LED is  $\sim 7.3$  ns, about four times longer than that of the  $300 \times 300 \mu\text{m}^2$  (11 $\bar{2}2$ ) FS-LEDs, which is  $\sim 1.66$  ns. This is consistent with previous results reported for c-plane and (11 $\bar{2}2$ ) LEDs [67, 69].

### 3.4.6-2 Data transmission measurement

The transmission data rate of the FS-LEDs was investigated. Data has been sent over several centimetres of free space with the same collecting set-up. To determine the transmission data rate of the LEDs, a  $2^7-1$  non-return-to-zero (NRZ) pseudo-random bit sequence (PRBS)-7 from a pattern signal generator (Anritsu MP1632A [70]) has been added at each DC bias. The eye diagram is the photoreceiver signal of a randomly generated digital signal and allows one to estimate the overall performance of an optical communication system. The large signal back-to-back data transmission rate was presented by “eye diagram”, which were collected by a digital oscilloscope (Agilent Infiniium DSO80804A [71]). The large-signal modulation is a 2 V peak-to-peak amplitude square-wave pattern, which is 200 times larger than the peak to peak amplitude sinusoidal wave of the small-signal modulation (10 mV) applied. When it is added to the bias tee with the LEDs being biased at 20 mA, the transmitted data rate for an open eye diagram can be up to 300 Mbps. A schematic diagram of the experimental set-up of data transmission measurement under the large signal modulation is exhibited in Fig. 3.31.

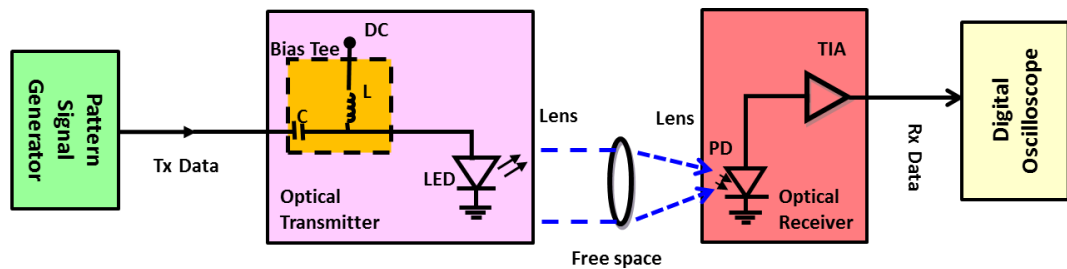


*Figure 3.31 A schematic diagram of data transmission measurement under large signal modulation experimental set-up.*

In the simple free-space optical communication system, the unpackaged FS-LED and the photoreceiver are separated over several centimeters of free space as shown in



Fig. 3.31. The data transmission measured for the LED at 20 mA injection current is presented as the eye diagram in Fig. 3.32.

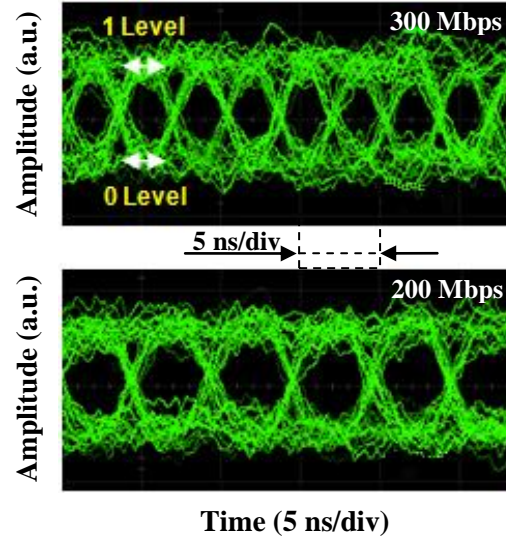


Figure 3.32 Eye diagrams of the free-standing semipolar (11 $\bar{2}$ 2) InGaN/GaN LED at 300 Mbps and 200 Mbps at  $I_{\text{inject}} = 20$  mA.

The eye diagrams of the FS-LED operating at 300 megabits per second (Mbps) and 200 Mbps are shown in Fig. 3.32. The time scale is 5 ns/division and the amplitude is 10 mV/division. The visual opening of the “eye” was used for the indication of digital data transmission of the LED, thus the amplitude value was not so critical and can be treated as arbitrary unit. From this figure, it indicates the digital signal level of the “1” state and the “0” state and the decision level (i.e. the boundary between what is interpreted by the photoreceiver as “0” and “1”). The figure also reveals the pattern “eye”, which shows a wide clear “open eye” on both transmitted data bit rates. It indicates that the LED allows for a low bit-error rate data transmission at these modulation frequencies applied on the LED. It is seen that the eye at 300 Mbps is slightly narrower compared to the eye at 200 Mbps, and the eye will close, as the data rate is further increased, thus the voltage signal representing the “0” and “1” levels as detected by the photoreceiver cannot be clearly distinguished which results in an increase in bit-error rate.

### 3.5 Conclusions

In this chapter, the LLO method was explored on the semipolar (11 $\bar{2}2$ ) GaN LED grown on patterned sapphire substrate. A relatively low energy density of a single laser pulse is required (i.e. 500 mJ/cm<sup>2</sup>) to achieve non-damage lift-off, because the laser-induced delamination of GaN strips is enhanced by the air-filled grooves at the substrate-GaN film-interface. In the CMP process, in order to obtain a smooth surface, the process parameters (head/ring pressure, polishing pad rotation speed, slurry flow) are the main contributor to surface smoothness. However, the uniformity of polishing within the wafer and the material removal rate are obviously affected by the wafer geometry and materials. Hence, the process parameters (recipes) of the semipolar GaN wafer samples can be different for the different geometries.

The fabrication of free-standing semipolar (11 $\bar{2}2$ ) InGaN/GaN MQW LED on HVPE-grown GaN template has been demonstrated by the use of both LLO and CMP. No detrimental effect on the light optical power was observed after the processes. Ni/Ag/Ni p-metal provided a better light extraction and low contact resistance for substrate emitting LEDs. The emission properties were quite stable with peak shift less than 2 nm. The output power of the CMP-LLO-LEDs was 0.87 mW at 20 mA without any extraction features or low refractive index encapsulation. The polarization ratio was 0.14, independent of the GaN v-groove features. The LEDs showed an electrical-to-optical bandwidth of 166 MHz at 20 mA and the signal transmission data rate of 300 Mbps that is promising for VLC applications.

### 3.6 References

- [1] S. Nakamura, T. Mukai, M. Senoh, "Candela-class high-brightness InGaN/AlGaIn double-heterostructure blue-light emitting diodes," *Appl. Phys. Lett.*, vol. 64, no. 16, pp. 87–89, Jan. 1994.
- [2] S. Nakamura, "The Roles of Structural Imperfections in InGaIn-Based Blue Light-Emitting Diodes and Laser Diodes," *Science*, vol. 281, no. 5379, pp. 956–961, Aug. 1998.
- [3] F. A. Ponce and D. P. Bour, "Nitride-based semiconductors for blue and green light-emitting devices," *Nature*, vol. 386, pp. 351–359, Mar. 1997.

- [4] T. Wang, D. Nakagawa, J. Wang, T. Sugahara and S. Sakai, "Photoluminescence investigation of InGaN/GaN single quantum well and multiple quantum wells," *Appl. Phys. Lett.*, vol. 73, no. 24, pp. 3571, Oct. 1998.
- [5] P. Waltereit, O. Brandt, A. Trampert, H. T. Grahn, J. Menniger, M. Ramsteiner, M. Reiche, and K. H. Ploog, "Nitride semiconductors free of electrostatic fields for efficient white light emitting diodes," *Nature.*, vol. 406, no. 6798, pp. 865-868, Aug. 2000.
- [6] M. C. Schmidt, K. C. Kim, H. Sato, N. Fellows, H. Masui, S. Nakamura, S. P. DenBaars, and J.S. Speck, " Demonstration of Nonpolar m-plane InGaN/GaN Laser Diodes," *Jpn. J. Appl. Phys.*, vol. 46, no. 2, pp. 8-11, Feb. 2007.
- [7] Y. Zhao, J. Sonoda, I. Koslow, C.C.Pan, H. Ohta, J. S. Ha, S. P. DenBaars, and S. Nakamura, "Optimization of Device Structures for Bright Blue Semipolar (1011) Light Emitting Diodes via Metalorganic Chemical Vapor Deposition", *Jpn. J. Appl. Phys.*, vol. 49, no. 7R, pp. 070206, July. 2010.
- [8] N. F. Gardner, J. C. Kim, J. J. Wierer, Y. C. Shen, and M. R. Krames, "Polarization anisotropy in the electroluminescence of m-plane InGaN-GaN multiple-quantum-well light emitting diodes," *Appl. Phys. Lett.*, vol. 86, no. 11, , pp. 111101 (1-3), Jan. 2005.
- [9] F. Scholz, "Semipolar GaN grown on foreign substrates: a review," *Semicond. Sci. Technol.*, vol. 27, no. 2, pp. 024002 (1-15), Jan. 2012.
- [10] T. Wunderer, M. Feneberg, F. Lipski, *et al.*, "Three-dimensional GaN for semipolar light emitters", *Phys. Stat. Soli. (b)*, vol. 248, no. 3, pp. 549-560, Mar. 2011.
- [11] H. Sato, H. Hirasawa, H. Asamizu, N. Fellows A. Tyagi, M. Saito, K. Fujito, J. S. Speck, S. P. DenBaars, and S. Nakamura, "High power and high efficiency semipolar InGaN Light Emitting Diodes," *J. Light Visual Environ.*, vol. 32, no. 2, pp. 107-110, Feb. 2008.
- [12] D. O'Brien, G. Parry, and P. Stavrinou, "Optical hotspots speed up wireless communication," *Nat. Photon.*, vol. 1, no. 5, pp. 245-247, May. 2007.
- [13] H. Elgala, G. Parry, and H. Haas, "Indoor optical wireless communication: Potential and state-of-the-art," *IEEE Commun. Mag.*, vol. 49, no. 9, pp. 56-62, Sep. 2011.
- [14] S. Haruyama, "Advances in visible light communication technologies," European conference and exhibition on optical communication, OSA, Sep. 2012
- [15] I. Takai, T. Harada, M. Andoh, K. Yasutomi, K. Kagawa, S. Kawahito, "Optical vehicle to vehicle communication system using LED transmitter and camera receiver," *IEEE Photo. J.*, vol. 6, no. 5, pp. 1-14, Oct. 2014.
- [16] D. F. Feezell, J. S. Speck, S. P. DenBaars, and S. Nakamura, "Semipolar (20-2-1) InGaN/GaN Light-Emitting Diodes for High-Efficiency Solid-State Lighting," *J. Display Technol.*, vol. 9, no. 4, pp.190-198, Apr. 2013.
- [17] C. Wetzel, M. Zhu, J. Senawiratne, T. Detchprohm, P. D. Persans, L. Liu, E. A.

Preble, D. Hanser, “ Light-emitting diode development on polar and non-polar substrates,” *J. Cryst. Growth*, vol. 310, no. 17, pp. 3987-3991, Aug. 2008.

[18] H. Sato, R. B. Chung, H. Hirasawa, N. Fellows, H. Masui, F. Wu, M. Saito, K. Fujito, J. S. Speck, S. P. DenBaars, and S. Nakamura, “Optical properties of yellow light-emitting diodes grown on semipolar (11-22) bulk GaN substrates,” *Appl. Phys. Lett.*, vol. 92, no. 22, 221110, pp. 1-3, Jun. 2008.

[19] S. H. Park, D. Mishra, Y. E. Pak, K. Kang, C. Y. Park, S. H. Yoo, Y. H. Cho, M. B. Shim, and S. Kim, “Polarization characteristics of semipolar (11-22) InGaN/GaN quantum well structures grown on relaxed InGaN buffer layers and comparison with experiment,” *Opt. Express.*, vol. 22, no. 12, pp. 14850-14858, Jun. 2014.

[20] N. Okada, K. Uchida, S. Miyoshi and K. Tadatomo, “Green light-emitting diodes fabricated on semipolar (11–22) GaN on r-plane patterned sapphire substrate,” *Phys. Stat. Soli. (a)*, vol. 209, no 3, pp. 469–472, Mar. 2012.

[21] D. V. Dinh, M. Akhter, S. Presa, G. Kozlowski, D. O' Mahony, P. P. Maaskant, F. Brunner, M. Caliebe, M. Weyers, F. Scholz, B. Corbett, and P. J. Parbrook, “Semipolar (11-22) InGaN light emitting diodes grown on chemically–mechanically polished GaN templates,” *Phys. Stat. Soli. (a)*, vol. 212, no. 10, pp. 2196–2200, Jun. 2015.

[22] T. Wernicke, C. Netzel, M. Weyers, and M. Kneissl, “Semipolar GaN grown on m-plane sapphire using MOVPE”, *Phys. Stat. Soli. (c)*, vol. 5, no. 6, pp. 1815-1817, Apr. 2008.

[23] Q. Sun, B. Leung, C. D. Yerino, Y. Zhang, and J. Han, “Improving microstructural quality of semipolar (11-22) GaN on m-plane sapphire by a two-step growth process,” *Appl. Phys. Lett.*, vol. 95, no. 23, pp.231904, Dec. 2009.

[24] P. de Mierry, N. Kriouche, M. Nemoz, S. Chenot, and G. Nataf, “Semipolar GaN films on patterned r-plane sapphire obtained by wet chemical etching,” *Appl. Phys. Lett.*, vol. 96, no. 23, pp. 231918, Jun 2010.

[25] N. Kriouche, P. Vennegues, M. Nemoz, G. Nataf, and P. de Mierry, “Stacking faults blocking process in (11-22) semipolar GaN growth on sapphire using asymmetric lateral epitaxy,” *J. Cryst. Growth*, vol. 312, no. 19, pp. 2625-2630, Sep. 2010.

[26] F. Brunner, F. Edokam, U. Zeimer, W. John, D. Prasai, O. Kruger, and M. Weyers, “Semi-polar (11-22)-GaN templates grown on 100 mm trench-patterned r-plane sapphire,” *Phys. Stat. Soli. (b)*, vol. 252, no. 5, pp. 1189–1194, May. 2015.

[27] B. Leung, Y. Zhang, C. D. Yerino, J. Han, Q. Sun, Z. Chen, S. Lester, K. Y. Liao, and Y. L. Li, “Optical emission characteristics of semipolar (11-22) GaN light-emitting diodes grown on m-sapphire and stripe-etched r-sapphire” *Semicond. Sci. Technol.*, vol. 27, no. 024016, pp. 1-7, Jan. 2012.

[28] D. Hanser, M. Tutor, E. Preble, M. Williams, X. Xu, D. Tsvetkov, and L. Liu, “Surface preparation of substrates from bulk GaN crystals,” *J. Cryst. Growth.*, vol. 305, no. 2, pp. 372-376, Jul. 2007.

- [29] K. Fujito, S. Kubo, I. Fujimura, “Development of bulk GaN crystals and nonpolar/semipolar substrates by HVPE”, *MRS BULL.*, vol. 34, pp. 313-317, May. 2009.
- [30] P. Schustek, M. Hocker, U. Simon, F. Scholz, and K. Thonke, “Spectroscopic study of semipolar (11-22)-HVPE GaN exhibiting high oxygen incorporation”, *J. Appl. Phys.*, vol. 116, no. 16, pp. 163515 (1-9), Oct. 2014.
- [31] P. B. Zantyea, A. Kumara, A. K. Sikder, “Chemical mechanical planarization for microelectronics applicatons”, *Materials Science and Engineering* vol. R 45, no. 3-6, pp. 89-220, Oct. 2004.
- [32] H. Zhu, L. A. Tassaroto, R. Sabia, *et al.*, “Chemical mechanical polishing (CMP) anisotropy in sapphire,” *Appl. Surf. Sci.*, vol. 236, no. 1-4, pp. 120-130, Sep. 2004.
- [33] X. F. Chen, X. G. Xu, X. B. Hu, *et al.*, “Anisotropy of chemical mechanical polishing in silicon carbide substrates,” *Mater. Sci. Eng. B*, vol. 142, no. 1, pp. 28-30. Aug. 2007.
- [34] P. R. Tavernier, T. Margalith, L. A. Coldren, S. P. DenBaars, and D. R. Clarke, “Chemical Mechanical Polishing of GaN,”*Electrochem. Solid-State Lett.*, vol. 5, no. 8, pp. G61-G64, May. 2002.
- [35] J. L. Weyher, S. Muller, I. Grzegory, and S. Porowski, “Chemical polishing of bulk and epitaxial GaN” *J. Cryst. Growth*, vol. 182, no. 1-2, pp. 17-22, Apr. 1997.
- [36] S. Hayashi, T. Koga and M. S. Goorsky, “Chemical Mechanical Polishing of GaN”, *J. Electrochem. Soc.*, vol. 155, no. 2, pp. H113-H116, Jan. 2008.
- [37] H. W. Jang, J. H. Son, and J. L. Lee, “Formation of High-Quality Ag-Based Ohmic Contacts to p-Type GaN,” *J. Electrochem. Soc.*, vol. 155, no. 8, pp. H563-H568, Jun. 2008.
- [38] Y. N. Zhang, B. Lin, and Z. C. Li, “An overview of recent advances in chemical mechanical polishing (CMP) of sapphire substrates”, *ECS Transactions*, vol. 52, no.1, pp. 495-500, 2013.
- [39] C. L. Zou, G. S. Pan, X. L. Shi, H. Gong, Y. Zhou, “Atomically smooth gallium nitride surface prepared by chemical-mechanical polishing with different abrasives”, *PROCEEDINGS OF THE INSTITUTION OF MECHANICAL ENGINEERS PART J- JOURNAL OF ENGINEERING TRIBOLOGY*” vol. 228, no. 10, pp.1144-1150, Apr. 2014.
- [40] K. Asghar, M. Qasim, and D. Dasz “Effect of Polishing Parameters on Chemical Mechanical Planarization of C-Plane (0001) Gallium Nitride Surface Using SiO<sub>2</sub> and Al<sub>2</sub>O<sub>3</sub> Abrasives”, *ECS Journal of Solid State Science and Technology*, vol. 3, no. 8, pp. P277-P284, Jun. 2014.
- [41] H. Gong, G. Pan, Y. Zhou, X. L. Shi, C. L. Zou, S. M. Zhang, “Investigation on the surface characterization of Ga-faced GaN after chemical-mechanical polishing”, *Appl. Surf. Sci.*, vol. 338, pp. 85–91, May. 2015.

- [42] H. Aidaa, H. Takedaa, S. W. Kima, N. Aotaa, K. Koyamaa, T. Yamazaki, T. Doi, "Evaluation of subsurface damage in GaN substrate induced by mechanical polishing with diamond abrasives", *Appl. Surf. Sci.*, vol. 292, pp.531–536, Feb. 2014.
- [43] J. Wang, J. T. Q. Wang, G. S. Pan, X. C. Lu, "Mechanism of GaN CMP Based on H<sub>2</sub>O<sub>2</sub> Slurry Combined with UV Light", *ECS JOURNAL OF SOLID STATE SCIENCE AND TECHNOLOGY*, vol. 4, no. 3, pp. 112-117, Dec. 2015.
- [44] K. Asghar, D. Das, "Influence of Polishing Parameters on Abrasive Free Chemical Mechanical Planarization (AFCMP) of Non-Polar (11-20) and Semi-Polar (11-22) GaN Surfaces", *ECS JOURNAL OF SOLID STATE SCIENCE AND TECHNOLOGY*, vol. 4, no. 7, pp. 242-250, Apr. 2015.
- [45] K. Asghar and D. Das, "Effect of polishing parameters on abrasive free chemical mechanical planarization of semi-polar (1122) aluminum nitride surface", *J. Semicond.*, vol. 37, no. 3, Mar. 2016.
- [46] F. Scholz, M. Caliebe, G. Gahramanova, D. Heinz, M. Klein, R. A. R. Leute, T. Meisch, J. Wang, M. Hocker, and K. Thonke, "Semipolar GaN-based heterostructures on foreign substrates," *Phys. Stat. Soli. (b)*, vol. 253, no. 1, pp. 13–22, Jan. 2016.
- [47] M. Caliebe, T. Meisch, M. Madel and F. Scholz, "Effects of miscut of prestructured sapphire substrates and MOVPE growth conditions on (11-22) oriented GaN," *J. Cryst. Growth*, vol. 414, pp. 100–104, Mar. 2015.
- [48] M. Caliebe, Y. Han, M. Hocker, T. Meisch, C. Humphreys, K. Thonke and F. Scholz, "Growth and coalescence studies of (11-22) oriented GaN on pre-structured sapphire substrates using marker layers," *Phys. Stat. Soli. (b)*, vol. 253, no. 1, pp. 46-53, Aug. 2015.
- [49] [https://www.tedpella.com/technote\\_html/821-1-2-3-4-6-TN.pdf](https://www.tedpella.com/technote_html/821-1-2-3-4-6-TN.pdf).
- [50] <http://www.axustech.com/g-p-poli-500>
- [51] T. Meisch, R. Zeller, S. Schörner, K. Thonke, L. Kirste, T. Fuchs and F. Scholz, "Doping behavior of (11-22) GaN grown on patterned sapphire substrates," *Phys. Stat. Soli. (b)*, vol. 253, no. 1, pp. 164-168, Jan. 2016.
- [52] <http://www.tek.com/keithley-source-measure-units>
- [53] <http://www.tek.com/keithley-multimeter-measure-units>
- [54] <https://www.newport.com/p/818-UV--DB>
- [55] <https://www.thorlabs.com/thorproduct.cfm?partnumber=FDS1010>
- [56] M. Funato, M. Ueda, Y. Kawakami, Y. Narukawa, T. Kosugi, M. Takahashi, and T. Mukai, "Blue, Green, and Amber InGa<sub>N</sub>/Ga<sub>N</sub> Light-Emitting Diodes on Semipolar (11-22) Ga<sub>N</sub> Bulk Substrates," *Jpn. J. Appl. Phys.*, vol. 45, no. 2, pp. 24-28, Jun. 2006.
- [57] S. Y. Bae, D. S. Lee, B. H. Kong, H. K. Cho, J. F. Kaeding, S. Nakamura, S. P. DenBaars, and J. S. Speck, "Electroluminescence enhancement of semipolar GaN

light-emitting diodes grown on miscut m-plane sapphire substrates,” *Curr. Appl. Phys.*, vol. 11, no. 3, pp. 954-958, May. 2011.

[58] D. S. Kim, S. Lee, D. Y. Kim, S. K. Sharma, S. M. Hwang and Y. G. Seo, “Highly stable blue-emission in semipolar (11-22) InGaN/GaN multi-quantum well light-emitting diode,” *Appl. Phys. Lett.*, vol. 103, no. 2, pp. 021111, Jul. 2013.

[59] S. Presa, P. P. Maaskant, M. J. Kappers and B. Corbett, “Fluorescence microscopy investigation of InGaN-based light-emitting diodes,” *IET Optoelectr.*, vol. 10, no. 2, pp. 39-43, Apr. 2016.

[60] <https://oceanoptics.com/product/usb2000uv-vis/>

[61] <https://oceanoptics.com/support/technical-documents/spectrasuite/>

[62] [http://www.femto.de/images/pdf-dokumente/de-hsa-x-s-1g4-si\\_r10.pdf](http://www.femto.de/images/pdf-dokumente/de-hsa-x-s-1g4-si_r10.pdf)

[63] B. Corbett, Z. H. Quan, D. V. Dinh, *et al.*, “Development of semipolar (11-22) LEDs on GaN templates”, in Proceedings of SPIE conference on Light-Emitting Diodes: Materials, Devices, and Applications for Solid State Lighting XX, vol. 97681G, Mar. 2016.

[64] J. Mckendry, R. P. Green, A. E. Kelly, Z. Gong, B. Guilhabert, D. Massoubre, E. Gu, M. D. Dawson, “High speed visible light communications using individual pixels in a micro light-emitting diode array,” *IEEE Photon. Tech. Lett.*, vol. 22, no. 18, pp. 1346-1348. Jul. 2010.

[65] J. Mckendry, D. Massoubre, S. Zhang, B. R. Rae, R. P. Green, E. Gu, R. K. Henderson, A. E. Kelly, and M. D. Dawson, “Visible-light communications using a CMOS-controlled micro-light-emitting-diode array,” *J. Lightw. Technol.*, vol. 31, no. 8, pp. 1211-1216, Jan. 2012.

[66] C. L. Liao, Y. F. Chang, C. L. Ho, and M. C. Wu, “High speed GaN-based blue light emitting diodes with gallium-doped ZnO current spreading layer,” *IEEE Electron Device Lett.*, vol. 34, no. 5, pp. 611-613, May. 2013.

[67] R. X. G. Ferreira, E. Xie, J. J. D. McKendry, H. Chun, G. Faulkner, E. Gu, R. V.enty, I. H. White, D. C. O’Brien, and M. D. Dawson, “High bandwidth GaN-based micro-LEDs for Multi-Gb/s visible light communications,” *IEEE Photon. Technol. Lett.*, vol. 28, no. 19, pp. 2023-2026, Jun. 2016.

[68] G. P. Agrawal, *FiberOptic Communication Systems*, Chap. 3, pp. 90–91, (Wiley, 3rd ed. 2002).

[69] Y. Ji, W. Liu, T. Erdem, R. Chen, S. T. Tan, Z. H. Zhang, Z. Ju, X. Zhang, H. Sun, X. W. Sun, Y. Zhao, S. P. DenBaars, S. Nakamura, and H. V. Demir, “Comparative study of field-dependent carrier dynamics and emission kinetics of InGaN/GaN light-emitting diodes grown on (11-22) semipolar versus (0001) polar planes,” *Appl. Phys. Lett.* vol. 104, pp. 143506(1)- 143506(5), Apr. 2014.

[70] <https://www.testequity.com/products/773/>

[71] <http://www.testequipmenthq.com/Agilent-DSO80804A-Datasheet.pdf>

## Chapter 4

### Fabrication of vertical conduction AlGa<sub>N</sub> membrane

This chapter describes the fabrication of a vertical structure conduction Al<sub>x</sub>Ga<sub>1-x</sub>N ( $0 < x < 1$ ) membrane as the critical process for implementation of AlGa<sub>N</sub> based vertical conduction deep ultraviolet (DUV) light-emitting diodes (LEDs). It presents a new structure scheme for laser lift-off (LLO) process on AlGa<sub>N</sub> membrane grown on AlN on c-plane sapphire substrate. An Au<sub>0.8</sub>Sn<sub>0.2</sub> eutectic alloy was applied to attach the metal-polar ((Al, Ga)-face) AlGa<sub>N</sub>/AlN/sapphire wafer on thin Au layer (~ 100-nm-thick) coated Si substrate (~ 500-μm-thick) as a mechanical support for LLO and electrode of metal contact. The LLO of AlGa<sub>N</sub> from AlN/sapphire has been successfully performed. The electrical properties of the metal contact to N-polar (nitrogen-face) Si-doped n-type AlGa<sub>N</sub> were investigated.

#### 4.1 Introduction

Al<sub>x</sub>Ga<sub>1-x</sub>N alloys have been used for the development of DUV LEDs operating from 200 nm to 360 nm [1-6]. As the next generation UV light source, AlGa<sub>N</sub> based DUV LEDs have been progressed using MOVPE for high quality and crack-free Al<sub>x</sub>Ga<sub>1-x</sub>N and AlN buffer layers prepared on sapphire substrate [7]. Al<sub>x</sub>Ga<sub>1-x</sub>N layers can be also grown on GaN [8, 9]; however, GaN is absorbing to wavelengths shorter than 360 nm. AlN serves as a more ideal template material, as the smaller in-plane lattice constant of AlN relative to Al<sub>x</sub>Ga<sub>1-x</sub>N device layers mitigates cracking [7, 10-12]. Moreover, AlN is ideally transparent to wavelengths greater than 200 nm. It has a high thermal conductivity that could improve the thermal management of the LED structure. However, the high resistivity of n-type Al<sub>x</sub>Ga<sub>1-x</sub>N, leads to current crowding [1, 13–15] and device self-heating which limit the achievable output power at high forward currents [16]. An ideal DUV LED would incorporate a heat-sink mount for a vertically conducting design to improve device series resistance, current spreading and thermal management [8, 9, 17, 18]. The development of vertical conduction DUV LEDs has been dominated by four issues associated with (a) high quality epitaxial structure with LLO sacrificial layer, (b) good electrical properties of the metal contact to backside N-polar AlGa<sub>N</sub>, (c) light extraction and (d) emission



area scalability. All of these issues are related to each other and affect the device performance and reliability.

Vertical conduction AlGaIn based DUV LEDs emitting from 280 nm – 325 nm have been demonstrated by other groups [8, 9, 17, 18]. Schematic diagrams of DUV LED structures with sacrificial layer are shown in Fig. 4.1. A GaN buffer layer has been utilized as a sacrificial layer that absorbs laser pulse to induce separation of a highly strained LED epitaxial layer stack from the sapphire substrate, which have been reported by Kawasaki *et al.* [8] and Zhou *et al.* [9], as shown in Figs. 4.1 (a) and (b). The use of GaN buffer layers (Fig. 4.1(a)) is ineffective for growth of high Al mole fraction ( $> 40\%$ ) AlGaIn layer for DUV LEDs because of cracking [12, 17-19]. Zhou *et al.* [9] used a conventional GaN/sapphire template with a low-temperature (LT-) AlN interlayer to achieve operation at  $\lambda = 280$  nm, as shown in Fig. 4.1(b). However, the insertion of the layer degraded the crystal quality of the over-grown AlGaIn layer compared with that of the underlying GaN templates, in terms of the edge dislocation density [18, 19]. Without a GaN sacrificial layer, Adivarahan *et al.* [17] first demonstrated a vertical conduction DUV LED by the use of a 10-period AlN (10 nm)/Al<sub>0.8</sub>Ga<sub>0.2</sub>N (10 nm) superlattice on an AlN/sapphire template, shown in Fig. 4.1(c). However, the growth of the superlattice layer needs be optimized and it is difficult to be removed after LLO. According to the vertical conduction LED fabrication reported for these 3 types of DUV LED structure, a dry-etch process had to be used to remove the remaining layers to access N-polar n-AlGaIn contact layer after LLO.

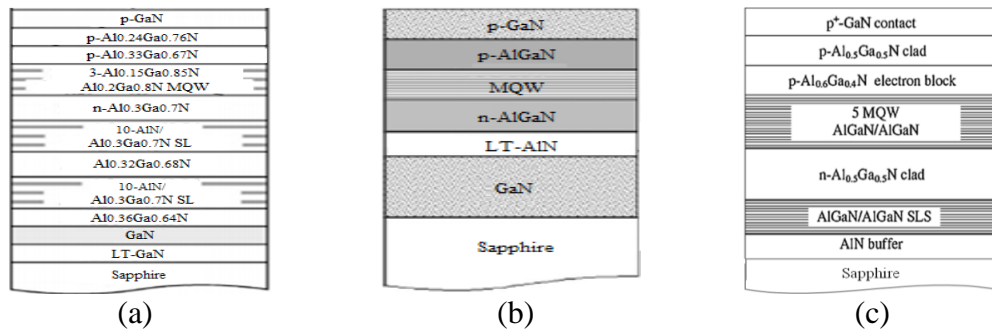


Figure. 4.1 Schematic diagrams of an AlGaIn-based DUV LED structure with sacrificial layer on a sapphire substrate for fabrication of vertical conduction thin-film LEDs: (a) DUV LED ( $\lambda=322$ nm) using a thin-GaN buffer (thickness  $< 150$  nm) as both a seeding and LLO sacrificial layer [8], (b) DUV LED ( $\lambda=325$  nm, 280 nm) using a GaN buffer as a sacrificial layer with an AlN interlayer [9], and (c) DUV LED ( $\lambda= 280$  nm) using an AlN/Al<sub>0.8</sub>Ga<sub>0.2</sub>N superlattice on AlN buffer [17].

However, the heat treatment induced by LLO on n-AlGaN contact layer of DUV LEDs, could produce thermal-annealing effect on the N-polar surface of n-AlGaN. It will not require inductively coupled plasma (ICP) etch to reach the backside of the n-contact as there are no remaining layers between n-AlGaN and AlN/sapphire template.

As to the sacrificial layers presented in fabrication of vertical conduction DUV LEDs [8, 9, 17], there are no reports of LLO directly on high Al-content ( $\sim 50\text{-}60\%$ ) n-AlGaN as both n-contact and sacrificial layer. Moreover, there are no reports of N-polar high Al mole fraction AlGaN and the electrical contact directly on the N-polar n-AlGaN created by LLO. Therefore, LLO of high Al mole fraction n-AlGaN (Al  $\sim 50\text{-}60\%$ ) is presented. Based on the development of LLO on AlGaN for vertical conduction structure, the LEDs can be initially flipped with metallic p-contacts downward bonded on electrical conductive layer that coated on a carrier substrate. Then, the sapphire substrate was removed by LLO; afterwards metallic n-contacts can be deposited on the N-polar surface of the n-AlGaN created after photolithography processes.

## **4.2 Fabrication of AlGaN membrane by laser lift-off**

This section presents the fabrication of a substrate lift-off n-AlGaN ( $\sim 1.5\text{-}\mu\text{m}$ -thick) membrane, including the description of 3 types of AlGaN epitaxial structure with sacrificial layer for LLO and the corresponding experimental results. Directly LLO on n-Al<sub>0.6</sub>Ga<sub>0.4</sub>N/AlN/sapphire is a promising candidate for DUV LED epitaxial layer grown on sapphire substrate. A single laser pulse of  $600\text{ mJ/cm}^2$  incident energy density exhibited a successful lift-off. This result was verified by simulation of the localized temperature distribution at the interface of Al<sub>0.6</sub>Ga<sub>0.4</sub>N/AlN induced by a single laser pulse. In order to guarantee the mechanical support of transferred AlGaN layer, an eutectic bonding method of the Au-AuSn foil-Au was employed to attach the AlGaN layer onto an Au-coated Si substrate before LLO. The method is described at the end of this section.

#### 4.2.1 Sacrificial layer

A photon-absorption layer is required to be grown on top of the AlN/sapphire template of the DUV LED epitaxy as a sacrificial layer for LLO. It is delaminated due to short wavelength laser pulse induced decomposition at the interface between the layer and AlN/sapphire template by LLO. In order to achieve this purpose, a few trade-offs of the sacrificial layer should be satisfied, which are described as follows:

- Strong absorption
- Low lattice mismatch for high quality crystal growth
- Strain management

According to the LLO on GaN described in Chapter 2, it is known that GaN layers of several micrometer thickness epitaxially grown on sapphire substrates are thermally decomposed at the GaN/sapphire by a laser pulse irradiation (photon energy  $E = 5.0$  eV). The remaining Ga droplets are melted at temperatures over  $30^\circ\text{C}$  [20], allowing easy separation of the epilayers from sapphire. Alternatively, n-AlGaN can be used both as a laser irradiation absorption layer and an n-contact layer. It has been reported that AlGaN or AlN epilayer cannot be easily removed from sapphire substrates by LLO. This has been attributed to the Al droplets generated by the LLO thermal decomposition being very rigid [21]. Therefore, the epilayer parts are mechanically cracked during the removal process from the substrates. In addition, the thermal shock induced by the laser irradiation very often leads to cracking during and/or after the LLO process [18]. However, no such results has been observed in the LLO AlGaN layers on AlN in this study. It might be due to the lower surface temperature of AlN (i.e. metal-polar AlN) at the AlGaN/AlN interface than the AlGaN (i.e. N-polar AlGaN) surface for the laser pulse induced heating, as heat conduction in AlN layer is faster than in sapphire (i.e.  $k_{\text{AlN}} = 350$  W/mK,  $k_{\text{sapphire}} = 35$  W/mK). Due to much higher melting temperature of Al ( $\sim 660^\circ\text{C}$ ) [22] than Ga ( $\sim 30^\circ\text{C}$ ), the majority of Al droplets could be intended to condense on the N-polar AlN surface at the interface. For that reason, the light-silver colour mirror-like surface was observed on the N-polar AlN surface after LLO.

To develop a high crystal quality, crack-free and substrate-lift-off capable n-AlGaN structure for implementation of vertical conduction DUV LEDs, 3 types of proposed n-type AlGaN structures were grown in the MOVPE reactor in the Tyndall National

Institute [23,24], that were investigated as the candidates for LLO, as shown in Fig. 4.2. Sample #A presents a 1- $\mu\text{m}$ -thick n-type  $\text{Al}_{0.5}\text{Ga}_{0.5}\text{N}$  was grown on 10-nm-thick GaN interlayer on 1- $\mu\text{m}$ -thick AlN buffer layer on (0001) double side polished sapphire substrate, shown in Fig. 4.2 (a). Samples #B and #C were grown on 2.5- $\mu\text{m}$ -thick (0001) AlN buffer layer on double polished sapphire. Sample #B consists of a 5- $\mu\text{m}$ -thick n- $\text{Al}_{0.75}\text{Ga}_{0.25}\text{N}$  layer with about 200-nm-thick n- $\text{Al}_{0.5}\text{Ga}_{0.5}\text{N}$  interlayer as seen in Fig. 4.2 (b), while only a 1.5- $\mu\text{m}$ -thick n- $\text{Al}_{0.6}\text{Ga}_{0.4}\text{N}$  single layer was grown as sample #C, as shown in Fig. 4.2 (c).

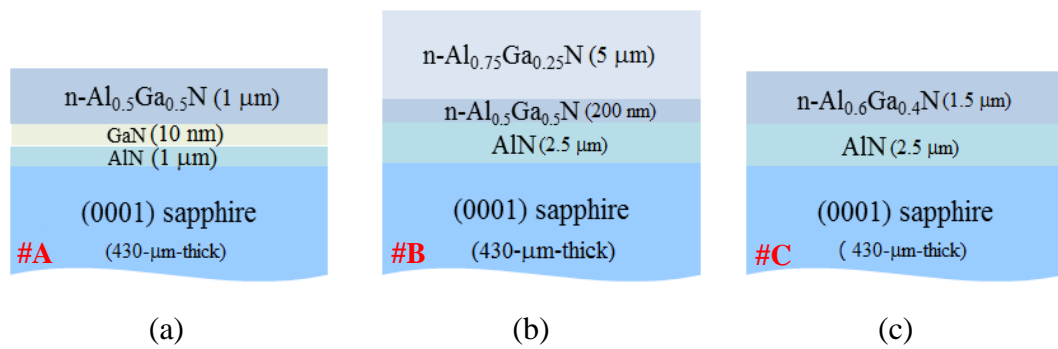


*Figure 4.2 Schematic diagrams of n-type AlGaN structure grown on AlN buffer layer on double polished (0001) sapphire substrate for laser-lift-off: (a) n- $\text{Al}_{0.6}\text{Ga}_{0.4}\text{N}$  layer with GaN interlayer, (b) n- $\text{Al}_{0.75}\text{Ga}_{0.25}\text{N}$  layer with n- $\text{Al}_{0.5}\text{Ga}_{0.5}\text{N}$  interlayer and (c) n- $\text{Al}_{0.6}\text{Ga}_{0.4}\text{N}$  layer.*

Due to the larger in-plane lattice constants of AlGaN than AlN, the AlGaN/AlN layers are inherently compressive stresses [25]. Thus, a metal bonding method was required for the wafer sample as both a carrier substrate and a good heat sink, before the LLO process. Thus, the eutectic bonding method of  $\text{Au}_{0.8}\text{Sn}_{0.2}$  soldering foil is introduced for sample bonding.

#### 4.2.2 Laser lift-off process for $\text{Al}_x\text{Ga}_{1-x}\text{N}$ epitaxial thin film

The bandgap energy of semiconductors can be adjusted by incorporation of alloys to achieve a desired emission/absorption wavelength. Al atoms are incorporated in GaN matrix to obtain AlGaN alloys to achieve shorter wavelengths. The bandgap energy of AlGaN alloys is given by:

$$E_g^{Al_xGa_{1-x}N} = (1 - x)E_g^{GaN} + xE_g^{AlN} - bx(1 - x), \quad (4.1)$$

Where  $E_g^{GaN} = 3.4$  eV and  $E_g^{AlN} = 6.0$  eV are the band gap energy of GaN and AlN, and the bowing parameter  $b$  is 1.3 eV [26]

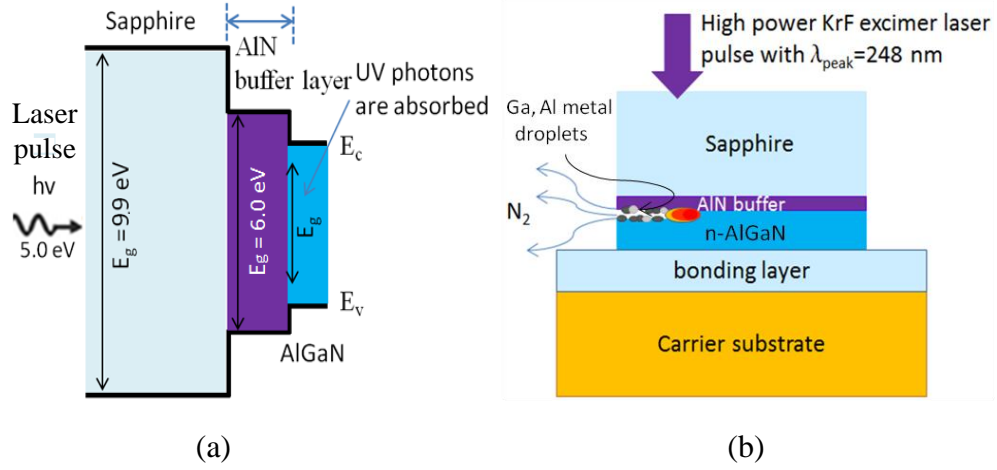
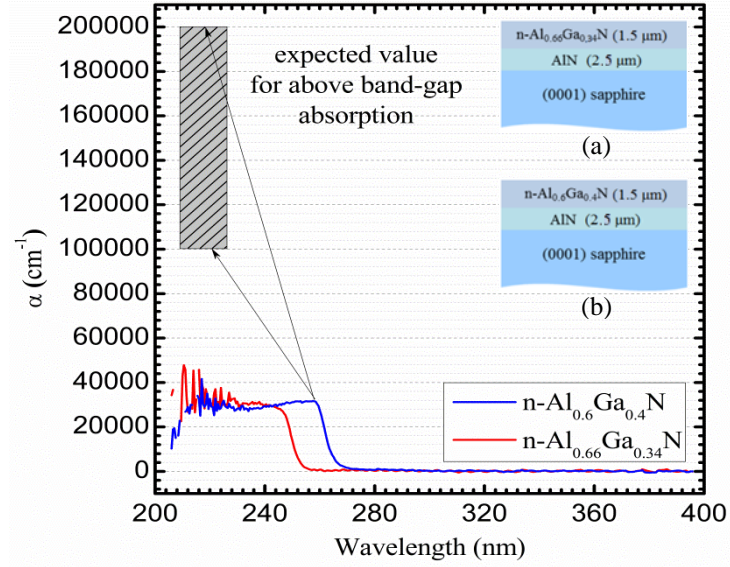


Figure 4.3 Schematic view of (a) band diagram of photoabsorption AlGaIn layer on AlN/sapphire, (b) the view of LLO process on an  $n-Al_xGa_{1-x}N$  ( $x \leq 60\%$ ). High intensity laser pulses enter the sample via the sapphire substrate and AlN buffer thermally decompose a thin AlGaIn layer at the AlGaIn/AlN interface.

From Fig. 4.3 (a), it can be seen the laser induced thermal decomposition of AlGaIn at the AlGaIn/AlN interface, similar to the laser interaction with GaN. Likewise, the laser pulse creates a localized explosive shock wave due to the debonding of the interface by the produced nitrogen gas. The localized temperature induced by the high power laser irradiation at the interface could be over  $2000^\circ\text{C}$ , resulting in the decomposition of AlGaIn to metallic Al, Ga droplets and gaseous nitrogen. Regarding the variation of Al mole fraction, the bandgap energy of the  $Al_xGa_{1-x}N$  alloys are in the range from 3.4 eV (emission wavelength of 360 nm) to 6.0 eV (emission wavelength of 200 nm). The LLO apparatus is based on 248-nm KrF excimer laser system that is only able to provide a photon energy of 5.0 eV. Thus, in principle, in order to cause photoabsorption in  $Al_xGa_{1-x}N$  alloys at certain Al mole fraction, the bandgap energy should be less than 5.0 eV (i.e.  $> 248$  nm), whereas, the predicted Al-content of AlGaIn alloys, which can be LLO processed, is no more than 60%. It was also confirmed by comparison of the measured optical absorption

spectrum and the transmission spectrum between n-Al<sub>0.66</sub>Ga<sub>0.34</sub>N and n-Al<sub>0.6</sub>Ga<sub>0.4</sub>N layers both were grown on 2.5-μm-thick AlN/sapphire (Fig. 4.4)



*Figure 4.4 Measured optical absorption spectra at RT of n-Al<sub>0.6</sub>Ga<sub>0.4</sub>N layer and n-Al<sub>0.66</sub>Ga<sub>0.34</sub>N layer grown on AlN/sapphire. The insertion (a) the sample structure of n-Al<sub>0.6</sub>Ga<sub>0.4</sub>N layer, (b) the sample structure of n-Al<sub>0.66</sub>Ga<sub>0.34</sub>N layer .*

As shown in Fig. 4.4, the absorption of light measured at room temperature (RT) of light spectrum through 1.5-μm-thick n-Al<sub>0.66</sub>Ga<sub>0.34</sub>N and n-Al<sub>0.6</sub>Ga<sub>0.4</sub>N layers were grown on 2.5-μm-thick AlN/sapphire. The absorption coefficient data of n-AlGaIn samples at wavelengths shorter than 250 nm are not valid due to stray light (full-spectrum white noise) [27]. This is caused by the limitation of measurement system. The monochromator detects all spectrum light, the light at optical wavelength less than 250 nm is fully absorbed in 1-μm-thick of both AlGaIn layers, but there still has stray light presented. The stray light was collected by the monochromator, therefore, low absorption coefficients were present at the wavelength less than 260 nm for the n-Al<sub>0.6</sub>Ga<sub>0.4</sub>N layer sample. Thus, the data in the wavelength less than 260 nm are not true and the absorption coefficient expected above band-gap absorption should be in the shaded-region labeled shown in Fig. 4.4. The sample n-Al<sub>0.66</sub>Ga<sub>0.34</sub>N at 248 nm wavelength is nearly transparent, which means that the KrF laser irradiation cannot be fully absorbed by the n-Al<sub>0.66</sub>Ga<sub>0.5</sub>N layer.

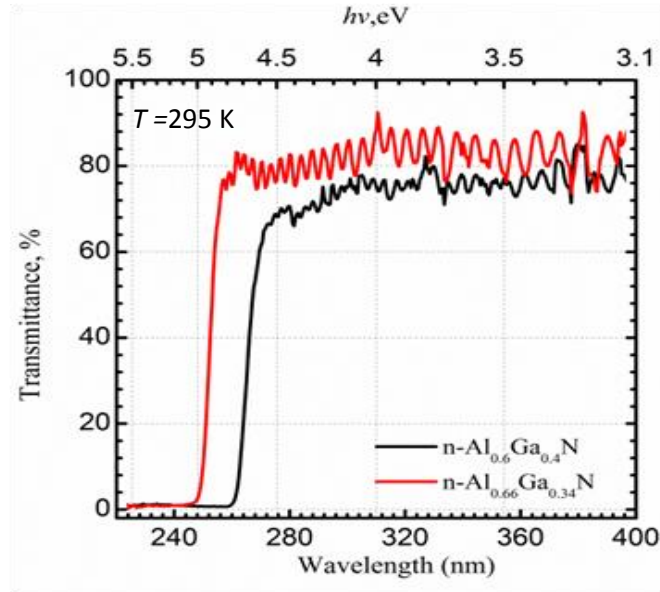


Figure 4.5 Measured transmission spectra of  $n\text{-Al}_{0.6}\text{Ga}_{0.4}\text{N}$  layer and  $n\text{-Al}_{0.66}\text{Ga}_{0.34}\text{N}$  layer samples both grown on AlN/sapphire.

Fig. 4.5 shows the transmittance curves of the  $n\text{-Al}_{0.6}\text{Ga}_{0.4}\text{N}$  and  $n\text{-Al}_{0.66}\text{Ga}_{0.34}\text{N}$  layers grown on AlN/sapphire templates. At the wavelength of 248 nm, the transmittance of  $n\text{-Al}_{0.6}\text{Ga}_{0.4}\text{N}$  is zero, however, the  $n\text{-Al}_{0.66}\text{Ga}_{0.34}\text{N}$  still has a transmittance of approximately 5%. Hence, the KrF laser irradiation can be fully absorbed in the  $n\text{-Al}_{0.6}\text{Ga}_{0.4}\text{N}$  layer to generate localized heating at the  $\text{Al}_{0.6}\text{Ga}_{0.4}\text{N}/\text{AlN}$  interface, which leads to the thermal decomposition of  $\text{Al}_{0.6}\text{Ga}_{0.4}\text{N}$ . In addition, the oscillations present on the transmittance curve at the flat top range in wavelengths from 280 nm to 400 nm of the  $n\text{-Al}_{0.6}\text{Ga}_{0.4}\text{N}$  layer and from 260 nm to 400 nm of the  $\text{Al}_{0.66}\text{Ga}_{0.34}\text{N}$  layer are due to the interference reflections from the interface of each layer material.

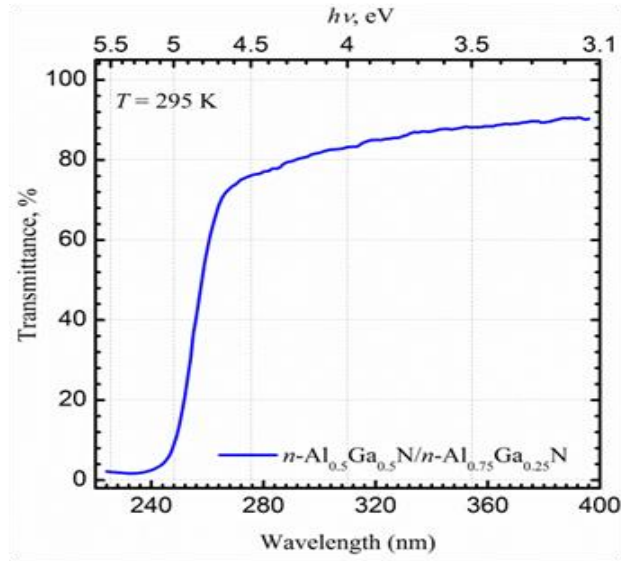


Figure 4.6 Measured transmittance of  $n\text{-Al}_{0.75}\text{Ga}_{0.25}\text{N}/n\text{-Al}_{0.5}\text{Ga}_{0.5}$  layer grown on AlN/sapphire.

Fig. 4.6 shows the transmission spectrum of the 200-nm-thick  $n\text{-Al}_{0.5}\text{Ga}_{0.5}\text{N}$  layer on 5- $\mu\text{m}$ -thick  $n\text{-Al}_{0.75}\text{Ga}_{0.25}\text{N}$  buffer layer grown on 2.5- $\mu\text{m}$ -thick AlN/sapphire. At a wavelength of 248 nm, the layer structure has a transmittance of approximately 10%, which is related to  $\text{Al}_{0.75}\text{Ga}_{0.25}\text{N}$ ; however, the  $\text{Al}_{0.5}\text{Ga}_{0.5}\text{N}$  layer should be not transparent to the KrF laser irradiation: as seen in Fig. 4.4, there was no transmission through  $n\text{-Al}_{0.6}\text{Ga}_{0.4}\text{N}/\text{AlN}$  layer at  $\lambda = 248$  nm. This  $n\text{-AlGa}\text{N}$  interlayer scheme can provide thicker  $n\text{-AlGa}\text{N}$  with Al mole fraction over 70% for AlGa $\text{N}$  based active region ( $\lambda \leq 280$  nm).

### 4.2.3 Thermal analysis

To verify the laser pulse energy density applied to LLO  $\text{Al}_{0.6}\text{Ga}_{0.4}\text{N}$  layer grown on AlN/sapphire, the 1-D finite element thermal diffusion model developed for Ga $\text{N}$  in Chapter 2 was modified to estimate temperature at the AlGa $\text{N}/\text{AlN}$  interface from a single laser pulse. In the model, the parameters of material properties of  $\text{Al}_{0.6}\text{Ga}_{0.4}\text{N}$  layer, AlN and sapphire are required. There is no experimental data reported on temperature dependent thermal conductivity of  $\text{Al}_x\text{Ga}_{1-x}\text{N}$  ( $x \geq 0.5$ ). The reported RT thermal conductivity varies in the range from 25 to 55 W/mK when the Al mole fraction changes from 0.4 to 0.1 [28]. The variation of the thermal conductivity presents a rather unusual temperature independence of thermal conductivity when



the Al mole fraction changes. As shown in Fig. 4.7, for both the theoretical curves and experimental data, the thermal conductivity variation with the Al mole fraction presented a characteristic abrupt reduction when  $x$  rises from 0.0 to about 0.1, followed by gradual approach to a minimum. The minimum thermal conductivity is achieved at approximately at  $x = 0.5$ . For Al mole fractions larger than 0.9, the thermal conductivity starts to increase rapidly, approaching the bulk AlN crystal value [28].

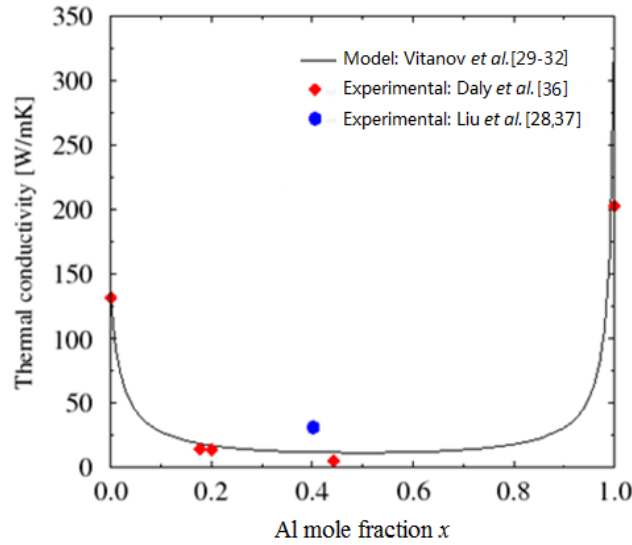


Figure 4.7  $\text{Al}_x\text{Ga}_{1-x}\text{N}$  thermal conductivity as a function of Al mole fraction  $x$  at room temperature [29, 37].

The experimental data of Daly *et al.* [36] and Liu *et al.* [28, 37] of  $\text{Al}_x\text{Ga}_{1-x}\text{N}$  thermal conductivity as a function of Al mole fraction at room temperature were presented with data from a model of Vitanov [29]. The expression below is used for RT thermal conductivity of  $\text{Al}_x\text{Ga}_{1-x}\text{N}$  alloys [30-32], where a mean value is used to model the conductivity at 300 K.

$$k_{300}^{\text{Al}_x\text{Ga}_{1-x}\text{N}} = \left( \frac{1-x}{k_{300}^{\text{AlN}}} + \frac{x}{k_{300}^{\text{GaN}}} + \frac{(1-x)x}{C_k} \right)^{-1}, \quad (4.2)$$

The  $k_{300}^{\text{Al}_x\text{Ga}_{1-x}\text{N}}$ ,  $k_{300}^{\text{AlN}}$ ,  $k_{300}^{\text{GaN}}$  is thermal conductivity of  $\text{Al}_x\text{Ga}_{1-x}\text{N}$ , AlN and GaN at 300 K respectively, A complement factor  $C_k$  value of 3.1 W/mK is used for the  $\text{Al}_x\text{Ga}_{1-x}\text{N}$ , which is in good agreement with a value previously reported for AlGaIn [30, 36, 37].

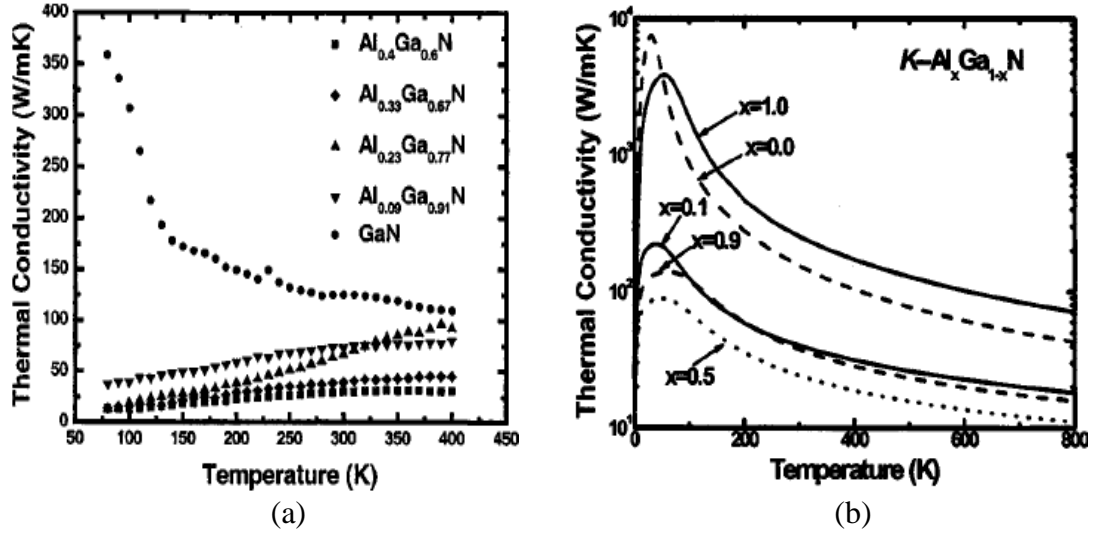


Figure 4.8 Temperature dependent thermal conductivities of  $Al_xGa_{1-x}N$  layer shown as (a) experimental measured thermal conductivities of HVPE GaN,  $Al_{0.09}Ga_{0.91}N$ ,  $Al_{0.23}Ga_{0.77}N$ ,  $Al_{0.33}Ga_{0.67}N$ , and  $Al_{0.4}Ga_{0.6}N$  layers in the temperature range from 80 to 400 K, (b) simulated thermal conductivity as a function of temperature for alloy  $Al_xGa_{1-x}N$  with  $x=1.0, 0.9, 0.5$ , and 0 [28].

According to Fig.4.7 and Fig. 4.8 reported [28, 29, 37], the higher Al mole fraction can make the thermal conductivity of  $Al_xGa_{1-x}N$  increase less which turns to be flat at higher temperatures from 350 to 400°C. In other words, the variation of  $k_{Al_xGa_{1-x}N}$  is less dependent on temperature. For AlN, the variation of the measured value of thermal conductivity is small, the thermal conductivity of AlN at RT is assumed as 350 W/mK [33] and it decreases with temperature [33-35],  $k_{AlN} = 350$  W/mK,  $k_{GaN} = 130$  W/mK. Recalling equation (2), the thermal conductivity of  $Al_{0.6}Ga_{0.4}N$  at RT can be calculated:

$$k_{300}^{Al_{0.6}Ga_{0.4}N} = \left( \frac{0.4}{350} + \frac{0.6}{130} + \frac{(1-0.6x) \cdot 0.4}{3.1} \right)^{-1} = 12 \text{ W/mK}, \quad (4.3)$$

Recalled the Vegard's law [38], the material density ( $\rho_{Al_xGa_{1-x}N}$ ) and heat capacity of  $Al_{0.6}Ga_{0.4}N$  ( $C_p$ ) can be expressed as:

$$\rho_{Al_xGa_{1-x}N} = x\rho_{AlN} + (1-x)\rho_{GaN}, \quad (4.4)$$

$$C_p = xC_{AlN} + (1-x)C_{GaN}. \quad (4.5)$$

Where calculated  $\rho_{\text{Al}_{0.6}\text{Ga}_{0.4}\text{N}}$  is 4420 kg/m<sup>3</sup> and its heat capacitance is 556 J/kg°C. The thermal parameters and material properties of Al<sub>0.6</sub>Ga<sub>0.4</sub>N, AlN and GaN for the simulation of temperature distribution induced by LLO are listed in Table 4.1.

Material	Diffusion length $\xi = 2\sqrt{6D}$	Thermal diffusivity $D = \frac{k}{\rho C_p}$	density $\rho$ (g/cm <sup>3</sup> )	Heat capacity $C_p$ (J/kg°C)	Thermal conductivity $k$ (W/m K)	Absorption coefficient at 248 nm $\alpha$ (cm <sup>-1</sup> )
Al <sub>0.6</sub> Ga <sub>0.4</sub> N	~ 0.31 $\mu\text{m}$	$4.11 \times 10^{-6}$	4.42	556	12	$\sim 2 \times 10^5$
AlN	~ 2.07 $\mu\text{m}$	$1.79 \times 10^{-4}$	3.266	600	350	0
Sapphire	~ 0.54 $\mu\text{m}$	$1.16 \times 10^{-5}$	3.980	875	35	0

*Table 4.1 Material properties used for thermal analysis of laser-lift-off on Al<sub>0.6</sub>Ga<sub>0.4</sub>N grown on AlN/sapphire [29,39,40].*

According to the epitaxial structure schematic shown in Fig. 4.2 (c), a 1.5- $\mu\text{m}$ -thick n-Al<sub>0.6</sub>Ga<sub>0.4</sub>N grown on 2.5  $\mu\text{m}$ -thick AlN on 430- $\mu\text{m}$ -thick sapphire with sample size after dicing of  $2 \times 3 \text{ mm}^2$  is used. A 1-D heat conduction model in COMSOL software was constructed and the temperature distribution of an Al<sub>0.6</sub>Ga<sub>0.4</sub>N thin film irradiated at the Al<sub>0.6</sub>Ga<sub>0.4</sub>N/AlN interface for a laser pulse incident energy density was simulated. The temperature-independent value for density  $\rho$ , heat capacity  $C_p$ , thermal conductivity  $k$ , reflection  $R$ , absorption  $\alpha$  of Al<sub>0.6</sub>Ga<sub>0.4</sub>N used in the finite element analysis calculations are shown in Table 4.1. It is assumed the ideal boundary condition (i.e. a constant temperature of 25°C) at the top surface of Al<sub>0.6</sub>Ga<sub>0.4</sub>N and the rest of boundary surfaces are thermal isolated. A single KrF excimer laser pulse irradiation at 600 mJ/cm<sup>2</sup> energy density and a pulse duration of 6 ns were employed to successfully lift off n-Al<sub>0.6</sub>Ga<sub>0.4</sub>N from AlN template for implementation of a transfer of an AlGa<sub>0.4</sub>N membrane onto a Si substrate. The interface was subjected to a 6 ns flat-top pulse profile to model the actual laser pulse with absorption of the irradiation occurring at the Al<sub>0.6</sub>Ga<sub>0.4</sub>N/AlN interface. The model in COMSOL calculated the temperature distribution every 0.1 ns from 0 ns up to an ending time of 50 ns. The laser pulse in flat-top profile started at 0 ns to 6 ns. As reported in the results of GaN in Chapter 2, the single pulse of 248 nm KrF laser has the energy density of approximately 400 mJ/cm<sup>2</sup> which was required to induce the surface decomposition temperature of GaN thin film (i.e. above 800°C). Due to

higher thermal decomposition temperature of  $\text{Al}_{0.6}\text{Ga}_{0.4}\text{N}$  than GaN, the incident laser pulse energy density required for LLO AlGaN is higher. The simulated results under the boundary conditions is shown below.

Fig. 4.9 presents the maximum temperature ( $T_{\text{AlGaN/AlN}}$ ) induced in the sample by an irradiation of a 6 ns KrF laser pulse at different energy density. A linear increase of the temperature with incident pulse energy density is revealed.

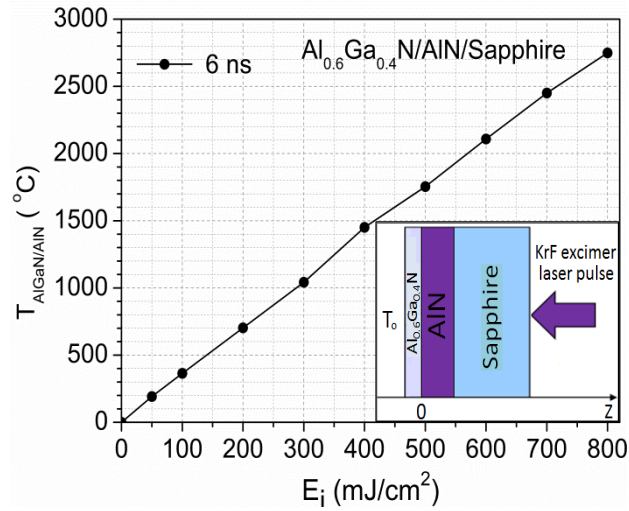


Figure 4.9 Simulated maximum temperature induced in  $\text{Al}_{0.6}\text{Ga}_{0.4}\text{N}/\text{AlN}/\text{sapphire}$  for a 6 ns KrF laser pulse at different energy density. Inset: schematic of 1-D laser induced heat conduction model with reference point  $z=0$  at  $\text{Al}_{0.6}\text{Ga}_{0.4}\text{N}/\text{AlN}$  interface.

The simulated temperature at different depth ( $z$ ) in the  $\text{Al}_{0.6}\text{Ga}_{0.4}\text{N}$  film from  $\text{Al}_{0.6}\text{Ga}_{0.4}\text{N}/\text{AlN}$  interface for the laser pulse at  $600 \text{ mJ/cm}^2$ , is shown in Fig. 4.10. The maximum temperature is induced at depth  $z = 60 \text{ nm}$  in the  $\text{Al}_{0.6}\text{Ga}_{0.4}\text{N}$  below the interface; however, it occurs at the GaN/sapphire interface ( $z = 0$ ) for LLO GaN/sapphire. It is due to the high thermal conductivity of AlN and the large thermal conductivity difference between  $\text{Al}_{0.6}\text{Ga}_{0.4}\text{N}$  and AlN. Similar to the LLO on GaN/sapphire described in section 2.14 of Chapter 2, the heating is produced in the laser pulse duration from 0 to 6 ns and the temperature induced exponentially decays with cooling time are illustrated for LLO  $\text{Al}_{0.6}\text{Ga}_{0.4}\text{N}/\text{AlN}$ , as shown in Fig. 4.10. A more detailed look of the temperature variation through the depth of  $\text{Al}_{0.6}\text{Ga}_{0.4}\text{N}/\text{AlN}/\text{sapphire}$  during the heating time, is presented for the time duration from 0 to 10 ns in Fig. 4.11.

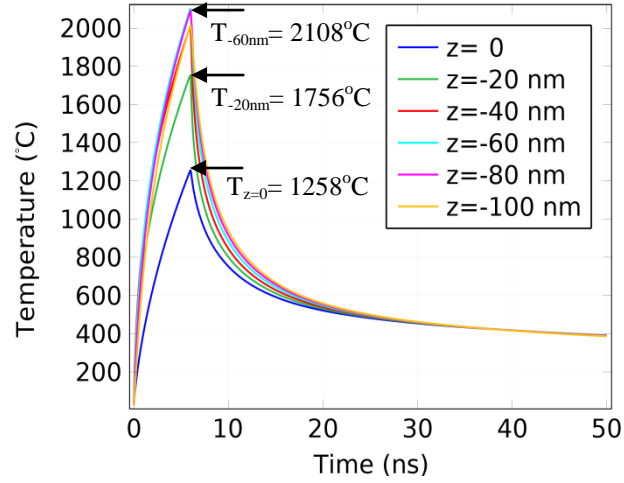


Figure 4.10 Simulated temperature in the  $\text{Al}_{0.6}\text{Ga}_{0.4}\text{N}$  film at different time ( $t$ ) from  $\text{Al}_{0.6}\text{Ga}_{0.4}\text{N}/\text{AlN}$  interface for a 6 ns KrF laser pulse, at energy density of  $600 \text{ mJ/cm}^2$ .

From Fig. 4.11, a dramatically temperature change is seen in the first 500 nm of  $\text{Al}_{0.6}\text{Ga}_{0.4}\text{N}$  film below the  $\text{AlGaN}/\text{AlN}$  interface and then diffused into AlN buffer and sapphire. The localized heat source in the sample is induced in the  $\text{Al}_{0.6}\text{Ga}_{0.4}\text{N}$  film and with its location moves slightly deeper inside the film, as the increase of heating time (e.g. from  $t = 2 \text{ ns}$  to  $6 \text{ ns}$ ).

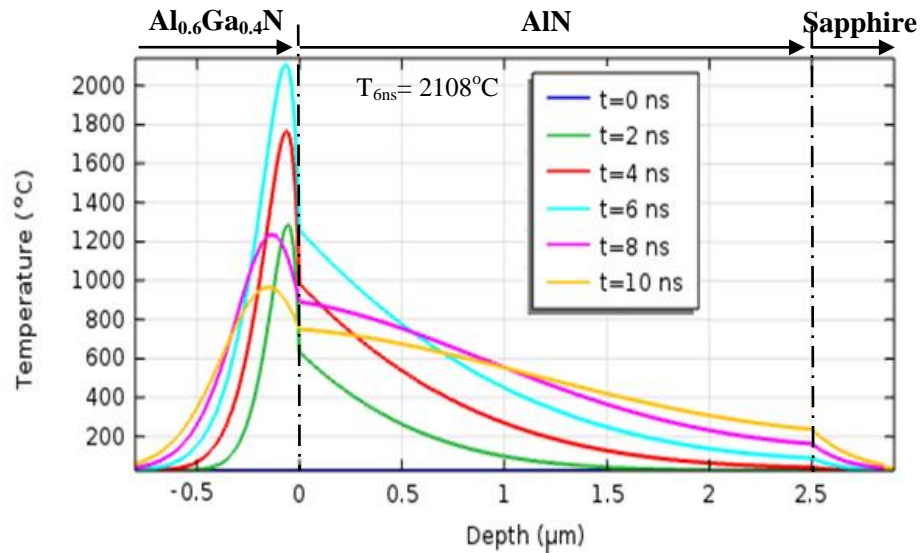


Figure 4.11 Simulated temperature at the  $\text{Al}_{0.6}\text{Ga}_{0.4}\text{N}/\text{AlN}$  interface v.s. depth ( $z$ ) for a 6 ns KrF laser pulse at energy density of  $600 \text{ mJ/cm}^2$ .

After 6 ns, the temperature starts to decrease and the heat induced diffuses into both  $\text{Al}_{0.6}\text{Ga}_{0.4}\text{N}$  and AlN. The overall temperature change can be demonstrated by time-resolved temperature distribution mapping shown in Fig. 4.12.

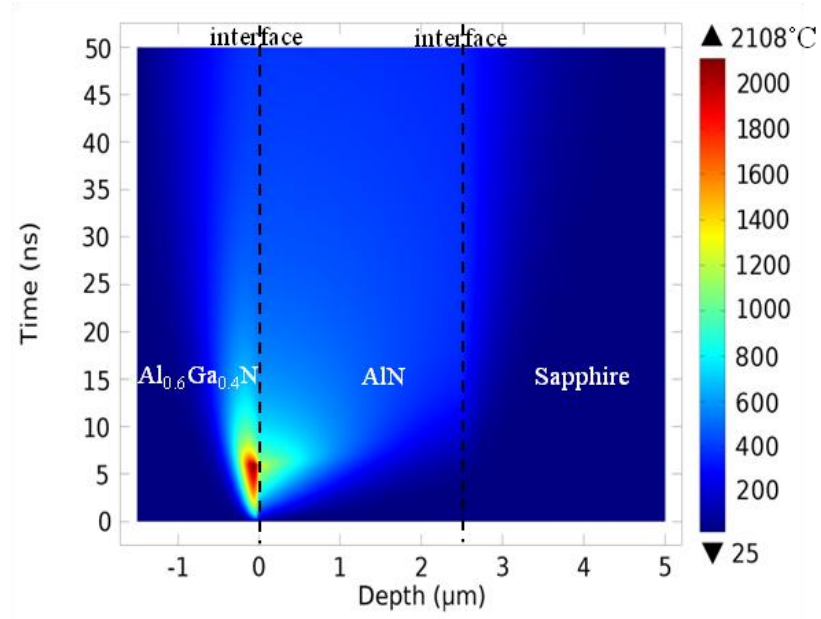


Figure 4.12 The temperature distribution of  $\text{Al}_{0.6}\text{Ga}_{0.4}\text{N}$  film irradiated at the  $\text{Al}_{0.6}\text{Ga}_{0.4}\text{N}/\text{AlN}$  interface for a 6 ns KrF laser pulse at energy density of  $600 \text{ mJ/cm}^2$ .

In Fig. 4.12, it was found that a highly localized heat region was originally generated at around 60 nm into the  $\text{Al}_{0.6}\text{Ga}_{0.4}\text{N}$  layer below the  $\text{AlGaIn}/\text{AlN}$  interface at the laser pulse duration time 6 ns. For  $600 \text{ mJ/cm}^2$  laser irradiation energy density, the maximum temperature generated in  $\text{Al}_{0.6}\text{Ga}_{0.4}\text{N}$  is  $2108^\circ\text{C}$  and the depth of heat transferred in the  $\text{AlGaIn}$  layer is less than  $1 \mu\text{m}$ , thus, the temperature at the depth of  $1 \mu\text{m}$  in  $\text{AlGaIn}$  below the interface is less than  $200^\circ\text{C}$ . The temperature at the  $\text{Al}_{0.6}\text{Ga}_{0.4}\text{N}/\text{AlN}$  interface is above the thermal decomposition temperature of GaN (i.e. above  $800^\circ\text{C}$ ) and higher than the growth temperature of AlN buffer layer studied here (i.e. above  $1100^\circ\text{C}$ ) [23, 41]. Temperature gradient across the thickness of the  $\text{AlGaIn}$  layer is smaller than the AlN layer, which is due to the large difference of the thermal conductivity of AlN related to  $\text{Al}_{0.6}\text{Ga}_{0.4}\text{N}$ . At the AlN/sapphire interface, due to the relatively higher thermal conductivity of AlN to sapphire, a weaker temperature gradient distributed in the sapphire. Therefore, a layer having a low thermal conductivity and being transparent to the laser light (e.g.  $\text{Al}_{0.8}\text{Ga}_{0.5}\text{N}$ ) can be added between the  $\text{AlGaIn}$  layer and AlN buffer layer to suppress diffusion of the heat generated in  $\text{AlGaIn}$  to AlN layer. It can result in even higher surface temperature at the  $\text{AlGaIn}/\text{AlN}$  interface; thus, a lower incident laser pulse energy density would be required for LLO  $\text{Al}_{0.6}\text{Ga}_{0.4}\text{N}$ .

### 4.3 Wafer bonding for AlGaIn and experiment

Direct bonding of the AlGaIn epitaxial layer itself or with coated-metal onto a carrier substrate is challenging, due to the surface roughness of the epitaxial layer (e.g.  $\sim 100$  nm), poor cleanliness at the bonding surface and optimized control of compression pressure. The use of transient-liquid phase to accommodate surface roughness by spreading laterally to fill voids has been shown to successfully bond ceramic materials for high temperature applications. According to the phase diagram of Au-Sn alloy [42], the eutectic AuSn alloy is 80%Au/20%Sn with the eutectic temperature of  $280^{\circ}\text{C}$  and starts to be reflowed at this temperature that permits bonding to a wide range of substrates. In this section, the eutectic reaction of AuSn binary system to Au layer as the bonding medium is briefly described. Relying on this bonding principle, a wafer bonding system was introduced to attach the AlGaIn wafer sample on Si substrate and a related AuSn reflow recipe was developed.

#### 4.3.1 Eutectic reaction of $\text{Au}_{0.8}\text{Sn}_{0.2}$ foil to Au layer

The eutectic reaction of  $\text{Au}_{0.8}\text{Sn}_{0.2}$  foil to Au layers coated on n-AlGaIn wafer sample and carrier substrate (e.g. Si substrate) was used for the wafer sample bonding. The minimum temperature required to reflow  $\text{Au}_{0.8}\text{Sn}_{0.2}$  soldering can be found in the Au-Sn alloy phase diagram

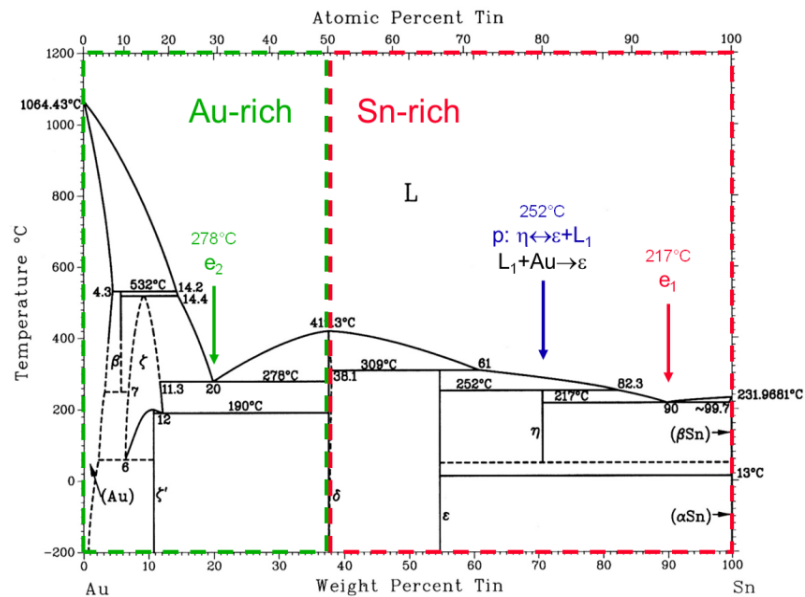


Figure 4.13 The phase diagram of Au-Sn alloy [42]

The phase diagram of Au-Sn is exhibited in Fig. 4.13, which depicts a complex combination of eutectic and peritectic systems. There are five intermediate phases:  $\zeta$  phase,  $\text{Au}_5\text{Sn}$ ,  $\text{AuSn}$ ,  $\text{AuSn}_2$ , and  $\text{AuSn}_4$ . The  $\zeta$  phase (hexagonal close-packed crystal structure) is homogeneous between 12% and 16% atomic percentage of Sn. The intermetallic compound  $\text{AuSn}$  has a very narrow range of solubility. The homogeneity range of  $\text{AuSn}_2$  and  $\text{AuSn}_4$  are also very narrow. The liquid phase is identified as L. The  $\text{L} \leftrightarrow [\zeta + \text{AuSn}]$  eutectic occurs at 278 °C with 29.5% atomic percentage of Sn. This is the most commonly used eutectic composition of 20 wt.% Sn and 80 wt.% Au. The  $\delta$  phase is determined as the  $\text{AuSn}$  intermetallic that has a melting point of 419.3°C. The homogeneity range extends from 50.0% to 50.5% atomic percentage of Sn. The  $\varepsilon$  phase is identified as the  $\text{AuSn}_2$  intermetallic compound. The temperature of the peritectic  $[\text{L} + \delta] \leftrightarrow \varepsilon$  reaction is 309°C, giving the liquid composition of about 72% atomic percentage of Sn. The homogeneity range of this phase is very narrow. The  $\eta$  phase is the  $\text{AuSn}_4$  compound. The temperature of the peritectic  $[\text{L} + \varepsilon] \leftrightarrow \eta$  reaction is 252°C, giving the liquid composition of about 88.5% atomic percentage of Sn. The  $\text{L} \leftrightarrow [\eta + \beta\text{Sn}]$  eutectic reaction occurs at 93.7% atomic percentage of Sn at 217°C, called as second eutectic reaction. Lastly, the allotropic temperature between two terminal solid solutions of ( $\beta$ -Sn) and ( $\alpha$ -Sn) is 13.05°C. The ( $\beta$ -Sn) solid solution has a solubility up to 0.2% atomic percentage of Au in  $\beta$ -Sn. The ( $\alpha$ -Sn) solid solution has a very limited solid solubility, that is, less than 0.006% atomic percentage of Au in  $\alpha$ -Sn [36].

#### 4.3.2 Wafer bonding system and laser lift-off experiment

The sample wafer-attached with Au-Sn soldering foil as bonding medium in thermal compression was used for bonding the AlGaIn wafer onto a Si substrate. The wafer-bonding process was performed using a fine flip-chip bonder as shown in Fig. 4.14, which is cable to provide a maximum bonding temperature of 400°C. The system is equipped with two resistive heaters (i.e. the top heater with bonding head and heat stage) and manually adjusted cantilever weight for mechanical pressure bonding. Wafer samples were attached with applied force of 25 N to join the Au layer coated Si substrate at 320°C. The temperatures of the two heaters were controlled by using the specific software with the wafer bonding system.



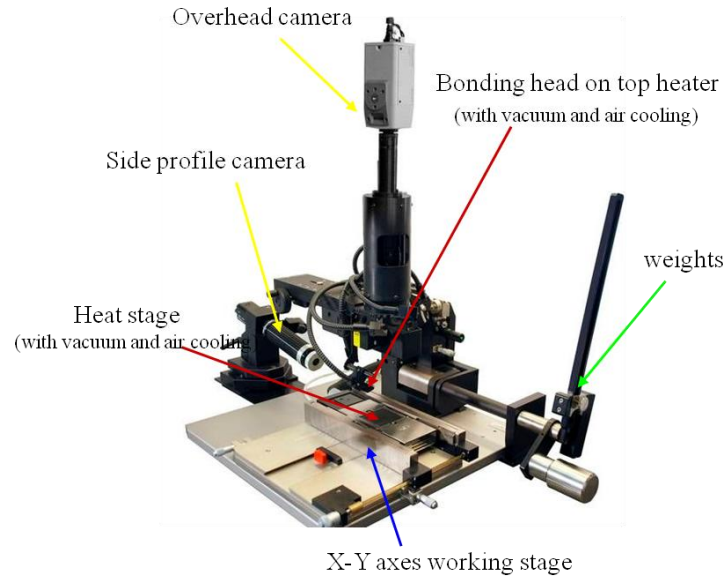


*Figure 4.14 Wafer-bonding system*

The metal Ti (20 nm)/Al (170 nm)/Ti (5 nm)/Au (100 nm) layer stack was initially deposited by e-beam evaporation on the AlGaIn thin film as a connecting layer. This metal stack is used as n-contact layer of n-AlGaIn on metal face. Ti/Au was deposited on a 500- $\mu\text{m}$ -thick Si carrier substrate as shown in Fig. 4.15 (a). Fig. 4.15 (b) shows the  $\text{Au}_{0.8}\text{Sn}_{0.2}$  soldering foil sheet in  $50 \times 9 \text{ mm}^2$ . The foil sheet is used to bond the sample and the substrate by the use of thermal compression. When it is heated up to the reflow temperature, the  $\text{Au}_{0.8}\text{Sn}_{0.2}$  reflows and reacts with Au layer deposited on the sample and the substrate. This 18- $\mu\text{m}$ -thick  $\text{Au}_{0.8}\text{Sn}_{0.2}$  soldering foil was cut to small pieces with a similar size as of the AlGaIn wafer sample, as seen in Fig. 4.16 and placed on the centre of the carrier substrate.

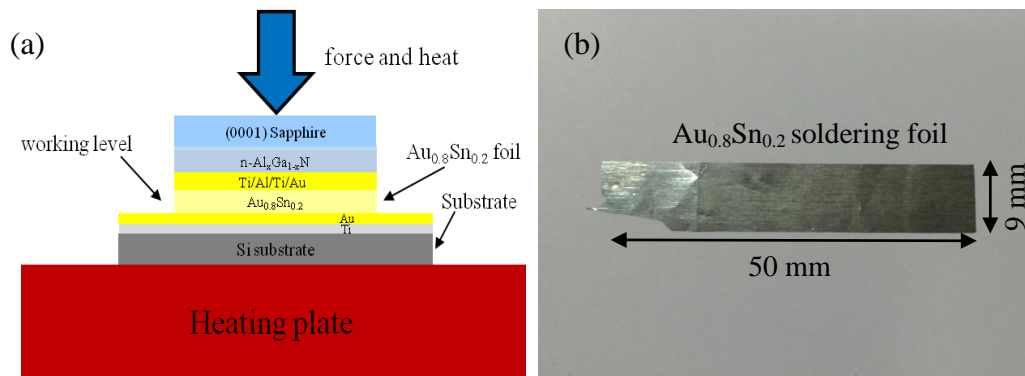


*Figure 4.15 (a) Schematic of bonding process for AlGaIn wafer onto Si substrate and (b)  $\text{Au}_{0.8}\text{Sn}_{0.2}$  soldering foil sheet.*

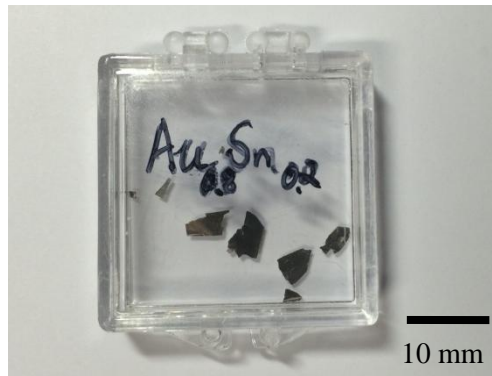


Figure 4.16  $Au_{0.8}Sn_{0.2}$  soldering foil pieces for test sample.

The Au-Sn reflow recipe developed is shown in the Fig. 4.17 below. The yellow line is the setting temperature profile; the green line is the temperature profile tracked from the bottom heater and the top heater. The peak annealing temperature is at 320 °C in the bell-shaped profile as shown in Fig. 4.17. The heating temperature of the bottom heater starts at 250 °C and sets 320 °C as the target temperature with temperature ramp of 20 °C/s, then stays at 320 °C for 30 s and the top heater was set at temperature 320 °C for 34 s. Afterwards, the system ramps down the temperature to 40 °C at rate of 20 °C/s.

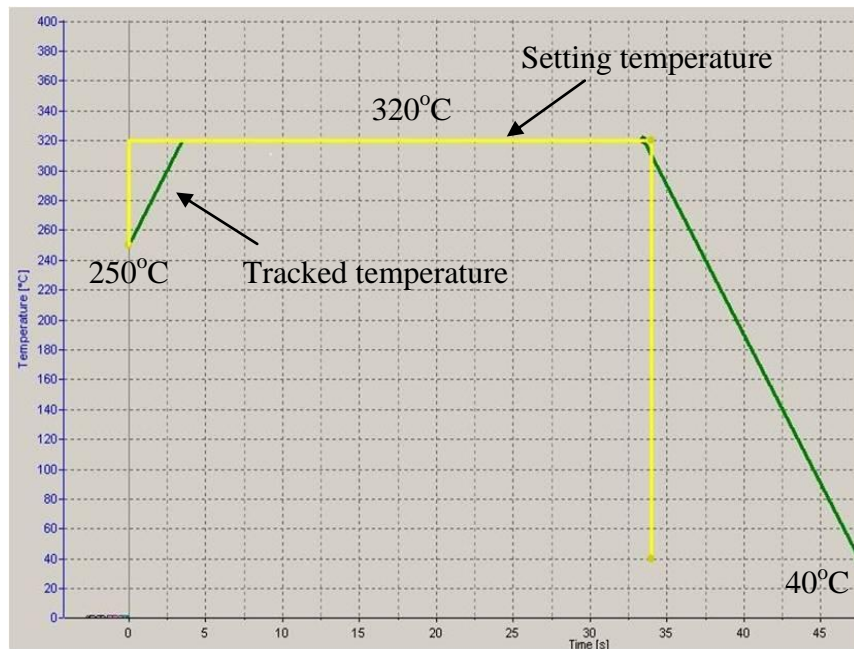
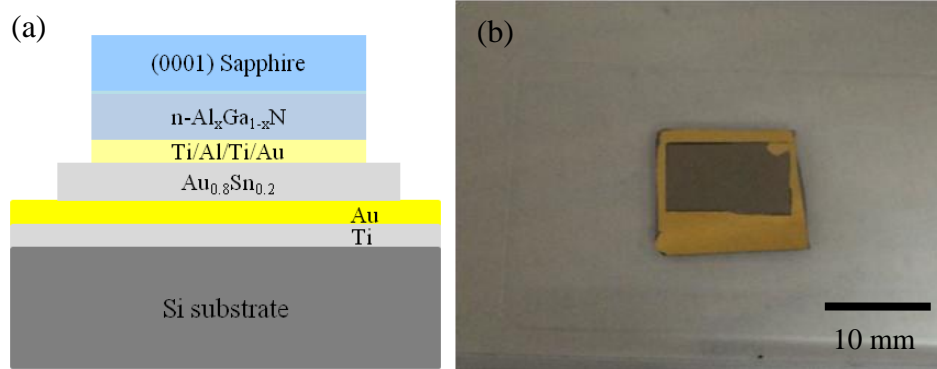


Figure 4.17 The temperature profile during the Au-Sn reflow. The yellow line is the setting temperature; the green line is the tracked temperature profile from the bottom heater and the top heater.



*Figure 4.18 (a) Schematic of an  $n\text{-Al}_{0.6}\text{Ga}_{0.4}\text{N}$  wafer sample after bonding and (b) Photograph of an  $n\text{-Al}_{0.6}\text{Ga}_{0.4}\text{N}$  wafer sample after bonding.*

In Fig. 4.18, it can be seen that an  $n\text{-Al}_{0.6}\text{Ga}_{0.4}\text{N}$  template ( $\sim 10 \times 5 \text{ mm}^2$ ) sample was flipped and successfully bonded on the Au coated Si substrate ( $\sim 16 \times 12 \text{ mm}^2$ ) with 25 N applied force on the back side of sapphire and annealed by using the temperature recipe as exhibited in Fig. 4.17. The bonded sample showed good adhesion to the Si substrate. Afterwards, LLO process was applied on the sample to remove the sapphire substrate at  $600 \text{ mJ/cm}^2$ . After LLO, the sample was dipped into diluted HCl solution (HCl: DI= 1:1) for 30s and then rinsed in DI water for 60s to clean the residue of metal droplets (i.e. metallic Ga, Al droplets) and then dry up with a  $\text{N}_2$  gas.

By the use of both wafer bonding and LLO, a  $1.5\text{-}\mu\text{m}$ -thick  $n\text{-Al}_{0.6}\text{Ga}_{0.4}\text{N}$  ( $10 \times 4 \text{ mm}^2$ ) was transferred on Si substrate. In order to study the electrical conduction behaviors of the metal on N-polar  $n\text{-Al}_{0.6}\text{Ga}_{0.4}\text{N}$  transferred on Si substrate, a metal stack in the form of circular transfer length method (c-TLM) patterns was deposited on the N-polar  $n\text{-Al}_{0.6}\text{Ga}_{0.4}\text{N}$  (shown in Fig. 4.19) after undergoing a standard photolithography. Ti/Al/Ti/Au is a metallization used as ohmic contact metal to metal-polar  $n\text{-AlGaIn}$ . Thus, as the initial test, the metal layers Ti/Al/Ti/Au were deposited on the N-polar surface by e-beam evaporator as n-metal without annealing, as seen in Fig. 4.19 (b).

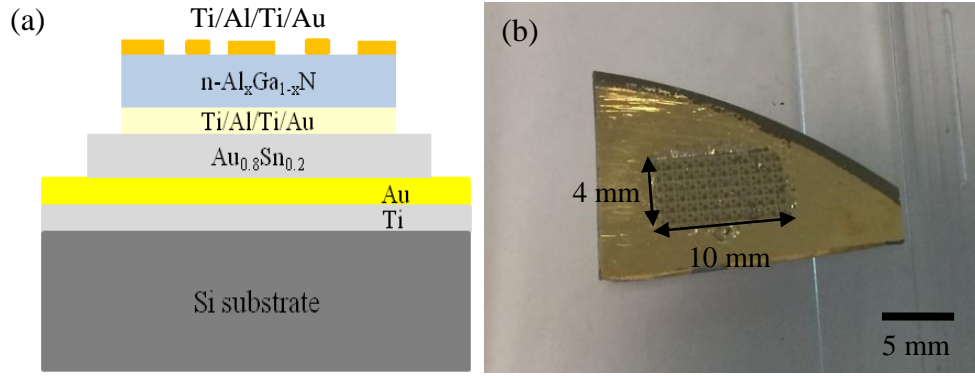


Figure 4.19 (a) Schematic of c-TLM patterns deposited on N-polar  $n\text{-Al}_{0.6}\text{Ga}_{0.4}\text{N}$  wafer sample bonded on Au coated Si substrate, (b) Photograph of c-TLM patterns deposited on N-polar  $n\text{-Al}_{0.6}\text{Ga}_{0.4}\text{N}$  layer.

The Nomarski image of c-TLM patterns deposited on N-polar  $n\text{-Al}_{0.6}\text{Ga}_{0.4}\text{N}$  created by LLO is shown in Fig. 4.20. The Ti(20 nm)/Al (170 nm)/Ti (15 nm)/Au (100 nm) c-TLM patterns with the internal disks of 50- $\mu\text{m}$ -diameter were deposited on the back surface of the  $n\text{-Al}_{0.6}\text{Ga}_{0.4}\text{N}$  and leave a circular space gap in diameters of 480  $\mu\text{m}$ , 280  $\mu\text{m}$ , 220  $\mu\text{m}$ , 140  $\mu\text{m}$  and 80  $\mu\text{m}$ . The measurement of I-V (current-voltage) characteristic from the c-TLM patterns will be described in the following section 4.4.3.

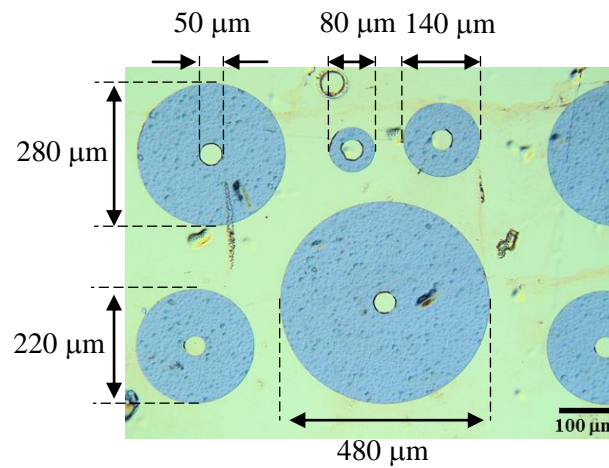


Figure 4.20 Optical microscope image of c-TLM patterns deposited on the N-polar  $n\text{-Al}_{0.6}\text{Ga}_{0.4}\text{N}$  wafer sample bonded on Au coated Si substrate.

## 4.4 Experimental characterizations

The 3 types of  $n\text{-Al}_x\text{Ga}_{1-x}\text{N}$  template with sacrificial layer shown in Fig. 4.2 were all demonstrated to be able to be LLO. Optical microscope images on the surfaces created by LLO are presented and the XRD  $\omega$ - $2\theta$  scans of the  $n\text{-AlGaIn}$  templates are shown to exhibit successful removed of the AlN/sapphire substrate at the  $n\text{-AlGaIn}/\text{AlN}$  interface. The current-voltage (I-V) characteristic of as-deposited Ti/Al/Ti/Au metal contact on N-face  $n\text{-Al}_{0.6}\text{Ga}_{0.4}\text{N}$  transferred onto Si substrate is reported.

### 4.4.1 Surface morphology of AlGaIn membranes after LLO

The  $n\text{-AlGaIn}$  structures were examined as promising candidates for a substrate lift-off structure. Nomarski images of all these 3 types of  $n\text{-AlGaIn}$  structure samples reveal successful LLO on the AlGaIn layers. Due to the stronger laser pulse absorption of GaN related to AlGaIn, a single pulse of  $500 \text{ mJ/cm}^2$  was applied to process sample #A, while  $600 \text{ mJ/cm}^2$  was used for both samples #B and #C. The sample #A has a thin GaN interlayer, both samples #B and #C only have AlGaIn layers.

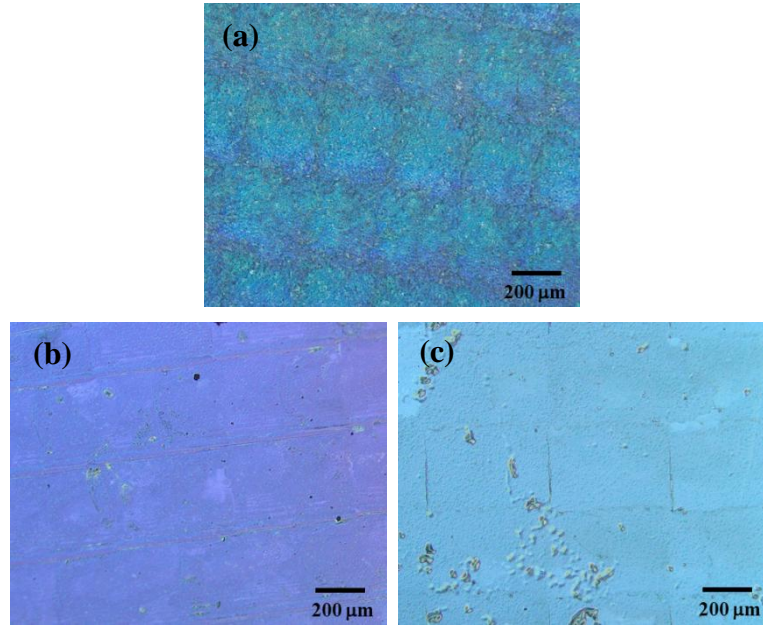


*Figure 4.21 (a) Transferred GaN interlayer/ $n\text{-Al}_{0.5}\text{Ga}_{0.5}\text{N}$  thin film by LLO on a Si substrate with a single laser pulse energy density of  $500 \text{ mJ/cm}^2$ , (b) transferred  $n\text{-Al}_{0.5}\text{Ga}_{0.5}\text{N}/n\text{-Al}_{0.75}\text{Ga}_{0.25}\text{N}$  thin film by LLO on a Si substrate at  $600 \text{ mJ/cm}^2$  and (c) transferred  $n\text{-Al}_{0.6}\text{Ga}_{0.4}\text{N}$  thin film by LLO on a Si substrate at  $600 \text{ mJ/cm}^2$ .*

After the LLO, it was found that no micro-cracking or buckling was formed on all samples as seen in Fig. 4.21. Meanwhile, it was also seen that the periodic rectangular patterns were presented on the laser irradiated surface on the GaN interlayer in sample #A, n-Al<sub>0.5</sub>Ga<sub>0.5</sub>N in sample #B and n-Al<sub>0.6</sub>Ga<sub>0.4</sub>N in sample #C. These patterns were produced by the laser pulse irradiation through the sapphire scanning across the whole area of the samples. However, as seen in Fig. 4.21 (c), several localized delaminated points were observed on the n-Al<sub>0.6</sub>Ga<sub>0.4</sub>N layer, which may be due to the weaker adhesion between the metal-polar n-AlGaN surface and the Ti/Al/Ti/Au layer. It might be caused by contamination (e.g. dust, organic residues) on a poorly cleaned surface (i.e. metal-polar) of the n-AlGaN before the deposition of Ti/Al/Ti/Au.

#### 4.4.2 X-ray diffraction scan intensity of layer structure after LLO

The  $\omega$ -2 $\theta$  scans of the n-AlGaN templates were measured by x-ray diffraction (XRD) to compare before LLO (as-grown) and after LLO. Fig. 4.22 shows the 2 $\theta$  scans of the n-Al<sub>0.5</sub>Ga<sub>0.5</sub>N layer with GaN interlayer grown on sapphire before and after LLO. Additionally, the GaN interlayer was fully removed after the sample was being dipped in NaOH solution (NaOH: DI=1:1) for 45s while the Al<sub>0.5</sub>Ga<sub>0.5</sub>N layer was remained.

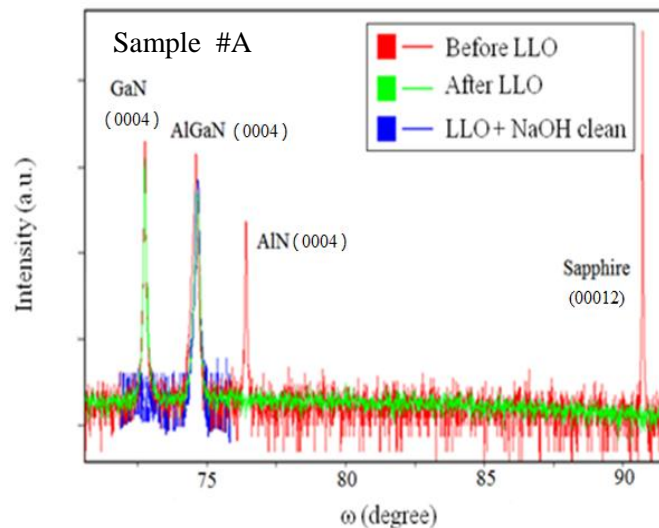


Figure 4.22 XRD 2 $\theta$  scan of (red plot) an as-grown n-Al<sub>0.6</sub>Ga<sub>0.4</sub>N sample, (green plot) an as-grown sample after LLO, and (blue plot) the sample after LLO with NaOH clean.



In Fig. 4.23, the  $n\text{-Al}_{0.6}\text{Ga}_{0.4}\text{N}$  layer on AlN/sapphire is 15% - 20% strained [24]. The  $\omega$ - $2\theta$  scans of the  $n\text{-Al}_{0.6}\text{Ga}_{0.4}\text{N}$  template in (0002) crystal plane as-grown sample (i.e. before LLO), as-deposited Ti/Al/Ti/Au bonding layers on as-grown sample and after LLO were measured. Compared with the XRD scan before LLO and after LLO, no presence of sapphire on the XRD scan after LLO was observed, however, a relatively weak (i.e. 4 orders of magnitude less) reflection of AlN still remained after LLO, which may indicate that a small amount of AlN residuals was presented on the laser irradiated surface on  $n\text{-Al}_{0.6}\text{Ga}_{0.4}\text{N}$  layer.

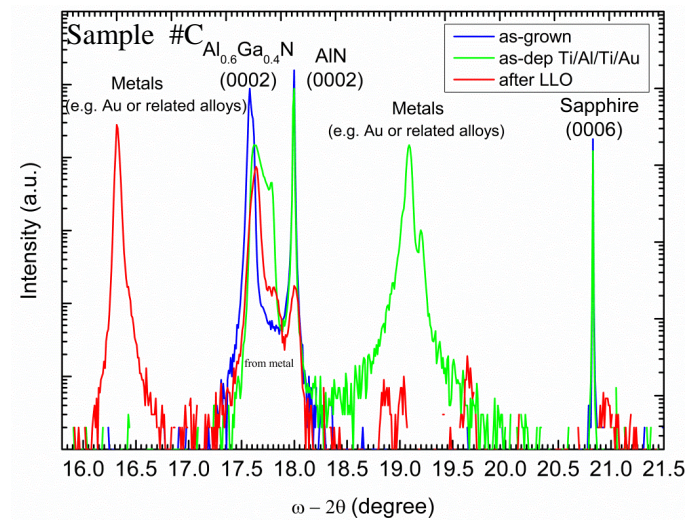


Figure 4.23 XRD  $\omega$ - $2\theta$  scans (blue plot) of an as-grown  $n\text{-Al}_{0.6}\text{Ga}_{0.4}\text{N}$  sample of, (green plot) an as-deposited Ti/Al/Ti/Au on the as-grown sample and (red plot) the sample after LLO.

#### 4.4.3 I-V characteristics of metal contact on N-face $n\text{-AlGaN}$

The quality of the  $n\text{-Al}_{0.6}\text{Ga}_{0.4}\text{N}$  should be known before any process, especially the electrical properties of the  $n\text{-Al}_{0.6}\text{Ga}_{0.4}\text{N}$  is vital for I-V characteristics on metal-polar  $n\text{-AlGaN}$  contacts. The metal contact of Ti/Al/Ti/Au was deposited on the metal-polar surface of an  $1 \times 1 \text{ cm}^2$   $n\text{-Al}_{0.6}\text{Ga}_{0.4}\text{N}$  wafer sample. Schottky behaviour of the metal contacts was presented on this as-deposited metal contact. Then, the metal contact on metal-polar of  $n\text{-Al}_{0.6}\text{Ga}_{0.4}\text{N}$  was annealed at  $850^\circ\text{C}$  in  $\text{N}_2$ . The Hall measurement was carried on the annealed metal contact of Ti/Al/Ti/Au. An ohmic behaviour to metal-polar  $n\text{-Al}_{0.6}\text{Ga}_{0.4}\text{N}$  was achieved, as seen in Fig. 4.24. The  $n$ -

$\text{Al}_{0.6}\text{Ga}_{0.4}\text{N}$  has the carrier concentration of  $9.5 \times 10^{18}/\text{cm}^3$ , hall mobility  $40.5 \text{ cm}^2/\text{Vs}$ , the resistivity of  $1.62 \times 10^{-2} \Omega \text{ cm}$ ,  $\rho_{\text{sheet}}$  (sheet resistivity) of  $1.08 \Omega/\square$ .

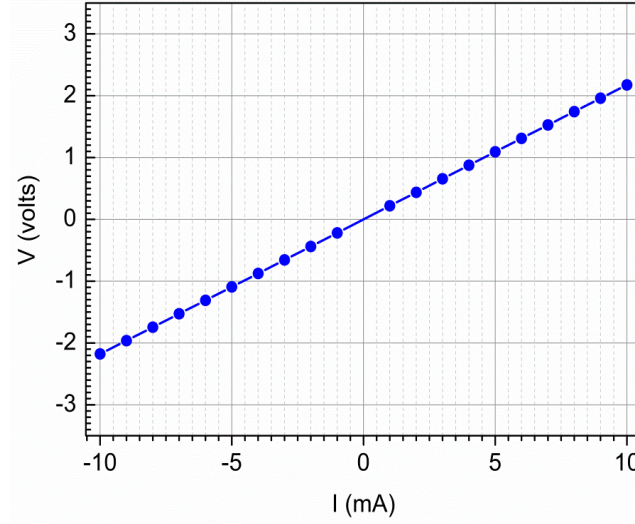


Figure 4.24 I-V characteristics of Ti/Al/Ti/Au contact to metal-polar  $n\text{-Al}_{0.6}\text{Ga}_{0.4}\text{N}$  template. The contacts were annealed at  $850^\circ\text{C}$  in  $\text{N}_2$ .

The  $n\text{-Al}_{0.6}\text{Ga}_{0.4}\text{N}$  membrane attached onto Si substrate was fabricated and described in section 4.3. The I-V measurement of the as-deposited Ti/Al/Ti/Au metal contacts on N-face  $n\text{-Al}_{0.6}\text{Ga}_{0.4}\text{N}$  was demonstrated in Fig. 4.25.

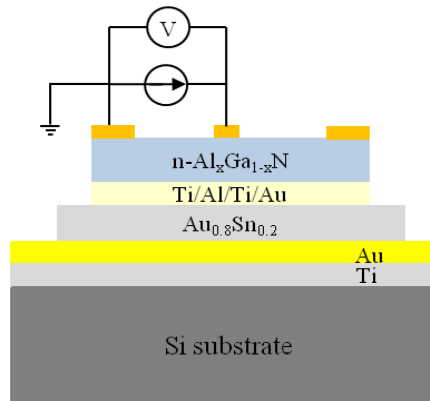
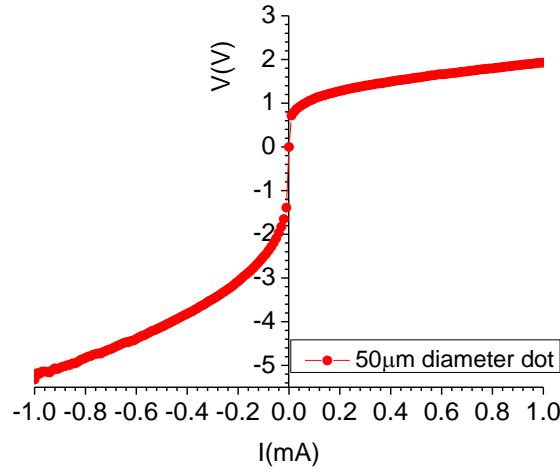


Figure 4.25 Schematic of I-V characterization on the metal contacts of N-polar  $\text{AlGaN}$ .



The I-V data collected are plotted in Fig. 4.25.



*Figure 4.26 I-V characteristics of the as-deposited Ti/Al/Ti/Au metal contacts to N-polar  $n\text{-Al}_{0.6}\text{Ga}_{0.4}\text{N}$*

Fig. 4.26 shows a Schottky contact behaviour of as-deposited Ti/Al/Ti/Au contacts on the N-face  $n\text{-Al}_{0.6}\text{Ga}_{0.4}\text{N}$  layer created by LLO, when probed at a 50- $\mu\text{m}$ -diameter metal dot to the surrounding metal in the current range from -1 mA to 1 mA with an increment of 1  $\mu\text{A}$ . This poor electrical behaviour of the metal contacts to N-face  $n\text{-Al}_{0.6}\text{Ga}_{0.4}\text{N}$  may be due to the AlN residuals, non optimized metallization metal contacts. It is noted that Ti/Al/Ti/Au alloys have been annealed at 850°C to achieve ohmic contacts on the metal-polar surface, while the Ti/Al/Ti/Au contacts on N-face  $n\text{-Al}_{0.6}\text{Ga}_{0.4}\text{N}$  have not been annealed. This is because the AuSn bonding layer can not stand for a temperature such high annealing temperature [43], and the metal contact of  $n\text{-Al}_{0.6}\text{Ga}_{0.4}\text{N}$  might be ohmic after annealing, therefore, further contact optimization is required.

## 4.5 Conclusions

Three types of AlGaN templates were proposed as the candidates for the epitaxial structure of DUV LEDs that contain an LLO sacrificial layer for the fabrication of vertical conduction thin film DUV LEDs. However, the templates without GaN interlayer (i.e. Sample #B consisting of an  $n\text{-Al}_{0.75}\text{Ga}_{0.25}\text{N}$  layer with a thin  $n\text{-Al}_{0.5}\text{Ga}_{0.5}\text{N}$  interlayer, while only an  $n\text{-Al}_{0.6}\text{Ga}_{0.4}\text{N}$  single layer is grown on sample #C) were recommended. Both the absorption and transmittance spectrum of

n-Al<sub>0.6</sub>Ga<sub>0.4</sub>N confirmed n-Al<sub>0.6</sub>Ga<sub>0.4</sub>N is near the 248-nm KrF laser irradiation absorption edge, thus, the maximum Al fraction of AlGa<sub>N</sub> that the LLO system can successfully process is 60%. Moreover, the 1-D temperature distribution at the Al<sub>0.6</sub>Ga<sub>0.4</sub>N/AlN interface of the sample was simulated for a single pulse energy density of 600 mJ/cm<sup>2</sup>. To verify this energy density, the successful LLO experiments on n-Al<sub>0.6</sub>Ga<sub>0.4</sub>N were applied. It found the maximum temperature induced by a laser pulse is at 60-nm-depth into Al<sub>0.6</sub>Ga<sub>0.4</sub>N film from the Al<sub>0.6</sub>Ga<sub>0.4</sub>N/AlN interface. With the aid of Au-Sn soldering bonding, the n-Al<sub>0.6</sub>Ga<sub>0.4</sub>N template was bonded on Si substrate for LLO. A vertical conduction n-Al<sub>0.6</sub>Ga<sub>0.4</sub>N thin film membrane was successfully fabricated by the wafer bonding process and the LLO on AlGa<sub>N</sub>/AlN template. Normaski images and XRD scans of the AlGa<sub>N</sub> templates showed before and after sapphire removal to assess the LLO process and its effect on the device performance. An initial test of electrical behavior of as-deposited Ti/Al/Ti/Au on N-face n-Al<sub>0.6</sub>Ga<sub>0.4</sub>N created by LLO was reported, but a Schottky contact behaviour was presented on the N-face n-metal contact. Therefore, in order to achieve vertical conduction DUVLEDs with lower forward voltage and less joule heating, new metallization scheme for an Ohmic contact to N-face n-AlGa<sub>N</sub> is desirable and should be investigated in future work.

## 4.6 References

- [1] A. J. Fischer, A. A. Allerman, M. H. Crawford et al., "Room-temperature direct current operation of 290 nm light-emitting diodes with milliwatt power level," *Appl. Phys. Lett.*, vol. 84, no. 17, pp. 3394, Apr. 2004.
- [2] K. H. Kim, Z. Y. Fan, M. Khizar, M. L. Nakarmi, J. Y. Lin, and H. X. Jiang, "AlGa<sub>N</sub>-based ultraviolet light-emitting diodes grown on AlN epilayers," *Appl. Phys. Letts.*, vol. 85, no. 20, pp. 4777, Nov. 2004.
- [3] H. Hirayama, T. Yatabe, N. Noguchi, T. Ohashi, and N. Kamata, "231–261 nm AlGa<sub>N</sub> deep-ultraviolet lightemitting diodes fabricated on AlN multilayer buffers grown by ammonia pulse-flow method on sapphire," *Appl. Phys. Lett.*, vol. 91, no. 7, pp. 071901-3, Aug. 2007.
- [4] T. Wang, K. B. Lee, J. Bai, P. J. Parbrook et al, "The 310-340 nm ultraviolet light emitting diodes grown using a thin Ga<sub>N</sub> interlayer on a high temperature AlN buffer," *J. Phys. D: Appl. Phys.*, vol. 41, no. 9, pp.094003, Apr. 2008.
- [5] H. Hirayama, S. Fujikawa, N. Noguchi, J. Norimatsu, T. Takano, K. Tsubaki and N. Kamata, "222-282 nm AlGa<sub>N</sub> and InAlGa<sub>N</sub>-based deep-UV LEDs fabricated on

high-quality AlN on sapphire,” *Phys. Stat. Sol. A.*, vol. 206, no. 6, pp. 1176-1182, Mar. 2009.

[6] H. Hirayama, N. Maeda, S. Fujikawa, S. Toyoda and N. Kamata, “Recent progress and future prospects of AlGa<sub>N</sub> based high efficiency deep-ultraviolet light-emitting diodes,” *Jpn. J. Appl. Phys.*, vol. 53, no. 10, pp. 100209, Sept. 2014.

[7] M. A. Khan, V. Adivarahan, J. P. Zhang, C. Chen, E. Kuokstis, A. Chitnis, M. Shatalov, J. W. Yang, and G. Simin “Strip geometry Ultraviolet Light Emitting Diodes at 305 nm using quaternary AlInGa<sub>N</sub> multiple quantum wells,” *J. Jpn. Appl. Phys.*, vol. 40, no. 12A, pp. L1308-L1310, Dec. 2001.

[8] K. Kawasaki, C. Koike, Y. Aoyagi and M. Takeuchi, “Vertical AlGa<sub>N</sub> deep ultraviolet light emitting diode emitting at 322 nm fabricated by the laser lift-off technique,” *Appl. Phys. Lett.*, vol. 89, no. 26, pp. 261114, Dec. 2006.

[9] L. Zhou, “Vertical injection thin-film AlGa<sub>N</sub>/AlGa<sub>N</sub> multiple-quantum-well deep ultraviolet light-emitting diodes,” *Appl. Phys. Lett.*, vol. 89, no. 24, pp. 241113-3, Dec. 2006.

[10] Y. Kida, T. Shibata, H. Naoi, H. Miyake, K. Hiramatsu, and M. Tanaka, “Growth of Crack-free and high-quality AlGa<sub>N</sub> with Al content using epitaxial AlN (0001) Films on Sapphire,” *Phys. Stat. Sol. (a)*, vol. 194, no. 2, pp. 498-501, Oct. 2002.

[11] Q. Sun, J. Wang, H. Wang, R. Jin, D. Jiang “High temperature AlN interlayer for crack-free AlGa<sub>N</sub> growth on Ga<sub>N</sub>,” *J. Appl. Phys.*, vol. 104, no. 4, pp. 043516, Aug. 2008.

[12] J. Kotani, S. Tomabechi, . Miyajima, N. Nakkamura, T. Kikkawa, K. Watanabe, and K. Imanishi, “Tensile strain-induced formation of micro-cracks for AlGa<sub>N</sub> Ga<sub>N</sub> heterostructures,” *Phys. Stat. Sol. C.*, vol. 10, No. 5, pp. 808-811, Feb. 2013.

[13] V. Adivarahan, S. Wu, J. P. Zhang, A. Chitnis, M. Shatalov, V. Mandavilli, R. Gaska, and M. A. Khan, “High-efficiency 269 nm emission deep ultraviolet light emitting diodes,” *Appl. Phys. Lett.*, vol. 84, no. 23, pp. 4726-4764, Jun. 2004.

[14] T. M. Katona, T. Margalith, C. Moe, M. C. Schmidt, S. Nakamura, J. S. Speck, S. P. DenBaars, “Growth and fabrication of short-wavelength UV LEDs,” *Proc. SPIE*, vol. 5187, pp. 250-259, Jan. 2004.

[15] A. Hanlon, P. M. Pattison, J. F. Kaeding, R. Sharma, P. Fini, and S. Nakamura, “292 nm AlGa<sub>N</sub> Single-Quantum Well Light Emitting Diodes Grown on Transparent AlN Base,” *Jpn. J. Appl. Phys.*, vol. 42, no. 6B, pp. L628, Jun. 2003.

[16] M. L. Reed, M. Wraback, A. Lunev, Y. Bilenko, X. Hu, A. Sattu, J. Deng, M. Shatalov, and R. Gaska, “Device self-heating effects in deep UV LEDs studied by systematic variation in pulsed current injection,” *Phys. stat. soli. (c)*, vol. 5, no. 6, pp. 2053-2055, Mar. 2008.

[17] V. Adivarahan, A. Heidari, B. Zhang, Q. Fareed, M. Islam, S. Hwang, K. Balakrishnan and A. Khan, “Vertical injection thin film deep ultraviolet light

emitting diodes with AlGa<sub>N</sub> multiple-quantum wells active region,” *Appl. Phys. Express*, vol. 2, no. 9, pp. 2102-2102-3, Sep. 2009.

[18] M. Takeuchi, T. Maegawa, H Shimizu, S. Ooishi, T Ohtsuka, and Y Aoyagi, “AlN/AlGa<sub>N</sub> short-period superlattice sacrificial layers in laser lift-off for vertical-type AlGa<sub>N</sub>-based deep ultraviolet light emitting diodes, *Appl. Phys. Lett.*, vol. 94, no. 6, pp. 061117, Feb. 2009.

[19] M. Iwaya, S. Terao, N. Hayashi, T. Kashima, H. Amano, and I. Akasaki, “Realization of crack-free and high-quality thick Al<sub>x</sub>Ga<sub>1-x</sub>N for UV optoelectronics using low-temperature interlayer,” *Appl. Surf. Sci.*, vol. 159-160, pp. 405-413, Jun. 2000.

[20] <https://en.wikipedia.org/wiki/Gallium>

[21] J. F. Kaeding, Y. Wu, T. Fujii, R. Sharma, P. T. Fini, J. S. Speck, and S. Nakamura, “Growth and laser-assisted liftoff of low dislocation density AlN thin films for deep-UV light emitting diodes,” *J. Cryst. Growth*, vol. 272, pp. 257-263, no. 1-4, Dec. 2004.

[22] <https://en.wikipedia.org/wiki/Aluminium>

[23] H. Li, T. C. Sadler, and P. J. Parbrook, “AlN heteroepitaxy on sapphire by metalorganic vapour phase epitaxy using low temperature nucleation layers,” *J. Cryst. Growth*, vol. 383, pp. 72-78, Nov. 2013.

[24] D. V. Dinh, P. Pampili, P. J. Parbrook, “Silicon doping of semipolar (11-22) Al<sub>x</sub>Ga<sub>1-x</sub>N ( $0.50 \leq x \leq 0.55$ ),” *J. Cryst. Growth*, vol. 451, no. 181, pp. 1-9, Jul. 2016.

[25] M. Jayasakthi, S. Juillaguet, H. Peyre, L. Konczewicz, K Baskar, S. Contreras, “Influence of AlN thickness on AlGa<sub>N</sub> epilayer grown by MOCVD,” *Superlattices and Microstructure*, vol. 98, no. 5, pp. 515-521, Aug. 2016.

[26] W. Shan, J. W. Ager III, K. M. Yu, and W. Walukiewicz, “Dependence of the fundamental band gap of Al<sub>x</sub>Ga<sub>1-x</sub>N on alloy composition and pressure,” *J. Appl. Phys.*, vol. 85, no. 12, Jun. 1999.

[27] <http://www.analiticaweb.com.br/newsletter/03/AN51170.pdf>

[28] W. Liu and A. A. Balandin, “Thermal conduction in Al<sub>x</sub>Ga<sub>1-x</sub>N alloys and thin films,” *J. Appl. Phys.*, vol. 97, no. 073710, pp. 1-5, Mar. 2005.

[29] Stanislav Vitanov, “Simulation of High Electron Mobility Transistors,” PhD dissertation, 2010.

[30] S. Adachi, “Lattice thermal conductivity of group-IV and III-V semiconductor alloys,” *J. Appl. Phys.*, vol. 102, no. 6, pp. 063502, Sep. 2007.

[31] B. Abeles, “Lattice thermal conductivity of disordered semiconductor alloy at high temperatures,” *Phys. Rev.*, vol. 131, no. 5, pp. 1906-1911, Sep. 1963.

[32] V. Palankovski, R. Schultheis, and S. Selberherr, “Simulation of power heterojunction bipolar transistors on gallium arsenide,” *IEEE Trans. Electron Devices*, vol. 48, no. 6, pp. 1264-1269, Jun. 2001.

- [33] A. Jacquot, B. Lenoir, A. Dauscher, P. Verardi, F. Cracium, M. Stolzer, M. Gartner, and N. Dinescu, "Optical and thermal characterization of AlN thin films deposited by pulsed laser deposition," *Applied Surface science*, vol. 186, no. 1-4, pp. 507-512, Jan. 2002.
- [34] G. Slack, R. Tanzilli, R. Pohl, and J. Vandersande, "The intrinsic thermal conductivity of AlN," *J. Phys. Chem. Solids*, vol. 48, no. 7, pp. 641-647, Jan. 1988.
- [35] G. Slack, L. Schowalter, D. Morelli, and J. Freitas, "Some effects of oxygen impurities on AlN and GaN," *J. Cryst. Growth*, vol. 246, no. 3-4, pp. 287-298, Dec. 2002.
- [36] B. Daly, H. Maris, A. Nurmikko, M. Kuball, and J. Han, "Optical pump-and-probe measurement of the thermal conductivity of nitride thin films," *J. Appl. Phys.*, vol. 92, no. 7, pp. 3820-3824, Apr. 2002.
- [37] W. Liu, A. A. Balandin, "Temperature dependance of thermal conductivity of AlGaIn thin films measured by the differential  $3\omega$  technique," *Appl. Phys. Lett.*, vol. 85, no. 22, pp. 5230-5232, Nov. 2004.
- [38] [https://en.wikipedia.org/wiki/Vegard's\\_law](https://en.wikipedia.org/wiki/Vegard's_law)
- [39] <http://www.ioffe.ru/SVA/NSM/Semicond/AlN/index.html>
- [40] O. Knacke, O. Kubaschewski, and K Hesselmann, "Thermochemical Properties of Inorganic Substances," (Springer Verlag, Berlin, 1991).
- [41] B. Poti, M. A. Tagliente, A. Passaseo, "High quality MOCVD GaN film grown on sapphire substrates using HT-AlN buffer layer," *J. Non-Cryst. Solids*, vol. 352, no. 23-25, pp. 2332-2334, Jul. 2006.
- [42] J. S. Kim, W. S. Choi, D. Kim, A. Shkel, C. C. Lee, "Fluxless silicon-to-alumina bonding using electroplated Au-Sn-Au structure at eutectic composition," *Materials Science and Engineering A*, vol. 458, pp. 101-107, Dec. 2006.
- [43] T. T. Seng, D. Sun, H. K. Koay, M. F. Sabudin, J. Thompson, "Characterization of Au-Sn eutectic die attach process for optoelectronics device," *International Symposium on Electronics Materials and Packaging*, pp. 118-124, Dec. 2005.

## Chapter 5

### Thermal modeling of transfer-bonder GaAs laser diode

In this chapter, the substrate-removal of a 3- $\mu\text{m}$ -wide-ridge AlGaAs/GaAs multiple-quantum well (MQW) edge-emitting laser diode (LD) that was fabricated in Tyndall National Institute is introduced. Two-dimensional (2-D) temperature distribution of the LD transfer-bonded to submounts with different thermal conductivities (e.g. GaAs, Alumina, Si) were simulated in finite element analysis (FEA) by the use of a commercial FEA software, COMSOL Multiphysics 5.0. The thermal resistance,  $R_{th}$ , was compared with a simplified steady-state analytic expression. The effects of laser cavity length, thickness of dielectric passivation layer, contact metal layer thickness and submount material were investigated in order to reduce the thermal resistance of the laser when referenced to LDs with a native GaAs substrate. The simulations show the importance of reducing the GaAs substrate thickness especially for short cavity lengths. The  $R_{th}$  of a 200- $\mu\text{m}$ -long LD with the substrate fully removed is 37.5 K/W, compared with 230 K/W for a 200- $\mu\text{m}$ -long LD with a 100- $\mu\text{m}$ -thick GaAs substrate. Increased p-contact metal thickness and reduced dielectric layer thickness further reduce  $R_{th}$ . The simulated 2-D temperature distributions of the LD without substrate transfer-bonded on 10- $\mu\text{m}$ -thick submount of alumina, GaAs, silicon were compared, which indicated the silicon submount above a perfect heat sink provided an acceptable low  $R_{th}$ .

#### 5.1 Introduction

While infra-red semiconductor laser diodes (LDs) are widely used in many diverse applications there is a new range of opportunities set by the need to co-integrate the LD with functional substrates. Examples include the integration of LDs with silicon-on-insulator waveguiding platform as a means of realising low-cost, energy-efficient transceivers in high-bandwidth, short-reach interconnects for data centres and supercomputers. LDs are required for high density heat assisted magnetic recording and directly integrating the device within the read-write head would simplify the packaging requirements and ease scaling to very large volume. There is also a target to integrate LDs onto polymer [1], glass and ceramic substrates to support

applications such as photonic integrated circuits, flexible, large-scale integrated electronics [2, 3], wearable electronics and for conformal bio-compatible sensors [4, 5]. In some of these applications, there is a requirement to remove the native growth substrate due to limited space. Such substrate removed devices can be realized using micro-transfer-printing [2]. The transfer-bonded thin film LD can also be realized by die or wafer bonding followed by removal of the growth substrate which can then be recycled. As an example shown in Fig. 5.1, the microscope images show the GaAs based ridge waveguide lasers were separated from GaAs grown substrate (Fig. 5.1(a)) and one of the laser device was picked up to transfer-bonded on a magnetic-recording read-write head transducer (Fig. 5.1(b)) as the light delivery source for next generation heat-assistant magnetic recording (HAMR) high data capacity storage hard drive [2].

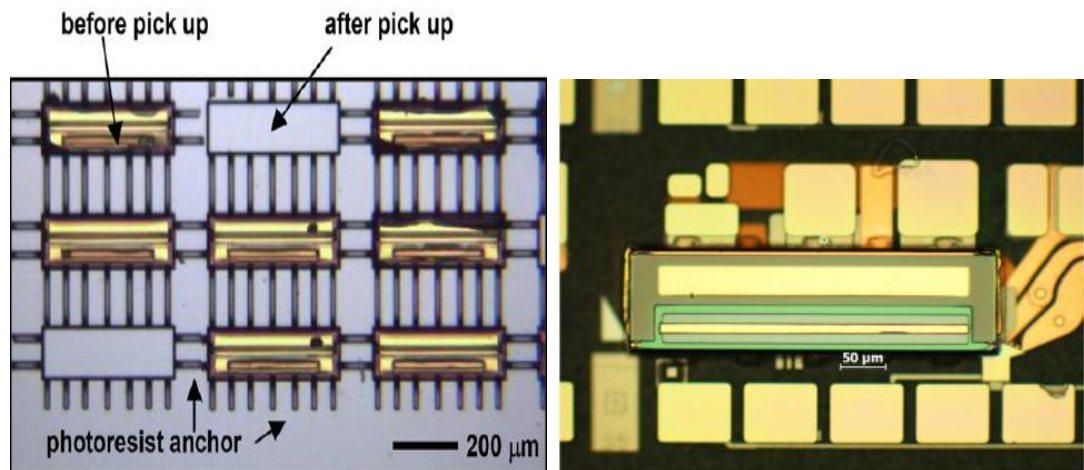


*Figure 5.1 Optical microscope image (top view) of (a) an array of lasers tethered to the GaAs growth substrate after the removal of sacrificial layer (AlAs), and some laser devices have been picked up by the use of transfer-printing elastomer stamp[6]; (b) a transfer-bonded ridge laser on part processed AlTiC substrate of a magnetic recording read-write head transducer for data storage hard drive[2]*

Transfer-bonding provides a low cost high-speed method with high chip yield and excellent overlay accuracy controlled by a structured elastomer stamp. It requires atomically smooth interface between a LD and a carrier substrate for an effective direct bonding. Alternatively, this issue can be bypassed by applying an adhesive layer such as photoresist resin, benzocyclobutene (BCB) and metal on the carrier substrate. A metal layer stack can contribute both as an adhesive and a thermally conductive interface. Heat management is a critical issue for lasers in general and

especially in these new integrated deployment environments. The performance of an LD is strongly dependent on the junction temperature which is set by the ambient temperature together with Joule heating in the device or from surrounding components, which leads to temperature gradients [7, 8] as the heat will be transferred to a heat sink. High junction temperature leads to a degradation of the electro-optical properties through loss in device efficiency or other premature failure mechanisms of the device. Furthermore, mechanical strain induced by thermal gradients is generally detrimental. Thus, to provide the best output power and emission spectral performance and assure the semiconductor laser lifetime, the diode junction temperature must be controlled [9, 10] by minimising the excess heat generation and managing its removal from the active region. The epitaxial layer design of LD, device geometry (contact size and resistivities, dielectric passivation composition and thicknesses, metallization thicknesses, substrate thickness) and carrier geometry are factors that affect the heat dissipation of the device. In conventional LD devices mounted with the epitaxial side up, the semiconductor substrate is the largest contributor to the total thermal resistance of laser chip body [11]. Hence, the removal of chip substrate can significantly reduce the thermal resistance of the transfer-bonded device.

A literature review reveals many examples of the thermal analysis of GaAs based LDs [6, 11-13], while Joyce and Dixon [13] gave a thorough analysis of the thermal resistance of LDs. Liu *et al.* [11] presented a finite-element thermal modelling analysis of a packaged high power pump laser with epi-up and epi-down bonding on a mounting substrate. Bezotosnyi *et al.* [12] reported the a 3-dimensional modelling in COMSOL of high-power laser diode at varied parameters (e.g. width, thickness) of different types of submounts. However, most of the papers describe edge-emitting GaAs based LDs with a thick GaAs substrate mounted with solder on a heat sink (e.g. Cu or diamond) [11-14]. The thermal properties of those devices can differ significantly from the GaAs based LDs with substrate removed and bonded on a Si submount. As the Si-based circuit integration approaches its scaling limits, the potential for Si-based photonics can improve the performance in future integrated circuit chips. It has created strong demand for efficient on-chip lasers [2]. Recently, Sheng *et al.* [6] demonstrated a thermal simulation together with experimental works of a transfer-bonded GaAs based LD printed on Si substrate with different interface



layers, such as GaAs, eutectic In/Ag and SU-8 photoresist. This chapter presents a 2-D finite element thermal modeling of the temperature distribution at the ridge region of a substrate removed GaAs based LD and the LD without substrate removal (i.e. with 100- $\mu\text{m}$ -thick GaAs substrate). The thermal resistance of both of them were calculated from the simulations and compared with analytical calculations. Moreover, the thermal distribution of transfer-bonded LD on different types of thin submount (i.e. interposer) without any interface material layer that only use the van der Waals forces between interposer and the LD device, was presented. To our best knowledge, there is no similar work that has been reported in literature.

## 5.2 The structure of the laser diode

In this section, the structure of transfer-bonded ridge LD is described. The LD considered is a multiple-quantum-well (MQW) AlGaAs/GaAs ridge waveguide device emitting around 830 nm with a 3- $\mu\text{m}$ -wide (w) etched ridge, and a length, L, is typically 200  $\mu\text{m}$ . The chip has an overall width, W, of 54  $\mu\text{m}$ . The LD is considered with a 100- $\mu\text{m}$ -thick GaAs substrate present and with the substrate fully removed (representing the transfer-bonded LD) leaving the 3.6- $\mu\text{m}$ -thick laser waveguide material layers. The bottom side of the chip is mounted on metal (Au) which is assumed to be a perfect heat sink. The device cross-section layout is shown in Fig. 5.2, where the ridge is clad by a dielectric ( $\text{SiO}_2$ ) of 270-nm-thick and a metal (Au) contact of thickness 275 nm.

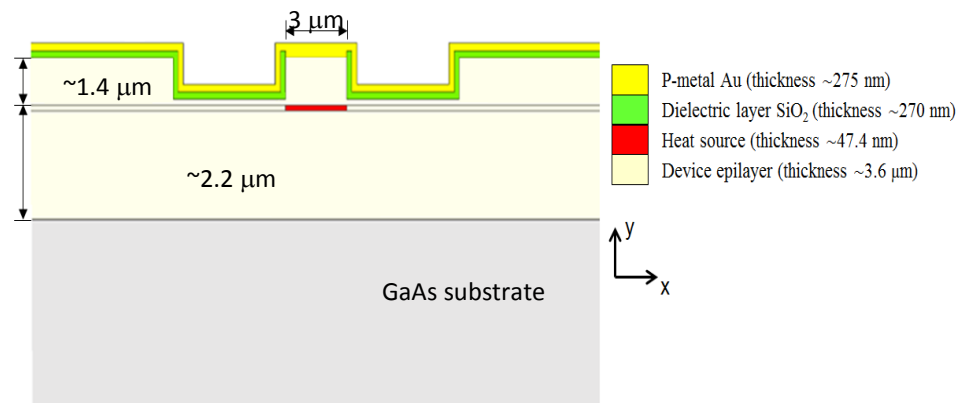


*Figure 5.2 Schematic of the GaAs based MQW LD cross-section and the location of the heat source.*

### 5.3 Thermal models of the laser diode

In this section, a simplified analytical model for thermal resistance calculation of the LD and a numerical model based simulation of thermal distribution in the transfer-bonded LD are presented.

Such a short cavity length is desired for future footprint and bandwidth requirements. As a result, the excess power is generated in a small volume leading to the need for high laser efficiency and excellent heat spreading. According to the light output-injection current-voltage (LIV) data of the LD, a 100 mW input power was applied on the LD and the measured light output power is 60 mW. Therefore, the heat power generated is 40 mW, which is to be dissipated from an area of  $3 \times 200 \mu\text{m}^2$  in the ridge confined active region of device. The thermal resistance and 2-D temperature distributions were simulated for different device configurations using the FEM software COMSOL Multiphysics 5.0. It can provide accurate temperature distribution for the specific geometries. As the simulation are time consuming for the large variation in critical dimensions in the laser structures, a simplified analytical model based on the work of Fu *et al.* [14] was also used to provide general guidelines for thermal management.

The current through a device is confined by the ridge and here it is taken that the excess power is created in the junction region as a narrow source of heat. 2-D steady state heat flow is described by heat conduction equation below [15]:

$$\nabla \cdot (k \nabla T) = Q \quad (5.1)$$

where  $k$  is the thermal conductivity and  $Q$  is the heat generation source. The thermal conductivities of all the materials are considered constant with temperature,  $T$ . The electrical power input to the LD is dissipated as optical output power and as heat. The heat generation is due to non-radiative recombination, Auger recombination, Joule heating effect, and optical absorption [16]. In steady-state, the overall heat generation ( $Q$ ) is the sum of those effects [7], which is equal to difference of the input power ( $P_{in}$ ) and the optical output power ( $P_o$ ),  $Q = P_{in} - P_o$  results in a junction temperature  $T_j$  rise. The temperature rise in the active region,  $\Delta T_j = T_j - T_0$ , is defined in terms of an overall thermal resistance  $R_{th} = \Delta T_j / Q$ , where  $T_0$  is the heat sink

temperature. The thermal resistance substantially depends on the thermal conductivity and geometry of the LD and submount (or heat spreader, interposer) located between the LD and the heat sink. Determining the thermal resistance requires the solution of the thermal conduction equation with non-trivial boundary conditions.

It is assumed that  $Q$  is uniformly dissipated across the source region. In the model, the heat source is a heat confined volume given by the product of the ridge width ( $w$ ), laser cavity length ( $L$ ) and MQW region thickness ( $d$ ), namely  $3\text{ }\mu\text{m} \times L\text{ }\mu\text{m} \times 0.0474\text{ }\mu\text{m}$ . The power density in the heat core is  $Q/(w \times L \times d)$  ( $\text{W}/\text{m}^3$ ). Thus, the power in the 2-D calculation ( $\text{W}/\text{m}^2$ ) is scaled by  $L$  with the heat generated in a cross section area  $A$  (i.e.  $w \times d$ ). In order to simplify the calculation in the analytical model, a uniformly distributed rectangular heat strip in the size of  $w \times L$  was applied as the heat source. The areal power density is  $Q/(w \times L)$  ( $\text{W}/\text{m}^2$ ). Therefore, the total heat power for the laser device is scaled by the cavity length  $L$  ( $\mu\text{m}$ ) in both models.

The simulated structure in the FEM modelling was based on the cross sectional geometry of a realised laser. It consists of an etched ridge structure of GaAs with a heat core with area ( $A$ ), Au layer as p-contact metal ( $\sim 275\text{ nm}$ ) and  $\text{SiO}_2$  ( $\sim 270\text{ nm}$ ) layer as the dielectric passivation. The heat source (active region) is  $47.4\text{ nm}$  thick, which is located below the etched surface of the ridge. 2-D simulations of selected LD structures were performed by using COMSOL to solve equation (5.1), subject to boundary conditions using Newton's law of cooling. It aimed to understand the individual contribution of the substrate and submount to the thermal performance of the LD. A static thermal analysis of the laser with a heat load uniformly distributed along the laser chip length,  $L$  at the active region was applied and the temperature on the bottom surface was assumed to be fixed at  $T_0^\circ\text{C}$  (i.e.  $20^\circ\text{C}$ ) as a perfect boundary condition. The heat generated inside the chip was assumed removed by conduction with both convective heat transfer and radiative cooling neglected [16].

As the temperature variation on the LD is less than  $200^\circ\text{C}$  during operation, the thermal properties of the materials are only slightly changed which could therefore be considered as being constant. Thus, the analytical and numerical modelling approach assume temperature independent properties, and the thermal properties

used are shown in Table 5.1.

Material	Thermal conductivity (W/m K)
GaAs	55
SiO <sub>2</sub>	1.4
Au	318
Alumina	1.35
Si	150

*Table 5.1 Thermal property of the materials[17-20]*

### 5.3.1 Analytical modeling of laser diode

The analytical method of Fu *et al.* [13, 14], was used where the heat dissipation in a LD can be represented as a thermal resistance circuit composed of individual thermal resistance components. The total thermal resistance was obtained by calculating the sum of parallel and series components. Similar to Fu's case, it is assumed a rectangular parallelepiped consisting of 2 layers below the heat source (GaAs waveguiding and GaAs substrate) and 3 layers above (GaAs upper cladding, SiO<sub>2</sub> dielectric and Au metal) are used as the laser geometry (see Fig. 5.3(a)) in the analytical model. A narrow heat source is located at the interface between layers 1 and 2 in Fig. 5.3(a). The thickness of the each layer is labeled as  $t_i$  ( $i = 1, 2, 3, 4, 5$ ). The corresponding thermal conductivities for the Au layer, SiO<sub>2</sub> dielectric layer, GaAs (layer 2), GaAs (layer 1) and the GaAs substrate layer are  $k_5$ ,  $k_4$ ,  $k_2$ ,  $k_1$ , and  $k_3$ , respectively. For simplifying the calculation in the analytical model, this rectangular slab layers stack (shown in Fig. 5.3) is used, instead of using the geometrical region of the LD in etched ridge structure (shown in Fig. 5.2). Fig. 5.3(b) shows a half of the simplified LD structure in Fig. 5.3(a). It is used to further simplify the calculation by taking advantage of the symmetry of the LD structure.

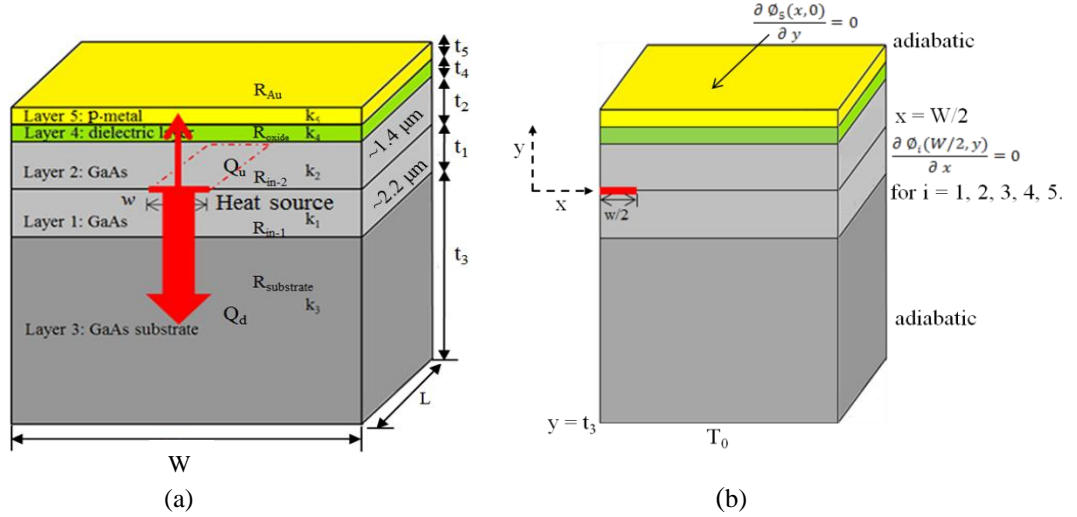


Figure 5.3 Schematic of a simplified laser thermal model consisting of heat flow (solid line with arrow) from a uniform heat source in the active region and the heat flow spreads from the active region both upward and downward. The device length, width and source width of the laser are labelled as  $L$ ,  $W$  and  $w$ . Other terms are as described in the text. (a) Schematic of the simplified laser structure used for the analytical model and (b) Device with symmetry at heat core position.

The heat flow from the heat source is considered in two parts: The primary part of the heat flow is downward ( $Q_d$ ) directly through the substrate to the heat sink, while the second part ( $Q_u$ ) which is more relevant with a thick heat spreader flows upwards and then enters the oxide layer and the Au layer before flowing downward. The heat flow through the device junction region, oxide barrier layer and metal layer, are taken to be planar. The thermal resistances of layer 1, layer 2, oxide layer and Au layer can be expressed as  $R_{in-1}$ ,  $R_{in-2}$ ,  $R_{oxide}$ ,  $R_{Au}$ , based on a 1-D heat conduction flow respectively. The downward heat flow in the substrate spreads in a 2-D fashion to the heat sink.

In order to derive the thermal resistance for  $Q_d$ , the maximum temperature at the active region is calculated first. For convenience, a dimensionless temperature distribution in rectangular coordinates  $\phi_i(x, y)$  where  $\phi_i = (T_i - T_0)/T_0$  is expressed for each layer [13-15]. Perfect thermal interface boundary conditions with continuous temperature and normal heat flow are assumed [13, 14]. The LD is assumed mounted on a perfect heat sink, with the interface between the laser substrate and the heat sink maintained at the same temperature as the heat sink ( $T_0 = 20^\circ\text{C}$ ). The heat escape through the sides of the LD and top surface exposed to the ambient are assumed negligible and heat dissipation is only due to heat conduction downward. Thus, the sides and top surface of the laser configuration can

be assumed as being thermally insulated and the bottom side temperature  $T_0$  is used as the boundary condition in the thermal resistance calculation.

The dimensionless temperature distribution function  $\phi_i$ , representing the 2-D distribution of temperature variation can be calculated by a separation of variables solution of Laplace's equation [13-15],

$$\phi_i(x, y) = B_{i,0}(1 - r_{i,0}y) + \sum_{n=1}^{\infty} B_{i,n} [\cosh(k_n y) - r_{i,n} \sinh(k_n y)] \cos(k_n x) \quad (5.2)$$

From the equation (5.2), the undetermined coefficient  $B_{i,n}$  and  $r_{i,n}$  ( $i = 1, 2, 3, 4, 5$ ) are required to calculate  $\phi_i(x, y)$ . The coefficients  $B_{i,n}$  and  $r_{i,n}$  contain the physical parameters of the laser, such as geometry size, thermal conductivities of materials, heat source power and ambient temperature. The  $r_{i,n}$  should be derived first and then substituted it into equation (5.2) to derive  $B_{i,n}$  by solving the corresponding partial differential equations (PDEs) for the selected boundary conditions. The thermal resistance can then be derived by substituting an expression for  $B_{i,n}$  in equation (3). For satisfying the requirement of no heat escape from all the sides  $\frac{\partial \phi_i(W/2, y)}{\partial x} = 0$ , the separation constant  $k_n = 2n\pi/W$  is required.

The boundary condition on the bottom surface of substrate is:

$$\phi_3(x, t_3) = 0 \text{ (i.e. } T_3 = T_0) \quad (5.3)$$

By using equations (5.2) and (5.3), we can obtain

$$\phi_3(x, t_3) = B_{3,0}(1 - r_{3,0}y) + \sum_{n=1}^{\infty} B_{3,n} [\cosh(k_n y) - r_{3,n} \sinh(k_n y)] \cos(k_n x) \quad (5.4)$$

By using the orthogonal property of  $\cos(k_n W)$  respect to the constant  $k_n W = 2n\pi$  [15, 21], then we can solve equation (5.4) to obtain the separation coefficients  $r_{i,n}$  for  $i = 3$ .

$$r_{3,0} = 1/t_3$$

$$r_{3,n} = \frac{\cosh(k_n t_3)}{\sinh(k_n t_3)} = \coth(k_n t_3) \quad (5.5)$$

Recall the equation (5.6) required by the boundary conditions and equation (5.5), the  $B_{3,0}$  and  $B_{3,n}$  are calculated to determine  $R_{\text{substrate}}$  and at least 100 terms are required to the summation terms in equation [13]:

$$\begin{aligned}\frac{\partial \phi_3(x,0)}{\partial y} &= \frac{Q_d}{T_0 k_3 L w}, \quad \left(0 \leq x \leq \frac{w}{2}\right) \\ \frac{\partial \phi_3(x,0)}{\partial y} &= 0, \quad \left(\frac{w}{2} \leq x \leq \frac{W}{2}\right)\end{aligned}\quad (5.6)$$

Integrating both side of the equations above from  $x = 0$  to  $x = W/2$  and recalling the orthogonal property of  $\cos(k_n W)$  [14, 21], we can obtain undetermined coefficients  $B_{3,0}$ ,  $B_{3,n}$  for layer 3 [13]. Substituting into equation (5.7), then the thermal resistance  $R_{\text{substrate}}$ , which expresses the thermal resistance of the heat flow downward from active region, can be calculated as [13, 14]

$$R_{\text{substrate}} = \frac{1}{w} \int_{-w/2}^{w/2} R_{\text{substrate}}(x) dx = \frac{1}{w} \int_{-w/2}^{w/2} \frac{T_0 \phi_3(x,0)}{Q_d} dx = \frac{T_0 B_{3,0}}{w Q_d} + \frac{2T_0}{w Q_d} \sum_{n=1}^{\infty} \frac{B_{3,n}}{k_n} \sin\left(\frac{k_n}{2} W\right) \quad (5.7)$$

Therefore, according to the parallel thermal resistance network of each component shown in Fig. 5.4, the total thermal resistance of the laser can be calculated below.

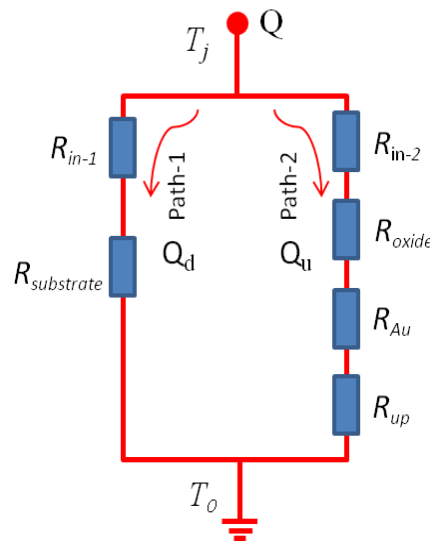


Figure 5.4 Thermal resistance network of the simplified analytical laser model.

$$R_{th} = \frac{(R_{in-1} + R_{substrate})(R_{in-2} + R_{oxide} + R_{Au} + R_{up})}{R_{in-1} + R_{substrate} + R_{in-2} + R_{oxide} + R_{Au} + R_{up}} \quad (5.8)$$

The thermal resistance aspect to the upward heat flow consists of the  $R_{in-1}$ ,  $R_{oxide}$ ,  $R_{Au}$  and thermal resistance component,  $R_{up}$ , for the heat flow bounds downward after  $Q_u$  spreads wider over ridge region when it reaches the top Au layer. However, due to the redistribution of upward heat flow from the Au layer down to the substrate, a suitable analysis with good assumptions would be required for simplifying analytical calculation in the thermal resistance of the  $Q_u$ .

$R_{up}$  has more effect only for a thick Au layer on the top of the device. The heat spreading is less obvious in a thin Au layer compared to a thick Au layer and negligible heat escape from the top surface of Au layer was assumed (i.e. thermal isolation). Moreover, the good thermal isolation of the dielectric layer ( $\text{SiO}_2$ ) blocks the upward heat flow from the active region, Thereby, for a device with a thin Au layer, the heat dissipation from active region is expected to be dominated by a 1-D heat flow downward. The relative separation coefficients  $r_{3,0}$ ,  $r_{i,n}$ ,  $B_{3,0}$ ,  $B_{3,n}$ , separation constant  $k_n$  and parameters including physical geometry and material thermal properties were all defined as variables in Matlab code [14, 15]. Afterwards, the thermal resistance of each components and the total thermal resistance of the LD can be calculated.

### 5.3.2 Numerical modeling of laser diode

In this subsection, the finite element method as an numerical approach for the modeling is introduced. The simulation results of the LD thermal model built in COMSOL Multiphysics are presented.

#### 5.3.2-1 Introduction of numerical approach

The numerical modeling of the laser was implemented by the use of finite element method (FEM), and was constructed in a commercial modeling software for finite element analysis. FEM is a numerical technique for finding approximated solutions to partial differential equations (PDEs) in boundary value problems. It provides an



analysis approach to understand practical application problems by subdividing a large problem into smaller, simpler parts, which is called finite elements. The domain of the problem is divided into a collection of subdomains (i.e. finite elements) by mesh generation techniques, with each subdomain represented by a set of element equations to the original problem, followed by systematically recombining all sets of element equations into a global system of equations for the final calculation. The global system of equations is calculated from the initial values of the original problem to obtain a numerical solution. The equations of the domain are often PDEs and the element equations of the subdomains are simple equations that locally approximate the PDEs. From the view of mathematics, it is to construct an integral of the inner product of the residual and the weight functions and set the integral to zero.

The method eliminates all the spatial derivatives from the PDEs, therefore the PDEs are locally approximated with a set of element equations, which are a set of algebraic equations for steady state problem and a set of ordinary differential equations for transient problems. Thus, a global system of equations is generated from the element equations through a transformation of coordinates from the subdomains' local nodes to the domain's global nodes. The spatial transformation includes appropriate orientation adjustments as applied in relation to the reference coordinate system. Usually, FEM modeling software can implement this procedure by using coordinate data generated from the subdomains [22].

The FEM method is often used in complex physical systems with the underlying physics expressed in either PDEs or integral equations, for example, the heat equation in LD. A complex physical problem can be divided into small elements representing different areas in this physical system. It is convenient to analyze problems in complicated geometries and domains. The FEM model has another clear advantage, as it can be easily adapted to other optoelectronic devices.

COMSOL Multiphysics is a powerful modeling and simulation software package based on finite element analysis, which uses FEM to solve the equations. The software package has over 26 different modules to provide software solutions of multiphysics problems. These modules can be easily coupled and applied to solve numerous engineering and physics based problems. Using the built-in physics

interfaces, it is possible to specify material and physical properties and define parameters. The heat transfer module with the built-in physics interfaces were used in the thermal modeling.

### **5.3.2-2 FEM thermal model of the laser diode**

The 2-D thermal model of LD was based on the geometry in Fig. 5.2 that was constructed in COMSOL Multiphysics and the material thermal property parameters were assigned to the layers of geometry. The physics module “Heat transfer in Solids” in COMSOL was applied in the model and preset the study in steady state for the simulation of temperature distribution in LD.

The 2-D steady state temperature distribution of a 200  $\mu\text{m}$  long laser with a 100- $\mu\text{m}$ -thick GaAs substrate (representing the reference laser) and with the substrate fully removed (representing the transfer bonded laser) is presented in Fig. 5.5. For continuous wave (CW) operating at room temperature ( $T_0 = 20^\circ\text{C}$ ) with a heat load of 40 mW, the highest junction temperature of  $29.2^\circ\text{C}$  was simulated in the laser with a 100- $\mu\text{m}$ -thick GaAs substrate, and  $21.5^\circ\text{C}$  in laser with the substrate fully removed with both mounted on a perfect heat sink. The LD junction temperature,  $T_{max}$ , can be estimated from the thermal resistance  $R_{th}$  of the structure. The corresponding  $R_{th}$  of the transfer bonded laser is 37.5 K/W, which is much less than the reference laser (230 K/W). As the GaAs substrate is the largest contributor to the total thermal resistance, reducing its thickness can significantly reduce the thermal resistance.

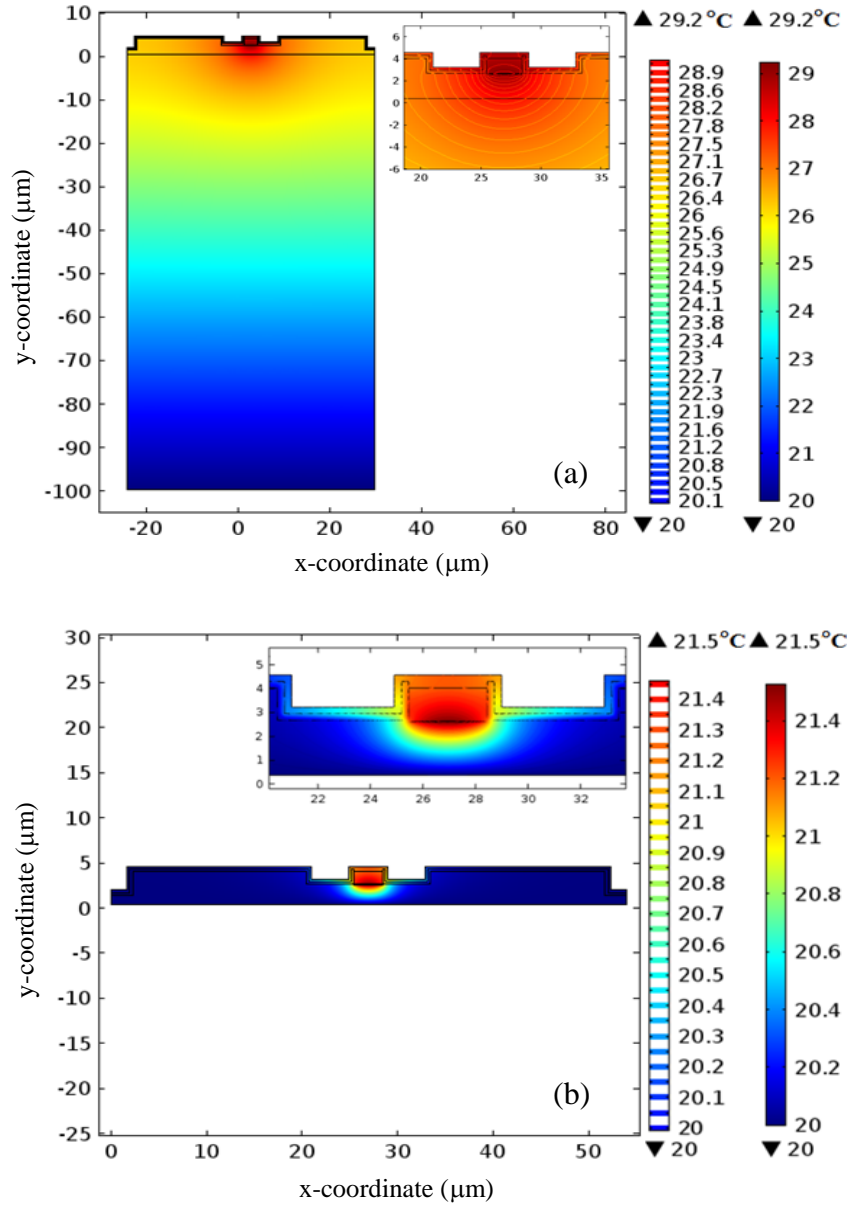


Figure 5.5 Simulated temperature profile and thermal contour plots of a laser with 40 mW heat load ( $L=200\text{ }\mu\text{m}$ ) for (a) Laser device with  $100\text{ }\mu\text{m}$  thick GaAs substrate; inset: thermal contour plot at the ridge region, and (b) Transfer-bonded laser (inset: thermal contour plot at the ridge region).

The poor heat conduction properties of the  $\text{SiO}_2$  dielectric layer on both sides of the etched ridge result in the heat flux being downward to the heat sink. Comparing Fig. 5.5a and Fig. 5.5b, it is seen that the heat flux for the transfer-bonded laser is oriented primarily in the transverse direction due to the proximity of the heat sink (Fig. 5.5b), while the temperature is 2-dimensionally distributed for the standard laser configuration due to the heat spreading (Fig. 5.5a). In order to further reduce the junction temperature in the transfer-bonded laser, the heat spreading at the ridge

region should be increased and additional heat removed in the upward direction by the metal contact and its associated spreading.

The thermal resistance of the laser as a function of cavity length ( $L$ ) for different thicknesses of Au, SiO<sub>2</sub>, and GaAs substrate shown in Table 5.2, were obtained by simulation using both the FEM model and simplified analytical model.

Device label	Au (nm)	SiO <sub>2</sub> (nm)	native GaAs substrate ( $\mu\text{m}$ )
Reference laser-FEM	275	270	100
G1-FEM	275	270	removed
G2-FEM	2000	270	100
G3-FEM	2000	270	removed
G4-FEM	2000	100	100
G5-FEM	2000	100	removed
$R_{\text{down}}$ calculated	275	270	100

Table 5.2 The list of laser device geometry simulated.

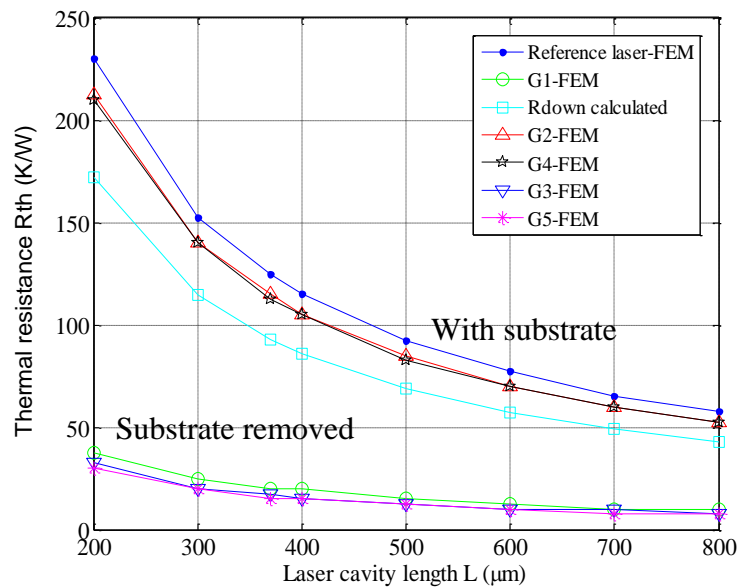
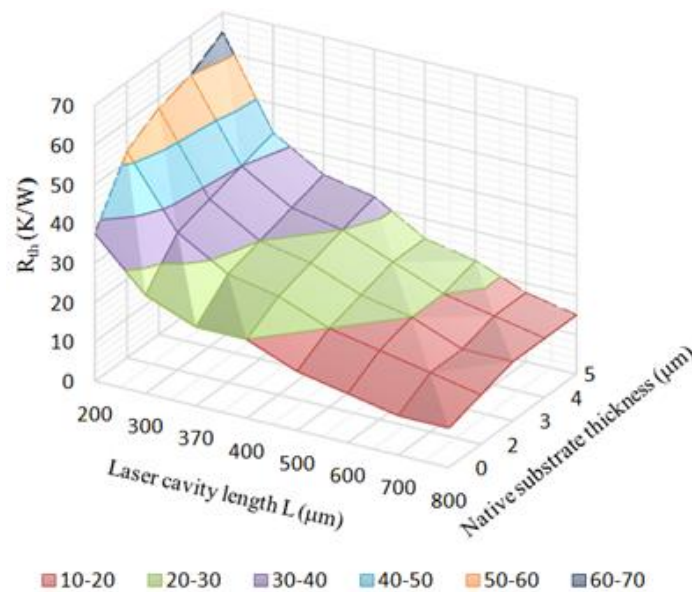


Figure 5.6 Comparison of the thermal resistances of a laser as a function of cavity length for the configuration with 100- $\mu\text{m}$ -thick GaAs substrate and with substrate fully removed and different thickness of p-metal (Au layer) and SiO<sub>2</sub> dielectric layer on a perfect heat sink at constant 40 mW heat load by FEM model. The thermal resistance  $R_{\text{down}}$  calculated by analytical method for downward heat flow is also presented.

In Fig. 5.6,  $R_{th}$  as a function of cavity length is compared using the FEM method and analytical method for the reference laser and the transfer-bonded laser. It shows a relatively small difference ( $\sim 27\%$ ) between  $R_{th}$  and  $R_{down}$  calculated by the FEM and analytical models respectively. It is due to the ridge structure in the configuration and the approximation made that assumed 1D heat flow in the analytical model. The upward heat flow is minimal, so the effect of the  $R_{up}$  is not so clear when the thermal resistance of downward heat flow dominates. Therefore,  $R_{down}$  is quite close to the  $R_{th}$  obtained by FEM model. The thermal resistances of both devices decay exponentially with the laser cavity length as the power is distributed over a larger area. The calculated thermal resistances using FEM model for laser cavity lengths of 200  $\mu\text{m}$  and 370  $\mu\text{m}$  are 230 K/W, 125 K/W for the reference geometry respectively and 37.5 K/W, 20 K/W for the transfer bonded laser respectively. The measured  $R_{th}$  for a 370  $\mu\text{m}$  long transfer bonded laser is around 15 K/W indicating that the model is reasonably accurate. Nevertheless, from Fig. 5.6, it is seen that increasing thickness of the p-metal (Au layer) is effective at reducing  $R_{th}$  (i.e. by increasing the thickness from 275 nm to 2  $\mu\text{m}$ ) for both the reference LD and transfer bonded LD, while  $R_{th}$  can be further slightly decreased by reducing the thickness of the  $\text{SiO}_2$  dielectric layer. The thick Au layer on top of the LD improves the heat spreading, therefore reducing the temperature at the ridge region.



*Figure 5.7 Thermal resistance of a laser for different residual GaAs substrate thicknesses and the laser cavity length on a perfect heat sink (corresponding to the bonding on metal) by FEM model.*

The combined effect of the laser cavity length and the residual substrate thickness on the thermal resistance has been investigated. The simulated  $R_{th}$  for GaAs substrate thicknesses between 0  $\mu\text{m}$  and 5  $\mu\text{m}$  is shown in Fig. 5.7. The highest  $R_{th}$  of 60 K/W to 70 K/W is calculated for the short (200  $\mu\text{m}$  long) cavity and thickest residual GaAs. For the 200- $\mu\text{m}$ -long cavity laser, the minimum  $R_{th}$  of 37.5 K/W is obtained for the substrate completely removed. However, there is no significant difference in  $R_{th}$  for laser cavity lengths from 500  $\mu\text{m}$  to 800  $\mu\text{m}$  with a residual substrate thickness between 0 and 5  $\mu\text{m}$ . Therefore, the shorter cavity laser benefits most from a thin residual substrate.

#### 5.4 Thermal analysis of laser diode on different types of submount

The substrate removed laser can be mounted on different materials by van der Waals forces. The 2-D temperature profile of a LD transfer-bonded to 10- $\mu\text{m}$ -thick submounts (180- $\mu\text{m}$ -wide) composed of alumina, GaAs, and Si was evaluated. The

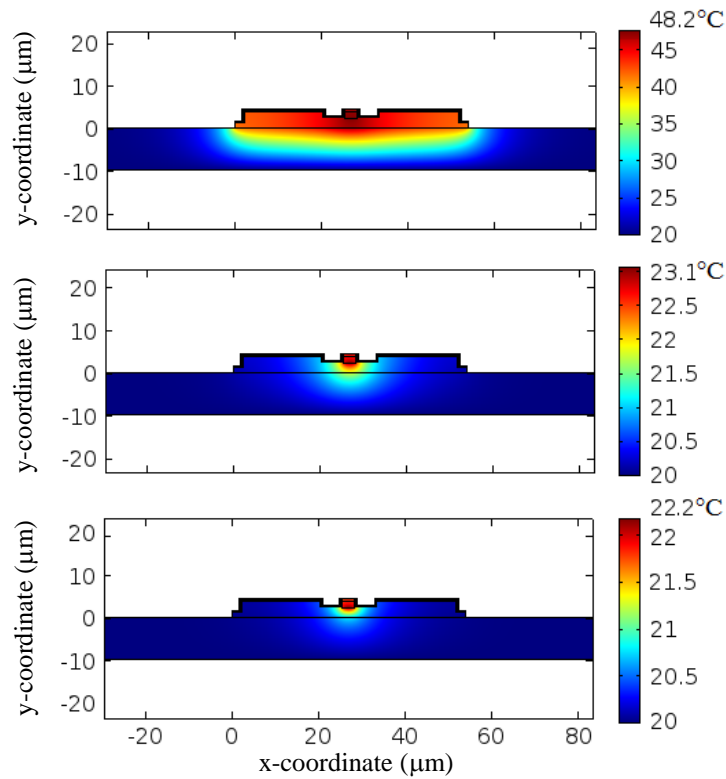


*Figure 5.8 Simulated temperature distribution of a transfer-bonded thin-film laser on 10  $\mu\text{m}$  thick submount ((a) alumina, (b) GaAs, and (c) Si at 40 mW heat load at room temperature  $T_0=20^\circ\text{C}$  by FEM model. A perfect heat sink is assumed on the bottom face.*

alumina (aluminium oxide) thermal properties are in line with those formed by sputtering where voids and other inclusions may be present. The thermal interface between the submount and device is assumed to be perfect. The bottom surface of submount is fixed at room temperature ( $T_0 = 20^\circ\text{C}$ ). The top surface and the surface on each side of both the LD and the submount are assumed to be thermally isolated.

Fig. 5.8a shows the 2-D temperature profile of the transfer-bonded laser on an alumina submount. Due to the low thermal conductivity of alumina, the heat spreads laterally resulting in a high junction temperature of  $48.2^\circ\text{C}$ . In Fig. 5.8b, the LD on GaAs shows a more obvious broad parabolic heat spreading from the ridge region. The thermal distribution profile of LD on Si as seen in Fig. 5.8c that shows a parabolic heat spreading and the lowest temperature rise at the junction.

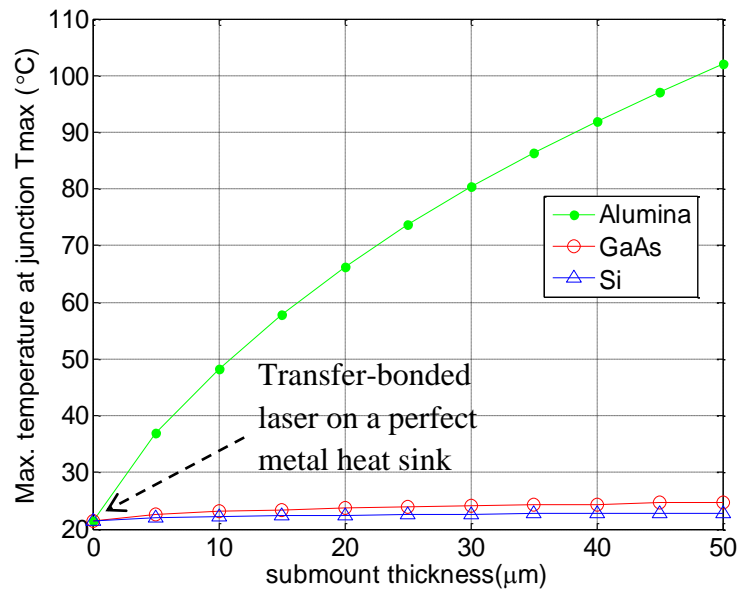


*Figure 5.9 Simulated temperature at the junction of a transfer-bonded thin-film laser with 40 mW heat load at room temperature ( $T_0 = 20^\circ\text{C}$ ) as a function of submount thickness composed of alumina, GaAs and Si respectively.*

Fig. 5.9 shows the calculated junction temperature of the LD as a function of submount thickness for different submount materials. It shows that the junction temperature of a transfer-bonded laser on alumina strongly depends on its thickness, while it is relatively independent of thickness for GaAs and Si. Thus, thickness of alumina should be minimised to reduce the heat conduction path between the ridge region and the heat sink.

## 5.5 Conclusions

The 2-D temperature distribution of an AlGaAs/GaAs MQW LD with a 3- $\mu\text{m}$ -wide ridge with 40 mW of power dissipated was modelled by FEM software for different cavity lengths and device configurations. The total thermal resistance was calculated by the FEM model and by an analytical model. The FEM model shows a reasonable matching with measured thermal resistance of LD. It is essential to reduce the thermal resistance for a 200- $\mu\text{m}$ -long cavity laser due to the high heat power density. This can be done by increasing the p-metal layer thickness in order to increase the lateral heat spreading. The heat flow from the heat source is dominated by the downward heat flow to the heat sink and the contribution from the upward heat flow is minimal. Comparing the simulated maximum temperature ( $T_{max}$ ) of the junction in the transfer-bonded LD on different submount materials (e.g. GaAs, alumina and Si), shows that reducing the alumina thickness is critical to decrease the junction temperature of the device. Both GaAs and Si submounts show a weak dependence of the junction temperature on thickness. For a 10- $\mu\text{m}$ -thick submount, Si provides the lowest  $T_{max}$  of about 22.2°C for 40 mW of power dissipation.

## 5.6 References

- [1] T. Amano, S. Ukita, L. Ma, *et al*, “Thermal Conductive Properties of a Semiconductor Laser on a Polymer Interposer”, *Jpn. J. Appl. Phys.*, vol. 52, no. 4s, pp. 04CG05, Mar. 2013.
- [2] B. Corbett, C. Bower, A. Fecioru, *et al*, “Strategies for integration of lasers on silicon”, *Semicond. Sci. Technol.*, vol. 28, no. 9, pp.1-6, Aug. 2013.
- [3] R. Saeidpourazar, M. Sangid, J. Rogers, *et al*, “A prototype printer for laser driven micro-transfer printing”, *Journal of Manufacturing Processes*, vol. 14, no. 14, pp. 416–424, Oct. 2012.
- [4] R. H. Kim, D. H. Kim, J. Xiao, *et al*, “Waterproof AlInGaP optoelectronics on stretchable substrates with applications in biomedicine and robotics”, *Nature Materials*, vol. 9, no. 11, pp. 929–937, Oct. 2010.
- [5] J. Yoon, A. J. Baca, S. I. Park, *et al.*: 'Ultrathin silicon solar microcells for semitransparent, mechanically flexible and microconcentrator module designs', *Nature Materials*, vol. 7, no. 11, pp. 907–915, Jan. 2008.
- [6] X. Sheng, C. Robert, S. Wang, G. Pakeltis, B. Corbett, J. A. Rogers, “Transfer printing of fully formed thin-film micro-scale GaAs lasers on silicon with a



thermally conductive interface material,” *Laser & photonics reviews*, vol. 9, no. 4, pp. L17-L22, July. 2015.

[7] H. Yi, J. Diaz, I. Eliashevich, *et al*, “Temperature dependence of threshold current density  $J_{th}$  and differential efficiency  $\eta_d$  of high-power InGaAsP/GaAs ( $\lambda=0.8\ \mu\text{m}$ ) lasers,” *Appl. Phys. Lett.*, vol. 66, no. 3, pp. 253–255, Jan. 1995.

[8] H. K. Choi, G. W. Turner, 'Mid-infrared semiconductor lasers based on antimonide compounds,' in Manasreh, M. O. (Ed.): “Optoelectronic properties of Semiconductors and Superlattices”, (Press, 1997), pp. 369–433.

[9] V. P. Gribkovskii, “Injection lasers,” *Prog. Quant. Electr.*, vol. 19, no. 1, pp. 41–88, 1995.

[10] L. A. Colden, and S. W. Corzine, 'Diode Lasers and Photonic Integrated Circuits' (John Wiley, 1995, 1st edn.)

[11] X. S. Liu, H. M. Hu, C. G. Caneau, *et al*, “Thermal Management Strategies for High Power Semiconductor Pump Lasers,” *IEEE Transactions on components and packaging technologies*, vol. 29, no. 2, pp. 268–276, Jun. 2006.

[12] V. V. Bezotosnyi, O. N. Krokhin, V. A. Oleshchenko, V. F. Pevtsov, Yu. M. Popov, E. A. Cheshev, “Thermal modeling of high-power laser diodes mounted using various types of submounts,” *Quant. Electr.*, vol. 44, no. 10, pp. 899–902, May. 2014.

[13] W. B. Joyce, R. W. Dixon, *et al*, “Thermal resistance of heterostructure lasers”, *J. Appl. Phys.*, vol. 6, no. 2, pp. 855–862, 1975.

[14] J. P. Fu, R. G. Yang, G. Chen, *et al*, “Integrated electroplated heat spreaders for high power semiconductor lasers,” *J. Appl. Phys.*, vol. 104, no. 6, pp. 4907–4911, 2008.

[15] H. S. Carslaw, and J. C. Jaeger, “Conduction of Heat in Solids” (Oxford University Press, 1959, 2nd edn. 1960)

[16] J. Piprek, “Semiconductor optoelectronic devices: Introduction to Physics and Simulation” (Academic Press, 2003, 1st edn.)

[17] <http://www.ioffe.ru/SVA/NSM/Semicond/GaAs/thermal.html>

[18] Y. S. Touloukian, R. W. Powell, C. Y. Ho, and P. G. Klemens, “Thermal Conductivity,” TPRC Data Series, vol. 2, Plenum, New York, 1970.

[19] T. M. Tritt, “Thermal conductivity: Theory, Properties, and Applications,” (Springer Science & Business Media, Berlin, 2005)

[20] S. Sze, “Physics of Semiconductor Devices”, (Wiley, New York, 1981, 2<sup>nd</sup> edn.)

[21] L. M. Jiji, “Heat conduction”(Springer. Verlag Berlin Heidelberg, 2009, 3<sup>rd</sup> edn.)

[22] J. N. Reddy, “An Introduction to the Finite Element Method”, (McGraw-Hill, 2006, 3rd edn.)

## Chapter 6

### Conclusions and future work

#### 6.1 Conclusions

For the integration of semiconductor optoelectronics devices on dissimilar material platforms in the applications of on-chip optical communications, next generation optical/biomedical sensors, and wearable optoelectronic systems etc., the thin film technology for optoelectronics is critical and is applied to separate the device epitaxial layers from their native substrate and transfer them onto new platforms. The thermal management of such devices is very important for effective control of device junction temperature. For visible to ultraviolet spectral range, high efficiency wide-band-gap III-nitride based emitters have been developed over last two decades. Compared with other methods (e.g. wet etch, mechanical removal, and chemical-mechanical-polishing), laser lift-off (LLO) is more effective to separate III-nitride layers from the sapphire substrate.

In this thesis, LLO processes/methods of III-nitride semiconductor materials to integrate on dissimilar substrates were described. The separation of III-nitride light-emitting diodes (LEDs) grown on sapphire substrate by LLO has been presented for (0001) GaN, semipolar (11 $\bar{2}$ 2) GaN, and (0001) n-Al<sub>0.6</sub>Ga<sub>0.4</sub>N layers. The thermal analysis of temperature distribution induced by a high-power 248-nm KrF excimer laser pulse irradiation on GaN and n-Al<sub>0.6</sub>Ga<sub>0.4</sub>N grown on sapphire was simulated using COMSOL Multiphysics software. Due to the high optical absorption coefficient of GaN at the KrF excimer laser wavelength, the laser pulse induced a hot spot localized at the GaN/sapphire interface. A one-dimensional thermal diffusion model showed that the temperature rise was over 1000°C, coupled with a steep temperature gradient across the GaN material at a pulse energy density ( $E_i$ ) of 500 mJ/cm<sup>2</sup>. It indicated that the peak temperature at the interface is higher than the GaN growth temperature (i.e. 900-1100°C) which induces the thermal decomposition of the GaN film surface. However, the laser pulse with  $E_i \geq 600$  mJ/cm<sup>2</sup> is able to successfully perform LLO on n-Al<sub>0.6</sub>Ga<sub>0.4</sub>N/AlN in experiment. Based on the simulation the localized heat source is at the depth of ~ 60 nm into the n-Al<sub>0.6</sub>Ga<sub>0.4</sub>N layer with a peak temperature of 2108°C.

The transfer of (0001) GaN thin films from sapphire onto epoxy-bonded glass substrate and soldering-metal bonded (100) Si substrate was successfully demonstrated. Characterization of the transferred film by x-ray diffraction (XRD), optical microscope, and scanning electron microscope (SEM) showed the successful separation.

Furthermore, free-standing (FS) semipolar (11 $\bar{2}$ 2) bulk substrate and InGaN/GaN MQW LEDs ( $300 \times 300 \mu\text{m}^2$ ) emitting at 445 nm on HVPE-grown GaN template on patterned (10 $\bar{1}$ 2) r-plane sapphire substrate (PSS) were first realized by the separation from PSS using LLO. No detrimental effect in the light optical power was observed after LLO. The chemical-mechanical polishing (CMP) process was applied on the FS-LED membrane to remove GaN grooves for improving the light emission uniformity. After CMP, the measured light output power of the FS-LEDs ( $300 \times 300 \mu\text{m}^2$ ) slightly increased (14%) after separation from sapphire and a power of 0.87 mW was realized at 20 mA. Electroluminescence peak emission was almost unchanged with a peak shift less than 2 nm. Based on the polarizer angle-resolved EL spectra measurement, the polarization ratio was 0.14 and was independent of the GaN v-groove features. The LEDs showed an electrical-to-optical bandwidth of 166 MHz at 20 mA and a signal transmission data rate of 300 Mbps which is promising for visible light communications applications.

Two types of AlGaIn layer structure with n-AlGaIn as both sacrificial layer and n-contact layer were proposed for vertical structure deep ultraviolet (DUV) LEDs and substrate lift-off flip-chip DUV LEDs. The transfer of AlGaIn films from AlN template onto eutectic  $\text{Au}_{0.8}\text{Sn}_{0.2}$  soldering foil on Au layer covered Si substrate was implemented by wafer bonding and LLO processes. Optical microscope and XRD measurements showed the successful separation of  $\text{Al}_{0.6}\text{Ga}_{0.4}\text{N}$  from AlN/sapphire. To make the integration process complete, the development of a thermal compressive wafer bonding process for low-temperature transient liquid-phase  $\text{Au}_{0.8}\text{Sn}_{0.2}$  soldering was presented.  $\text{Au}_{0.8}\text{Sn}_{0.2}$  soldering metal-bonding was utilized to form a thermally and electrically conductive interface between the transferred GaN and carrier substrate. The bonding technique was applied at 320°C to form an eutectic compound for constructing Au- $\text{Au}_{0.8}\text{Sn}_{0.2}$ -Au layer. When an  $\text{Au}_{0.8}\text{Sn}_{0.2}$  foil is heated, the  $\text{Au}_{0.8}\text{Sn}_{0.2}$  layer melts to fill any voids or rough surface at the interface

of AlGaIn film/carrier-substrate. In order to attach the sample on the carrier substrate, a force of 30 N was applied on the bonding, while  $\text{Au}_{0.8}\text{Sn}_{0.2}$  reacts with Au to form the intermetallic compound. The versatility of  $\text{Au}_{0.8}\text{Sn}_{0.2}$  soldering foil eutectic thermal-compressive wafer-bonding was demonstrated by successfully joining and transfer of AlGaIn onto Si substrate, which made it possible to directly evaporate n-metal Ti/Al/Ti/Au on the exposed N-polar n-AlGaIn films to implement a vertical conducting configuration. However, the I-V characteristic of the electrical contacts on the N-polar n-AlGaIn showed non-ohmic behavior, which might be due to AlN residual on the interface of AlN/sapphire after LLO, a low donor concentration in the AlGaIn thin film and/or non-optimized n-contact metallization.

As a thermal evaluation of transfer-bonded ultra-thin optoelectronics emitters on dissimilar substrates, two-dimensional temperature distribution of transfer-bonded 3- $\mu\text{m}$ -wide-ridge AlGaAs/GaAs MQW thin film laser diodes with different cavity lengths and device configurations (e.g. p-metal thickness,  $\text{SiO}_2$  passivation layer thickness and with/without 100- $\mu\text{m}$ -thickness GaAs substrate) was modeled by the finite element method in COMSOL Multiphysics software. At the fixed ridge width and power dissipation (i.e. 40 mW), the maximum temperature at the junction can be effectively controlled by the thermal conductivity of the interposer (i.e. submount), thickness of submount and p-contact metal. It can be utilized to optimize the thermal management of the transfer-bonded thin film optoelectronics emitters.

## 6.2 Future work

The LLO process and wafer attachment method can be successfully used to implement the transfer of (0001) GaN, semipolar (11 $\bar{2}2$ ) GaN and (0001) AlGaIn on different substrate materials. However, more optimization of the LLO process on larger-scale wafer samples is required. For transfer-printing the GaN LEDs, a good anchor-holding structure and trench etching of the device mesa will be required for LLO which will enable transfer-print of GaN LEDs by a pick and place on Si based microsystem.

According to the high bandwidth and performance of the macro-scale (300  $\times$  300  $\mu\text{m}^2$ ) FS-(11 $\bar{2}2$ ) InGaIn/GaN MQW LEDs, a further improvement

of the devices should be investigated for optimization of the mesa size, metal contact scheme, geometry configuration and heat sink which are required to enhance the bandwidth and data transmission for visible light communication applications. Moreover, the polarization angle of the LED membrane should be studied for deeper understanding, which will be vital for a novel device.

The AlGaIn based DUV LEDs suffer serious heating issues and, thus, the transfer of the DUV LED epitaxial layer to a dissimilar substrate of high thermal conductivity, such as Si, Cu, and AlN, will be a good option. The AlGaIn sacrificial layer based n-AlGaIn template grown on sapphire substrate was proposed and successfully LLO processed. Optimization of the metal bond, either by varying the temperature and applied compression or with different metals systems, can be performed to increase the thermal stability of the bond interface. A better understanding of the n-metal scheme and N-polar n-AlGaIn to form ohmic contacts is vital for improving the devices.

The 2-dimensional finite element thermal model of the transfer-bonded thin film GaAs based laser diode, is built in COMSOL Multiphysics. It provides an easier way to simulate heat distribution in the laser diode at steady state, which can contribute to optimize the performance of transferred thin film optoelectronics devices. For the dynamic thermal performance of the devices, a self-consistent thermal model can be developed.